DEVELOPMENT OF MANUFACTURING TECHNIQUES FOR TI-BASED FUNCTIONALLY GRADED COATINGS

REZA MAHMOODIAN

THESIS SUBMITTED IN FULFILLMENT

OF THE REQUIREMENTS

FOR THE DEGREE OF DOCTOR OF PHILOSOPHY

FACULTY OF ENGINEERING

UNIVERSITY OF MALAYA

KUALA LUMPUR

2013

ABSTRACT

Coating techniques are commonly used in the ceramic-lined piping industries. However, the obtained ceramic layers are too brittle and fail under piping processes such as branching and making orifices. This is in consequence to improper manufacturing techniques, which do not guarantee functionally graded coatings or the local reinforcement of coatings. Therefore, to overcome such setbacks, the current research focuses on the development of manufacturing techniques for in-situ, locally reinforced composites with good mechanical properties. Various manufacturing techniques for the fabrication of ceramic and composite coatings have been proposed, designed, and implemented. Titanium carbide, silicon carbide, and alumina composite phases were processed under different manufacturing conditions. The developed centrifugal self-propagating high-temperature synthesis (SHS) technique helped to fabricate an in-situ titanium carbide-alumina-iron composite with several intermetallic phases successfully. The SHS reaction under centrifugal force design was such as to combine with a chain reaction between titanium and carbon elemental powders.

The developed centrifugal-assisted thermite method served to fabricate ceramic products in embedded and offset specimen positions. The elemental powders of titanium (Ti), carbon (C), and silicon (Si) were ball-milled and compacted into pellets, then exposed to a massive amount of heat generated from the thermite reaction of Fe_2O_3 and Al in a steel tube mounted in the developed centrifugal accelerator machine. The result was the formation of titanium carbide (TiC) and Al_2O_3-Fe composites. Evidently, the centrifugal force facilitated the formation of multi-component products and particle segregation during the process. In addition, centrifugal acceleration had a significant effect on both metallurgical alloying and mechanical interlocking between different sample layers when forming in-situ functionally graded coating with enhanced hardness

and good fracture toughness. Processing silicon carbide (SiC)-based composite coating was not feasible, unlike the successful formation of TiC.

A ceramic-coated pipe was produced using a conventional centrifugal thermite process. Consequently, the effects of an unexpected phase formed at the pipe's head on the joining and post-processing of the ceramic-lined composite pipe with Al_2O_3 and Fe layers were studied.

A plasma-assisted processing method was developed to fabricate ceramic parts and pellets under normal gravity and centrifugal force. Plasma-assisted reactions under normal gravity were successfully applied to fabricate SiC with large crystals of 270 μm and TiC with a highly crystallized super hard phase of 3660 HV hardness.

The analytical and modified smoothed particle hydrodynamic (MSPH) computational technique simulated the molten particles' motion on multi-scale analysis levels. The radial velocity and radial velocity gradient of molten alumina and iron infiltration inside the TiC product along with viscosity rate variations during the coating process were also simulated. The obtained results and conclusions are ultimately discussed, after which suggestions for future work are proposed.

ABSTRAK

Teknik salutan sering diaplikasi dalam industri perpaipan berasaskan seramik. Walau bagaimanapun, lapisan seramik yang diperoleh terlalu rapuh sehinggakan proses perpaipan seperti pencabangan dan pembukaan paip tidak dapat dijalankan. Oleh itu, untuk mengatasi masalah tersebut, penyelidikan ini memberi tumpuan kepada pembangunan teknik pembuatan untuk TiC-Fe komposit bersama dengan sifat mekanik yang baik. Teknik pembuatan yang berbeza untuk pembikinan seramik dan salutan seramik telah dicadangkan dan dikaji. Fasa titanium karbida, silikon karbida, alumina komposit telah diproses dalam keadaan yang berbeza. Pembuatan komposit titanium karbida-alumina-besi dengan beberapa fasa antara logam menggunakan pendekatan *"In-Situ"* telah berjaya dicapai dengan teknik penyebaran sintesis bersuhu tinggi (SHS). Tindak balas SHS dengan daya empar telah direka untuk menggabungkan tindak balas rantai antara unsur titanium dan serbuk karbon.

Kaedah empar dan proses pemanasan yang sedia ada telah diigunakan untuk pembikinan bahagian ceramik dalam posisi sampel terbenam dan ternaik. Serbuk titanium (Ti), sernuk karbon (C), dan serbuk silikon (Si) telah dikisar menggunakan pengisar bebola dan dipadatkan dalam bentuk pelet, kemudian didedahkan kepada haba yang besar yang dijana dari reaksi pemanasan Fe_2O_3 dan Al dalam tiub keluli yang dipasang dalam mesin pemecut empar yang telah dibangunkan.

Daya empar memudahkan pembentukan produk berbilang komponen dan pengasingan zarah semasa proses tersebut. Titanium karbida (TiC) dan komposit Al_2O_3 -Fe, adalah produk asas reaksi dari pemanasan telah terbentuk. Kewujudan pecutan daya empar mempunyai kesan yang baik terhadap pengaloian kedua-dua logam dan kunci ikatan mekanikal antara lapisan yang berbeza untuk membentuk fungsi *"In-Situ"* salutan bergred.

Paip seramik bersalut telah dihasilkan menggunakan proses pemanasan empar konvensional. Kesan lapisan Al_2O_3 dan Fe yang terhasil di kepala paip semasa pasca-pemprosesan paip garisan seramik kompositt elah dikaji. Hasil dari corak pembelauan sinar-X (XRD), menunjukkan bahawa keamatan fasa Alumina bertambah apabila jarak bertambah daripada kepala paip.

Kaedah pemprosesan plasma terbantu telah dibina untuk menghasilkan bahagian seramik dan pelet dibawah graviti normal dan tinggi. Reaksi dari plasma terbantu di bawah graviti normal telah digunakan dalam pembikinan silikon karbida dengan kristal sebesar 270 μm. Fasa titanium karbida dengan penghabluran tinggi dan dan berkerasan tinggi sehingga 3660 HV telah diperolehi.

Model beranalisis dan berangka telah dibangunkan untuk mengkaji kadar kelajuan penyusupan besi di dalam produk TiC dan perubahan kadar kelikatan semasa proses salutan. Teknik zarah hidrodinamik terlicin (MSPH) telah digunakan untuk mensimulasikan pergerakan zarah lebur pada tahap analisis berbilang skala. Halaju jejari adan kecerunan halaju jejari bagi peleburan alumina dan besi didalam produk TiC, serta kadar kelikatan variasi semasa proses salutan dilakukan telah disimulasikan. Keputusan yang diperolehi telah dibincangkan dan perancangan kerja masa depan telah dicadangkan.

ACKNOWLEDGEMENT

"He who taught by the pen, taught man that which he knew not" 4-5, Sura 'Alaq (The Clot) No. 96. Thank you, Lord, for helping and protecting me.

My dear supervisors, Prof. Dr. Mohd Hamdi bin Abd Shukor, and A/P Dr. Mohsen, thank you for your full support and guidance throughout my PhD research work. Thank you for showing me routes to success, such as applying analytical methods. I feel that I could never sufficiently acknowledge your impact on my life.

My gratitude also goes to the centre of advanced manufacturing and material processing (AMMP), its members, and staff for their support, especially Dr. Farazila Yusof, Mr. Fadzil Jamaludin, and Mr. Mahdi Sparham. I would like to thank Prof. Dr. Rosiyah Bt Yahya and Dr. Reza Rahbari G. for sharing their comments.

Special thanks to the Azarin Kar Industrial Company (AKIC), whose facilities were available for experimentation without limits. Thanks to the CEO, Mr. Ali Mahmoodian, my father, for the excellent technical consultation and facility preparation. Thanks to Mr. Sajjad Ghadirian, the AKIC research staff for his kind assistance.

Last not the least; my special thanks extends to my beloved wife, Leila, who has been always there and motivated me. Countless thanks go to my great parents in Iran, who have supported and motivated me morally and financially, so that I would stay on a straight path and pursue my goal. Thanks to my parents in-law, all the people and friends who have assisted me, but whose names are too numerous to list.

TABLE OF CONTENTS

LIST OF TABLES

LIST OF FIGURES

LIST OF SYMBOLS AND ABBREVIATIONS

Symbols and Abbreviation	Description
°C	Degrees Celsius
°K	Degrees Kelvin
a	Acceleration
AC	Alternating Current
Al	Aluminum
Al_2O_3	Alumina
Ar	Argon gas
CLCCP	Ceramic-Lined Compound Copper Pipe
Cm	Centimeters
Co.	Company
C-T	Centrifugal Thermite
DC	Direct Current
DIN	Deutsches Institut für Normung (German Institute For Standardization)
E	Elasticity Modulus
Eit	Elasticity Modulus
ed	Edition
EDX	Energy-Dispersive X-Ray Spectroscopy
exp	Exponential
F	Force
Fe	Iron
Fe_2O_3	Iron oxide III
FESEM	Field Emission Scanning Electron Microscope
FGMs	Functionally Graded Materials
g	Gravitational Acceleration
HV	Vickers Hardness
Kg	Kilograms
kJ	Kilojoules
kW	Kilowatts
L	Length

LOM	Light Optical Microscope
Lp	Pitch Length
m	Meters
mm	Millimeters
mm/s	Millimeters per second
MSPH	Modified Smoothed Particle Hydrodynamics
n	Rotational Speed
N	Newton
η	Viscosity
ω	Angular Velocity or Circular Frequency
Pa	Pascal
π	Pi
ProE	Pro Engineer Software
r	Radius
RPM	Revolution per Minute
RPS	Revolution per Second
SEM	Scanning Electron Microscopy
SHS	Self-Propagating High-Temperature Synthesis
Si	Silicon
SiC	Silicon Carbide
SPH	Smoothed Particle Hydrodynamics
t	Time
Ti	Titanium
TiC	Titanium Carbide
W	Weight
WC	Tungsten Carbide
WC-EDM	Wire Cut Electrical Discharge Machine
XRD	X-Ray Diffraction

CHAPTER 1:INTRODUCTION

1.1 General background

Steel pipe life span is very short for transporting abrasive and corrosive materials, which results in costly replacement and maintenance. There are two ways to overcome this problem. One of the best, economical solutions to increase the life span of steel pipes is to coat their internal surface with a ceramic layer.

Traditionally, ceramic lined the interior of pipes, as glued ceramic pieces side by side. This method is very time consuming, costly and usually unreliable. Such ceramic coating is dependent on the skills of workers. Besides, the maintenance for abrasive powder and transport of chemicals is very costly and time consuming, and at times unplanned shutdowns occur. A ceramic-lined steel pipe produced by thermite-based self-propagating high-temperature synthesis (SHS) method under centrifugal force is one of the optimal solutions to overcome these drawbacks.

Thermite reactions produce an enormous amount of energy as heat. The generated heat is occasionally enough to instigate another reaction that requires some initial energy. The alternative of using other methods would be restricted if the second reaction had to undergo centrifugal force simultaneously. Thus, combining the thermite reaction and a second reaction under centrifugal acceleration is a key point.

1.2 Self-propagating high-temperature synthesis

Self-propagating high-temperature synthesis (SHS) leads to the in-situ production of composites with reactive initial substances via exothermic chemical reaction (Odawara, 2010). The heat produced by the reaction ignites and sustains a propagating combustion front through the reactants, creating the anticipated product (Wang & Yang, 2007). SHS,

also known as combustion synthesis, is characterized by high temperatures that make it an alternative, economical method for ceramic industries compared to conventional ceramic processing. SHS is a feasible technique for producing advanced ceramics, catalysts, and nanomaterials (Greco et al., 2009). Combustion synthesis is a versatile means of synthesizing a variety of technologically useful solid materials, such as binary and ternary metal borides (Yeh & Wang, 2011), carbides (Jin et al., 2009), silicides, chalcogenides, and nitrides (Rubtsov et al., 2010), hydrides (Park et al., 2012), alloys (Feng et al., 2012), composites (Burkes & Moore, 2006), cemented carbides (Feng et al., 2010) or nano-composite materials (Lin et al., 2010) in a single processing step in contrast to conventional ceramic processing. The main advantages of SHS are:

- It requires less energy than conventional methods;
- The short reaction intervals result in lower operating and processing cost along with time reduction;
- No expensive processing equipment is required;
- Inorganic materials can be synthesized and aggregated into a final product in a single step by using the reactants' chemical energy;
- The high reaction temperature may expel volatile impurities and oils, and thus result in highly pure products;
- The high thermal gradient and rapid cooling may yield non-equilibrium phases (Schubert & Hüsing, 2005).

SHS reactions feature adiabatic combustion temperatures (T_{ad}). This can be deliberated by assuming that the enthalpy of the reaction heats up the products and that no energy is lost by heating the adjacent surroundings. Thus, T_{ad} is a degree of the exothermicity of the reaction and outlines the upper limit for any combustion system. Empirically, if $T_{ad} < 1200$ ˚C, combustion does not take place, and if $T_{ad} > 2200$ ˚C, self-

propagating combustion occurs. In the range of $1200 < T_{ad} < 2200$ ˚C, a combustion wave cannot propagate but can be prompted to, by a particular method such as pre-heating the reactants; for instance, the reaction $\mathrm{Si + C \rightarrow SiC}$ $\left(T_{ad} = 1527, T_{ad} = 1300\ ^{\circ}C\right)$ is not self-sustaining when T_{start} = 25 ˚C, whereas $\mathrm{Ti + C \rightarrow TiC}$ $\left(T_{ad} = 2937, T_{ad} = 1027\ ^{\circ}C\right)$ (Schubert & Hüsing, 2005).

$$Fe_2O_3 + 2Al \rightarrow Al_2O_3 + 2Fe + 836\,kJ\,mol^{-1} \qquad \text{Eq. 1.1}$$

$$Ti + C \rightarrow TiC + 183\,kJ\,mol^{-1} \qquad \text{Eq. 1.2}$$

$$\mathrm{Si + C \rightarrow SiC} + 75\ kJ\,mol^{-1} \qquad \text{Eq. 1.3}$$

Combustion synthesis reactions are challenging to control due to the extreme reaction rates. However, a number of control means are possible. First, the relevant reaction factors that control self-propagating high-temperature reactions have been examined (Mossino, 2004; Persson et al., 2002). The factors are reactant particle shape and size, green density, powder mixing and compaction, impurities, reaction stoichiometry, volatiles and diluents, reaction environment, mode and technique of ignition, heating speed, and the effect of these parameters on heat generation, exothermicity and SHS reaction mechanism (Lee & Chung, 1997).

- Adding diluents that do not partake in the reaction to the green mixture nevertheless increases the system's thermal mass and decreases T_{ad}. The diluents can be from the anticipated product. In case of thermite reactions, Al_2O_3 or ZrO_2 play an inert role in the reaction.
- Using a bigger particle size of the reactants leads to lowered combustion wave speed and increased reaction rate, as expected for solid-solid reactions.

1.3 Ti-based functionally graded coating

Processing functionally graded materials (FGMs) using centrifugal SHS was introduced by Lai et al. (1997). Subsequently, several researchers have attempted to facilitate and model SHS FGMs (Birman & Byrd, 2007; Gowtam et al., 2008; He et al., 2009; Watanabe et al., 2009). Munir et al. (2000) categorized ceramic-lined composite pipes as FGMs. Moreover, earlier research mainly focused on the implementation of SHS processes into different aspects of ceramic-lined pipes.

So far, there remain certain technical problems regarding the post-processing of ceramic-lined tubes in industries. For instance, pipe failure may occur when making an orifice or opening in a ceramic-lined pipe. The ceramic layer could also sustain macro cracks followed by crack propagation, which would reduce pipeline service life and potentially cause unplanned plant shutdowns (Odawara, 1990; Yu et al., 2006). Diverse methods have been proposed to address these issues, including suggestions to employ different pipe materials like stainless steel (Xi et al., 2000) or copper (Du et al., 2005). Yet, no proposals have been made to apply locally reinforced pipes in a single-step SHS process to obtain FGMs coating. However, various local reinforcement components such as titanium-based FGMs are expected to prevent crack propagation at joints and holes.

In this thesis, single-step manufacturing techniques of Ti-based functionally graded coating for ceramic-lined composite pipes have been developed. The techniques utilize the thermite reaction between Al and Fe_2O_3 under centrifugal acceleration to fabricate locally TiC reinforcing pellets at desired positions of the inner pipe surface. Centrifugal acceleration significantly affects both metallurgical alloying and mechanical interlocking between different layers during product formation and enhances the functionally graded mechanical properties in a radial direction.

Therefore, the formed coating is a strong FGM with a titanium aluminide intermetallic layer. It is necessary to examine the mechanical properties, chemical composition, and

microstructure of the produced coating over the radial direction. The variations can thereby be customized according to the desired mechanical properties.

1.4 Importance of study

The high cost of steel pipe maintenance in various industries, especially those utilizing steel pipes to carry coal, ores, or any abrasive and corrosive materials, has increased the need for longer service life and new products. Any increment in the lifetime of steel pipes might be significant, particularly when the benefits loss of having plant using old pipes while the plant halts due to unplanned shutdowns or repetitive planned shutdowns are greater than using ceramic-lined steel pipes as an alternative. In piping industries, whole-length pipes are not always being used. The desired pipe length is supplied to the welders by cutting, sectioning, getting a branch, or making orifices. The local reinforcement of composite pipes in from of Ti-based functionally graded coating can increase the service life of a pipe. In such case, due to a decrease in overall maintenance time, the use of ceramic lined steel pipes is feasible and sustainable to plant productivity.

1.5 Study Objectives

The objectives of this thesis are as follows:

- To develop, design, and fabricate manufacturing techniques for Ti-based functionally graded coatings under centrifugal and normal gravity conditions;
- To analyze and evaluate the developed manufacturing techniques for TiC-Fe-$TiAl/TiAl_3$ and SiC in ceramic-lined composite pipes;
- To model and analyze the deposition and infiltration mechanism under centrifugal acceleration in the developed technique by smoothed particle hydrodynamics (SPH) and analytical model.

1.6 Motivation

The aim of increasing the service life of products in manufacturing plants has always been a topic of interest. Greater product service life would diminish shutdown time as well as emergency maintenance. Ceramic-lined composite pipes were initially introduced as replacement for sticking ceramic pieces. In the piping of industrial plants, branches are inevitable, necessary components of sub-lines. The ceramic-lined pipes can show weakness during post-processing, when the transporting fluid is corrosive and eroding. Therefore, this study focuses on the development of manufacturing techniques Ti-based functionally graded coating for the local reinforcement of ceramic-lined pipes using in-situ SHS.

1.7 Research scope

The scope of the research is to integrate manufacturing with material engineering. Developing a special test rig is required to conduct new research on centrifugal SHS products. In the current research work, a test rig was built to facilitate the study after performing a few preliminary experiments. The apparatus was made as simple as possible to maintain the feasibility of the SHS concept and so that it can be adopted in laboratories to a broad range of exothermic ceramic lining techniques. The centrifugal thermite reaction plays a fundamental key role in facilitating the fabrication of locally reinforced functionally graded coatings.

1.8 Contribution

In this thesis, the experimental techniques have been simplified so they can be reproducible. Five processing methods were developed and evaluated. Functionally graded coatings made of TiC-Al_2O_3-Fe, TiC/C, and SiC were produced. Numerical and analytical models were successfully employed to understand and simulate the particle deposition rate, velocity, and velocity gradient. The immediate outcome and contribution

of this research work to the world of knowledge comprises three high-impact ISI publications and some under preparation and review.

1.9 Outline of the thesis

The outline of this thesis is as follows. The opening chapter introduces the importance of the study, Ti-based coatings, SHS, and the current problems that need to be resolved. Chapter 2 covers a background into various states of matter. It provides a brief review of combustion synthesis, the smooth particle meshless method, TiC-Fe, and SiC properties. Chapter 3 represents an overview of the experimental methods adopted in the study, the characterization technique, as well as the Nano and Micro mechanical methods used. Chapter 4 primarily concerns the test rig designs for centrifugal and plasma-assisted methods as well as safety considerations in the design process. Chapter 5 elaborates the experimental works and processing according to the five proposed experimental methods. Analytical and modified smoothed particle hydrodynamics (MSPH) models for the simulation of centrifugal-assisted TiC-Fe-Al_2O_3 combustion synthesis are presented in Chapter 6. The properties of molten alumina and iron, such as velocity, velocity gradient, and viscosity, are simulated. A profound result illustration and a discussion of the obtained products are presented in Chapter 7. Finally, Chapter 8 concludes and provides recommendations for possible areas of new work in the future.

CHAPTER 2:LITERATURE REVIEW

2.1 Introduction

The current chapter contains a brief review of existing works on combustion synthesis, and centrifugal-assisted combustion synthesis of thermite reactions, titanium carbide, and silicon carbide.

2.2 Background on Combustion Synthesis

In self-propagating high-temperature synthesis (SHS), primary reagents, upon ignition, rapidly transform into new products due to the exothermic reaction (Merzhanov, 2011; Odawara, 2010). The same process is known by other technical expressions like combustion synthesis, gasless combustion, and self-propagating exothermic reaction (Munir, 2001; Patil et al., 2002). This process has been developed over time from studies done on the combustion of solid cylindrical compacts such as Ti-B mixtures by Merzhanov and Borovinskaya (1971) at the Institute of Chemical Physics, Academy of Sciences of the former Soviet Union (USSR) in Chernogolovka near Moscow. Activities followed in America, Japan, China and other places subsequent to Crider's publication on this technique in 1982 (Crider, 1982; Munir, 2001; Zhu et al., 2011).

Countless attempts are made to do SHS research in a logical way, as seen in many relevant examples from literature. As mentioned earlier, combustion synthesis entails highly exothermic reactions. Such reactions usually have immense activation energies and produce extensive amounts of heat (Merzhanov, 1996; Moore & Feng, 1995; Subrahmanya & Vijayakumar, 1992). Once the reaction is initiated by the fast input of energy from an external source, such as an electrical arc, oxyacetylene flame, laser pulse, microwave field, a spark or chemical reaction, sufficient heat is released to render the

reactions self-sustaining (Hobosyan et al., 2011; Korchagin et al., 2003; Mousavian et al., 2011) or in the form of mechanical activation (Mousavian et al., 2011). Accordingly, the reactants are heated quickly to a very high temperature. The reactions are so rapid that they are pseudo-adiabatic; for example, all the energy created by the exothermic reaction heats up the specimen. Combustion synthesis may be managed in self-propagating and simultaneous combustion modes, with many reactions in between (Schubert & Hüsing, 2005).

In the self-propagating method, also known as "steady mode," the combustion reaction begins at one point and then propagates quickly through the reactant green mixture in the form of a combustion wave. In this case, the heat from the reaction ensures the energy required for the rest of synthesis (Odawara, 1982).

Combustion synthesis is a flexible way of synthesizing a diversity of technologically functional solid materials, such as binary and ternary metal borides (Yeh & Wang, 2011), carbides (Greenwood & Earnshaw, 1997; Jin et al., 2009), silicide, chalcogenides, and nitrides (Rubtsov et al., 2010), hydrides (Park et al., 2012), alloys (Feng et al., 2012), composites (Burkes & Moore, 2006), cemented carbides (Feng et al., 2010), or composite materials (Lin et al., 2010) in a single processing step in contrast to conventional ceramic processing, which is among the main advantages of SHS processing (Schubert & Hüsing, 2005).

2.3 Centrifugal thermite SHS process

Serkov, Maksimov, and Merzhanov first studied the influence of centrifugation on the combustion of gasless systems in 1968. Centrifugal acceleration up to 900g could cause a six-fold increase in the combustion velocity in a thermite system (Yukhvid et al., 2000).

When centrifugation performs in thermite mixtures, it provides liquid-phase products since SHS is a multi-state process. Generally, a multi-state process includes:

1- Combustion and design of the chemical composition of the melted product

2- Lamination of jointly insolvable metallic and oxide phases

3- Crystallization and development of the SHS products' phase composition and structure

Each state includes a number of simultaneous chemical and physical processes. Centrifugation has considerable effect on all of these processes. The course of phase separation in centrifugal thermite can be determined from the difference between the metal and oxide (ceramic) phase densities. Hence, reducing the metallic phase by adding extra aluminum to the CrO_3-Al or Fe_2O_3-Al mixture led by reverse phase separation of the liquid phase combustion products, Cr-Al and Al_2O_3 or Fe-Al and Al_2O_3 (Munir et al., 2000). Figure 2.1 illustrates the general steps of a combustion reaction in a solid-solid system.

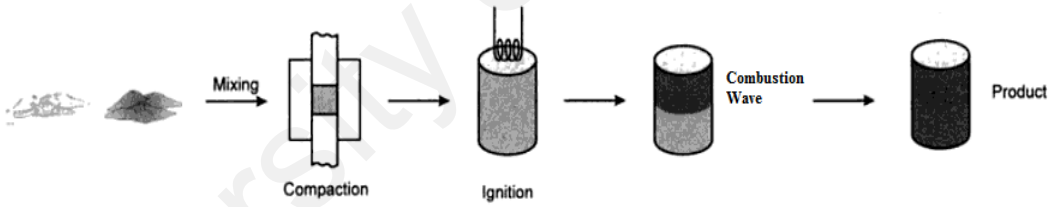

Figure 2.1: Schematic illustration of the self-propagating combustion mode (Schubert & Hüsing, 2005)

2.3.1 Centrifugal and centripetal forces

When a body revolves about an axis, it is forced to deviate toward the axis constantly. This opposing force is known as centripetal force. The equal and opposite resistance offered by the body to the connection is called the centrifugal force.

The acceleration toward the center necessary to keep a particle moving in a circle about that axis is v^2/r .

$$Centrifugal\ Force = {w.v^2}/{g.r} = {m.v^2}/{r} = {w.\omega^2.r}/{g}$$

where w and m are the weight and mass of the whole body, respectively; r is the distance from the axis about which the body is rotating to the body's center of gravity; w is the angular velocity of the body about the axis in radians/sec; and v is the linear velocity of the center of gravity of the body (Avallon et al., 1996).

2.3.2 Required rotation speed to satisfy acceleration needs

Simply put, centrifugal force is:

$$F = ma = \frac{mv^2}{r} = \frac{\mathrm{m}.v^2}{r} = \frac{m\left(\frac{2\pi N}{60}.r\right)^2}{r} = \frac{m.\pi^2.N^2.r}{900}$$

$$N = \frac{1}{\pi}\sqrt{\frac{900.a}{r}} \qquad \text{Eq. 2.1}$$

where m = mass (kg), v = speed m/s, r = pipe radius (m), N = rpm, g is gravity acceleration = 9.81 ${m}/{s^2}$, and the required centrifugal acceleration is a = n.g ${m}/{s^2}$ where n is the scale factor.

2.3.3 Advantages of SHS

Rogachev and Baras (2007) discussed the main advantages of the SHS process, which are summarized below.

- The SHS process requires less energy than conventional methods;
- The short reaction time of SHS results in low operating and processing cost as well as time reduction;
- Expensive processing equipment is not necessary for SHS;

- Inorganic material can be synthesized and merged into a final product in one step by employing the chemical energy of the reactants;
- The high reaction temperatures in SHS may expel volatile impurities and thus result in highly pure products;
- The high thermal gradients and rapid cooling rates can give rise to non-equilibrium phases;
- The process can be used not only for producing various high temperature materials but also to produce near net-shape components by combining the exothermic heat with processes such as casting, consolidation and coating.

2.3.4 Controlling the SHS processes

Combustion synthesis is difficult to control because of the high reaction rates. However, some methods of controlling SHS include:

- Addition of diluents that are not involved in the reaction, but which increase the thermal mass of the system and decrease adiabatic temperature. The diluents may be one of the products (e.g., the rate of the highly exothermic reaction of aluminum and ferrous oxide III reduces by adding some alumina powders), or an inert compound (Sen et al., 1997).
- Increasing the reactant particle size will surge the thermal mass of the combustible mixture. Consequently, combustion wave velocity and reaction rate decrease as expected for solid-solid reactions (Sen et al., 1997).
- Cooling the sample during the SHS reaction lowers the temperature and combustion wave velocity.

2.3.5 Centrifugal force

A common method of SHS product densification is to exert centrifugal force onto the products of the exothermic reaction. This approach is widely practiced when producing hollow cylindrical shapes from high-temperature materials.

2.3.6 Centrifugal SHS general scheme

The universal scheme of centrifugal SHS products from the ensuing reaction is shown in Eq. 1.1. Centrifugal machines of various designs have been developed at the Institute of Structural Macrokinetics of the USSR Academy of Sciences. There are two types of such machines, radial and axial. They work in open and tight combustion modes, as well as in dosed gas discharge from the chamber by Yukhvid (1992). The third combustion mode is the most expedient since it allows the combination of g-load (g is the free-fall acceleration or gravitational acceleration magnitude) action with the gas pressure and does not need remote gas release control. The existing radial designs of centrifugal machines make it possible to produce g-loads of up to 2000g and to obtain cast items of up to 1kg. Drill bit blocks and cutting picks, rings and bushing made of hard alloys on the base of titanium-chromic carbide, gas torch nozzles, and protective wear-resistant elements from gradient and oxide-cermets materials are manufactured with the aid of these machines. Hard alloys based on titanium-chromic carbide have hardness values of up to 90HRA (Rauscher et al., 2000).

2.3.6.1 Centrifugal SHS Mechanism

This process mechanism is based on the rate of a thermite reaction comprising Fe_2O_3 and aluminum in a field of centrifugal forces, and it facilitates the preparation of coatings comprising a ceramic layer of alumina in the innermost region of the pipe and an iron layer between the steel pipe and alumina. The effect of various operating parameters on coating stratification and adhesion is studied using this scheme. The centrifugal

acceleration appears to be the most significant processing control variable by altering the rotating speed of the pipe using a computer (Orru et al., 1996).

Munir et al. (2000) mentioned this as a novel aspect of the imposition of centrifugal force during the combustion synthesis of composite materials for structural, optical, or electronic applications; the outcome is that the composition and particle size of the metallic (or ceramic) constituent varies continuously throughout the thickness of the product.

Lin et al. (2002) found that thermite combustion is predominantly controlled by gas phase reactions. If the thermite mixture loosely fills the pipe or there are holes in the thermite, the gas phase diffuses through the thermite under the pressure of molten products, resulting in a rapid combustion rate. While the thermite densely fills the pipe and there are no holes, the greater filling density hinders gas phase diffusion, resulting in a slow combustion rate. Furthermore, combustion rate increases with greater inclined pipe angle.

According to Odawara (1988), owing to the thermal expansion and shrinkage of each layer throughout the C-T process, some interruption is anticipated in the outer metal layer compared to the product layers. Subsequently, the melting point of the formed ceramic is much higher than that of the metal, and the heat propagates in a radial direction. The outer pipe would still be expanding when the produced ceramic starts to solidify and it would shrink because of the delay in temperature increase. After the outer steel pipe's temperature begins cooling, the metallic layer contracts much more than the ceramic layer. Therefore, the compression stress remains in the ceramic layer. The size of the pipes produced is always a little smaller in diameter and length, so that the intermediate metal layer formed plays a role in balancing the residual stress of each layer. The combustion temperature would be above 2400°K.

A molten mixture including molten metal (e.g., Fe) and molten oxide (e.g., Al_2O_3) will be separated and arranged under the effect of centrifugal force and density difference; also, alumina may cover the innermost layer and form a ceramic film (Mu et al., 1997).

The estimated speed of reaction propagation along the pipe between specific points was 200-700 $mm.s^{-1}$ for a one-ended closed pipe, while for an open-ended pipe the velocity started between 600 to 1500 $mm.s^{-1}$. The thermite reaction progressed in the following way: upon sample ignition, the reaction propagated along the interior surface and then continued to the outer pipe wall. According to the results, high-temperature vapor generated by the thermite reaction propagated very fast on the inner tube. Next, the reaction propagated from the inner surface of the thermite mixture to its outer surface at the metallic pipe wall (Miyazaki & Odawara, 2000).

2.3.6.2 Ceramic-lined composite pipe applications

A ceramic-lined composite pipe is a sort of high-performance, high temperature-resistant, anti-corrosion and wear-resistant tube. It is widely applied in several fields, such as the petrochemical industry and metallurgy, is very suitable for the transport of abrasive materials, and finds a wide range of functions in mining, power plants, water conservation, coal, building material industries, cement industries, chemical industries, and so on (Wang & Yang, 2007; Zhang et al., 2002).

2.3.6.3 Centrifugal thermite process

The centrifugal SHS process of Fe_2O_3 and Al is a spontaneous reaction propagation and simultaneous rapid synthesis under the effect of centrifugal force. The reaction takes place in the inner surface of the pipe after melting the Al and reducing the Fe_2O_3 in the initial stage (Yu et al., 2010). A self-sustained exothermic reaction (Eq. 1.1) propagates through a premixed powder in the form of a high-temperature reaction wave with fast heating rate and short reaction time. This is followed by phase separation and the

solidification of Al_2O_3 and Fe products (Li et al., 2003). The product of the centrifugal SHS reaction between Fe_2O_3 and Al is a metal-ceramic Al_2O_3-Fe composite (Rogachev & Baras, 2007). The adiabatic combustion temperature of the centrifugal SHS reaction can reach up to 2400ºC, which is higher than the melting points of Al and Fe_2O_3 (Chatterjee et al., 2008; Sun et al., 2008). The advantage of this procedure is that once ignited, no further externally applied energy is necessary. The processing time is reduced and the products are normally of high purity (Merzhanov, 1990; Yu et al., 2010). The general scheme of ceramic-lined steel pipe production using the centrifugal SHS technique is sketched in Figure 3.1.

Thus, the simple, rapid, and economical centrifugal SHS process has been employed to produce various types of metal-ceramic composite pipes. Ceramic-lined pipes have so far been applied in several areas, such as petrochemical, metallurgy, chemical and mining industries (Andreev et al., 2011; Lai et al., 1997; Zhou et al., 2010).

2.3.6.4 Efforts on modifying the SHS technique

In recent years, a number of papers have reported on the centrifugal thermite (C-T) process and demonstrated the importance of this procedure. Some significant attempts to optimize the SHS process are presented in the following reports.

Pei et al. (2009) fabricated bulk Al_2O_3 by combustion synthesis melt casting under ultra-high gravity bulk. The densification of Al_2O_3 could be followed quickly complete such a melt-casting process in contrast to conventional sintering approaches. A fundamental practice of this technique was to create pores with superheating melt mixtures of metal (Ni) and ceramic (Al_2O_3) by employing the exothermic heat from the combustion synthesis reaction, followed by the separation of the three phases comprising molten metal, molten ceramic and the pores, by virtue of the three phases' density difference. Bulk dense Al_2O_3 with well developed (1 1 0) and (2 1 1) texture was

processed by combustion synthesis melt-casting under an ultra-high gravity process to produce a non-equilibrium structure with distinctive properties and possible new functions.

Meng et al. (2007) studied the microstructure and mechanical properties of multilayer-lined composite pipes prepared by SHS centrifugal-thermite process. An Al2O3–TiO2–TiC multiphase ceramic coating was produced on the inner surface of the pipe with the centrifugal combustion synthesis technique. The coating contained an intermetallic layer of AlFe–AlCrFe–NiFe and a multiphase ceramic layer. The addition of Ti, Ni, and B_4C enhanced the metallurgical joining of the intermetallic layer to the ceramic layer and substantially enhanced the pipe's mechanical properties. The shear and compressive strengths of the multilayer-lined pipes enhanced compared to values obtained for pipes from the Fe_2O_3 + Al reaction system prepared with the SHS C-T process.

Some researchers have been working on other substrates rather than steel, such as copper. Du et al. (2005) started to study a ceramic-lined compound copper pipe (CLCCP) produced by centrifugal combustion synthesis casting. The thermite with CuO and Al powders released a massive amount of heat after the thermite reaction, which led to an immediate increase in system temperature to 2844°K. The products Al_2O_3 and Cu rapidly melted. Because of the products' density disparity, CLCCP with good wear resistance, corrosion resistance and heat resistance is achievable under the action of centrifugal force. Adding SiO_2 and CrO_3 to the thermite could diminish the porosity of the ceramics and improve the densification grade. The SiO_2 would also decrease the hardness of ceramics. Adding $Na_2B_4O_7$ to the thermite may improve the compression-shear strength of the CLCCP, while adding ZrO_2 could enhance the toughness of the ceramics. The service life of CLCCP is reportedly two times longer than that of ordinary copper pipes (Du et al., 2005).

In this research, an SHS-centrifugal machine was uniquely fabricated to produce ceramic-lined steel pipes from a Fe_2O_3+Al mixture. Fe_2O_3 and Al powders were mixed based on reaction stoichiometry, in a similar way to Odawara (1990) combination in terms of mixture. The process was based on the thermite reaction of Fe_2O_3 and Al under centrifugal force to produce Al_2O_3 ceramic in the innermost layer and molten Fe that diffused into the steel pipe.

2.4 Carbide compounds for key industrial applications

Greenwood and Earnshaw (1997) defined carbide as a compound composed of carbon and a less electronegative element. Then they classified carbides by chemical bonding type as follows: (i) salt-like, (ii) covalent compounds, (iii) interstitial compounds, and (iv) "intermediate" transition metal carbides. Examples include titanium carbide, silicon carbide, tungsten carbide (often called simply carbide), and cementite, each used in key industrial applications. In this research study, the term carbide refers to the interstitial compound carbide.

2.5 Titanium properties

Titanium is a metallic element with low density (4.506 $g \cdot cm^{-3}$), high melting point (1668 °C) and high strength-to-weight ratio (Boyer, 1996). Titanium is a very reactive element when exposed to oxygen. It becomes oxidized and forms a surface layer of titanium dioxide with a thickness of approximately several nanometers, which functions as a protective layer (Zhang et al., 2001).

As an alloy, titanium is resistant to corrosion (Vasilescu et al., 2012) and is considered a high-temperature service material. Titanium has high hardness but not as high as certain grades of heat-treated steel, it is non-magnetic and is a poor heat and electricity conductor. Machining requires precaution, as the material will soften and gall if sharp tools and correct cooling approaches are not used (Kakani, 2006). The metal is a dimorphic

allotrope whose hexagonal closed packed (HCP) alpha form modifies into a body-centered cubic (lattice) β form at 882 °C (Pop et al., 2011).

2.5.1 Titanium Carbide (TiC)

Titanium carbide (TiC) formed from Ti and C self-sustained reaction is characterized by high hardness, good wettability, low density, chemical stability (Das et al., 2002) which is typical of transition metal carbides, and high melting point (Friedrich et al., 2011). Titanium carbide powder can be synthesized by various approaches, including self-propagating high-temperature synthesis (Holt & Munir, 1986), carbothermal reduction of oxides (Koc & Folmer, 1997), thermal-plasma synthesis (Tong & Reddy, 2005), chemical vapor deposition (Pearce & Marek, 1968) and sol–gel process (Rambo et al., 2005). The combustion (reaction) between titanium and carbon elemental powder is exothermic and the liberated heat produces titanium carbide (Holt & Munir, 1986). Titanium carbide (TiC) formed from a Ti and C self-sustained reaction features high hardness, good wettability, low density and chemical stability with an Fe-based matrix (Das et al., 2002).

The hardness properties of TiC produced via single-stage SHS are not desirable because of the compact nature of the green powder (Du et al., 2013). Therefore, a special plasma reaction chamber was developed to produce TiC under extreme thermal conditions and to maintain a sufficiently high temperature to allow the initial compacted powder to react, melt, and re-crystallize. TiC has the capacity to be used as a machining insert tool, local enforcement of a secondary process such as ceramic-lined composite pipes, and as a thin product in super-capacitor industries (Sonnenburg et al., 2009).

2.5.1.1 Titanium carbide properties

Titanium carbide is relatively oxidation-resistant up to 1100 ˚C due to the formation of titanium oxides. These oxides also reportedly act as a good solid-state lubricant

(Hamedi et al., 2011). The excellent properties have brought it to attention for high performance applications. TiC particulate application has been noted in wear-resistant parts, thermal fatigue, erosion-resistant materials, and high performance tooling (Koc & Folmer, 1997; Maitre et al., 1997). The hardness of stoichiometric TiC apparently has values of up to 3200 HV (31.38 GPa) (Tjong & Ma, 2000).

2.5.2 TiC-Fe-Al_2O_3 functionally graded materials and its intermetallic components

There are a number of publications on the synthesis of TiC-reinforced Fe-based composite (Bandyopadhyay et al., 2004) using different starting compounds under non-centrifugal acceleration. Gowtam et al. (2008) investigated Fe-TiC steel functionally-graded materials (FGMs) using SHS reaction followed by centrifugal casting. FGMs are characterized by continuous, smooth variations in microstructure and/or composition to encounter functional performance necessities that differ with position within a part (Gao & Wang, 2000).

In another study conducted by Huang et al, TiC-TiB_2 ceramics were prepared using combustion synthesis under a high gravity field (Huang et al., 2012). The adiabatic combustion temperatures of the SHS reactions of Fe_2O_3+Al and Ti+C reached up to 3622 and 3290 ºC (Gowtam et al.), which are higher than the melting points of Al and Fe_2O_3 (Patil et al., 1997). The advantage of this process is that once ignited, no further externally applied energy is required to complete the reaction (Merzhanov, 1990). The formation behavior of TiC in the Fe–Ti–C system during combustion synthesis was studied by Zhang et al., who found that with Fe content increment, the ceramic particle sizes and adiabatic reaction temperatures markedly decreased (Zhang et al., 2011).

As explained earlier, the centrifugal SHS process of Fe_2O_3 and Al is a spontaneous reaction propagation and simultaneous rapid synthesis under the effect of centrifugal acceleration. The reaction occurs in the inner surface of the centrifugal tube where the Al

melts and Fe_2O_3 reduces in the initial stage. The self-sustained exothermic reaction propagates through a pre-mixed powder in the form of a high-temperature reaction wave with rapid heating rate and short reaction time. This is followed by phase separation and solidification of the Al_2O_3 and Fe products (Li et al., 2003). Finally, the product of the centrifugal SHS reaction between Fe_2O_3 and Al is a metal-ceramic Al_2O_3-Fe composite (Rogachev & Baras, 2007). The post-processing of the ceramic-layered tubes may pose some disadvantages for the ceramic layer. However, various local reinforcement components such as titanium carbide composites can assist in this regard.

Titanium carbide (TiC) has many desirable properties, among which are high hardness, low density, high melting temperature, high modulus, great corrosion resistance and excellent wetting properties to Fe (Jiang et al., 2005; Luo et al., 2012). The application of TiC particulate has been noted in wear-resistant parts, thermal fatigue, erosion-resistant materials, and high performance tooling. The most frequently reported TiC-Fe composite is fabricated either by ex-situ methods like powder metallurgy or in-situ in the medium of Fe (Razavi et al., 2010; Wen et al., 2012). TiC is thermodynamically stable in steels, and thus provides fine reinforcement for wear-resistant applications (Xi et al., 2012).

The TiC resulting from the reaction between Ti and C starting powders is characterized by high hardness, good wettability, low density, and chemical stability with the Fe-based matrix. In-situ functionally graded materials (FGMs) consisting of ceramic and intermetallic components are appropriate for a number of post-processing applications, including piping branches, and orifice nibs of thick ceramic-coated pipes, etc. They enhance the innermost layer of the ceramic surface undergoing mechanical damage and crack propagation while transporting fluids or material. Then the ceramic surface of the pipe would erode, corrode, or crack excessively.

Ferro-TiC is a super-wear cermet with good erosion resistance, machinability and hardenable properties (Rahimipour & Ahmadi, 2010). TiC-Fe cermet has low soldering

or brazing capabilities under atmospheric conditions with large surfaces (Nowacki, 2012). Therefore, ex-situ TiC-Fe is not economical when used as an insert in the case of ceramic-lined pipes. A number of papers have been published on the synthesis of TiC-reinforced Fe-based composites (Bandyopadhyay et al., 2004; Razavi & Rahimipour, 2009; Zhang et al., 2012) using different starting materials under normal gravity conditions and with powder metallurgy technique. The advantage of powder metallurgy is that the product's surface quality and precision are excellent; however, production cost is high, while product shape and size are limited. For this reason, various works on the liquid-based means have been published in the past decade (Das et al., 2002).

Gowtam et al. (2008) studied Fe-TiC steel FGMs using SHS reaction followed by centrifugal casting (Fe_2O_3, MnO_2, and TiO_2 powders in the presence of C), in-situ TiC-reinforced steel composites (Wang & Wang, 2007), cast-sintering (Fengjun & Yisan, 2007), as well as spark plasma sintering (Li et al., 2009) and chemical vapor deposition (Voudouris & Angelopoulos, 2011). In another study conducted by Huang et al., TiC-TiB_2 ceramics were prepared via combustion synthesis under a high gravity field (Huang et al., 2012). Recently, Shi et al. reported a processing and abrasive wear study of Fe-Al_2O_3-TiC composite by pressure-less Ti-activated reactive melt infiltration (Shi et al., 2012). The production of an in-situ TiC-Fe-Al_2O_3 composite system under centrifugal force utilized the heat generated by the highly exothermic thermite reaction of Fe_2O_3 and Al, whereby the reaction of Ti and C is achievable at rapid heating rates and short reaction times. The adiabatic combustion temperatures of the SHS Fe_2O_3+Al and Ti+C reactions can reach 3622 and 3290 ˚C, respectively (Gowtam et al.), which is much higher than the melting points of Al and Fe_2O_3 (Patil et al., 1997). The advantage of this process is that once ignited, no further externally applied energy is required to complete the reaction (Merzhanov, 1990). Al_2O_3-Ti-TiAl/Ti_3Al processing using SHS is reported elsewhere but not under centrifugal processing conditions (Horvitz et al., 2002; Shen et al., 2011). So

far, to the best of the author's knowledge, no report has been published describing the production of an in-situ TiC-Fe-Al_2O_3-TiAl/Ti_3Al composite system under centrifugal force using Fe_2O_3, Al, Ti, and C as starting materials. In this paper, locally reinforced Ti-based functionally graded coating and the intermetallic layers of the composite product before and after immersion into a humid environment are investigated.

2.6 Silicon carbide (SiC)

Crystalline cubic silicon carbide (3C-SiC) is a wide energy gap material with excellent properties, among which high temperature, mechanical and chemical stability, and high irradiation resistance (Niu et al., 2011; Ryu et al., 2001). Its equivalents, nanocrystalline SiC (β-SiC) and amorphous SiC (α-SiC), have likewise attracted substantial study attention as they have superior physical, chemical and electrical properties than nanocrystalline and amorphous Si and are potential materials for making high-efficiency solar cells, light-emitting diodes, and have been widely applied as thermal coating layers and diffusion barriers against both metal and dopant diffusion (Yang et al., 2012). In this thesis, the formation of three different SiC methods is investigated.

2.6.1 SiC mechanical properties

Silicon carbide has attracted the interest of industries for its extreme hardness (Rendtel et al., 2008), high abrasive capability, high Young's modulus, high temperature resistance of up to 1500 ˚C, and high resistance to abrasion (Yamamura et al., 2011). The high residual porosity of SiC imposes limitations in terms of mechanical strength (Washburn & Coblenz, 1988). Therefore, investigating its mechanical properties is an important phase in this thesis.

2.7 SHS modeling and simulation technique

Numerous simulation techniques are applied to SHS, such as finite difference numerical method (Gennari et al., 2003), numerical modeling of field-activated combustion synthesis process (Zhang et al., 2011), modeling the solidification of functionally graded materials by centrifugal casting (Birman & Byrd, 2007; Gao & Wang, 2000), analytical models (Advani et al., 1992; Song et al., 2000), and so forth. To date, to the best of the author's knowledge there are no reports regarding meshless particle methods such as modified smoothed particle hydrodynamics (MSPH) for simulating SHS particle behavior including velocity, viscosity, and displacement.

In a research by Gao et al. (2008) in China, W-C-Fe cermet-lined steel pipes were produced by SHS centrifugal process while Wang and Yang (2007) did a finite element analysis of residual thermal stress in ceramic-lined composite pipes prepared by centrifugal SHS. This model may assist in determining the thickness of SHS layers via nonlinear transient thermal analysis, by which ceramic-lined composite pipes can be prepared. Evidently, there are circumferential compressive stresses in the Al_2O_3 and Fe layers and tensile stresses in the steel film. The circumferential thermal stress ceases at the interface of dissimilar materials. In the steel layer, the peak circumferential tensile stress is on the inner surface. The simulation results also indicate that the circumferential thermal stress in each layer increases as the SHS layer becomes thicker. Hence, the pipe's residual stress diminishes when suitably and rationally selecting SHS layer thickness to fabricate a centrifugal SHS composite pipe. Consequently, the reliability of the ceramic-lined composite pipe improves.

2.8 Thermite reaction safety precautions

As explained in the literature, the reaction between Fe_2O_3 and Al is highly exothermic and produces molten Fe and Al_2O_3. A self-sustained chemical reaction propagates

through a premixed powder in the form of a high-temperature reaction front (Zhou et al., 2010). Ceramic-lined composite pipes belong to the combustion synthesis, or self-propagating high-temperature synthesis (SHS) family. The melting of elemental alloy accompanies SHS. The combustion temperature of the C-T reaction can reach up to 3000ºC, which is higher than the boiling points of Al and Fe_2O_3 (Odawara & Ikeuchi, 1986). Essentially, the reaction would occur in the inner surface as an early-stage gas phase mixture, followed by phase separation and solidification of the Al_2O_3 and Fe products. CS processes exhibit elevated temperatures, rapid heating rates, and short reaction times. These specifications make CS an attractive method for manufacturing technologically useful materials at lower costs compared to conventional ceramic processes. However, the challenge with this technology regards safety risks when dealing with high-temperature materials at high-speed rotation. Open literature has not thus far reported on the magnitude of reaction violence, human factors, and safety matters. Such disruptions may cause unpredictable burning incidents, losses, or damage during reaction. A special test rig was developed to run the centrifugal-assisted SHS experiment coupled with an infrared pyrometer that measured the real-time process temperature.

2.9 Summary

From the above-mentioned literature study, it is clear that the development of a conventional SHS centrifugal machine that can produce ceramic-lined steel pipes with the Fe_2O_3+Al mixture is essential. Fe_2O_3 and Al powders were mixed based on reaction stoichiometry, comparable to Odawara (2010) mixture.

A special plasma reaction chamber was additionally developed, which is able to produce TiC/SiC under extreme thermal conditions and maintain sufficiently high temperatures to facilitate the reaction, melting, and re-crystallization of the compacted, starting powder.

Locally reinforced functionally graded coatings (Ti and Si-based) and the intermetallic layers of the composite product before and after immersion into a humid environment have not been investigated adequately in open literature. Therefore, it is necessary to synthesize an embedded pellet (mixture of elemental powder) and expose it to a centrifugal SHS reaction.

Furthermore, available published literature does not provide a simple mathematical model based on the particle meshless method. For that reason, the modified smoothed particle hydrodynamics (MSPH) method is employed to simulate iron and alumina particle behavior, such as velocity, viscosity, and displacement during the centrifugal SHS reaction. This is important to understand the infiltration rate of molten alumina and iron into titanium carbide porous media.

CHAPTER 3:METHODOLOGY

3.1 Introduction

In this chapter, five different methods of composite graded processing is drafted and briefly discussed. The methods were applied to create the final products. The details of each experiment are described in chapter five, experimental works.

3.2 Processing methods

The list of the most effective applied methods and the corresponding starting material is listed in Table 3.1. The following sections will elaborate each method illustrated with a process flowchart.

Table 3.1: List of processing methods and starting materials

Description	Applied Method	Starting material	Test code
Conventional centrifugal thermite	(1)	Fe_2O_3, Al	SM01
M+C embedded centrifugal thermite	(2)	Ti, C, Fe_2O_3, Al	SM05
M+C embedded centrifugal thermite	(2)	Ti, C, Fe_2O_3, Al	SM06
M+C embedded centrifugal thermite	(2)	Ti, C, Fe_2O_3, Al	SM07
M+C embedded centrifugal thermite	(2)	Si, C, Fe_2O_3, Al	SM08
Ti+C offset centrifugal thermite	(3)	Ti, C, Fe_2O_3, Al	SM09
Plasma assisted centrifugal thermite	(4)	Si, C	SM10
M+C DC-focused plasma arc	(5)	Si, C	SM02
M+C DC-focused plasma arc	(5)	Ti, C	SM03
Hot crucible*	-	Ti, C	SM04

* The hot crucible is an isolated, fundamental, preliminary means of understanding the behavior of the Ti+C mixture when exposed to certain heat.

3.2.1 Method (1): Conventional centrifugal thermite reaction

The schematic representation of the centrifugal thermite process and its experimental procedure flowchart are shown Figure 3.1, and Figure 3.2, respectively. In this method, two coating layers in consequence to the thermite reaction formed in the innermost layer of a pipe. As the pipe rotated at high acceleration, phase separation occurred since it was in a molten medium and it solidified in a short time. The required characterization was performed after the tube cooled down. Experiment SM01 was carried out using this method to perceive the centrifugal thermite process, reaction behavior, as well as feasibility of operating a centrifugal thermite-assisted process more comprehensively.

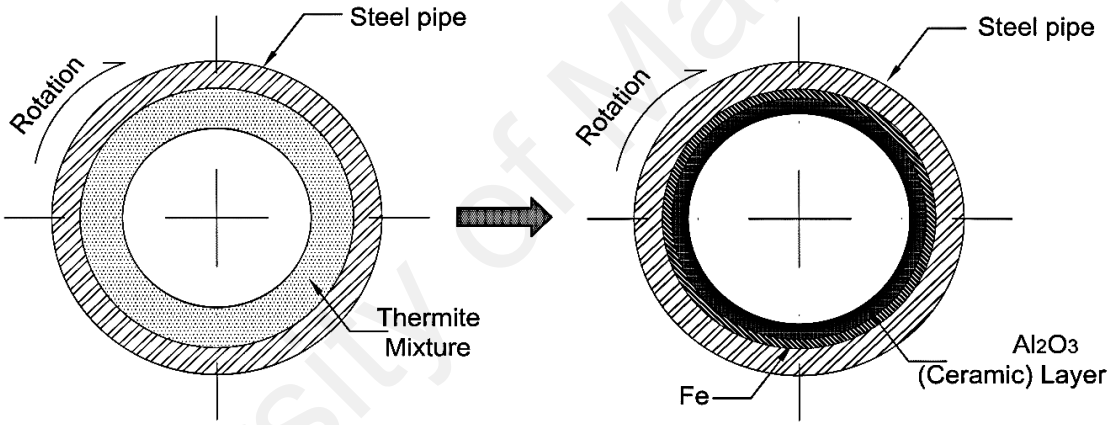

Figure 3.1: Centrifugal thermite reaction for producing ceramic-lined composite pipes (Method 1)

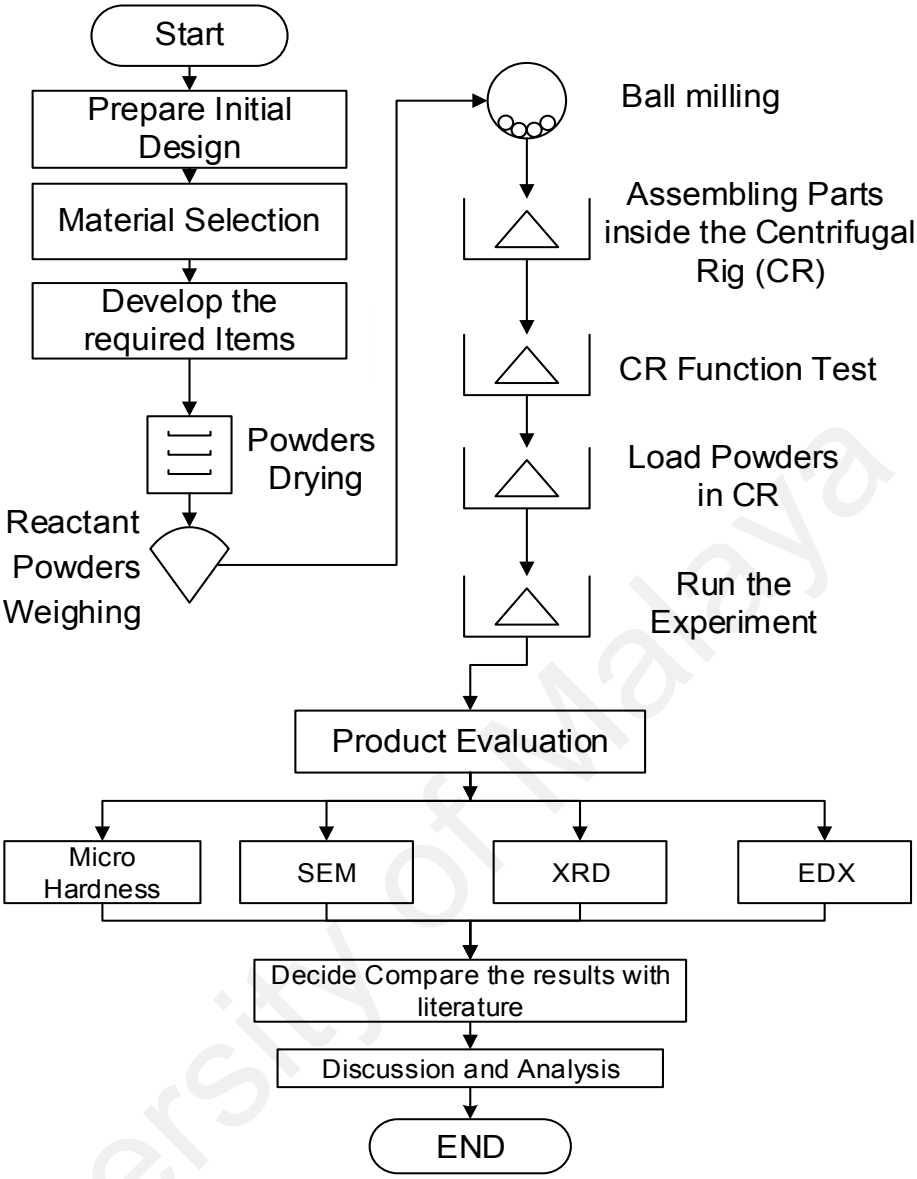

Figure 3.2: Methodology flowchart for general ceramic-lined composite pipe production (Method 1)

3.2.2 Method (2): M+C embedded centrifugal thermite

In this method, the scheme was to investigate the formation of TiC or SiC during the centrifugal thermite process. Here, M+C represents Ti+C or SiC, meaning that this method is applicable to Ti+C and Si+C pellets. An M+C pellet was embedded in a compacted graphite mold in a steel tube mounted in a centrifugal machine. The same material as in method (1) was fed into the tube while it was rotating. Then the mixture was ignited and the product removed from the chamber for further characterization. A diagram and the process flowchart are depicted in Figure 3.3 and Figure 3.4, respectively. Experiments SM05, SM06, SM07, and SM08 were performed using this method.

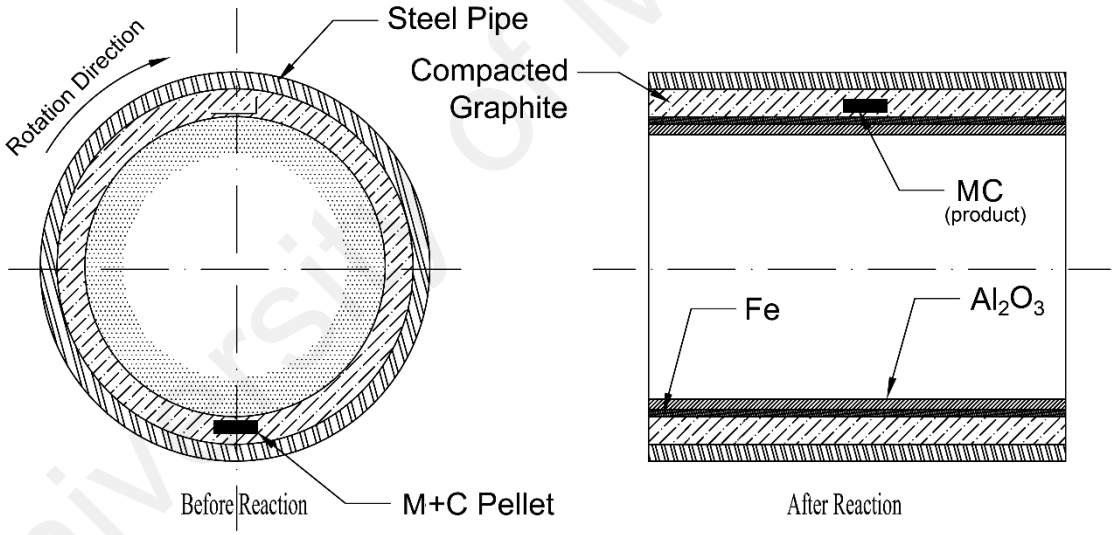

Figure 3.3: Schematic diagram illustrating M+C embedded centrifugal thermite and a compacted graphite crucible assembly charged with the loaded green mixture; A: before reaction (left), B: after reaction (right), while subjected to centrifugal force (Method 2)

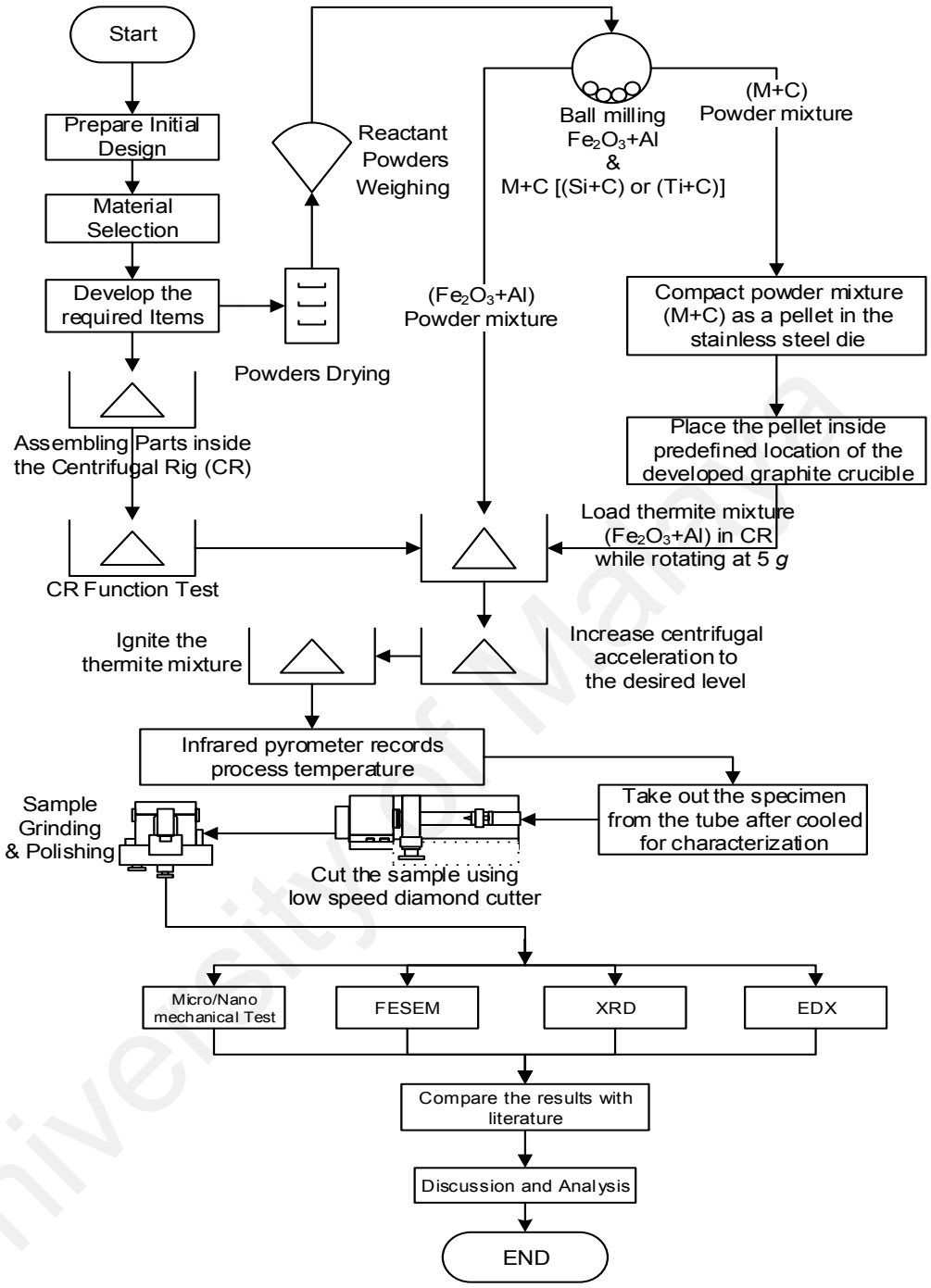

Figure 3.4: Experiment flowchart of processing M+C embedded and Fe/Al_2O_3 composite under centrifugal acceleration (Method 2)

3.2.3 Method (3): Ti+C offset centrifugal thermite

This method is relatively similar to method (2), whereby the notion was to investigate the formation of TiC during the centrifugal thermite process. Essentially, with this technique Ti+C was processed as starting material. A Ti+C pellet was mounted in a specimen holder set in a steel tube. The tube was installed in a centrifugal machine. The same material as for methods (1) and (2) was fed into the rotating tube. The mixture was then ignited and the result removed from the chamber for additional characterization. The schematic diagram and process flowchart are depicted in Figure 3.5 and Figure 3.6, respectively. Experiment SM09 employed this method.

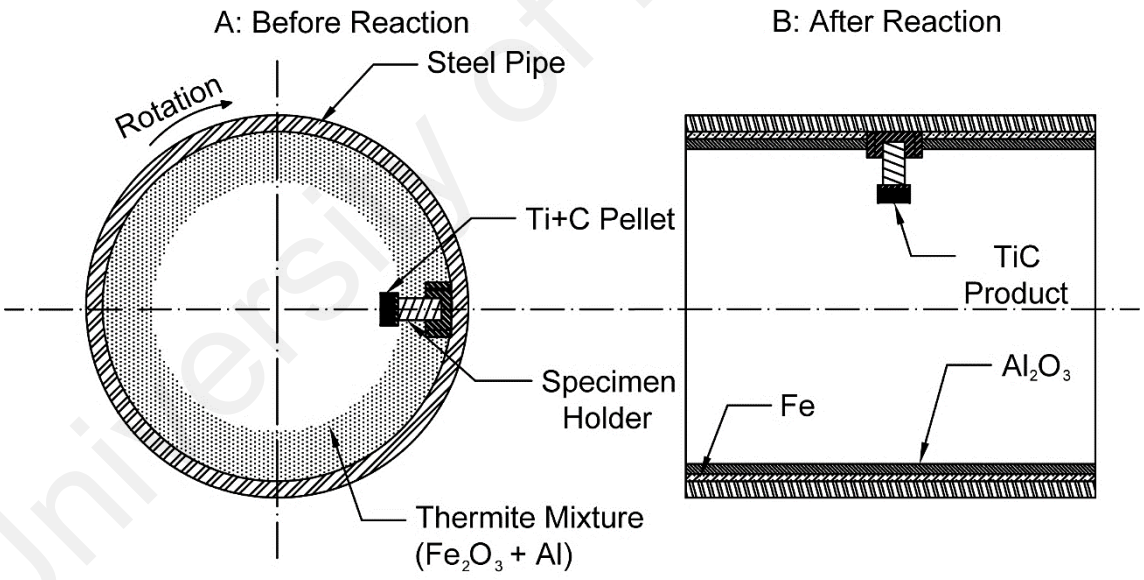

Figure 3.5: Ti+C offset centrifugal thermite to produce ceramic parts and pellets under centrifugal acceleration (Method 3)

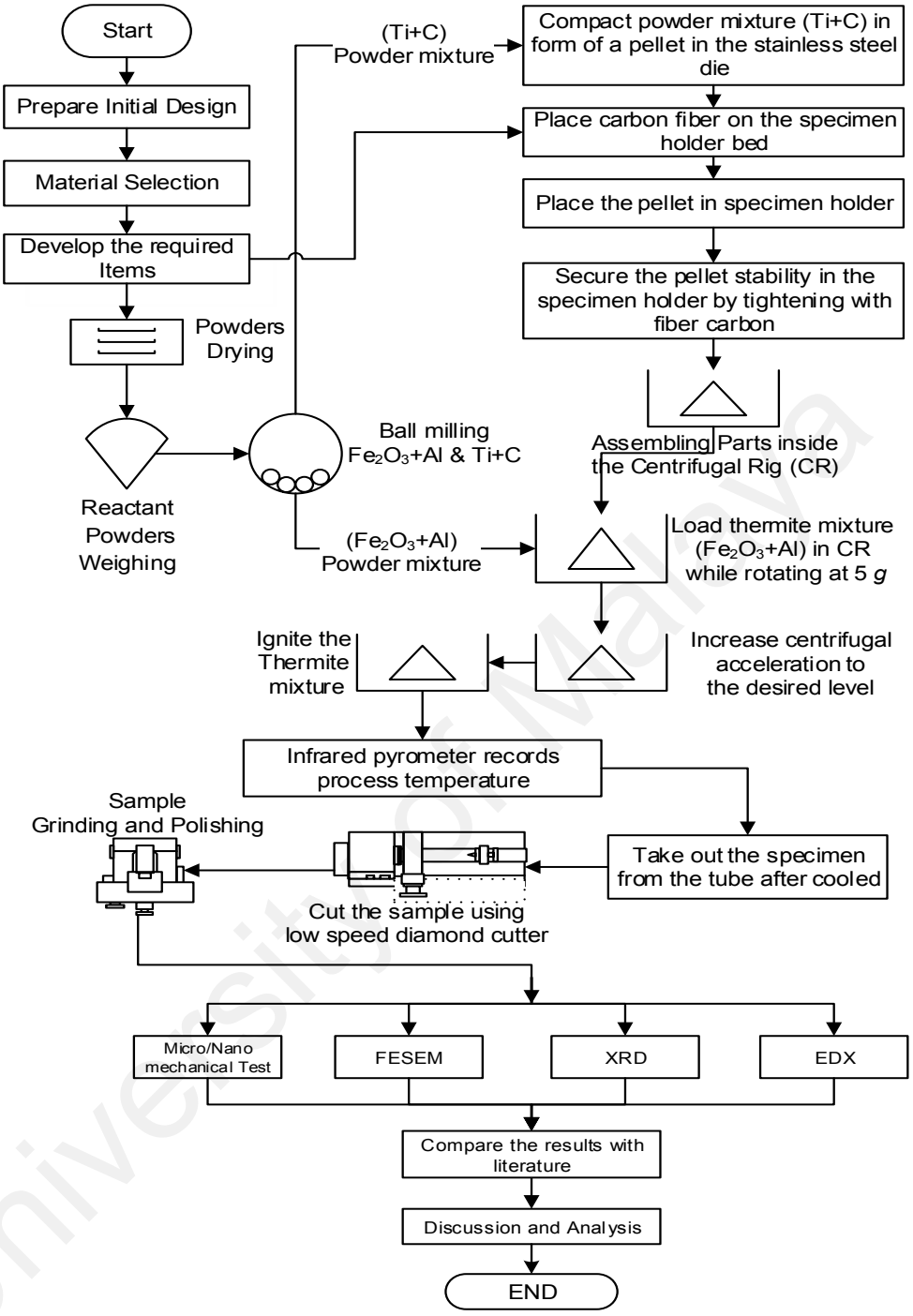

Figure 3.6: The flowchart of Ti+C offset composite processing under centrifugal acceleration (Method 3)

3.2.4 Method (4): Plasma-assisted centrifugal SHS

This method investigated the formation of SiC during the centrifugal process while being exposed to a plasma arc. A silicon and carbon mixture in the form of pellets was the starting material. The Si+C pellet was placed in a specimen holder mounted in a steel tube. The tube was installed in a lathe (turning) machine. A graphite electrode was set up on the moving support of the lathe machine to facilitate effortless electrode position control. The electrode was connected to a positive pole while the workpiece was connected to a negative pole of a DC power supply with 200 A. After a stream of argon gas was introduced to the system, the electrode distance with the specimen holder became zero and a plasma arc was then initiated. The mixture was ignited and the product taken out from the chamber for further characterization. The diagram and process flowchart are illustrated in Figure 3.7 and Figure 3.8, respectively. Experiment SM10 utilized this method.

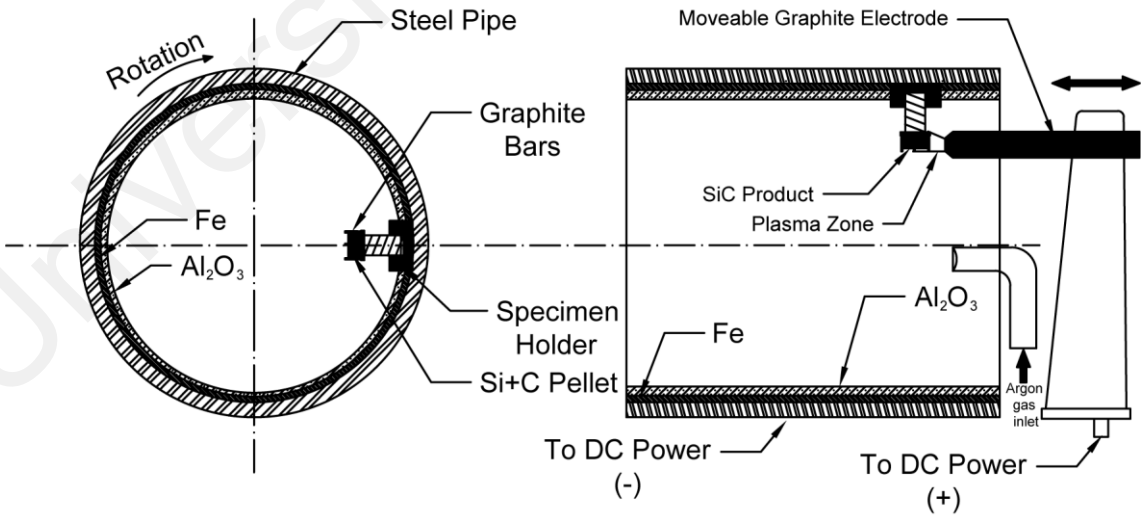

Figure 3.7: Plasma-assisted centrifugal method to produce ceramic parts and pellets under centrifugal acceleration (Method 4)

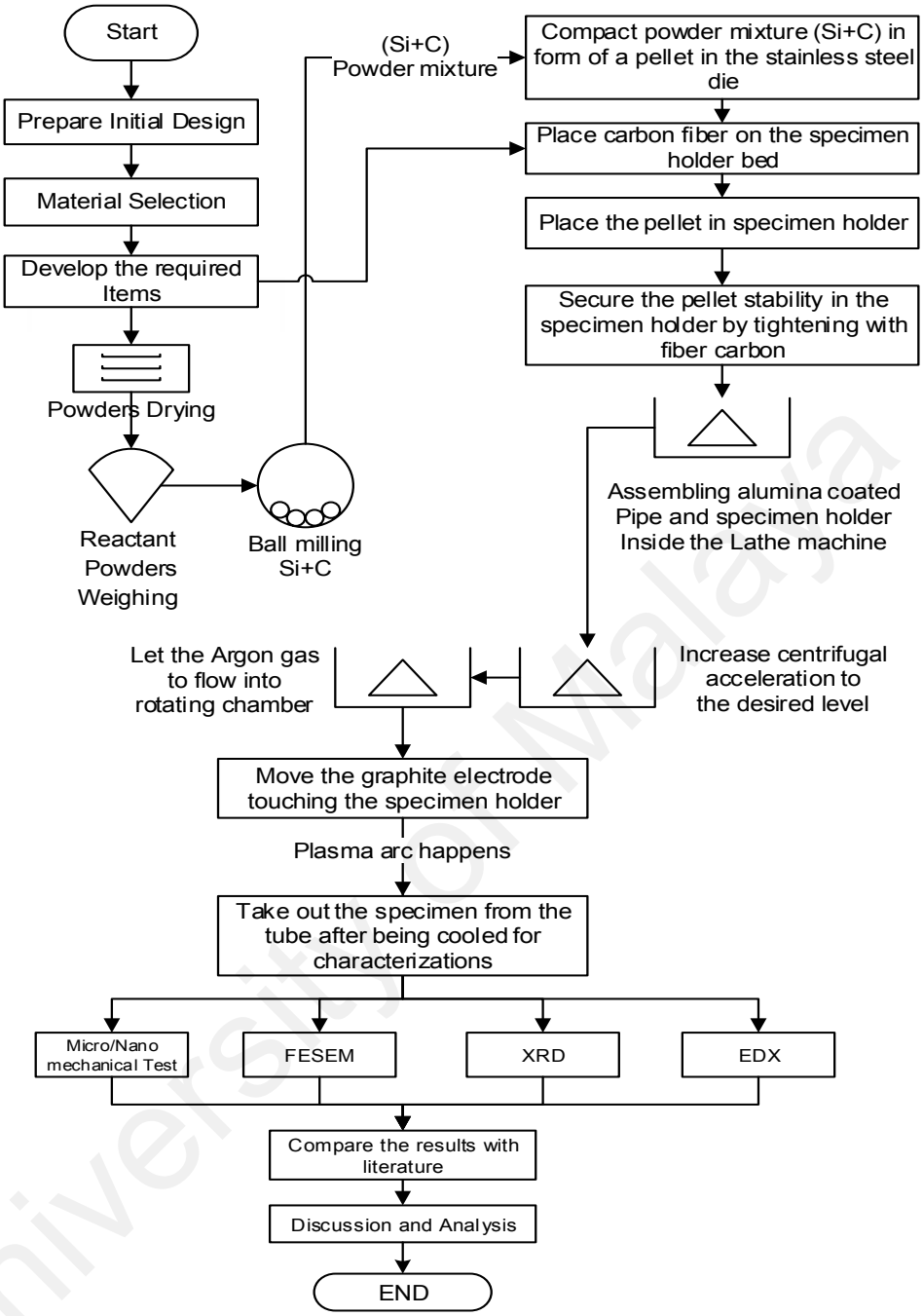

Figure 3.8: The process flowchart of Si+C plasma-assisted centrifugal acceleration (Method 4)

3.2.5 Method (5): DC-focused plasma arc

In method (5), TiC and SiC were synthesized in a high temperature plasma chamber. Here, M+C stands for Ti+C and SiC, indicating that this method applies to both Ti+C and Si+C pellets. An M+C pellet was placed on the carbon fibers in a graphite crucible. Argon gas was introduced to the chamber. The plasma initiated once the graphite electrode position changed. The released heat synthesized the pellet, and the product was removed from the chamber for further characterization. The schematic diagram and process flowchart are depicted in Figure 3.9 and Figure 3.10, respectively. Experiments SM02 and SM03 were run using this method.

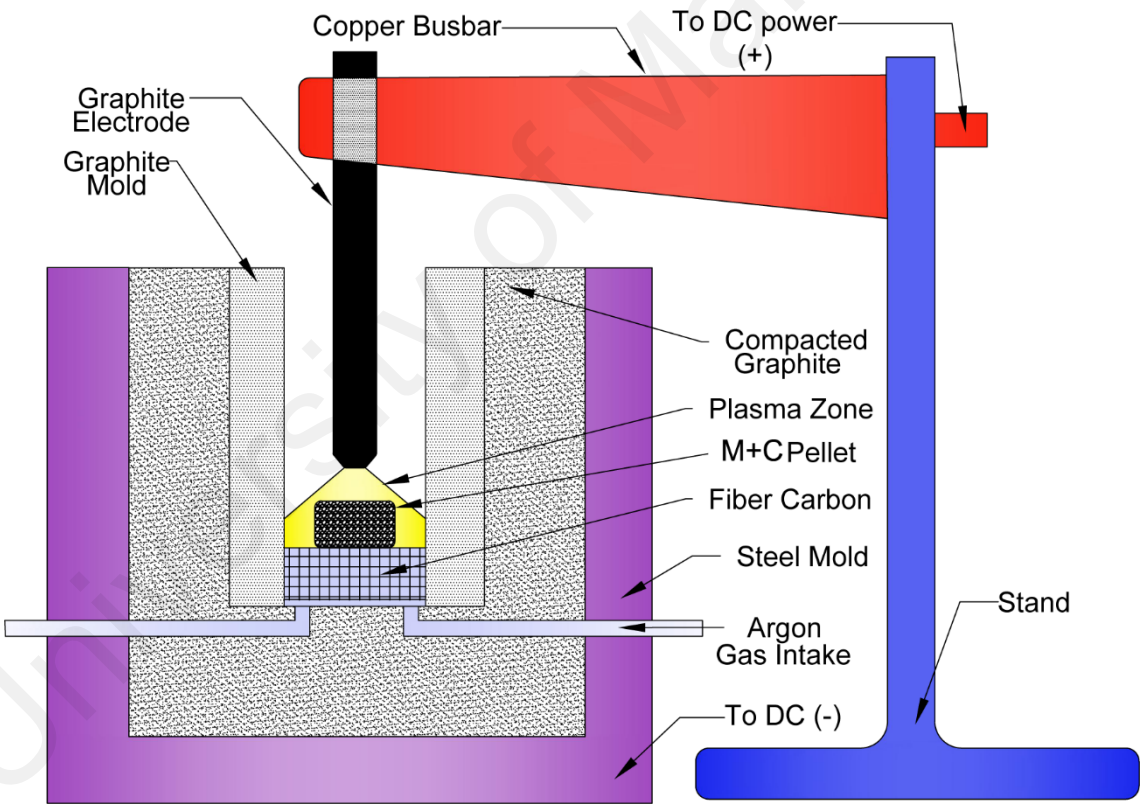

Figure 3.9: Schematic diagram of the developed DC-focused plasma arc reaction chamber (Method 5)

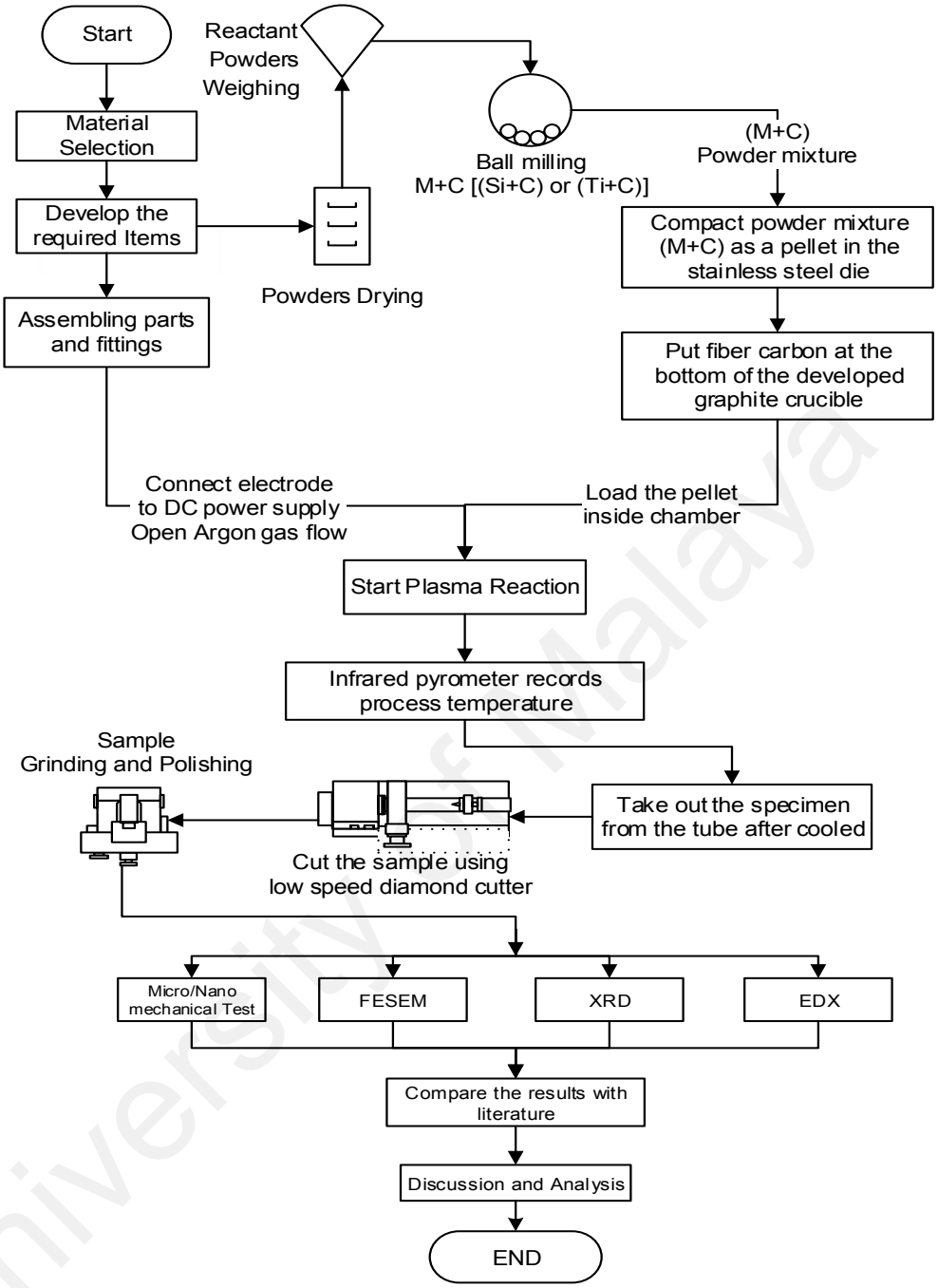

Figure 3.10: The process flowchart diagram for TiC and SiC using a DC-focused plasma arc under normal gravity (Method 5)

3.3 Product characterization methods

The following characterization techniques were employed where applicable. Depending on the subjects, some characterization approaches may only be relevant to certain specimens.

3.3.1 Sample preparation for characterization

Ceramic materials have very weak tension, thus particular consideration must be given to select a proper cutting process. Particularly, in the case of ceramic-coated pipes, careful attention should be paid if a ring is required from cutting by using a turning machine from the product. During this process, some factors need to be controlled. The flow rate of the coolant must be managed; oil-based coolant should not be used; the material rate of removal (MRR) must be kept low to avoid excessive vibration transfer and provide less shock when moving from the outermost to the innermost layer. Cleaning porous samples stained with oil is very difficult because the pores absorb oil. Not only the cutting process necessitates certain precautions, but so does fixing and holding the pipe in the turning machine. Fastening the turning machine's three chucks too firmly can damage and break the ceramic layer inside the pipe. It is advisable to use a wire cut electrical discharge machine (WC-EDM) to prepare suitably sized samples for characterization in order to avoid any negative influence on the cutting zone and specimen properties.

3.3.2 Specimen surface preparation after processing

Samples need to be ground and polished to a near-mirror finish prior to analysis under light optical microscope (LOM) to obtain good quality images. A Rax Vision Metapol-2 device performed the grinding and polishing. The specimen was ground with 300, 800, 1200, and 2400 grit emery paper. Following grinding, the sample was polished with cotton and alumina paste with 3-μm particle size to reduce surface scratches and attain a mirror finish with minimum defects.

3.3.3 Vickers hardness (HV) test

A Shidmazu micro-hardness tester measured the micro-hardness at various points several times to obtain an average HV value. Hardness measurement result can also help determine fracture toughness. HV is calculated using the following formula:

$$HV = 1.8544 \frac{P}{d^2} \quad \text{(MPa)} \qquad \text{Eq. 3.1}$$

where P is the indentation load (N) and d^2 is the diagonal of the indentation mark (μm).

3.3.4 Nanomechanical characteristics (Nano-indentation)

The coatings' mechanical properties were investigated by nano-indentation using a commercial nano-indenter, a Shimadzu Dynamic Ultra Micro Hardness Tester (DUH-211S, Shimadzu Co. Ltd.) with continuous stiffness measurement capability where applicable. The nano-indentation experiments were performed using a Berkovich diamond tip (edge angle: 115°). Load and hardness calibration was done on a reference sample of fused silica. The indentation velocity varied according to loading conditions, and upon reaching the maximum prescribed depth, loading stopped and was maintained for 2-10 sec. The source of variations gathered from five test sites is within the limit for each sample.

The nanoindentation method was developed over a few decades, and the mechanical properties on a sub-micron or nano scale are extensively discussed. The techniques are expected to be valuable for measuring the mechanical properties of thin films or the local structure of various materials (Kurosaki et al., 2004). Nevertheless, only few attempts to apply nanoindentation to evaluate the mechanical properties of Ti-based coatings have been made.

In commercial nanoindenters, the load and displacement are typically recorded continuously during the indentation process, resulting in a load displacement curve that describes the interaction between the tip and sample during indentation (Figure 3.11).

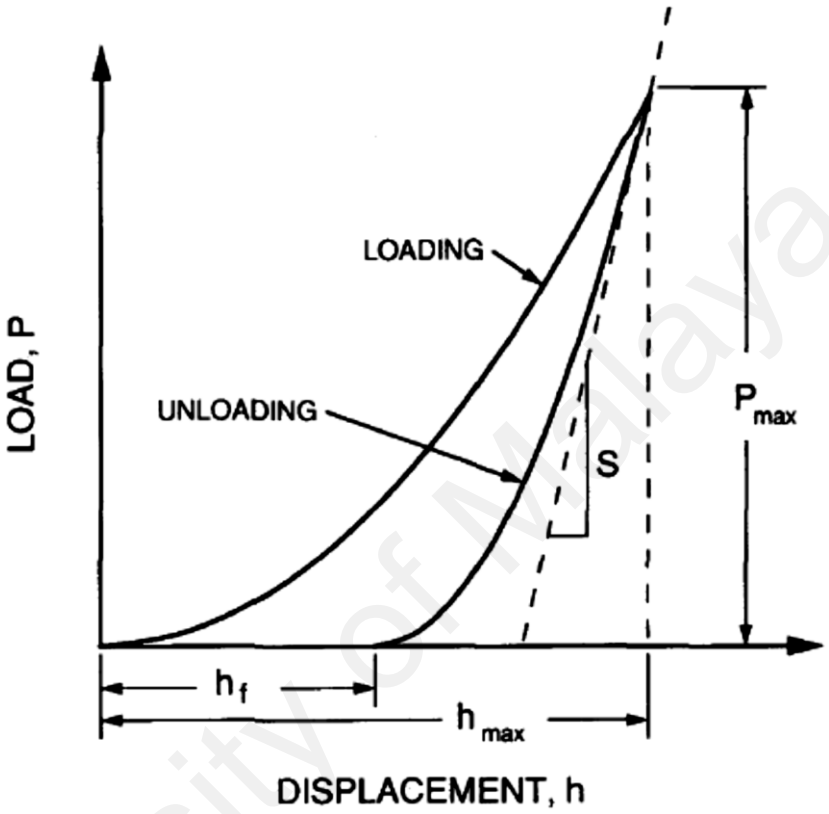

Figure 3.11: Diagram of an indentation force-displacement curve with several important parameters (Oliver & Pharr, 1992)

In recent years, numerous studies on material properties have focused on measuring Young's modulus (E) and indentation hardness (H) from indentation data (Ebenstein & Pruitt, 2006; Oliver & Pharr, 2004). The hardness and Young's modulus parameters are independent from one another. Hardness and material parameters were evaluated in accordance to standard ISO 14577-1. Young's modulus was calculated using the following equations:

$$E_r = \frac{dP}{dh}\frac{1}{2}\frac{\sqrt{\pi}}{\sqrt{A}} \qquad \text{Eq. 3.2}$$

where E_r is the reduced elastic modulus, which accounts for the fact that elastic deformation occurs in both the sample and the indenter; *dP/dh* is the initial unloading stiffness (the slope of the unloading curve *dP/dh* evaluated at maximum load); and *A* is the projected contact area between the indenter tip and the sample at maximum load. The reduced modulus relates to Young's modulus *E* through the relationship:

$$E_{it} = \left(1-\upsilon_s^2\right)\left(\frac{1}{E_r}-\frac{1-\upsilon_i^2}{E_i}\right)^{-1} \qquad \text{Eq. 3.3}$$

where subscript *i* refers to the indenter material, subscript *s* refers to the substrate material, and υ is Poisson's ratio. The indenter material properties are usually known (*Ei* = 1141GPa, υ_i= 0.07 for diamond, a common tip material), so the Young's modulus of a material can be calculated from the reduced modulus if the Poisson's ratio of the sample material is known. If the sample's Poisson's ratio is unknown, the plane strain modulus Er = $E/(1-\upsilon^2_s)$ can be reported. The above formula is automatically calculated by the DUH software interface.

3.3.5 Determining the fracture toughness

The stress intensity Factor (K_{IC}) is a quantitative parameter of fracture toughness defining a maximum value of stress that could be applied to a specimen having a crack of a specific length.

The fracture toughness can be determined using the indentation technique. A polished specimen would be indented at different, remote locations. The size of the cracks proceeding the corners of the Vickers indentations to be measured. Measurements should be performed immediately after each indentation.

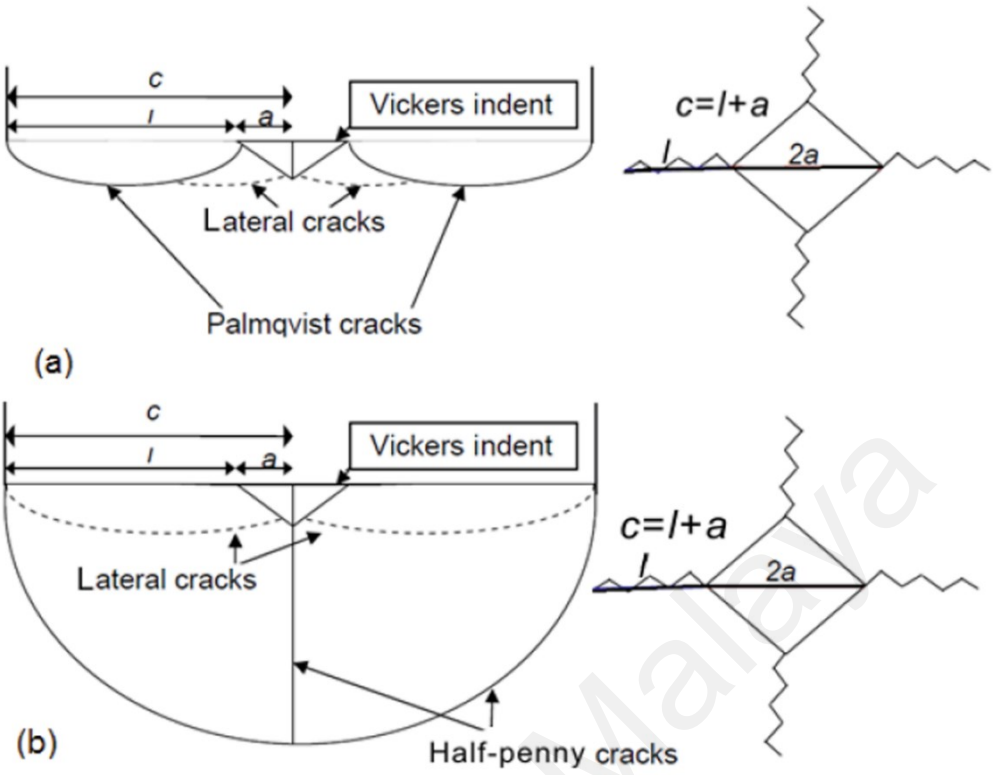

Figure 3.12: (a) Palmqvist crack model; (b) half-penny cracks (Moradkhani et al., 2013)

The indentation fracture toughness, K_{IC}, was determined by considering the c/a-ratio as proposed by (Denry and Holloway (2004); Niihara (1983)). If c/a < 3.5 the crack pattern is of the Palmqvist type and the fracture toughness is calculated as:

$$K_{IC} = 0.0084\left(\frac{E}{H}\right)^{0.4}\left(\frac{P}{c^{1.5}}\right) \qquad \text{Eq. 3.4}$$

If c/a > 2.5, half penny-shaped crack patterns are generated, as proposed by Anstis et al. (1981) and K_{IC} is calculated according to the following equation:

$$K_{IC} = 0.016 \pm 0.004\left(\frac{E}{H}\right)^{0.5}\left(\frac{P}{c^{1.5}}\right) \qquad \text{Eq. 3.5}$$

where E represents the elastic modulus (GPa) which was determined using Nano-indentation, H the Vickers hardness (GPa), P the applied load (N), and c are parameters of the Vickers indentation mark (μm). The unit of K_{IC} is $MPa \cdot m^{1/2}$.

3.3.6 Surface roughness

A Mitutoyo SJ 201 profilometer measured the smoothness of the product's innermost surface. This instrument was calibrated to avoid reading errors. After calibration, the samples' smoothness was measured at three different locations in each region.

3.3.7 FESEM -EDX

Sample morphology was observed using a high-resolution FEI Quanta 200 F (FEI, USA) field emission scanning electron microscope (FESEM) coupled with Energy Dispersive X-ray Analysis (EDAX).

3.3.8 Light optical microscope (LOM)

An Olympus BX 61 metallographic LOM with 5X to 100X magnification was employed to investigate the order of layers and surface morphology.

3.3.9 XRD Analysis

Sample X-ray diffraction (XRD) patterns (as prepared samples) were recorded on an Empyrean X-ray diffractometer with Cu Kα radiation (λ=1.54178 Å) operating at 45kV and 30mA with a step size of 0.026°, scanning rate of 0.1°/s and 2θ range from 5° to 80°.

The Rietveld method (Young, 1993) served as part of the quantitative phase analysis following XRD to calculate the phase content in the specimen. In the Rietveld method, crystal structure and peak profile parameters are refined in several stages (Rietveld, 1967).

Phase analysis was performed to determine the weight (or volume) quantity of crystalline and amorphous phases that were present in the sample. In the current dissertation, the entire XRD quantitative phase analysis was performed using the Rietveld method on X'Pert HighScore Plus® software, version 3.0d, developed by PANalytical

CHAPTER 4:TEST RIGS DESIGN

4.1 Introduction

This chapter presents the design and fabrication of three test rigs, or reaction chambers. The chapter consists of two sections. The first part addresses the centrifugal SHS test rig as well as safety protection considerations, and then the development of the two DC-focused plasma reaction chambers is explained.

4.2 Design of centrifugal machine applied in methods 1, 2, 3, and 4

Certain important points need to be considered in machine design and fabrication in order to produce reliable devices in accordance with the requirements.

The centrifugal machine in this project is intended for the laboratory-scale production of ceramic-lined steel pipes. The rotation speed, ease of use, ergonomic factors, safety, stability, and low vibration aspects of this machine were considered. The process necessitates the high centrifugal acceleration of a rotary machine. The steel pipe was fixed inside the rotary machine, which provided the necessary rotational speed to raise the required acceleration according to Eq. 2.1. An embedded module for the controllable electric motor managed the rotational velocity of the reaction chamber to provide the essential centrifugal acceleration.

4.2.1 Apparatus design

Anthropometry information collected from 32 students in 2007-2008 at the University of Malaya was adopted for the test rig design. This data is likely to cover 95% of the potential user population in terms of hand grip area and height (Schlick, 2009). Figure 4.1 shows a detailed schematic view of the designed centrifugal machine.

The machine underwent high centrifugal acceleration and a rapid rise in temperature during testing. The steel pipe was fixed inside the reaction chamber as seen in Figure 4.1. A high performance infrared thermometer, Raytek MM1MHSF3L, recorded real-time temperature data readings, which were stored on-site in a computer.

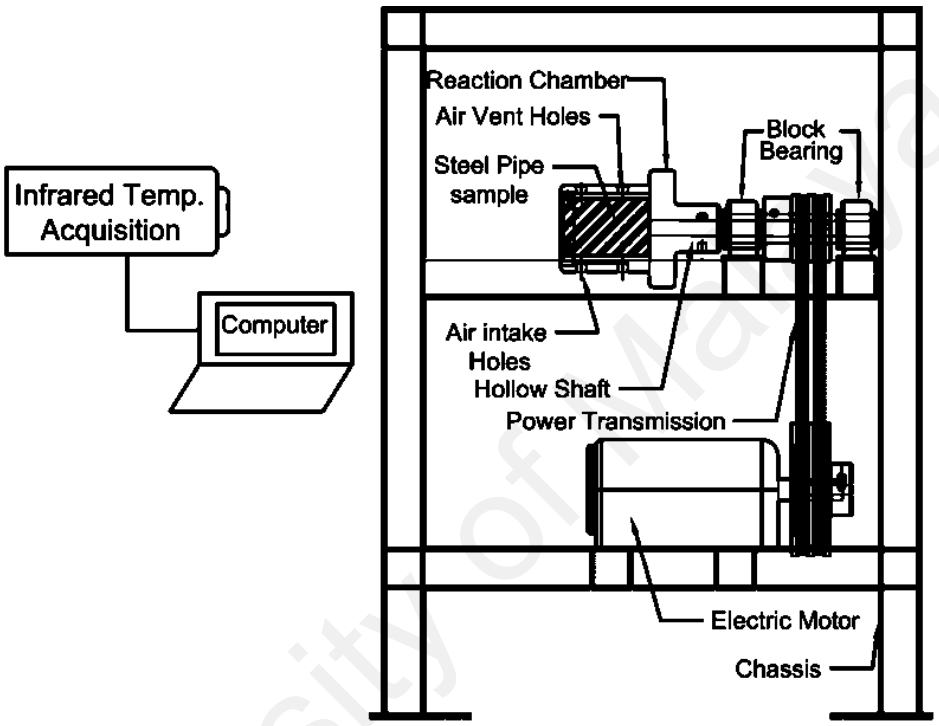

Figure 4.1: Schematic view of centrifugal thermite machine coupled with an infrared temperature acquisition unit

4.2.2 Reaction chamber

The reaction chamber is made from gray cast iron with 11 mm wall thickness to provide stability at cyclic temperatures during the reaction. Six holes in the chamber wall were created to assist heat convection by drawing air in and venting it out. The chamber was open-ended and the inside was not pressurized throughout the reactions.

The chamber (Figure 4.2) was attached to a chamber-shaft fixing head using six 12mm screws. The chamber-shaft fixing head was press-fitted onto the shaft, which was also fixed with three 120 ˚ screws (Figure 4.3-C) to prevent possible axial sliding.

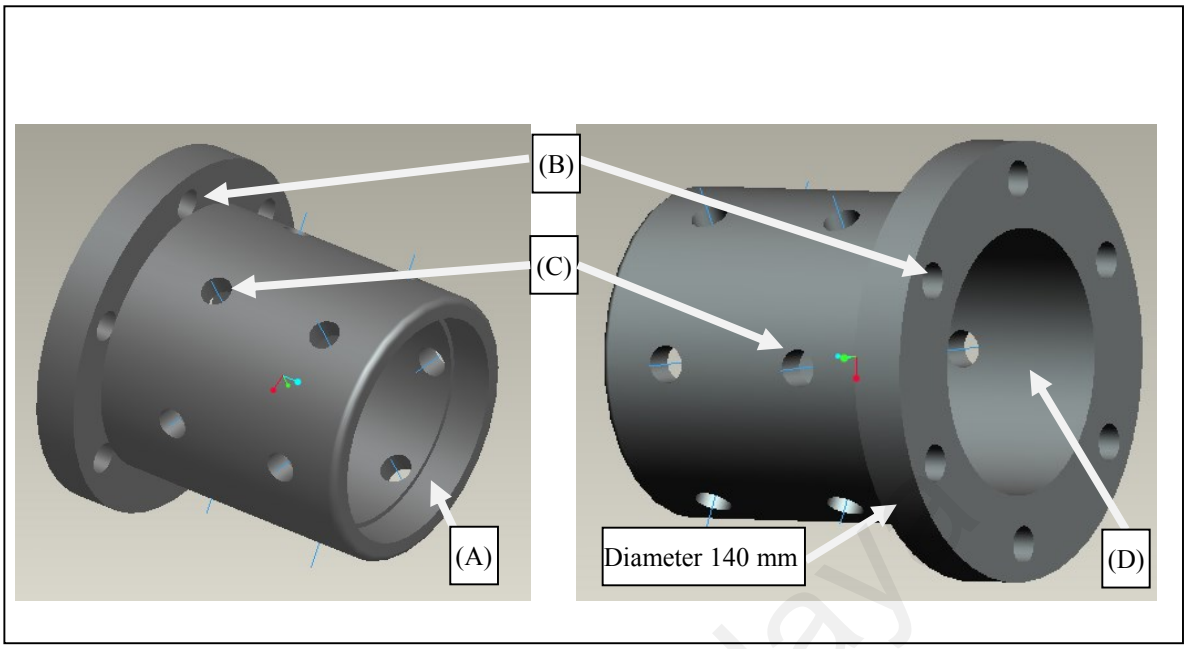

Figure 4.2: Main chamber components

(A) Blind trap (prevents the pipe's head blind from going further inside), d = 87 mm

(B) Six threaded holes (M 12) for attachment to the reaction chamber connector denoted by B in Figure 4.3

(C) Six threaded holes (M 10) in three rows with 120 degrees from each other to fix the pipe inside

(D) Reaction chamber effective diameter, d = 85 mm

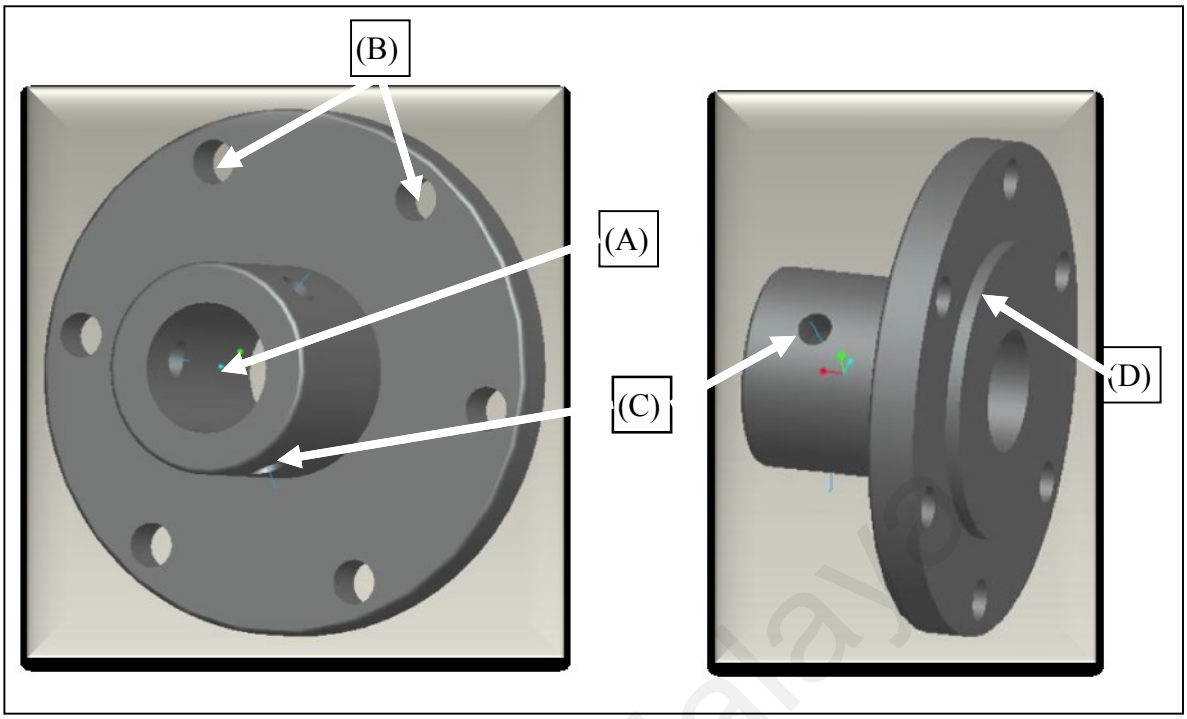

Figure 4.3: Reaction chamber connector (fixture) to the shaft

(A) Central hole for securing the shaft

(B) Six holes for reaction chamber attachment to point B from Figure 4.2

(C) Three threaded holes (M 10) and screws to prevent sliding movement along the shaft

(D) Knob with 85 mm diameter, which fits inside hole D from Figure 4.2 to make the assembly more reliable, keep the reaction chamber and shaft on the same axis and avoid off-centering. This connector was designed for assemblage onto the shaft according to press-fit (IT7 H7/u6) standard, as there is no significant force on the chamber to resist running.

4.2.3 Chassis design

The chassis should hold all components together and be rigid and strong enough to avoid excessive vibration and deflections. The structure material is mild steel (st37) as a hollow square section with 50 mm welded joints. Figure 4.4 illustrates the designed chassis.

Finally, this structure must be fixed onto the floor with four expansion bolts. Rubber is also recommended to damp possible vibrations.

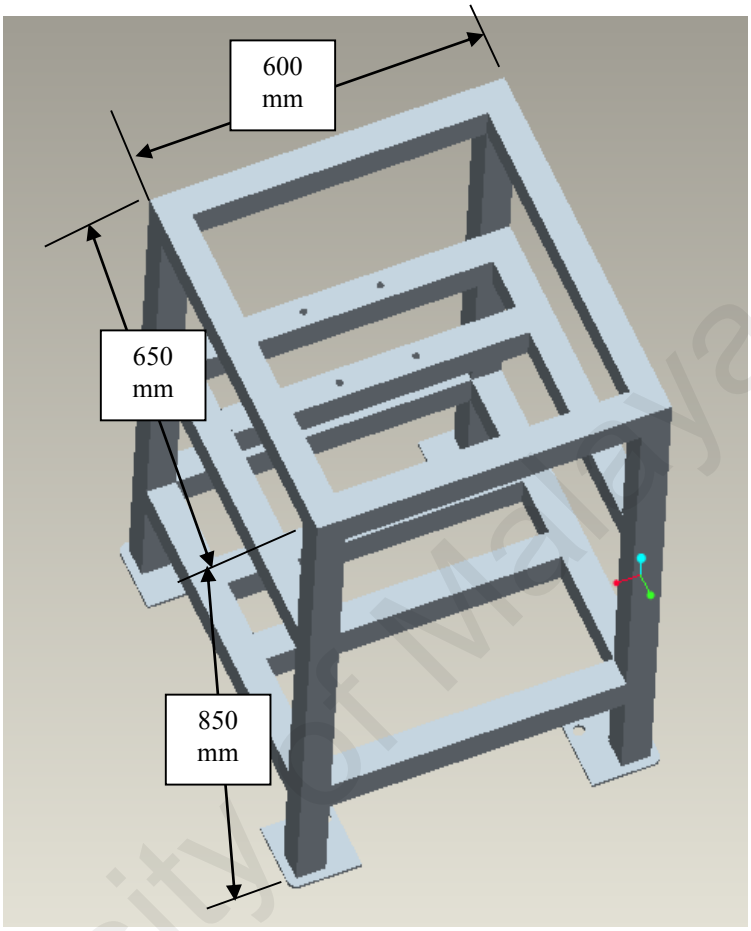

Figure 4.4: Chassis machine structure design

4.2.4 Final assembly onto the structure

The motor, rotor and components assembled to the chassis are depicted in Figure 4.5-a, while the reaction chamber and components connected to the rotor are shown in Figure 4.5-b.

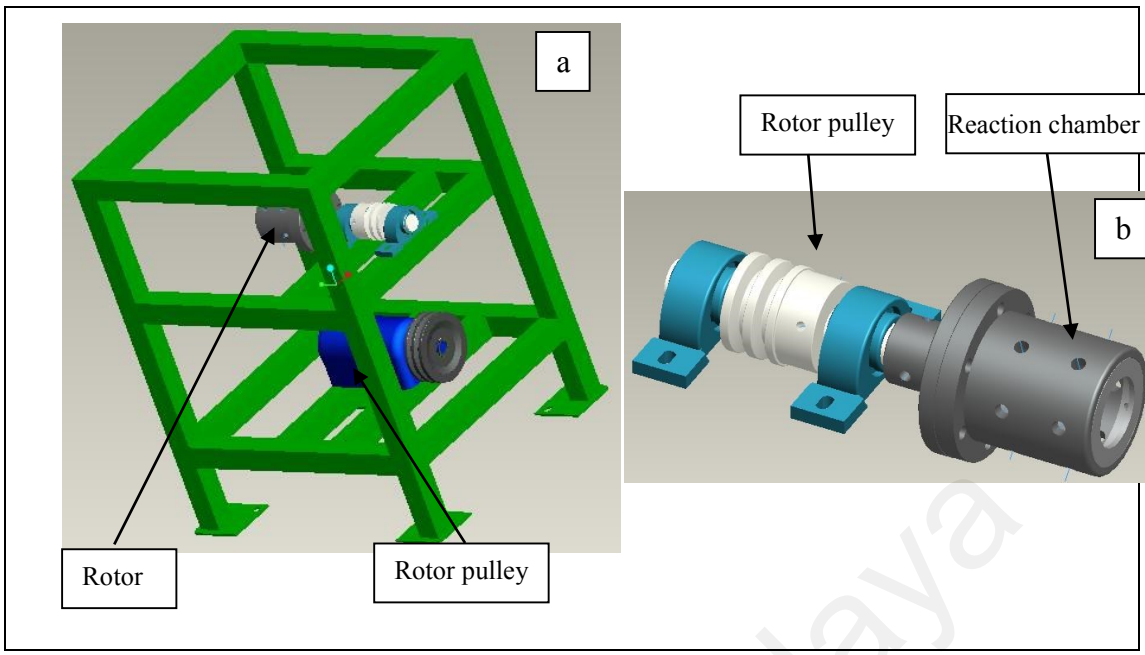

Figure 4.5: (a) Final rotor, motor, and components assembly; (b) the main chamber (reaction chamber) and rotor components

4.2.5 Electrical devices and components

4.2.5.1 Electro-motor Selection

From among the different available motors, a three-phase, two-pole AC induction motor EleDelta Tt, with 1.5kW power and 2850 rpm was selected as the electro-motor that fulfills the requirements.

4.2.5.2 Inverter selection

An inverter can alter the motor's speed with minimal efficiency loss, unlike mechanical or hydraulic speed control systems. The resulting energy reductions usually compensate for the inverter cost in a relatively short time.

A HITACHI L200 inverter (Figure 4.6) was chosen to satisfy conditions including motor change, and angular speed, current, and frequency display, overload trip, etc.

Figure 4.6: Hitachi inverter used to regulate and adjust the motor's rotation speed

4.2.6 Fabrication

The reaction chamber was machined with bulk, gray cast iron with internal and external diameters of 105 mm and 85 mm, respectively, and 125 mm length; the chamber was connected to a hollow shaft. This reaction chamber can be substituted with another chamber of any size. Six holes with certain angles were considered for the chamber, as seen in Figure 4.1.

The program-embedded tunable inverter controlled (Figure 4.6) the rotational speed of the reaction chamber to provide the required centrifugal acceleration. Centrifugal acceleration ranging from a = 2*g* up to a = 380*g* was achievable.

4.2.7 Centrifugal SHS safety precautions

The fabricated SHS-centrifugal machine had six doors assigned to protect users from any flying objects. A double-layer mesh guard was placed on the side doors. In addition, the whole assembly was protected using a safety box (Figure 4.7 and Figure 4.8).

According to the preliminary study, safety issues should be taken into consideration because of the violent properties of the thermite reaction (e.g. fast heating rate, short

reaction time). Airborne molten particles were observed during the preliminary work. A few papers have been published on controlling reaction parameters not specifically the about released thermite side-products (Fan et al., 2006; Orru et al., 1996). However, their papers are mostly not applicable to this project, which particularly needs to employ high temperature levels and rapid reaction times. Nonetheless, the reported works attempt to present diluents or larger particle sizes to reduce the total thermite energy (Le et al., 2008).

The most reliable method is to isolate the reaction chamber and surrounding area, an approach that was utilized in this experimental research. A special sight glass was considered for real-time monitoring by video camera and infrared pyrometer. The design schematic of the safety containment is illustrated in Figure 4.7 and Figure 4.8.

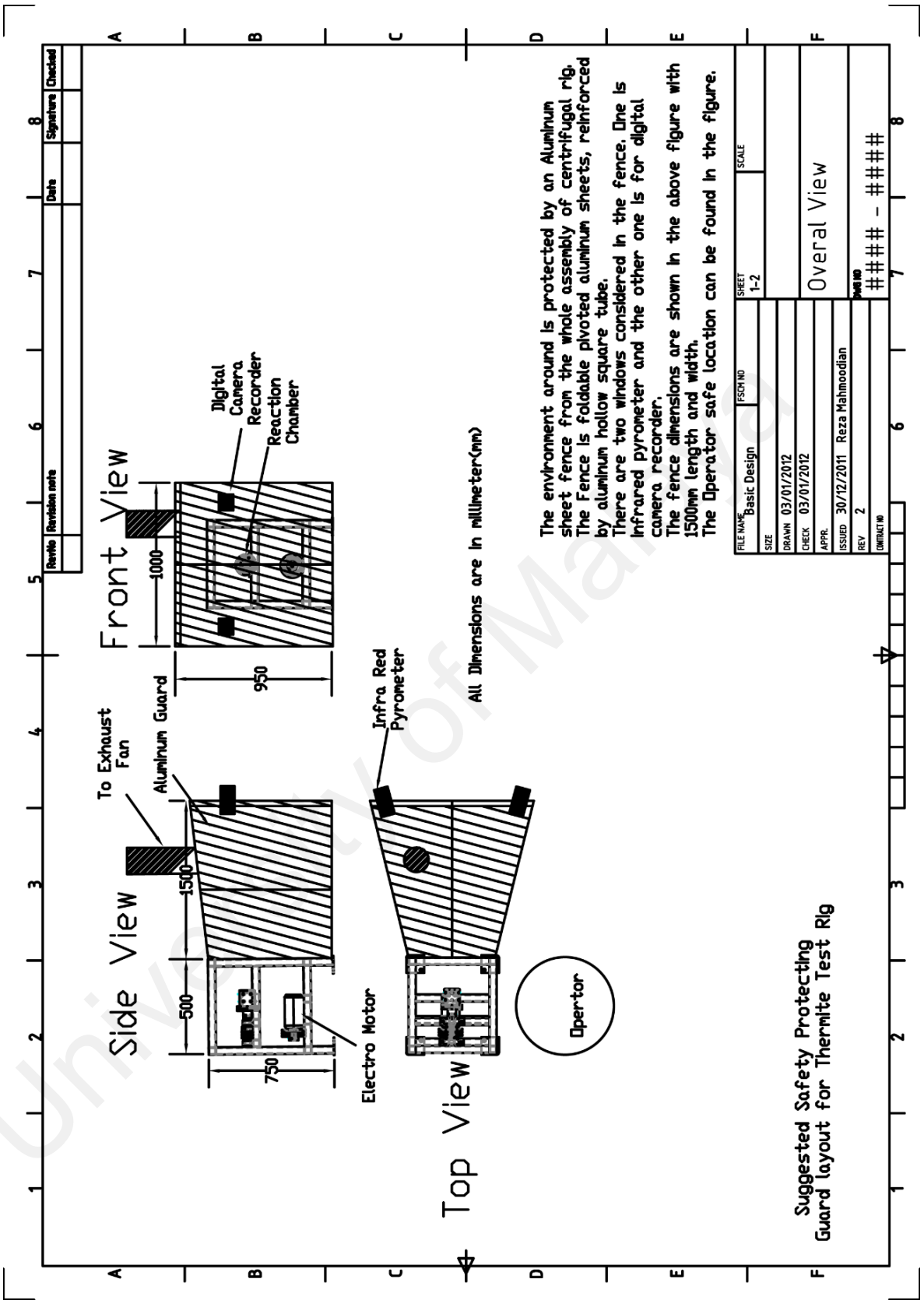

Figure 4.7: Schematic view of the safety protecting guard (sheet 1)

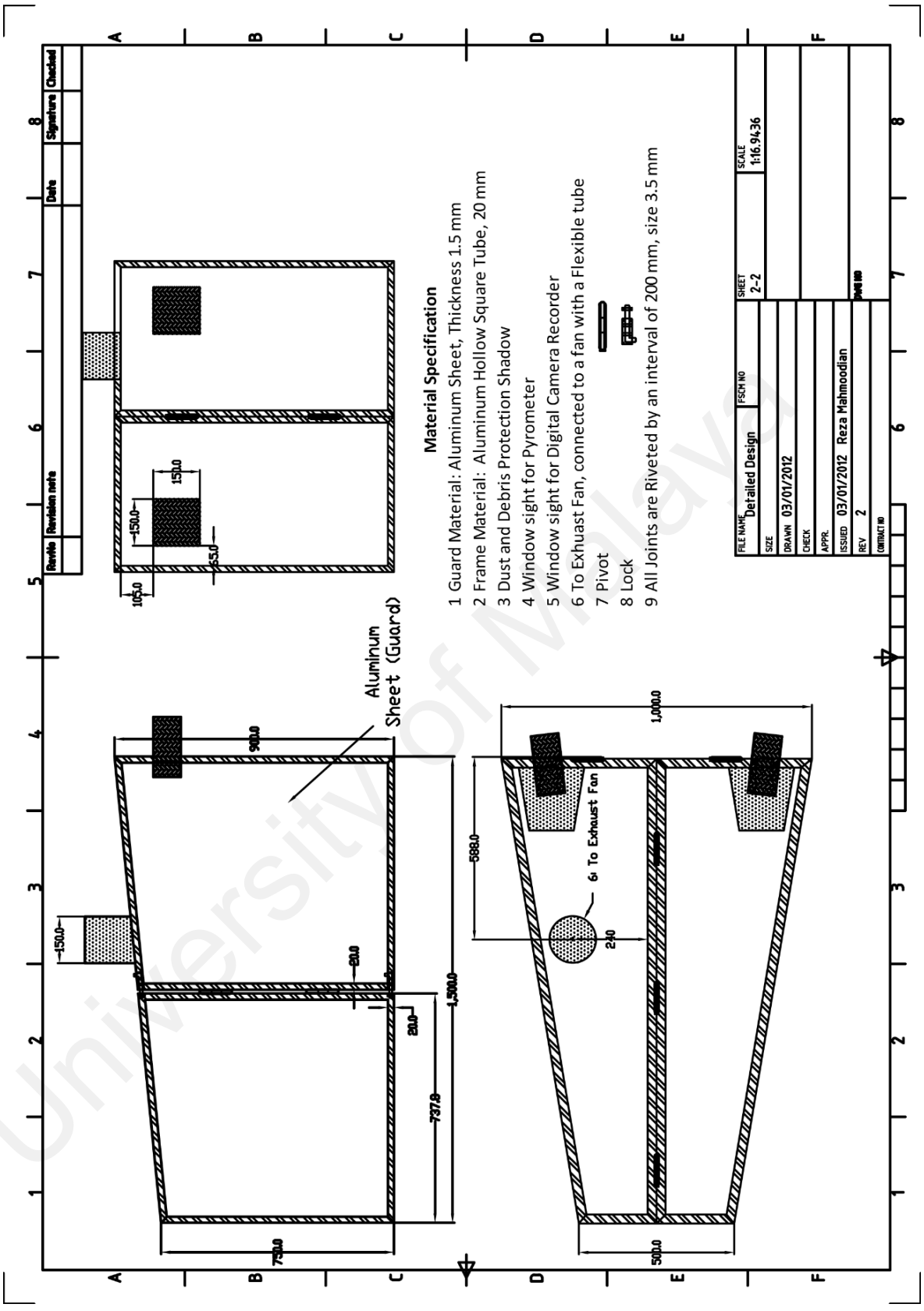

Figure 4.8: Schematic view of the safety protecting guard (sheet 2)

4.3 Plasma-assisted reaction chamber design: Method (5)

Originally, tungsten contamination occurred in a preliminary study that employed a tungsten electrode. Therefore, a graphite electrode was utilized in this experiment. This may be helpful in reducing contamination due to the high temperature process produced by the electrode. Any other dust or materials should be cleaned and remnants left to evaporate during the experiment.

There is an opening at the center of the cap for electrode introduction. Carbon fibers were placed at the bottom of the crucible in order to ease the argon gas flow and to shield the pellet. The other advantage of using carbon fibers is that they help the pellet not touch the base of the crucible. The fibers were roughly 10 mm high.

4.3.1 Reaction chamber with two gas inflow channels

A diagram of the DC-focused plasma arc reaction chamber is illustrated in Figure 4.9. The crucible was designed to have two argon gas intake channels. The chamber frame is made from mild steel material so it can tolerate thermal shock (Figure 4.10a). Figure 4.10 (b) presents a top view of the chamber with distinct cylindrical hollow carbon in the core and compacted graphite between the carbon and steel frame.

The mild steel material of the reaction chamber has some advantages compared to other materials in terms of machining ease and lower cost as well as enhanced performance in instances of thermal fluctuation. The steel mold was filled with compacted graphite powder and a graphite tube (mold) at the center with 21 mm diameter. Two channels were made in the reaction chamber wall for argon gas intake.

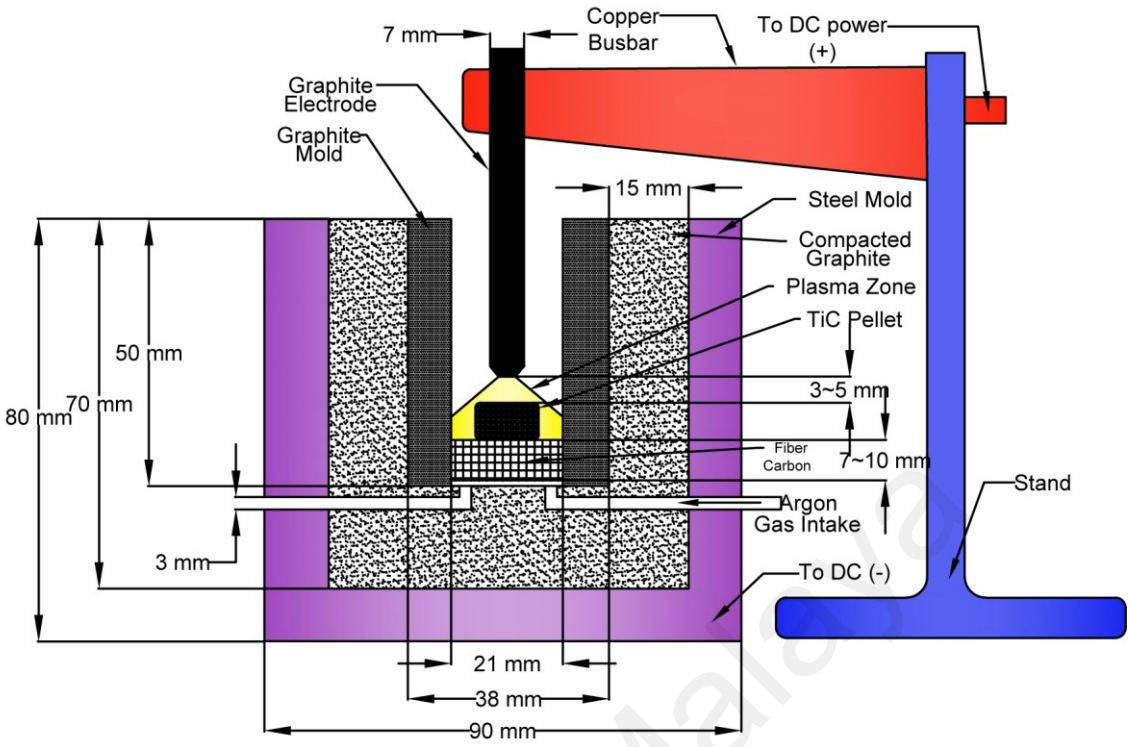

Figure 4.9: Drawing of DC-focused plasma arc reaction chamber

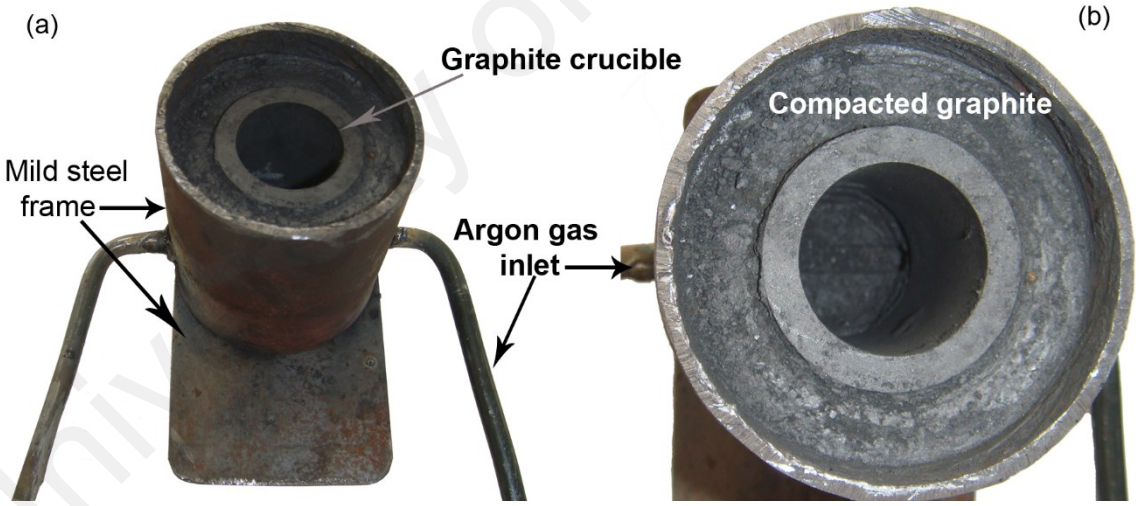

Figure 4.10: Developed graphite crucible for synthesizing high temperature material

This experiment was run in a plasma reaction chamber, and the reaction was developed for this purpose. An image of the reaction chamber is provided in Figure 4.10. The experimental setup and method are elaborated in Figure 3.9 and Figure 3.10, respectively. Figure 3.9 illustrates a graphic drawing of the high temperature crucible assembly. The argon gas had the role of protecting the high temperature zone from oxygen (Tian et al., 2006) and aid in the formation of plasma (Shinde et al., 2010). An electrode fixture held

the graphite electrode at the desired position and elevation. The electrode was connected to the positive pole and the mold to the negative pole of a direct current (DC) power supply from a tungsten inert gas (TIG) device producing a plasma arc between a tungsten electrode and the workpiece. The crucible assembly design is depicted in Figure 3.9. Inert gas protects the arc, electrode, and molten pool from atmospheric contamination (Fujii et al., 2008; Huang, 2009).

4.3.2 Reaction chamber with four gas inflow channels

Mild steel material was taken into account when fabricating the reaction chamber for ease of machining, lower cost, and better performance in cases of thermal fluctuation.

The outer diameter of the chamber was 110 mm, the inner diameter of the reaction chamber steel was 72 mm and the depth was 60 mm (Figure 4.11-a). Six valves were made in the reaction chamber wall. Four of the valves were for argon gas intake (two valves on each side) and two other valves served as air vents (Figure 4.11-b). There was an opening at the center of the cap, which served as an entrance for the electrode. The electrode's location at the middle of the reaction chamber is shown Figure 4.11-a. Slots were made in the reaction chamber cap to attain better mechanical interlocking during graphite powder compaction and to keep the compacted powder in place when the cap faced downward (Figure 4.11 (a) (b), left images). Three sorts of progressive jigs and dies were designed in order to compress graphite in the reaction chamber and on the cap. This compressed graphite powder had a thickness of 15 mm (Figure 4.11-b, right image). A control panel was devised to control argon flow into the reaction chamber, with two on-off electrical values controlled by two switches (Figure 4.11-c).

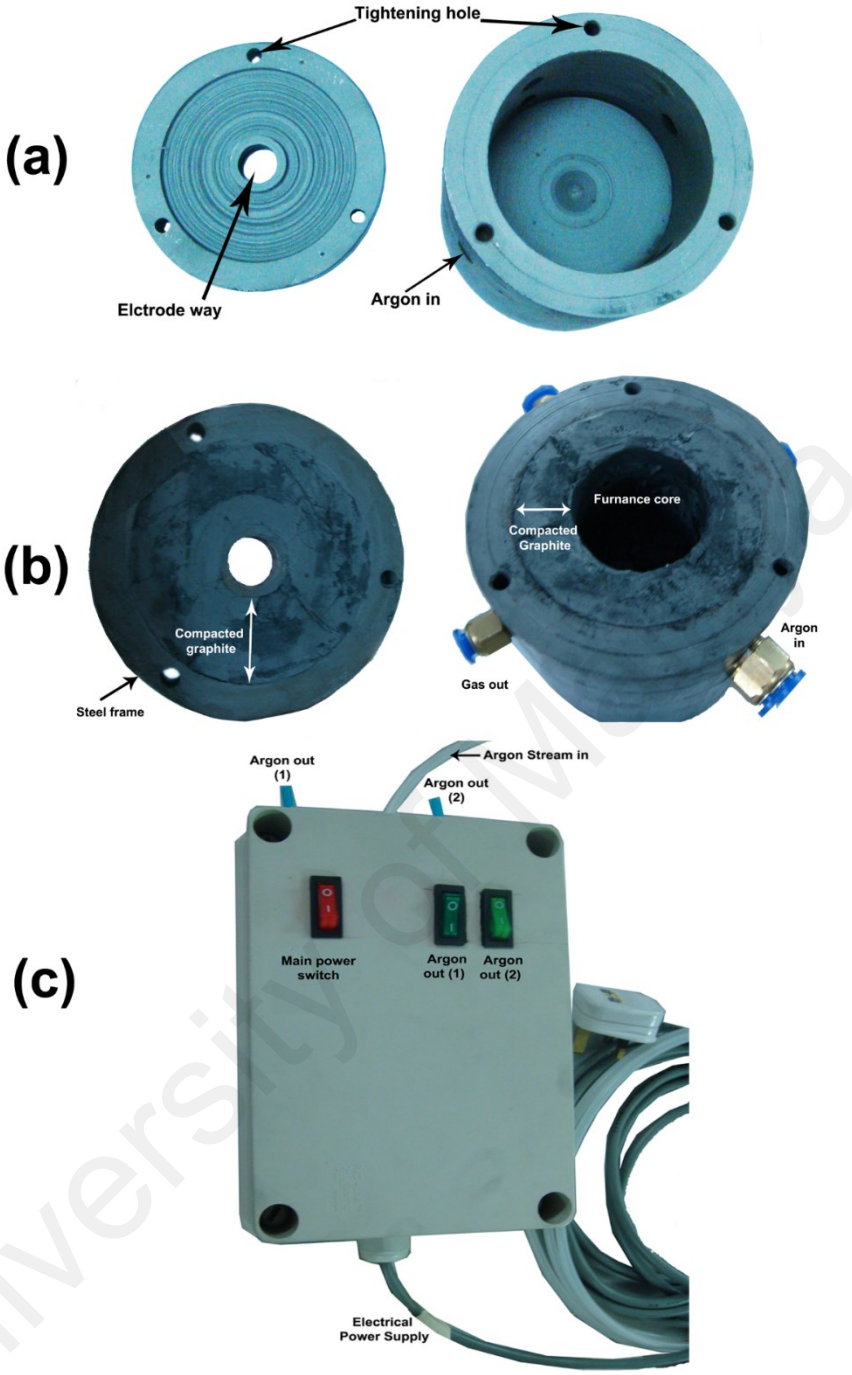

Figure 4.11: Plasma reaction chamber and its argon flow control panel

CHAPTER 5:EXPERIMENTAL WORK

5.1 Introduction

In this chapter, the experimental work is presented in six categories. Five different production and synthesis methods were utilized in conducting the experiments.

5.2 Conventional ceramic-lined composite pipe production using method (1)

5.2.1 Reactant powders

The reactant powders employed in this research are listed in Table 5.1, and Table 5.2 provides the carbon steel pipe dimensions.

Table 5.1: Characteristics of the reactant powders

Powder	Size (μm)	Purity (%)	Mass (gr)	Vendor (Company)
Al	Fine Powder <75	99	28	Sigma Aldrich
Fe_2O_3	<5	97	83	Sigma Aldrich

Table 5.2: Steel pipe dimensions utilized in the centrifugal SHS process

Outer Diameter (mm)	Inner Diameter (mm)	Thickness (mm)	Length (mm)
78	72	3	115

5.2.2 Mixture preparation

Al and Fe_2O_3 powders were weighed on a Kshida Shinko weighing machine with up to 0.001 gr accuracy. The powders were dried at 110 °C for 8 hours. The stoichiometric Fe_2O_3+2Al mixture was prepared and mixed in a ball mill for 7 hours. The ball mill was

maintained at a relatively slow rotational speed (150 rpm) to avoid potential thermite reaction initiation in the mixture. The ratio of Zirconia ball mass to powder mass was 4:1.

5.2.3 Pipe and blind

The steel pipe and refractory blind (leveler) component are shown in Figure 5.1. The refractory thin blind was designed and set up to keep the powder mixture inside the pipe at a specific level. The blind prevented the powders and melted material from flying out during the process. The complete pipe assembly (Figure 5.1) was fixed inside the reaction chamber of the centrifugal SHS apparatus (Figure 4.1).

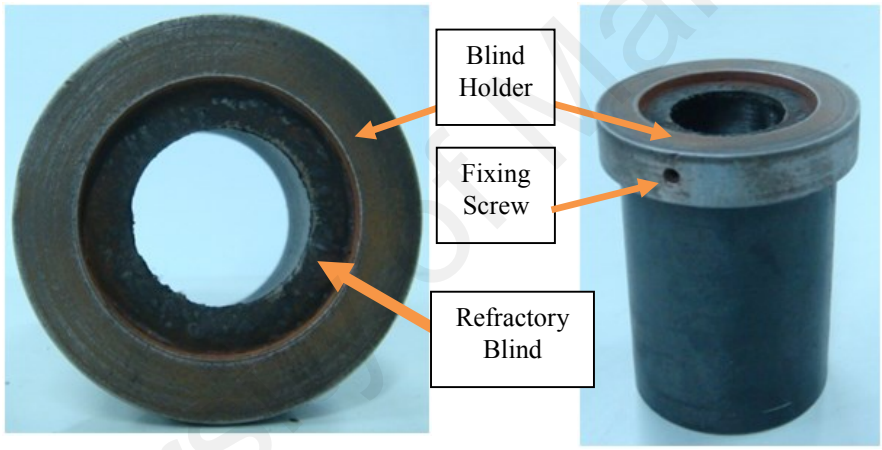

Figure 5.1: A steel pipe and its hollow blind used in a typical centrifugal SHS process

5.2.4 Pre-test Run

The machine (Figure 4.1) was prepared for the combustion experiment. Machine pre-testing was performed to ensure parameter and safety control. Upon pre-testing completion, all necessary precautions and safety arrangements were considered.

5.2.5 Combustion experiment:

The combustion reaction in the main chamber occurred in the following course of action:

1. The pipe and attached blind (Figure 5.1) were placed inside the CT machine, and material was fed into the rotating machine at 5*g* acceleration
2. After supplying the material completely, the rotation speed was increased slightly using an inverter to achieve the desired centrifugal acceleration according to Equation 2-1.
3. The mixture was then ignited with an oxyacetylene flame. At the onset of the reaction, the flame protruded from the reaction chamber opening.
4. Igniting the rotating substrate and powder mixture made the powders react and propagate along the pipe at high velocity. The velocity could reach up to 1500 mm/s (Miyazaki & Odawara, 2000) and lead to high temperature flames and fumes emerging from the hollow body pipe.
5. The reaction lasted only a few seconds. The rotation continued after combustion finished, confirming that complete phase separation occurred. A particular holding time was required to achieve a safe, lower temperature before removing the sample from the reaction chamber.
6. Another effect of centrifugal force was the phases separating from each other after meltdown. These were ranked according to their relative densities.

5.3 A preliminary study on the effect of a hot argon inert crucible on the phase formation of a Ti-C pellet (SM04)

A preliminary experiment was conducted in order to simulate the behavior of a Ti-C pellet exposed to heat released by a thermite reaction. A Ti-C pellet mixture of the same starting chemical composition as that used in the centrifugal thermite-assisted Ti-C method was compacted in a round section stainless steel die. The compact pressure was 3.5 tons and the pellet had a 12 mm diameter and 5 mm thickness.

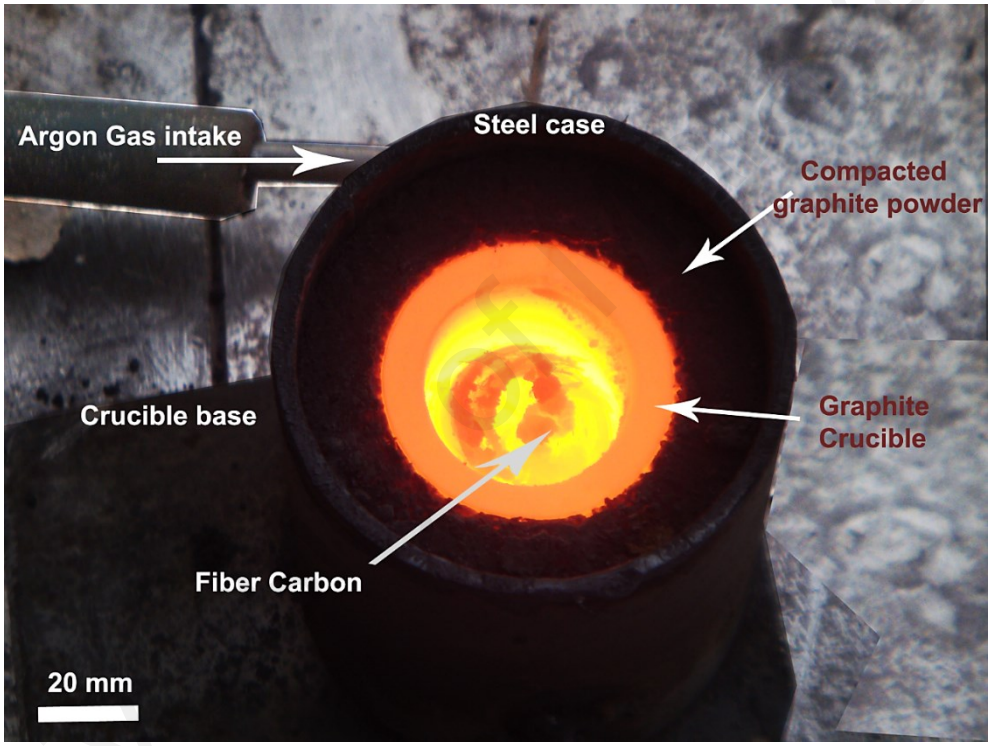

Figure 5.2: Graphite crucible with argon gas flow intake at elevated temperature

Figure 5.2 shows a simple graphite crucible with argon gas intake heated up to 2610˚C and kept at that temperature for 30 s. A Ti-C compacted pellet was released into the super-heated crucible (Figure 5.2). Argon gas flow purged the chamber at 1.8bars/s and no other external heat was applied to the pellet during the process. An infrared pyrometer monitored the crucible temperature for system cooling behavior observation. Experiment SM04 was carried out to gain insight into how a Ti+C pellet behaves when subjected to sudden heat and monitored cooling. The aim of SM04 was to substantiate the notion of centrifugal-assisted TiC processing. The as-sintered specimen was subsequently removed

from the chamber for further characterization (FESEM, XRD) and Nano-mechanical measurement.

5.3.1 Nano-indentation test

Nano-indentation was done to find the Young's modulus of the specimen by applying the load-unload technique, which was elaborated in Section 3.2.4. The polished specimen was indented (loaded-unloaded) using a three-faced Berkovich tip by Shimadzu DUH-211S.

The sample was mounted using a Bohler hot mounting device (surface up) and ground with 120, 300, 800, 1200, and 2400 grit paper, then polished with cotton and alumina paste with 0.2 μm particle size. The polished sample was cleaned in an ultrasonic cleaning bath for 10 min and air-dried. The test parameters are listed in Table 5.3. The SM04 specimen was indented and the arithmetic average of three different indentations from the same level was applied to obtain Young's modulus.

Table 5.3: Nano-indentation test parameters of a Ti-C specimen

Initial condition		
Indenter type	Triangular115	
Hardness unit	Dynamic hardness	
Readings	3	
Indenter elastic modulus	1.14E+06	N/mm^2
Indenter Poisson's ratio	0.07	
Test condition		
Test mode	Load-unload	
Test force	196.13	mN
Minimum force	1.96	mN
Loading speed	5	(2.6648mN/sec)
Hold time at load	10	sec
Hold time at unload	5	sec
Poisson's ratio	0.22	

The Poisson's ratio of the sample was extracted from the CRC Materials Science and Engineering handbook and the value of 0.22 was selected for input in the software to calculate Young's modulus (Carter & Norton, 2007).

5.4 M+C-Fe-Al_2O_3 FGMs production: Method (2)

Four experiments were conducted based on method (2) with Ti+C, Si+C, and Fe_2O_3+Al as starting materials. In order to deliver a comparison study, three experiments employed centrifugal acceleration. The list of experiments is summarized in Table 3.1. Specimens labeled SM05, SM06, SM07, and SM08 were produced using method 2 (with centrifugal-assisted thermite process), as per Figure 3.3.

The reported temperature of the thermite reaction between Al and Fe_2O_3 was as high as 3400 ºK (Odawara, 1988). The released heat from thermite reaction initiated a chain reaction between Ti and C as well as Si and C. The reported temperature is much higher than the ignition temperature of TiC or SiC reactions (i.e. T_{ig}=1027 ºC (Schubert & Hüsing, 2005)).

The mechanism of structure formation and phase penetration formed in the exothermic reactions between Fe_2O_3+Al with Ti+C and Si+C under centrifugal force was investigated. Temperature–time profile, composition, microstructure, and micro hardness analyses were used to evaluate the phase formation.

The following sections provide details on four of the experiments. The first section deals with SM05 and SM06 processing, while the second section addresses the synthesis environmental effects on SM07. Finally, the last sub-section demonstrates the experimental method and properties of the SiC-based experiment on specimen SM08.

5.4.1 TiC-Fe-Al_2O_3 functional material production (SM05, SM06)

5.4.1.1 Experimental procedure

Aluminum (< 75 µm, 99% purity, Sigma Aldrich) and Fe_2O_3 (< 5 µm, 97% purity, Sigma Aldrich) powders were dried for 8 hours and mixed with a Retsch PM 200 planetary ball mill for 4 hours at 30-minute intervals. The green powder stoichiometric mixture was prepared according to Eq. 1.1 (Odawara, 1988).

Titanium (Sigma Aldrich, -100 mesh, 99.7% purity) and Carbon (Sigma Aldrich, -1000 mesh, 99.9% purity) powders were dried for 8 hours at 115 ºC. Then, the dried powders were mixed using a planetary ball mill (Retsch PM 200) according to Eq. 1.2.

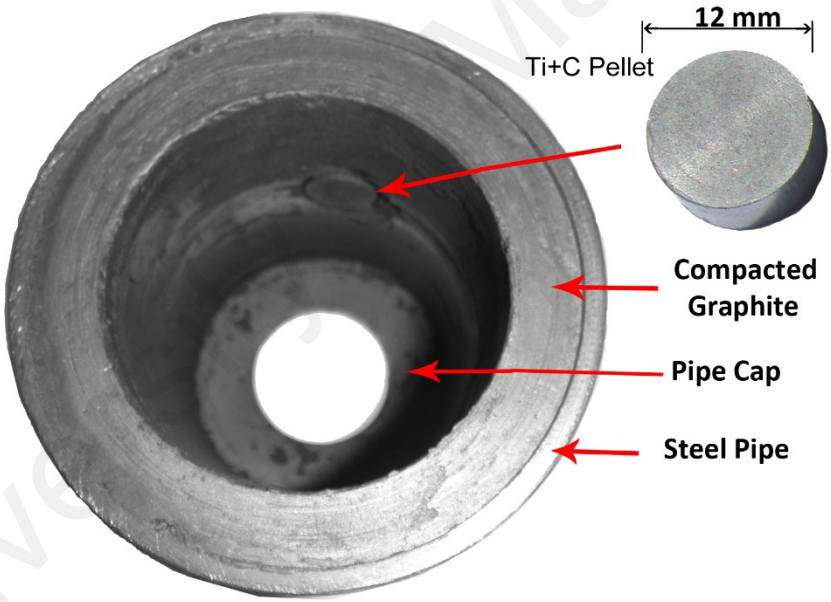

Figure 5.3: Centrifugal crucible constituting compacted graphite and embedded pellet

A carbon steel pipe 75 mm long with inner and outer diameters of 69 mm and 75 mm, respectively, was the bulk holder of graphite. Some graphite was compacted inside the pipe to form a hollow cylindrical graphite crucible, as shown in Figure 5.3. The hollow compacted graphite centrifugal crucible was made using a progressive jig and mold set under 80 tons of pressure (Figure 5.3). The details of utilizing a centrifugal machine to

produce ceramic coating in metallic pipes are provided in Section 5.2. Since the reaction was under the influence of centrifugal acceleration, the TiC formed joined the Al_2O_3-Fe composite. Two Ti+C pellet specimens 7 mm thick and with 12 mm diameter (setting 1 and 2 [Figure 5.5]) were engraved in the hollow graphite crucible (Figure 5.3).

Figure 5.4: Graphite crucible used in the centrifugal thermite-assisted reaction

Two steel caps with holes in the center were placed at the pipe ends to level out the thermite powder (Figure 5.4). The assembly comprising the pipe, crucible, and caps was fixed inside the reaction chamber. The centrifugal crucible was charged with the green powder thermite mixture while rotating as low as 5g acceleration.

The SHS experiment used a horizontal centrifugal machine (Figure 4.1). The technical requirements for high temperature and high-speed reactions in the small chamber were predetermined during preliminary testing. This type of machine facilitates high centrifugal acceleration and rapid temperature increase during the experiment. A graphite compacted crucible attached to a steel pipe (Figure 5.3 and Figure 5.4) was fastened inside the reaction chamber (Figure 4.1) while a high performance infrared thermometer, Raytek MM1MHSF3L, recorded real-time temperature data.

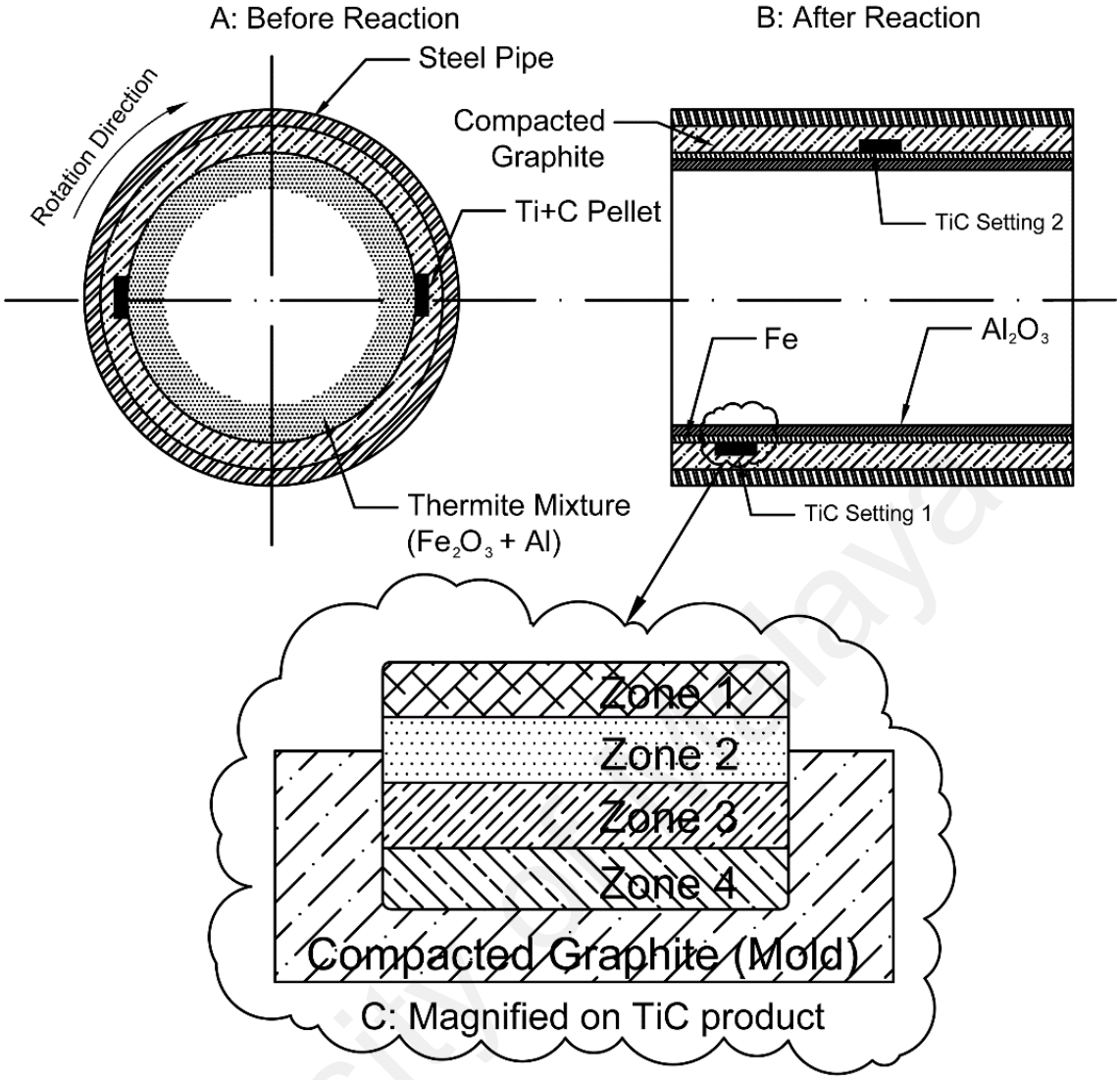

Figure 5.5: Diagram of steel pipe and graphite crucible assembly charged with the green mixture; A: before reaction (top left), B: after reaction (top right) while subjected to a centrifugal force, and C: Magnified TiC product (method 2)

Experiments SM05 and SM06 were conducted under the scheme of method (2), whereby Figure 3.3 corresponds to settings 1 and 2 of Figure 5.5. The rotational speed was fixed at 58 s^{-1} during reaction to ensure reaction uniformity and completion inside the tube. An embedded speedometer monitored the rotational speed of the pipe in the centrifugal SHS machine throughout the experiment, as seen in Figure 4.1. The overall experimental setup scheme before and after reaction is shown displayed in Figure 5.5. A TIG machine with 200A of direct current (DC) was utilized to ignite the mixture. In this

experiment, a graphite electrode was used instead of tungsten in the TIG machine to avoid tungsten contamination.

The naturally violent exothermic behavior of the SHS reaction was evident in the experiment (Li et al., 2005). SHS reaction violence signifies the start of the reaction inside the tube. The exothermic reaction between Fe_2O_3 and Al inside the pipe produced high temperature Al_2O_3 ceramic and molten Fe. Al_2O_3 and Fe phase formation from the products was followed by phase separation under centrifugal force at high rotational speed (Orru et al., 1996). The generated heat was sufficient to ignite the Ti+C reaction. In addition, the molten Fe+Al_2O_3 was forced to the surface of the TiC pellets by the centrifugal force. The tube was kept rotating at a fixed rotational speed from the beginning of the reaction until product solidification completed. The cooled tube was taken out for characterization. The ceramic phase formation, microstructure, and micro-hardness were measured at different points on the surface of TiC and Al_2O_3. The micro hardness was measured using a Vickers indenter at 1.961 N loads.

5.4.2 TiC-Fe-Al_2O_3 functional material production (SM07)

5.4.2.1 Reactant materials

A centrifugal thermite (CT) machine facilitated rapid centrifugal acceleration as well as temperature increase during the experiment. A bi-layer graphite-steel compacted mold was secured inside the CT reaction chamber. A high performance infrared thermometer, Raytek MM1MHSF3L, recorded the experimental real-time temperature data. The detailed procedure of using the centrifugal machine for thermite processing in metallic pipes is explained in Section 5.2.

The starting materials, namely Al (< 75 μm, 99% purity, Sigma Aldrich) and Fe_2O_3 (< 5 μm, 97% purity, Sigma Aldrich) powders, were dried for 8 hours and mixed in a Retsch PM 200 planetary ball mill for 4 hours at 30-minute intervals. The green powder stoichiometric mixture was prepared according to the following reaction equation: $Fe_2O_3+2Al \rightarrow Al_2O_3+2Fe$, $\Delta H = -768.75$ $kJmol^{-1}$ (Odawara, 1988). Titanium (Sigma Aldrich, -100 mesh, 99.7% purity) and carbon (Sigma Aldrich, -1000 mesh, 99.9% purity) elemental powders were dried for 7 hours at 125 ˚C, following which they were mixed using a planetary ball mill (Retsch PM 200) according to the reaction equation $Ti+C \rightarrow TiC$, $\Delta H = -183$ $kJmol^{-1}$. A 75 mm long carbon steel pipe with inner and outer diameters of 69 and 75 mm, respectively, served as a bulk holder for graphite. The dried Ti+C green powder was pressed into a pellet, which was inserted into a pre-defined location into the graphite mold as shown in (Figure 5.3, and Figure 5.6).

The thermite mixture was fed into the tube. The rotation speed was raised to 280-g acceleration, followed by igniting an electric arc with a graphite electrode. The onset of the thermite reaction was trailed by a titanium and carbon reaction, which occurred in response to the heat generated by the thermite (first) reaction. The released temperature was logged by the infrared pyrometer.

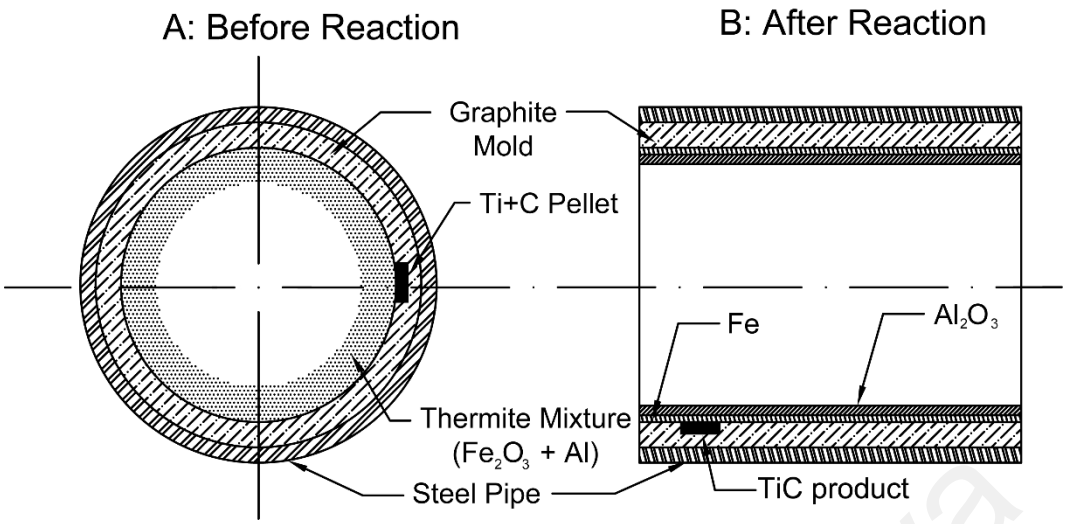

Figure 5.6: Schematic diagram of the assembly: (A) before reaction, and (B) after reaction

5.4.2.2 Environmental conditions

A cross-section of the composite was prepared with a low-speed diamond cutter prior to being polished and cleaned in an ultrasonic acetone bath. The product was not etched. Subsequently, the sample was released and exposed to room air and environmental conditions (e.g. high humidity, up to 80%).

Nano-mechanical test

Nano-indentation was carried out to determine the Young's modulus of the specimen by applying the load-unload method. This method was explained in Section 3.2.4. A cross-section of the sample was mounted using a Bohler hot mounting device, then ground with 120, 300, 800, 1200, and 2400 grit paper and then polished with cotton and alumina paste (0.2 μm particles).

The polished specimen was indented (load-unload) using a three-faced Berkovich tip by Shimadzu DUH-211S. The applied parameters were set at 300 *m*N of load and 3 μm depth. The test parameters are presented in Table 5.4. The material was indented at two different zones on SM05, SM06, and SM07. Each value is the arithmetic average of three different indentations at the same level.

Table 5.4: Nano-indentation test parameters for the TiC-Fe-Al_2O_3 specimen

Initial condition		
Indenter type	Triangular115	
Hardness unit	Dynamic hardness	
No. of readings	3	
Indenter elastic modulus	1.14E+06	N/mm^2
Indenter Poisson's ratio	0.07	
Test condition		
Test mode	Load-unload	
Test force	300	mN
Minimum force	1.96	mN
Loading speed	5	(14.0134mN/sec)
Hold time at load	10	sec
Hold time at unload	5	sec
Poisson's ratio	0.22	

5.4.3 Synthesis of embedded Si+C under centrifugal thermite reaction (SM08)

The effect of thermite energy (heat) on a Si+C pellet under centrifugal acceleration is studied in this section. A Si+C pellet was processed with Method (2) at higher gravity force. As previously explained, the thermite mixture liberates an abundance of energy in the form of heat upon ignition. The released thermal energy is given in Eq. 1.1. The aim of this study is to employ the generated heat to process a Si+C pellet and convert it into a secondary product, preferably silicon carbide (SiC).

Eq. 1.3 indicates that the reaction between Si and C elemental powder is exothermic. Nevertheless, the adiabatic temperature is not enough to propagate along the sample unless the environment is satisfactory (Seo et al., 2010). Preliminary studies showed that the centrifugal thermite temperature increased up to 2900 ˚C. Therefore, this experiment was set up according to the experimental procedure using method (2) and Figure 5.7. The schematic diagram of this process was shown in Figure 3.3.

5.4.3.1 Reactant powders

The reactant powders for this experiment, namely silicon (Sigma Aldrich, -325 mesh, 99% purity) and carbon (Sigma Aldrich, -1000 mesh, 99.9% purity) were dried for 8 hours

in a 115 ˚C chamber, then loaded in a ball mill and mixed at 250 rpm at 20-minute intervals for 5 hours according to the stoichiometry ratio in Eq. 1.3. The mass of the Zirconia balls used for the ball-milling phase was 5 times that of the mixed powders. After mixing the starting powders, the mixture was compressed with 4 tons of pressure into pellets with 12 mm diameter and 8 mm height.

Graphite powders were compacted in a steel pipe with 70 mm outer diameter and 64 mm inner diameter using a progressive die set. The compression was done layer-by-layer under 8 tons of pressure. The respective image is displayed in Figure 5.7.

The Si+C pellet was embedded inside the compacted graphite mold, as per Figure 5.7-a. A steel cap placed on the pipe head secured the molten level when subjected to a centrifugal field (Figure 5.7-b). The complete assembly with the crucible, pellet, and caps was fixed inside the reaction chamber of the centrifugal thermite test rig (Figure 4.1).

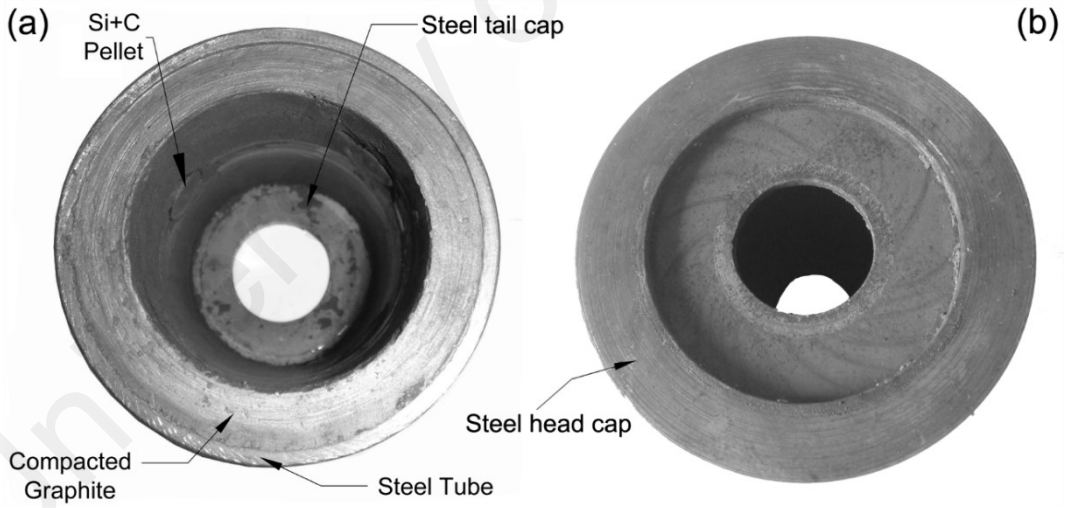

Figure 5.7: Centrifugal crucible with (a) Si+C pellet embedded inside the graphite crucible, (b) the pipe assembly ready for process

The thermite starting materials, namely Al (< 75 μm, 99% purity, Sigma Aldrich) and Fe_2O_3 (< 5 μm, 97 % purity, Sigma Aldrich) powders were dried for eight hours and mixed in a Retsch PM 200 planetary ball mill for 4 hours at 30-minute intervals. The green powder stoichiometric mixture was prepared according to Eq. 1.1.

The thermite mixture was fed into the crucible assembly, which was rotating at 5g acceleration. The rotation acceleration increased to 150g once feeding was completed. Safety precautions should be considered when working with centrifugal thermite reactions.

A TIG Direct Current (DC) machine initiated the thermite mixture ignition, and a graphite electrode was used instead of tungsten for arc initiation. The current was set to 150A, while the infrared temperature acquisition unit captured instant temperature values of the reaction and recorded them in a computer. The specimen was removed from the chamber after cooling. The reaction began immediately after ignition and propagated along the sample, and was accompanied by a huge stream of explosions.

5.5 Ti-C-Al-Fe/TiN composite product under offset thermite centrifugal process (Method 3)

5.5.1 Reactant powders

The reactant powders utilized in this experiment are listed in Table 5.5 and Table 5.6 provides the carbon steel pipe dimensions. The elemental powders were dried for 7 hours at 125 ˚C, following which they were mixed separately using a planetary ball mill (Retsch PM 200) with a Zirconia ball according to Eq. 1.1 and Eq. 1.2.

Table 5.5: Characteristics of the reactant powders

Item	Powder	Size (μm)	Purity%	Mass (gr)	Vendor
1	Al	Fine Powder <75	99	36	Sigma Aldrich
2	Fe_2O_3	<5	97	107	Sigma Aldrich
3	Ti	200	99.7	2	Sigma Aldrich
4	C	< 3	99	0.5	Sigma Aldrich

A steel specimen holder gripped the specimen while rotating at high velocity. The specimen holder level was adjusted to a desired radius relative to the pipe axis using a self-screwing nut embedded in the steel tube wall.

Table 5.6: Carbon steel pipe dimensions used in the centrifugal SHS reaction

Outer Diameter (mm)	Inner Diameter (mm)	Thickness (mm)	Length (mm)
153	143	6	300

5.5.2 Experimental procedure

Carbon fibers covered the inside of the specimen holder (the bed) in order to gain distance from the steel bed. 2.5 grams of Ti+C powder was compacted in a stainless steel die using 5 tons of pressure. The compacted pellet consisting of Ti+C was inserted into the specimen holder. The holder's teeth were then braided with carbon fibers to fix the

pellet inside. Later the specimen holder, containing the sample (Ti+C pellet), was fixed into the steel tube (Figure 5.8-a, b). A welded hollow cap at the pipe head secured the ensuing liquid phase (molten material) level.

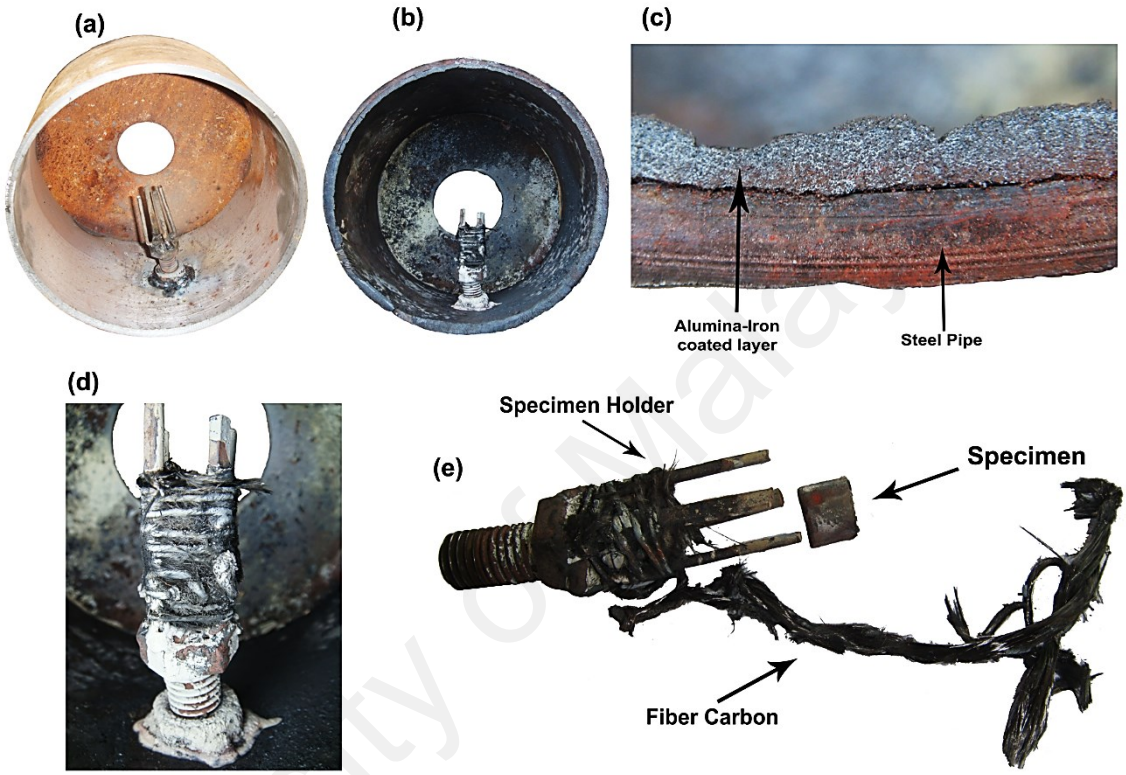

Figure 5.8: Ti+C synthesis using thermite energy under offset centrifugal acceleration

The entire assembly was fixed inside the centrifugal machine according to the setup seen in Figure 3.5. The machine started rotating at around 10g acceleration while the thermite mixture was fed into the steel pipe. Upon feeding completion, the centrifugal acceleration increased up to 250g.

The thermite mixture was ignited using an oxyacetylene gas flame. Safety precautions should be observed due to the highly exothermic behavior of the thermite reaction. The thermite reaction propagated along the pipe and released ample energy that sustained it until all the accessible starting powder was finished and converted into the final product.

Figure 5.8 (a) and (b) show the steel pipe before and after the centrifugal thermite reaction, respectively. A composite of aluminum oxide and iron was deposited on the inner surface of the tube. The phases were separated according to their relative densities. Based on the literature, the thermite reaction's temperature abruptly increased up to 2550˚C and rapidly cooled down. It is likely that a reaction occurred between Ti and C in the pellet fixed inside the tube, since the pellet was in a very high temperature medium.

Figure 5.8 (c), (d), and (e) illustrate the final thermite SHS reaction products, which simultaneously ensued as the Ti+C reaction under centrifugal acceleration. The specimen holder was un-tightened and the specimen removed from the pipe for electron microscopy (SEM) and energy-dispersive X-ray spectroscopy (EDS) using Tescan SEM Electron Microscope Oxford INCA EDS SEM/EDS and PAnlytical XRD characterization. XRD phase quantification was calculated using the Rietveld quantification method.

5.6 Si+C processing using DC plasma-assisted centrifugal method (4)

Silicon carbide (SiC) has excellent electrical and mechanical properties and can operate at elevated temperatures as well. Processing directional SiC has been tried before. In this work, an attempt is made to synthesize SiC using method (4) by employing centrifugal acceleration and plasma synthesis. The test procedure and setting are elaborated in Figure 3.7 and Figure 3.8.

5.6.1 Reactant powders

The reactant powders used in this experiment, silicon (Sigma Aldrich, -325 mesh, 99% purity) and carbon (Sigma Aldrich, -1000 mesh, 99.9% purity), were dried for 7 hours in a 115 ˚C chamber and then loaded in a ball mill and mixed at 250 rpm at 15-minute intervals for 5 hours according to the reaction stoichiometry ratio in Eq. 1.3. The mass of the Zirconia balls used for mixing was 5 times greater than the mass of the starting

powders. The starting powders were compressed under 4 tons of pressure into pellets with 12 mm diameter and 9 mm height, Figure 5.9 (b).

The experimental setup and items are shown in Figure 5.9, where Figure 5.9 (a) represents the specimen holder with a carbon rod positioned, Figure 5.9 (b) illustrates the compressed SiC pellet, and Figure 5.9 (c) and (d) demonstrate how the pellet was placed inside the specimen holder and braided using carbon fibers. The carbon fibers acted as support to secure the pellets during rotation and stopping. Figure 5.9 (e) shows the way the specimen holder was placed inside a ceramic-coated pipe with 200 mm diameter and 6 mm thickness. The pipe was coated using method (1) with alumina that acted as a thermal barrier. In plasma state, the temperature reaches over 10000 ˚C at the local plasma points, which would consequently raise the system temperature. Steel cannot operate well above 700 ˚C. Thus, an alumina-coated layer helped induce a thermal barrier to boost the safety, service condition, and lifespan of the pipe during reaction.

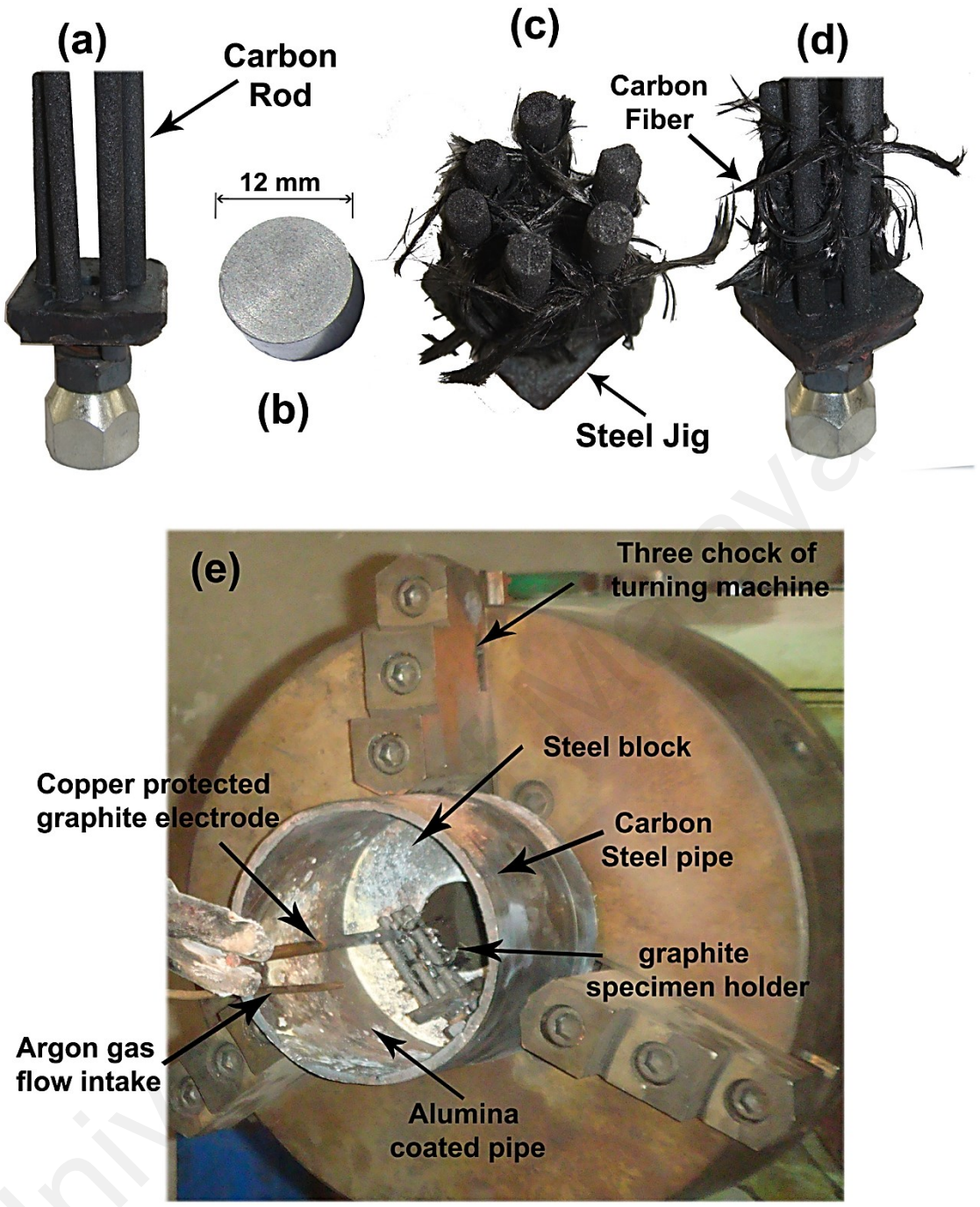

Figure 5.9: Experimental setup of plasma-assisted centrifugal method

The entire assembly was secured inside a lathe machine to satisfy constant centrifugal acceleration. Figure 5.9 (e) shows that an argon gas pipe was positioned inside the pipe while a graphite electrode is nearby and connected to a TIG machine with direct current (DC) supplying enough current to initiate an arc. The electrode was coupled with the tool holder of the lathe machine, to allow the researcher to adjust the plasma gap smoothly and precisely.

The assembly, as shown in the figure, rotated at around 200g acceleration. The distance between the graphite electrode and carbon rod of the holder decreased to nearly zero. An arc was initiated between these two parts and the argon stream converted the sparking state into local plasma. A rotating hot crucible formed during rotation at high velocity. The operation was continued for about 60 sec and then stopped, after which the specimen was taken out of the chamber for further characterization.

5.7 Processing M+C with DC-focused plasma arc technique using method (5)

Two experiments are discussed in this section as well as an evaluation of Ti+C and Si+C pellets as they were exposed to plasma-generated heat. SM02 addresses the possibility of SiC processing under plasma condition and SM03 refers to TiC processing.

5.7.1 SiC processing using DC-focused plasma arc (SM02)

High purity silicon carbide (SiC) possesses excellent properties that benefit electronic and manufacturing industries, and it can operate at elevated temperatures as well (Yang et al., 2012). In this experiment, SiC synthesis using method (5) by employing argon shielded plasma synthesis in normal gravity was attempted. The test procedure and setting were presented in Figure 3.8 and Figure 3.9.

5.7.1.1 Reactant powders

The reactant powders used in this experiment, Silicon (Sigma Aldrich, -325 mesh, 99% purity) and Carbon (Sigma Aldrich, -1000 mesh, 99.9% purity) were dried for 8 hours in a 115 ˚C chamber, loaded in a ball mill and mixed at 250 rpm at 20-minute intervals for 5 hours according to the stoichiometry ratio in Eq. 1.3. The Zirconia balls used for mixing had 5 times the mass of the powders. The milled powders were compacted under 5 tons of pressure at room temperature without any lubricant in a stainless steel die set with 12 mm diameter.

A TIG machine with 210A of direct current (DC) initiated an arc with two argon gas intake channels. The reaction chamber was shown in Figure 4.11. The argon flow rate was 1.4bars/s and the active plasma duration was 60s. The electrical buttons allowed for simple flow rate control, while the four argon intake channels surrounding the specimen made it easier for plasma to form all around the sample. A state of local plasma is highly likely if the argon does not equally surround the specimen. The sample temperature was measured using an infrared high temperature pyrometer.

The electrode was removed from the chamber and isolated, while a positive low argon pressure continued to be added to the system to diminish product oxidation until the chamber cooled to room temperature. The as-sintered specimen was taken out for FESEM, EDS and XRD characterization.

5.7.2 TiC/C composite processing using DC-plasma arc (SM03)

5.7.2.1 Introduction

Titanium carbide (TiC) resulting from a Ti and C self-sustained reaction, is characterized by high hardness, good wettability, low density, and chemical stability (Das et al., 2002). TiC is also a typical transition metal carbide with a high melting point (Friedrich et al., 2011).

The hardness properties of TiC produced using single-stage SHS are not desirable owing to the green powder compact nature. Therefore, a special plasma reaction chamber was developed to produce TiC under extreme thermal conditions and to maintain the temperature high enough to let the compacted starting powder react, melt, and re-crystallize. The formation of TiC/C was investigated, with the results characterized using micro-hardness, microstructure, elemental composition, and x-ray diffraction. This product has the capacity to be used as a machining insert tool, local enforcement of a secondary process (e.g. ceramic-lined composite pipes), as well as a thin component in super-capacitor industries (Sonnenburg et al., 2009). Super-hard materials are those with Vickers hardness (HV) values greater than 40 GPA (Vepřek, 2008).

5.7.2.2 Experimental Procedure

The starting materials, namely titanium (Sigma Aldrich, -300 mesh, 99.7% purity) and carbon (Sigma Aldrich, -1000 mesh, 99.9% purity) powders were dried for 8 hours at 115ºC. Then, the dried powders were mixed using a planetary ball mill (Retsch PM 200) for 6 hours at 20-minute intervals according to Eq. 1.2.

The milled powders were compacted at 1GPa air pressure at room temperature with no lubricant. The pressure die had a 12 mm diameter and the powders were pressed for 8 min. The surface of the compacted specimens was polished carefully for subsequent hardness measurements. A TIG machine with 170A of direct current (DC) was utilized to initiate an arc with two argon gas intake channels. The argon flow rate was 1.6bars/s and the active plasma duration was 300 s. The electrode was removed from the chamber and isolated while positive, low-pressure argon kept being introduced into the system to minimize product oxidation until the chamber cooled to room temperature.

5.7.2.3 Nano-mechanics

Nano indentation was carried out to determine the Young's modulus of the specimen via the load-unload method, which was explained in Section 3.2.4. The test parameters are given in Table 5.4. The calculated elastic modulus is the arithmetic average of five different indentations from the same level.

Table 5.7: Nano-indentation test parameters of a TiC/C specimen

Initial condition		
Indenter type	Triangular115	
Hardness unit	Dynamic hardness	
No. of readings	3	
Indenter elastic modulus	1.14E+06	N/mm^2
Indenter Poisson's ratio	0.07	
Test condition		
Test mode	Load-unload	
Test force	300	mN
Minimum force	1.96	mN
Loading speed	5	(14.0134mN/sec)
Hold time at load	10	sec
Hold time at unload	5	sec
Poisson's ratio	0.189	

The Poisson's ratio of the sample was extracted from the CRC Materials Science and Engineering handbook and set at a value of 0.189 in the software to calculate Young's modulus (Carter & Norton, 2007).

CHAPTER 6: ANALYTICAL AND NUMERICAL MODELS FOR CENTRIFUGAL THERMITE METHOD

6.1 Introduction

In this chapter, viscosity variation and the corresponding infiltration rate of iron and alumina are solved numerically and analytically. Empirical formula testing is done using modified smoothed particle hydrodynamics (MSPH).

6.2 Mathematical modeling of the SHS joining mechanism

6.2.1 Model description

A schematic illustration of material deposition is presented in Figure 6.1. This was developed according to the physical phenomenon during centrifugation (Gowtam et al., 2008) and FESEM observations (Figure 7.15). Figure 6.1 (a) illustrates compacted Ti+C powder and thermite powder mixture prior to the reaction occurring. Figure 6.1 (b) corresponds to region (i) of Figure 7.1, and it describes the reaction when exposed to centrifugal force (CF). The green mixture reacted and produced molten Al_2O_3 and Fe, and the generated heat led to the initiation of TiC reaction.

Figure 6.1 (c) shows the motion of the particles during the solidification process of Al_2O_3, which occurred in region (ii) of Figure 7.1. During this stage, the molten Al_2O_3 has lost its heat and solidified, whereas the molten Fe will infiltrate into the TiC porous site due to the high CF. The CF for a given mass of the particle, m_p, revolutions per second (n) and the particle position (R) is simply calculated as $CF = 39.4 m_p R n^2$ if the gravity force is neglected (Ksandopulo, 2011).

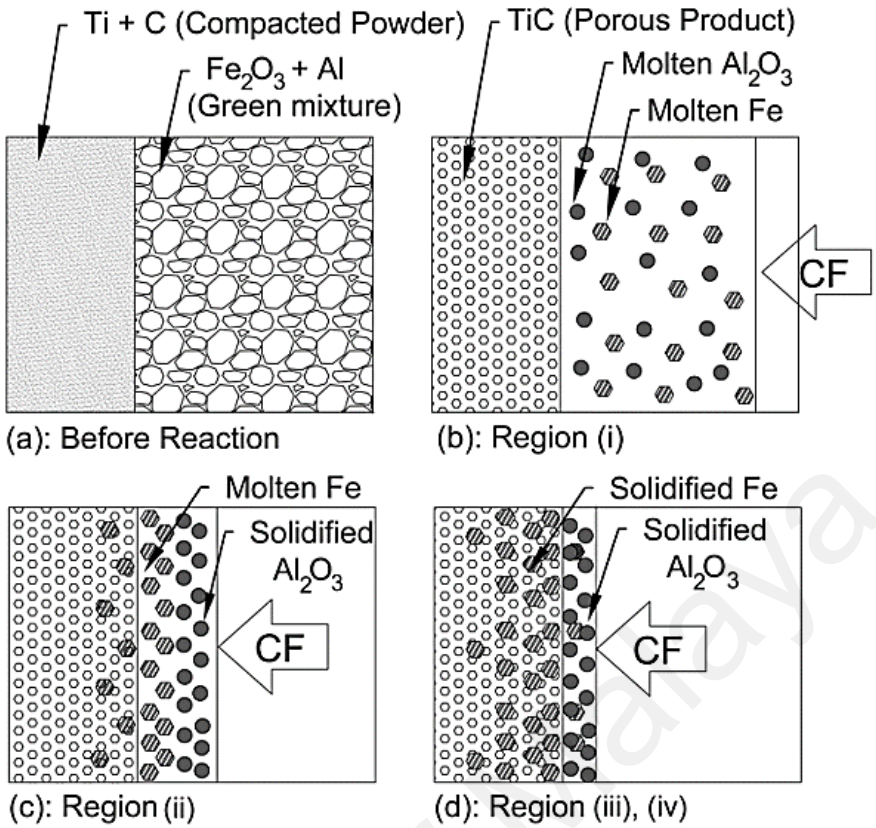

Figure 6.1: The effect of centrifugal force (CF) on material particles during the SHS joining process

Figure 6.2 illustrates the schematic diagram of four forces acting on a particle during the SHS joining process. Since the axis of rotation is horizontal, the centrifugal and gravity forces are working in the same direction and perpendicular to the cylinder axis of rotation. Viscosity (F_η) and repulsive (F_R) forces work against the particle motion towards the cylinder wall and on the same line of action as the centrifugal force. Therefore, the summation of forces acting on a particle at position R (t) from the horizontal axis and near the solid-liquid interface region is:

$$F_\omega + F_g - F_\eta - F_R = F_{nett} \qquad \text{Eq. 6.1}$$

F_R in Eq. 6.1 can be neglected since it is only significant when the particle is close to the solid-liquid interface (Balout & Litwin, 2012). Therefore, the net force becomes:

$$F_\omega + F_g - F_\eta = F_{nett} \qquad \text{Eq. 6.2}$$

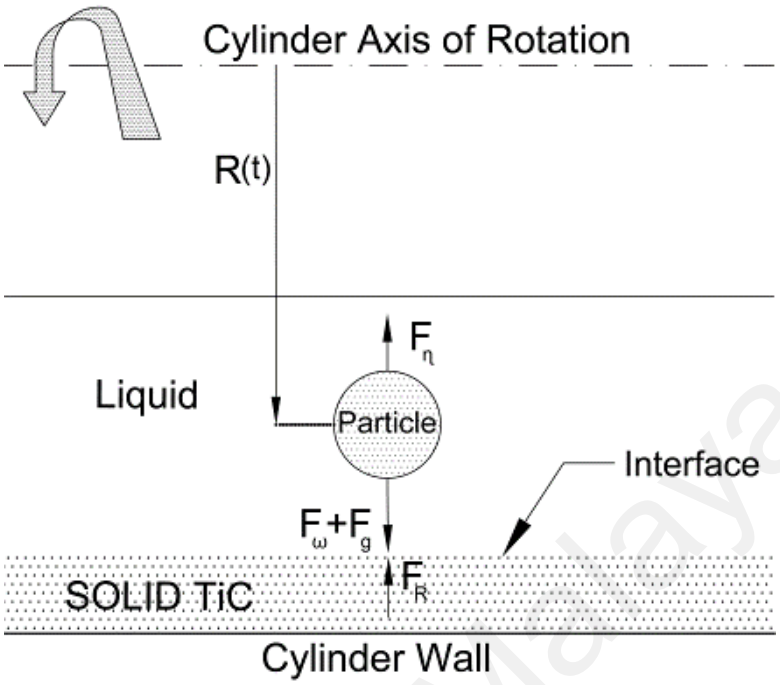

Figure 6.2: Schematic representation of forces acting on a moving particle during the SHS joining process

6.2.2 Particle velocity

Based on Eq. 6.2, the velocity of a spherical particle (deposition velocity) of diameter (d) which is moving in liquid under gravity acceleration (g) is expressed as:

$$V(T_c,t) = \frac{d^2(\rho_o - \rho_m)(39.4Rn^2 + g)}{18\eta} \qquad \text{Eq. 6.3}$$

$$R(t) = R_o exp\left[\frac{d^2(\rho_o - \rho_m)(39.4n^2 + g)}{18\eta}t\right] \qquad \text{Eq. 6.4}$$

$$\eta(T_c) = \eta_o exp\left(\frac{Q}{R_g.T_c}\right) \qquad \text{Eq. 6.5}$$

where V (T_C,t), R_o and R (t) are the velocity, initial and current positions of the particle; η is the current viscosity of the molten metal; and ρ_o and ρ_m are the particle density and melt density, respectively.

6.2.2.1 Calculations of deposition velocity and viscosity

Eq. 6.5 was calculated for the initial viscosity of molten steel $\eta_O = 0.0065 kg.m^{-1}.s^{-1}$ (Ho & Hwang, 1996), total activation energy Q = 706 $kJ.mol^{-1}$ of Al-Fe_2O_3 and Ti-C (Fan et al., 2006; Munoz et al., 1997), the gas constant $R_g = 8.31441\ J.K^{-1}.mol^{-1}$ (Balout & Litwin), and the other thermophysical properties are listed in Table 6.1.

Table 6.1: Thermophysical properties of Fe-Al_2O_3-TiC particles

	Reaction 1		Reaction 2
	Fe	Al_2O_3	TiC
C,J kg^{-1} K^{-1}	473	880	881.98
m, kg	9.19E-02	8.39E-02	3.30E-03
ρ $kg\ m^{-3}$	7800	3950	4930
Q $kJ\ mol^{-1}$	145		560
q $kJ\ mol^{-1}$	836		183

The measured temperature versus time in Figure 6.3 was used to calculate the current viscosity η(Tc) of molten metal before calculating the deposition velocity. This procedure was repeated to solve Eq. 6.5 for the time range of 0.0-2.5s and temperature range of 2830 to 1330 ºC. The calculated values of particle velocity (Eq. 6.3) and viscosity (Eq. 6.5) versus time are plotted in Figure 6.4 and Figure 6.5 respectively.

Odawara, 2010where d = 1.00E-04 m, n = 58 RPS, $\rho_o = 7800\ kgm^{-3}$, $\rho_m = 2700\ kgm^{-3}$, R = 2.50E-02 m. Rapid heating occurred at 0.0s followed by a super cooling process from 0.0 to 2.5s in a single reaction step to produce Al_2O_3-Fe composite joined to TiC. The general trend of the velocity curve decreases with time as the relative viscosity increases.

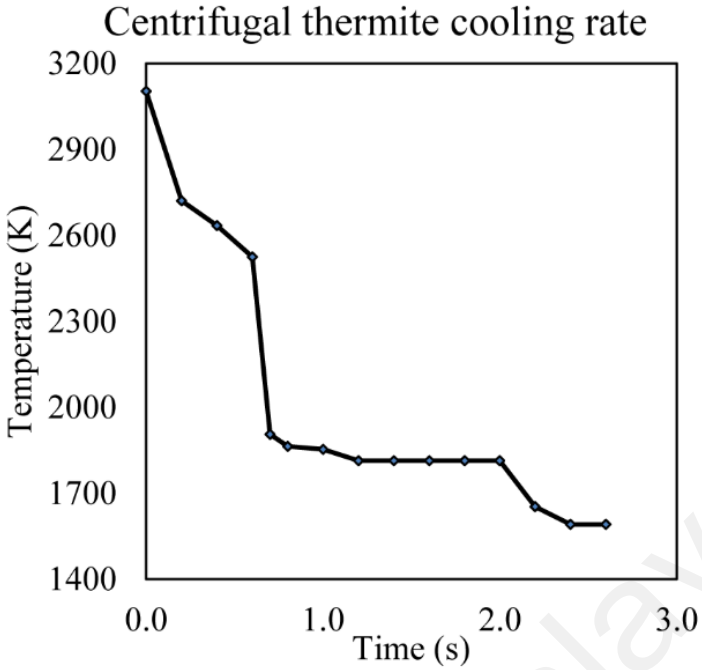

Figure 6.3: Temperature-time cooling profile of the thermite and Ti+C reaction under centrifugal acceleration recorded by the infrared pyrometer

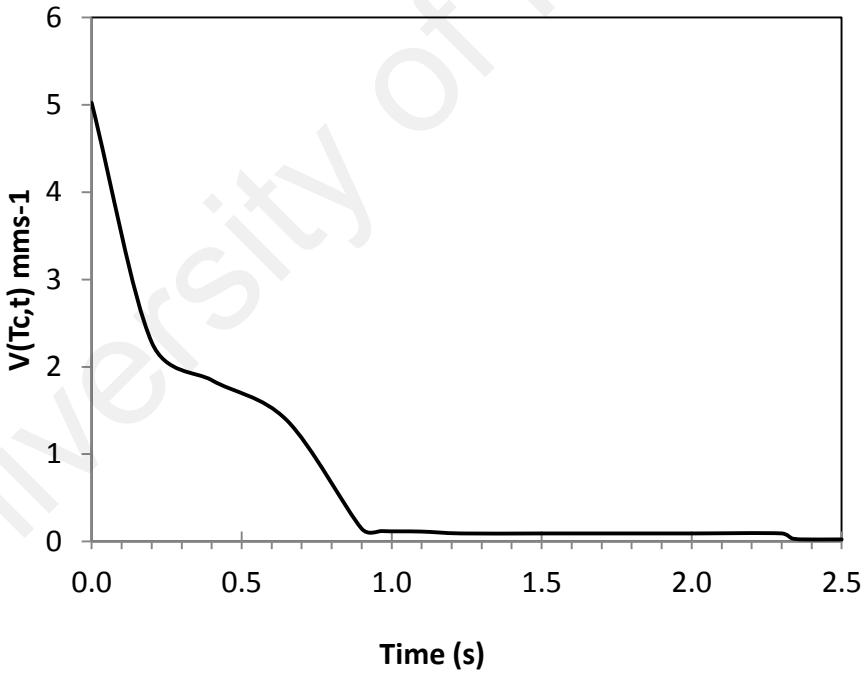

Figure 6.4: Calculated values of deposition velocity versus time of an iron particle in the Ti-based functionally graded coating process

In the time range of 0.0 to 0.2s, which corresponds to region (i) in Figure 6.3, the particle deposition velocity declined sharply since the relative viscosity nearly doubled. In region (ii), the particle velocity V (Tc, t) continued to show a significant decrease with time up to 1.0s, because the Al_2O_3 particles solidified faster. However, in region (iii),

from 1.0 to 2.3 s V (Tc, t) does not show any significant changes. This phenomenon can be attributed to the constant infiltration rate of Fe particles into the TiC product. In region (iv), after 2.3s, the velocity dropped to 0.0 due to a sudden increase in relative viscosity from 97.3 to 376 kg m^{-1} s^{-1}. The governing equations (Eq. 6.3, Eq. 6.4, and Eq. 6.5) were solved in the next section by modified smoothed particle hydrodynamics (MSPH) technique in order to overcome complex boundary conditions and estimate the velocity and displacement gradient during the infiltration and solidification stages.

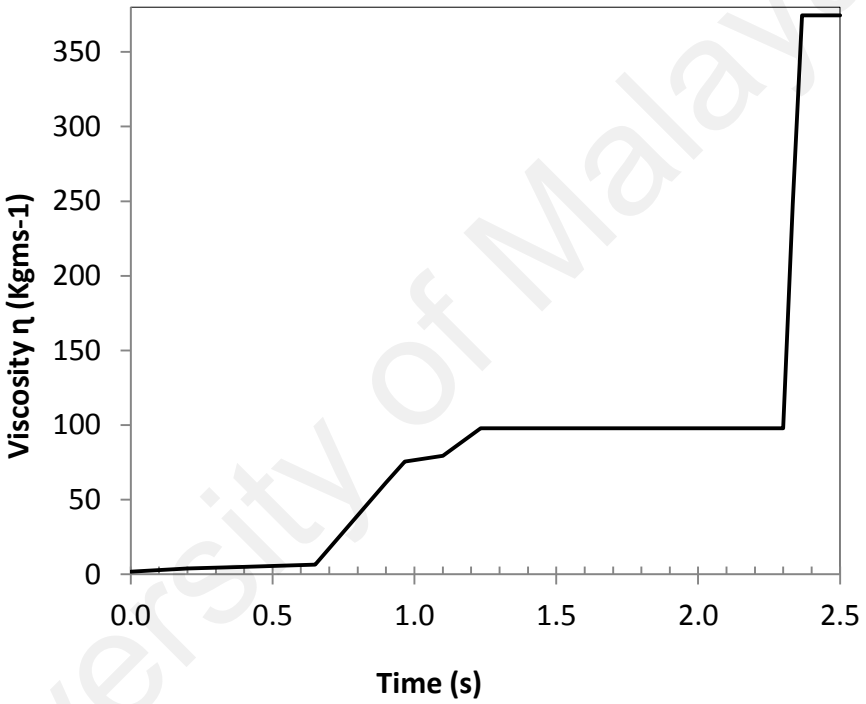

Figure 6.5: Calculated values of viscosity versus time of molten iron in the Ti-based functionally graded coating process

6.3 Smoothed Particle Hydrodynamics

6.3.1 General definition

Smoothed Particle Hydrodynamics (SPH) is a meshless Lagrangian particle method for obtaining approximate numerical solutions of the fluid dynamics equations, which was initially developed by Lucy (1977). Originally, the SPH method was developed for astrophysical applications, and it was gradually expanded to problems concerning incompressible fluids by using either a weakly compressible model of the fluid, or by algorithms designed to solve the full incompressible equations (Monaghan, 2011). The fluid is replaced by a set of particles (Liu & Liu, 2010; Monaghan, 2005). SPH has a wide range of applications in many fields, such as astrophysics, hydrodynamics, head conduction, gas explosions, micromachining, and granular flow, as it demonstrates the ability to simulate highly non-linear free-surface flows including wave overturning, jets, and the formation of spray and droplets (Cleary & Monaghan, 1999; Muhammad et al., 2013).

At first, the SPH method was used by Gingold and Monaghan (1977) for astrophysical phenomena with no boundaries. Gradually, it was vastly developed for different applications including underwater explosion (Liu & Liu, 2010), wave propagation (Monaghan, 2005), magnetohydrodynamics (Price, 2012), material deformation (Takaffoli & Papini, 2012), and particle motions (Monaghan, 2011).

6.3.1.1 Advantages of SPH

- Computational effort is not wasted on empty grid cells
- Deals with free surface boundaries effortlessly
- Can calculate forces on objects in the flow
- The method can deal with a variety of problems

- The absence of a grid means it can cope with complex flows without grid tangling

SPH is capable of solving complex, splash-free surface flows and the differential motion of multiple solid-casting processes owing to its mesh-free nature. SPH can handle boundaries using its nodes; therefore, it may be used to apply fragment-free surface flow and the motion of solid particles (Cleary et al., 2004).

Mathematically, SPH is independent of meshes. The objective of mesh-free methods is to remove at least a portion of the mesh dependence by creating the approximation completely in terms of nodes known as particles in the context of mesh-free techniques. The varieties of problems with the potential to be solved by mesh-free methods are much more numerous than by mesh-based methods. Furthermore, since the approximation is not based on elements whose distortion may degrade accuracy mesh-free methods can handle large deformations much better. It is thus helpful in both fluid and solid calculations (Belytschko et al., 2004).

Despite the method's growing appeal, SPH has a number of key issues that must be overcome before its full potential can be realized in scientific and engineering applications. Among the issues to address are that SPH is of low order, requires a high degree of tuning, and is inherently unstable. Additionally, there exists slight analytic basis or fundamental understanding of the method to guide the many ad-hoc tuning and empirical fixes (Kiara, 2010)

6.3.2 Conventional SPH Formulation

In the SPH method, a window function acts as a kernel function, (smoothing kernel) for solving the original equations. Upon solving the kernel, the result appears for the major function. SPH is based on integral interpolation (Gingold & Monaghan, 1977; Lucy, 1977).

In the SPH method, the approximate value *f(x)* of a function *f* at a point *x* is given by:

$$\tilde{f}(x) = \int_{\Omega} f(\xi)\ W(x-\xi,h)\,\mathrm{d}\xi \qquad \text{Eq. 6.6}$$

where $W(x-\xi)$ is the smoothing function (kernel). The approximate value of $\tilde{f}$ of f depends on two parameters, kernel *W* and dilation *h,* which determine the support of *W*. The kernel function, W, is required to satisfy the following attributes:

i. $W(x-\xi,h) = 0$ for $|x-\xi| \geq 2h$,

ii. $\int_{\Omega} W(x-\xi,h)\,\mathrm{d}\xi = 1$,

iii. $\lim_{h\to 0} w(x-\xi,h) = \delta(x-\xi)$ where δ is the Dirac delta function,

iv. $W(x-\xi,h) \geq 0$,

v. $W(x-\xi,h) = W(\xi-x,h)$.

The spatial derivative, ∇f, at point x is approximated by

$$\nabla\tilde{f}(x) = \int_{\Omega} \nabla f(\xi)\ W(x-\xi,h)\,\mathrm{d}\xi = -\int_{\Omega} f(\xi)\ \nabla W(x-\xi,h)\,\mathrm{d}\xi \qquad \text{Eq. 6.7}$$

Where it is integrated by parts and used property (i) of the kernel function *W*.

For the mathematical work, the integral (formula 2.3) is approximated by imagining that the mass in Ω is divided into *N* particles of masses $m_1, m_2, \ldots, m_N$ and densities $\rho_1, \rho_{2,\ldots,} \rho_N$ respectively. The value of *f* I of the integral (Eq. 6.8) for the *i*th particle is approximated by:

$$f_i = \sum_{j=1}^{N} m_j f_j W_{ij} \quad W_{ij} = W\left(x^{(i)} - \xi^{(j)}\right) \qquad \text{Eq. 6.8}$$

Approximations may be done discretely by a summation interpolant.

$$\tilde{f}(x) \approx \sum_{j=1}^{N} f(x_j)\, W(x - x_j, h) \frac{m_j}{\rho_j} \qquad \text{Eq. 6.9}$$

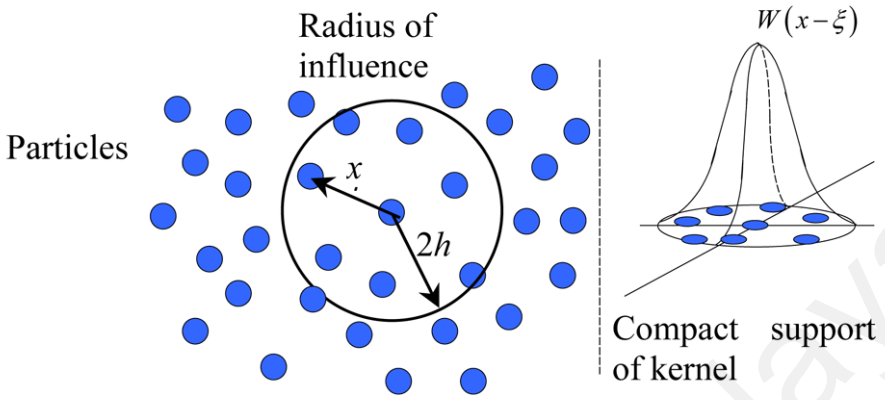

Figure 6.6: Particles and SPH

In mathematics, the Dirac delta function, or δ function, is a generalized function on the real number line that is zero everywhere except at zero, with an integral of one over the entire real line. The delta function is sometimes assumed as an infinitely high and thin spike at the origin with a total area of 1 under the spike and that physically represents an idealized point mass or the point charge (Hassani, 2009).

6.3.3 Modified smoothed particle hydrodynamics (MSPH)

Conventional smoothed particle hydrodynamics require certain modifications to improve the accuracy of approximation, especially at points near the boundary of the domain (Batra & Zhang, 2008; Zhang & Batra, 2004).

Cylindrical coordinates (R, θ, Z) were used to analyze axisymmetric deformations of a circular cylindrical body, and a function, f, describing a deformation variable is independent of the angular position, h, of a material point. When suitable, it was denoted as (R, Z) by x with x_1 = R and x_2 = Z. The Taylor series expansion of a function f(R, Z) about point (R_i, Z_i) is:

$$f(R,Z) = f(R_i,Z_i) + \frac{\partial f}{\partial R}(R-R_i) + \frac{\partial f}{\partial Z}(Z-Z_i) + \frac{1}{2}\frac{\partial^2 f}{\partial R^2}(R-R_i)^2 + \frac{1}{2}\frac{\partial^2 f}{\partial Z^2}(Z-Z_i)^2 + \frac{\partial^2 f}{\partial R \partial Z}(R-R_i)(Z-Z_i) + \ldots \quad \text{Eq. 6.10}$$

where derivatives are assessed at point (R_i, Z_i). Neglecting the third and higher order derivative terms on the right-hand side of Eq. (6-11), multiplying both sides of the equation with a positive-valued kernel function W(x-ξ,h) of compact circular support with radius 2h and center at point x, its first derivatives $W_R = \partial W/\partial R$ and $Wz = \partial W/\partial Z$, its second derivatives $WRR = \partial 2W/\partial R2$, $WZZ = \partial 2W/\partial Z2$ and $WRZ = \partial 2W/\partial R\partial Z$, and integrating the resulting equations over the domain, Ω, gives:

$$\begin{aligned}
\int_\Omega f(\xi)W d\xi &= f_i\int_\Omega W d\xi + f_{\alpha i}\int_\Omega \left(\xi_\alpha - x_\alpha^{(i)}\right)W d\xi + f_{\alpha\beta i}\int_\Omega \left(\xi_\alpha - x_\alpha^{(i)}\right)\left(\xi_\beta - x_\beta^{(i)}\right)W d\xi \\
\int_\Omega f(\xi)W_R d\xi &= f_i\int_\Omega W_R d\xi + f_{\alpha i}\int_\Omega \left(\xi_\alpha - x_\alpha^{(i)}\right)W_R d\xi + f_{\alpha\beta i}\int_\Omega \left(\xi_\alpha - x_\alpha^{(i)}\right)\left(\xi_\beta - x_\beta^{(i)}\right)W_R d\xi \\
\int_\Omega f(\xi)W_Z d\xi &= f_i\int_\Omega W_Z d\xi + f_{\alpha i}\int_\Omega \left(\xi_\alpha - x_\alpha^{(i)}\right)W_Z d\xi + f_{\alpha\beta i}\int_\Omega \left(\xi_\alpha - x_\alpha^{(i)}\right)\left(\xi_\beta - x_\beta^{(i)}\right)W_Z d\xi \quad \text{Eq. 6.11} \\
\int_\Omega f(\xi)W_{RR} d\xi &= f_i\int_\Omega W_{RR} d\xi + f_{\alpha i}\int_\Omega \left(\xi_\alpha - x_\alpha^{(i)}\right)W_{RR} d\xi + f_{\alpha\beta i}\int_\Omega \left(\xi_\alpha - x_\alpha^{(i)}\right)\left(\xi_\beta - x_\beta^{(i)}\right)W_{RR} d\xi \\
\int_\Omega f(\xi)W_{ZZ} d\xi &= f_i\int_\Omega W_{ZZ} d\xi + f_{\alpha i}\int_\Omega \left(\xi_\alpha - x_\alpha^{(i)}\right)W_{ZZ} d\xi + f_{\alpha\beta i}\int_\Omega \left(\xi_\alpha - x_\alpha^{(i)}\right)\left(\xi_\beta - x_\beta^{(i)}\right)W_{ZZ} d\xi
\end{aligned}$$

where $fi = f(x^{(i)})$, $f_{\alpha i} = \partial f/\partial x_\alpha^{(i)}$, and $f_{\alpha\beta i} = \partial^2 f/\partial x_\alpha^{(i)}\partial x_\beta^{(i)}$, α, β = 1,2 and $x_1 = R$, $x_2 = Z$. Because the kernel function W is 0 when the distance | x - ξ | is greater than 2h (h is the smoothing length), the integration domain Ω can be substituted with the compact support of the kernel function. Eq. 6.11 can be inscribed in matrix form as:

$$BF = T \text{ or } B_{IJ}\, F_J = T_I,\ I = 1,\ 2,\ \ldots,\ 6 \quad \text{Eq. 6.12}$$

where,

$$B_{IJ} = \int_\Omega \Phi(I)\Theta(J)d\xi = \sum_{j=1}^{N} \Phi(I)\Theta(J)\, m_j / \rho_j \quad \text{Eq. 6.13}$$

$$\Phi(1) = W_{ij},\ \Phi(2) = W_{ij,1},\ \Phi(3) = W_{ij,2}\ ,$$
$$\Phi(4) = W_{ij,11},\ \Phi(5) = W_{ij,22},\ \Phi(6) = W_{ij,12}\ ,$$
$$\Theta(1)=1,\ \Theta(2)=R_j-R_i,\ \Theta(3)=Z_j-Z_i\ , \qquad \text{Eq. 6.14}$$
$$\Theta(4)=\frac{1}{2}\left(R_j-R_i\right)^2,\ \Theta(5)=\frac{1}{2}\left(Z_j-Z_i\right)^2,\ \Theta(6)=\left(R_j-R_i\right)\left(Z_j-Z_i\right)\ ,$$

$$F = \left\{f_i, f_{1i}, f_{2i}, f_{11i}, f_{22i}, f_{12i}\right\}^T,$$

$$T_I = \int_{\Omega} f(\xi)\Phi(I)d\xi = \sum_{j=1}^{N} f_j \Phi(I)\frac{m_j}{\rho_j},$$

$$W_{IJ} = W\left(x^{(i)} - \xi^{(j)}, h\right),$$

$$W_{ij,\alpha} = \left.\frac{\partial W}{\partial x_\alpha}\right|_{x=x^{(i)},\xi=\xi^{(j)}},\ W_{ij,\alpha\beta} = \left.\frac{\partial W}{\partial x_\alpha \partial x_\beta}\right|_{x=x^{(i)},\xi=\xi^{(j)}} \qquad \text{Eq. 6.15}$$

Here, N equals the number of particles located in the compact support of the kernel function W(x - ξ,h). These equations are similar to those in plane strain problems except that the mass, m_j, now equals the mass of a circular ring rather than that of a cylinder of unit length.

If N = at least 6 and particles are randomly scattered in the compact support of the kernel function, then the determinant of matrix B is not zero and Eq. 6.12 can be rewritten as:

$$F_j = B_{IJ}^{-1} T_1, \qquad \text{Eq. 6.16}$$

where $^{-1}$ denotes the inverse of a matrix. Eq. 6.16 gives values of function *f* and of its first- and second-order derivatives at point x in terms of *f* values at points in the neighborhood of x; the number N of these points is determined by the radius, 2h, of the compact support of the kernel function W. Eq. 6.16 can be simply written as:

$$f(x) = B_{I1}T_1 = \sum_{J=1}^{N} B_{I1}\Phi(I)\frac{m_J}{\rho_J} f_J,$$
$$\frac{\partial f(x)}{\partial x_1} = B_{I2}T_1 = \sum_{J=1}^{N} B_{I2}\Phi(I)\frac{m_J}{\rho_J} f_J, \qquad \text{Eq. 6.17}$$
$$\frac{\partial^2 f(x)}{\partial x_1^2} = B_{I4}T_1 = \sum_{J=1}^{N} B_{I4}\Phi(I)\frac{m_J}{\rho_J} f_J,$$

In FEM terminology, functions $B_{I1}\Phi(I)m_J/\rho_J$ qJ, I = 1; 2; . . . ; 6 can be viewed as shape functions for function f. Correspondingly, functions $B_{I4}\Phi(I)m_J/\rho_J$ qJ, I = 1; 2; . . . ; 6 can be considered shape functions for $\partial f(x)/\partial x_1$ and $\partial^2 f(x)/\partial x^2_1$, respectively. Thus, shape functions for f(x), its first and second derivatives at point x are different. Recall that in FEM:

$$\frac{\partial^{\alpha+\beta+\gamma}}{\partial x_1^{\alpha}\partial x_3^{\beta}\partial x_3^{\gamma}} f(x) = \sum_{J=1}^{N} \frac{\partial^{\alpha+\beta+\gamma}}{\partial x_1^{\alpha}\partial x_3^{\beta}\partial x_3^{\gamma}} N_J f_J \qquad \text{Eq. 6.18}$$

For $\alpha = \beta = \Upsilon = 0$, Eq. 6.18 gives the function's approximate value in FEM, which is identical in form as in the MSPH method. Of course, the shape functions for MSPH and FEM are different. Furthermore, the estimated values of the first and second function derivatives at point x in the MSPH technique are dissimilar from those in FEM. In order to calculate the estimated derivative values of the function in the MSPH method, differentiating the basic functions is not required. Instead, another set of basic functions is used. For values of constants in Eq. 6.17 to identify approximate values of function f(x), its first and second derivatives at point x are determined concurrently.

6.3.4 MSPH implementation in the centrifugal thermite method

Smoothed particle hydrodynamics (SPH) is a particle-based method of modeling fluid and solid deformation. It is used for flow analyses of a fluid mixture, solid phase, and functionally graded materials (FGMs) (Takamiya et al., 2011). It has been successfully employed to model particle velocity and first derivative (particle velocity gradient), and

second or third derivative in one, two, and three dimensions. This method is implemented to solve iron and alumina infiltration into TiC in a centrifugal-assisted SHS method. Figure 6.7 displays a schematic drawing of a TiC pellet just before the molten alumina and iron come into contact. The particles are distinct in the Figure 6.7.

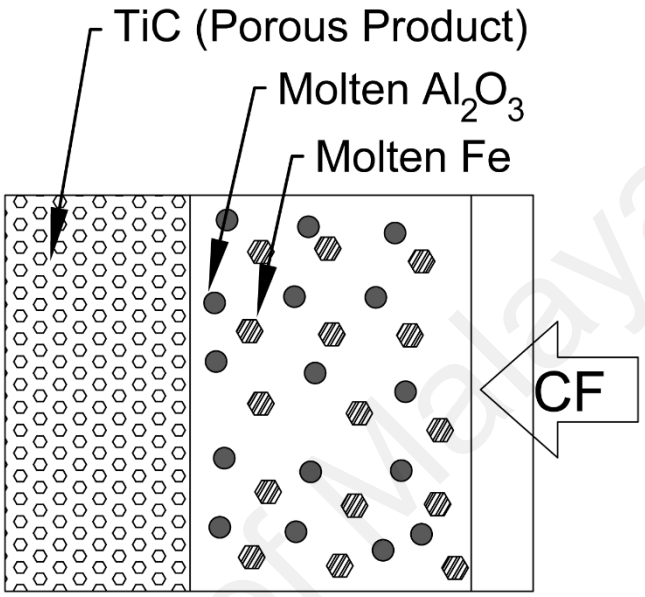

Figure 6.7: A schematic drawing of a TiC pellet just before the molten alumina and iron come into contact

6.3.4.1 Governing equations:

$$V(T_c,t)=\frac{d^2\left(\rho_o-\rho_m\right)\left(39.4Rn^2+g\right)}{18\eta} \qquad \text{Eq. 6.19}$$

$$\eta(T_c)=\eta_o exp\left(\frac{Q}{R_g.T_c}\right) \qquad \text{Eq. 6.20}$$

Approximated MSPH forms of Eq. 6-17, 6-18.

$$V(r)=B_{I1}T_1=\sum_{J=1}^{N}B_{I1}W_{IJ}\frac{m_J}{\rho_J}V_J,$$
$$\frac{\partial V(r)}{\partial r}=B_{I2}T_1=\sum_{J=1}^{N}B_{I2}W_{IJ}\frac{m_J}{\rho_J}V_J, \qquad \text{Eq. 6.21}$$

$$T_I = \int_{\Omega} f(\xi)\Phi(I)d\xi = \sum_{j=1}^{N} f_j W_{IJ} \frac{m_j}{\rho_j}, \qquad \text{Eq. 6.22}$$

It is evidently seen that for the MSPH method, kernel approximations of the second derivatives, first derivative and the function are consistent of orders (n - 2), (n - 1) and n, respectively, if up to n order terms are reserved in the Taylor series expansion, Eq. 6.10. The following revised Gauss function W(x-ξ, h) as the kernel function is used:

$$W(x-\xi,h) = \begin{cases} \dfrac{1.10081}{(h\sqrt{\pi})^2}\left(e^{-\left|x-\xi\right|^2/h^2} - e^{-4}\right) & ; \quad \left|x-\xi\right| \le 2h, \\ 0 & ; \quad \left|x-\xi\right| > 2h, \end{cases} \qquad \text{Eq. 6.23}$$

and note that the integral of W(x-ξ, h) over its compact support equals one. Interaction radius: (h), (Figure 6.6) is selected such that 15-20 particles are interacting on average (Zhang & Batra, 2004).

6.3.5 Coding and simulations procedure

MATLAB, Mathworks ® version 2012a was employed to model the MSPH and compare the result with the exact solution. The fluids (iron and alumina) viscosity, particle speed in radial direction, gradient of speed, and particles position are simulated and presented in this section. In order to verify MSPH code, the exact solution of velocity Eq. 6.3 and its MSPH code are plotted accordingly.

Interaction radius: (h) is chosen such that 15-20 particles are interacting on average (Zhang & Batra, 2004), where the number of particle is 29. The MSPH simulation parameters of two materials are given Table 6.2.

Table 6.2: MSPH parameter of iron and alumina particles

Material	Particle Size code	Interaction radius: h (m)	Rotation speed n (rps)	Melt density R_m (Kg/m^3)	Initial density R_o (Kg/m^3)	Particle size dp (m)
Iron	dp	2.5×10^{-3}	58	2700	7800	1.0×10^{-4}
Iron	dp2	3.5×10^{-3}	58	2700	7800	1.2×10^{-4}
Iron	dp3	1.5×10^{-3}	58	2700	7800	0.7×10^{-4}
Alumina	dp	2.5×10^{-3}	58	2750	3950	1.0×10^{-4}
Alumina	dp2	3.5×10^{-3}	58	2750	3950	1.2×10^{-4}
Alumina	dp3	1.5×10^{-3}	58	2750	3950	0.7×10^{-4}

The relative parameters of the MSPH simulation of iron and alumina particles are extracted from the existing literature. Where molten iron $\eta_o = 0.0065$ $kg.m^{-1}.s^{-1}$ (Ho & Hwang, 1996), total activation energy, $Q = 706$ $kJ.mol^{-1}$ of Al-Fe_2O_3 and Ti-C (Fan et al., 2006; Munoz et al., 1997), the gas constant is $R_g = 8.31441$ $J.K^{-1}.mol^{-1}$ (Balout & Litwin). $R_m = 2750$ Kg/m^3 for molten alumina density (Glorieux et al., 1999); $R_o = 3950$ Kg/m^3 (Rahimian et al., 2010), $\eta_o = 0.052$ $N.s/m^2$ is the liquid viscosity of alumina at 2408 K (Quang, 2008). The other thermophysical properties are listed in Table 6.1.

The time-viscosity plot of a centrifugal thermite reaction is illustrated in Figure 6.8. The temperature data are extracted from the pyrometer reading data where the reaction cooling temperature is plotted versus time. The temperature data are embedded in the Figure 6.8. The time-viscosity plot is the exact calculations using Arrhenius adopted equation (Eq. 6.5). The viscosity is used to calculate the particle velocity and location at any given time. The particle velocity, position of alumina and iron were calculated using Eq. 6.3, and Eq. 6.4, respectively.

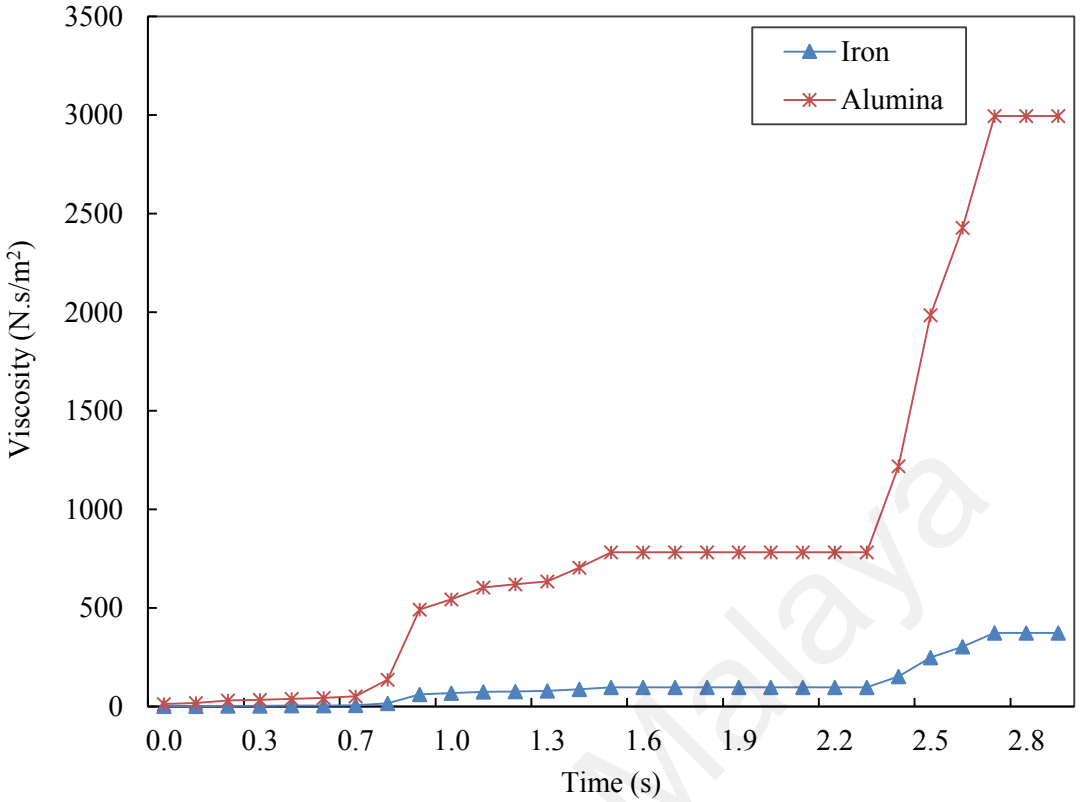

Figure 6.8: Viscosity rate plot of iron and alumina (Eq. 6.5)

The exact solution of a particle velocity and the corresponding SPH simulation is plotted in Figure 6.9. The simulation parameters are listed in Table 6.2. The MSPH simulation is solved using Taylor's series expansion in MATLAB.

The particle velocity SPH simulation is closely correlated with the exact solution one. This empowers the idea that allows running the first derivative of Taylor's expansion series where the SPH particle velocity can be simulated. The first derivative of the speed equation as a function of particle velocity gradient estimated using SPH kernel is depicted in Figure 6.10.

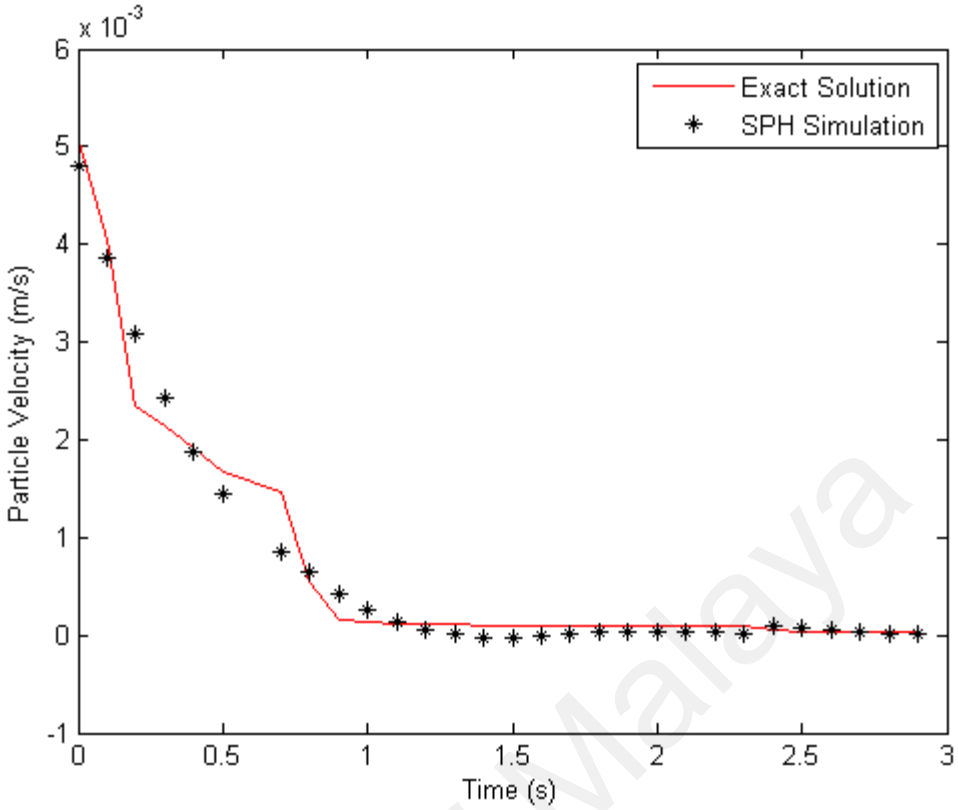

Figure 6.9: Comparison of the particle velocity of exact solution (the red line) and prediction of MSPH method (star) using 29 particles (particle size 1.0 e -4 m)

At the beginning, it was speeding up and then at round time 0.5 up to 1.5 s decelerates. It was almost around the ramp. After that, the gradient is constant near zero that means the velocity is getting zero. At the time over three seconds, the particle movement has already ended. The current change of particle radial position is calculated using Eq. 6.4 and the calculated results are shown in Figure 6.11 for the given parameter in Table 6.2.

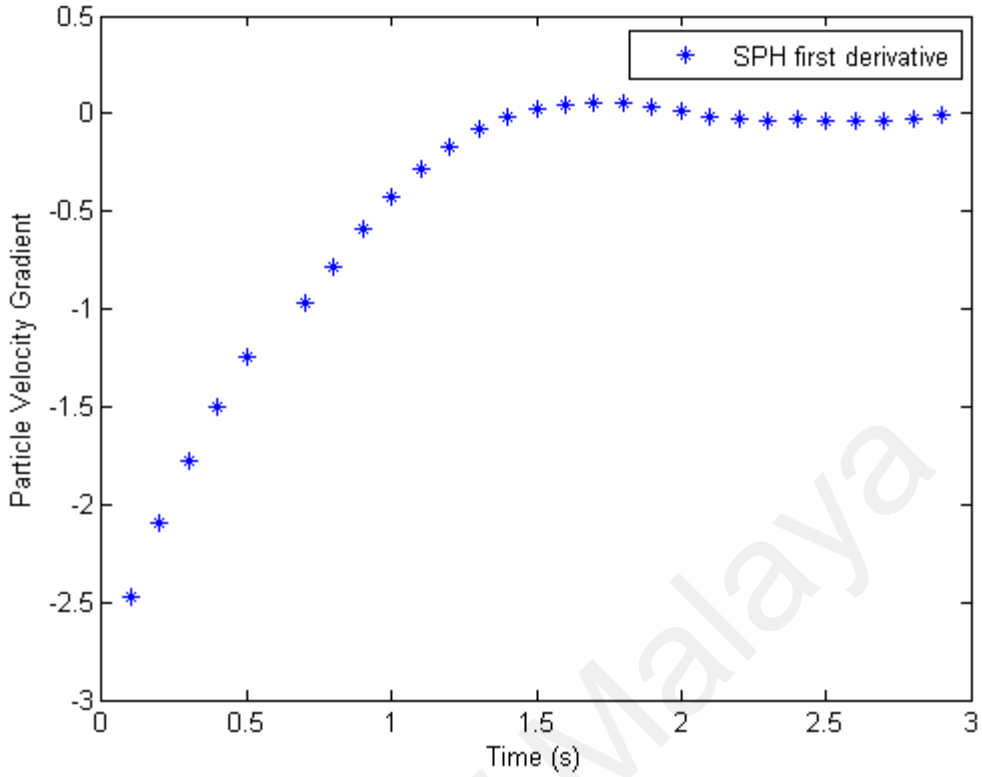

Figure 6.10: MSPH estimates the particle velocity gradient (PVG) in the radial direction

The result of Figure 6.10 and Figure 6.11 are closely in correlations. Whereas, the changes of particle position trend is showing how it tends to zero when the first derivative of speed, PVG, approaches zero and then continues close to zero. At this stage, there might not be molten phase diffusion but still solid-state diffusion phenomenon is probably happening (Fan et al., 1999; Feng et al., 2012).

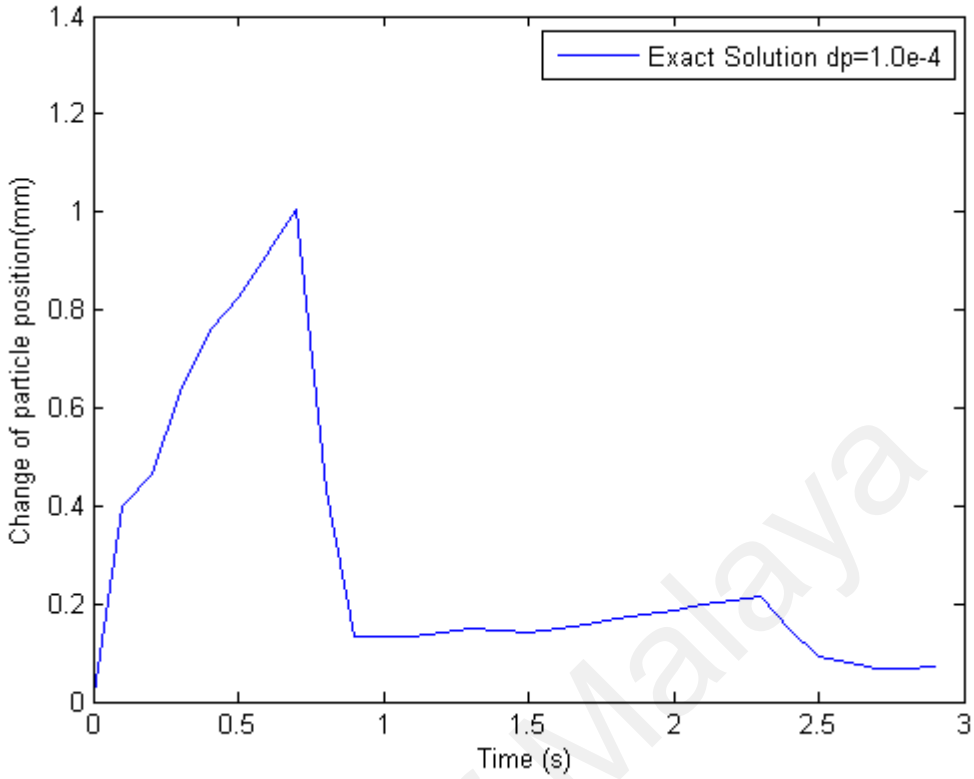

Figure 6.11: Instantaneous change in radial particle position versus time during the deposition process

The solid-state diffusion is widely accepted with respect to combustion synthesis processing. Where the material has less motion in the liquid phase and due to the in-situ high temperature gradient, the particles diffuse with each other and form an alloy or cermet. If this phenomenon combines with centrifugal force, there would be extra external force acting beyond the viscosity increment, which would resist against the particle motion. Finally, there would more of the obtained product than expected.

The simulation parameters of three SPH particles are listed in Table 6.2. The Matlab code run for the three particles and the corresponding results of particle position changes, particle velocity and particle velocity gradient (PVG), are shown in Figure 6.12, Figure 6.13 and Figure 6.15, respectively.

Particle position modifies as viscosity decreases, and it would have no relative motion or displacement as a molten particle after 0.7 s. However, the particle can undergo solid

diffusion. Consequently, the particle diffusion speed would tend toward zero. Although the formula has an exponential factor, it will become zero in infinity.

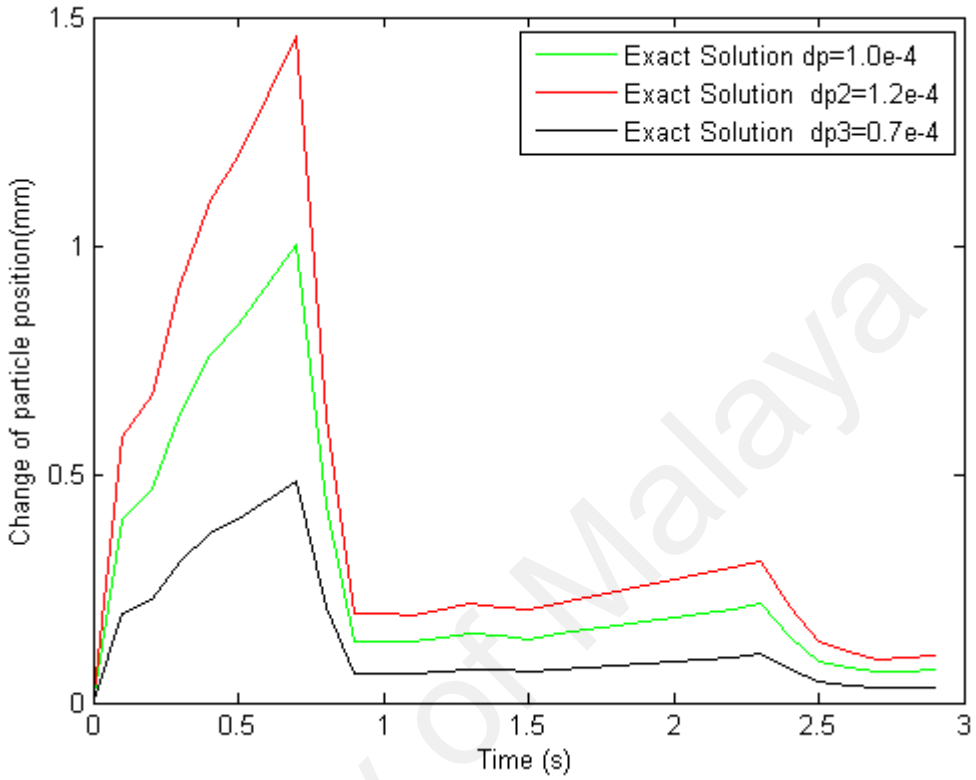

Figure 6.12: Current change in radial particle position versus time during the deposition process for three particle sizes

Figure 6.13 shows continuous deceleration of the MSPH iron particle since it was in a molten state followed by the thermite reaction. The increasing viscosity (Figure 6.8) would naturally affect the particle movement. The gradient of velocity (Figure 6.15) and movements (Figure 6.12) in a radial direction are in direct relation to particle size. If the particle size increases, the velocity slope is greater and the particles will decelerate faster. However, all types of particle speed gradient will tend toward zero almost simultaneously.

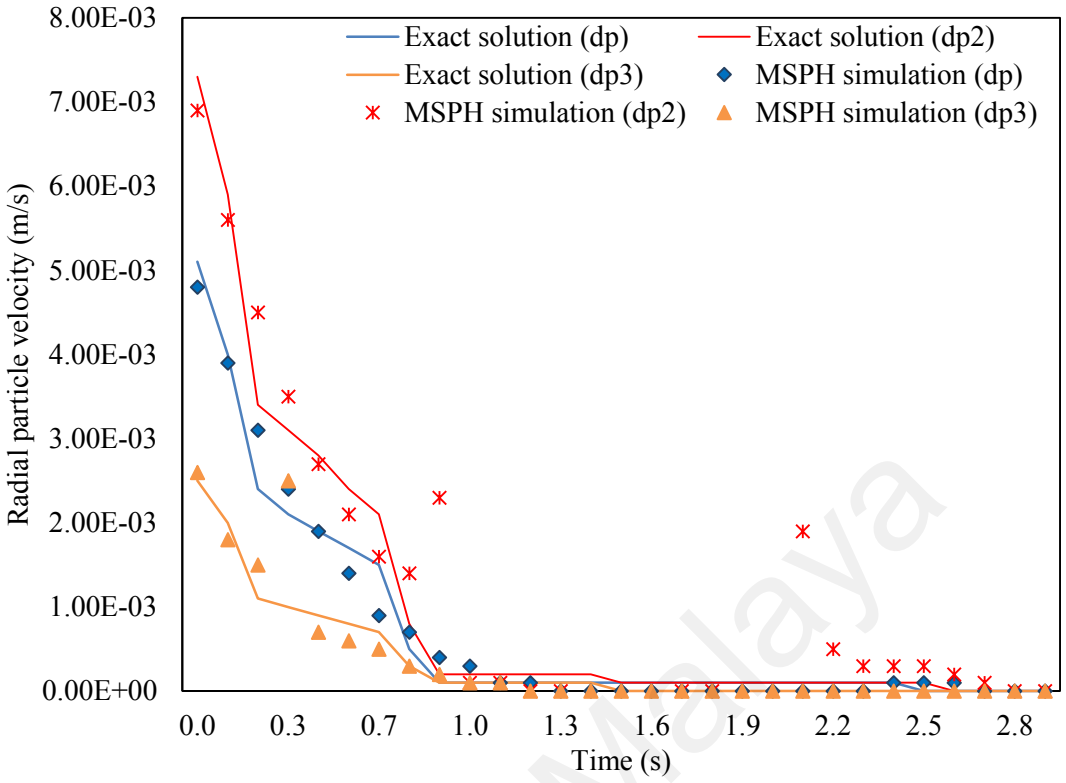

Figure 6.13: Radial iron particle velocity versus time obtained from the analytical model and MSPH predictions for different particle sizes

In terms of physical behavior, SPH particle migration rate (velocity) would tend toward zero if the viscosity increases or the particle reaches a boundary that halts further movement. Under the centrifugal field where particles are larger, the initial speed is higher than for smaller particles. However, the particle velocity gradient (Figure 6.15) can describe it as endures deceleration with different gradients based on particle and domain size. Molten alumina particle radial velocity (three particle sizes) and the corresponding MSPH simulation are shown in Figure 6.14. The particle velocity of alumina seems to be approximately half that of iron particles for the corresponding particle sizes.

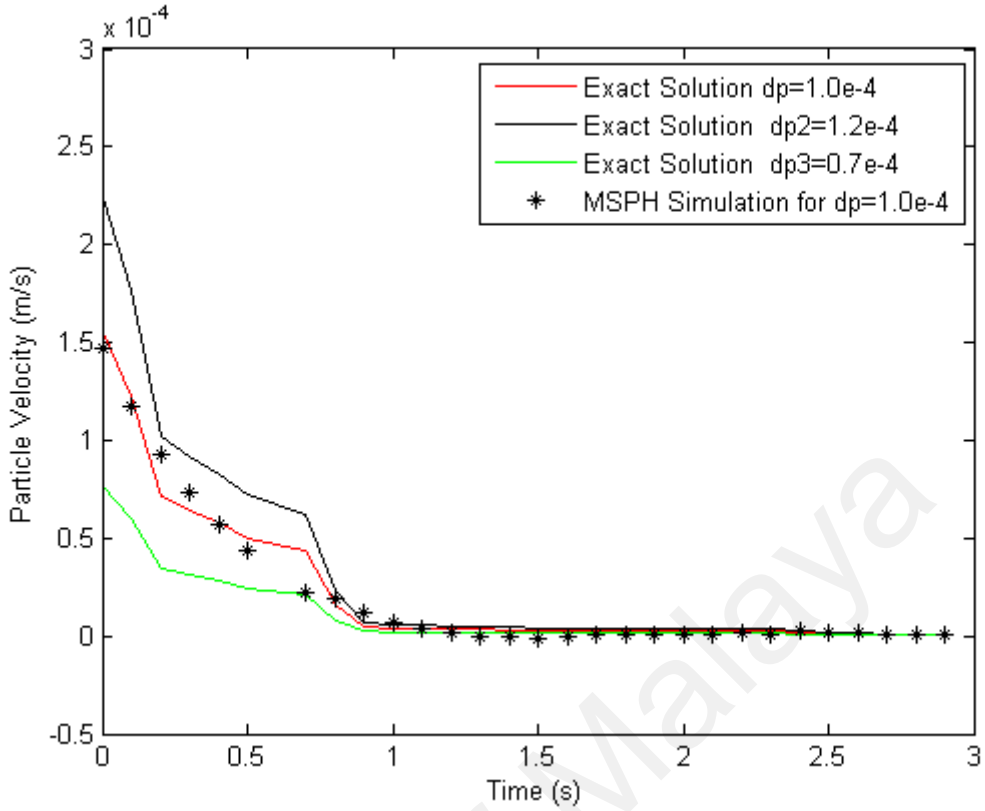

Figure 6.14: Alumina particle radial velocity (three particle sizes) and the corresponding MSPH simulation

The instantaneous position change of six different particles of alumina and iron is depicted in Figure 6.16. It is evident that the alumina particles are not moving toward the TiC pellet, but the iron particles are (Figure 6.16). The alumina particles would mostly be deposited at the boundary of the TiC pellet (Figure 6.7), also called the top surface, where the relative viscosity increases rapidly (Figure 6.8). Viscosity is defined as the resistance to flow in a fluid. The viscosity of alumina increases in a fraction of a second while the viscosity of iron does not do so as much (Figure 6.8). Therefore, iron will continue to penetrate or diffuse into the TiC porous media and alumina flow stops. Figure 6.16 shows that the alumina particles are expected to diffuse into TiC between 15 to 45 μm, depending on particle size.

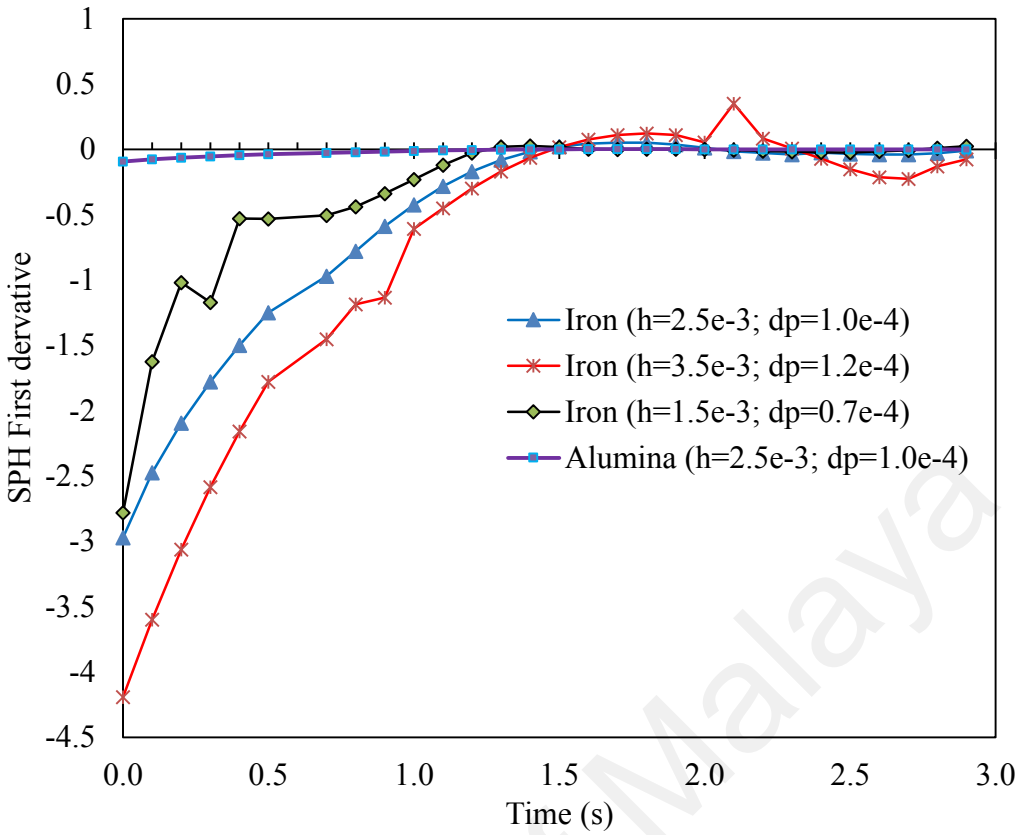

Figure 6.15: MSPH estimates the particle velocity gradient (PVG) in a radial direction for three different particle sizes of alumina and iron

The speed gradient simulation for four MSPH particles is presented in Figure 6.15. The speed gradient plot is in agreement with that for particle position change (Figure 6.16). The figure illustrates the relative speed gradient where the alumina SPH particle has the least value and is close to zero. The iron particles of different sizes demonstrate greater change in speed compared with the alumina particles. Moreover, it seems that the alumina particles are at the boundary of the TiC pellet and iron particles have infiltrated the TiC porous medium. Figure 6.1, Figure 6.16, and Figure 6.15 provide complementary analysis. The current findings are in good accord with the centrifugal thermite and TiC infiltration mechanism (Figure 6.1).

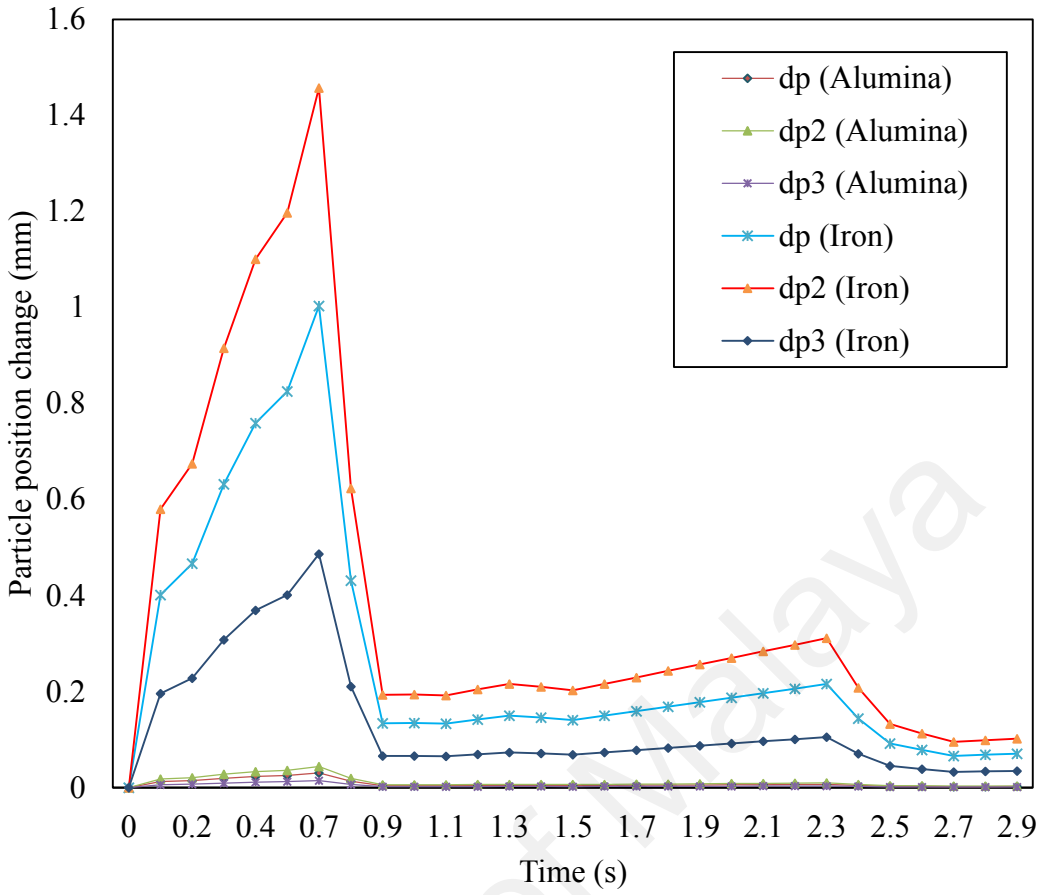

Figure 6.16: Instantaneous change in radial direction versus time of alumina and iron particles during the deposition process (Eq. 6.4)

This section represents the reason alumina was stocked at the innermost layer relative to the rotation axis compared to the iron particles. Alumina viscosity increased faster than iron and shielded it. In addition, iron remained in a molten medium for a longer period than alumina. This phenomenon allowed the iron particles to wet and infiltrate the TiC porous media and form a strong composite. The corresponding discussion follows in Section 7.4.

CHAPTER 7:RESULTS AND DISCUSSION

7.1 Introduction

The present chapter contains analysis and discussion on the conducted experiments. Ten experiments and specimens are investigated using available characterization and analysis techniques.

7.2 Alumina-Fe ceramic-lined pipe production using method (1)

The phase formation and separation aspects of the centrifugal thermite reaction between Fe_2O_3 and Al powders were studied at three locations from the pipe head. Figure 7.1 describes an ideal reaction product. The pipe head is divided into three regions on an XY plane. Region (A) is from the pipe head up to 10 mm (0-10 mm); region (B) is 10-20 mm and region (C) is theoretically from 20 mm up to the other end of the pipe, all in the X direction. Regions (A), (B), and (C) are presented in the respective figures.

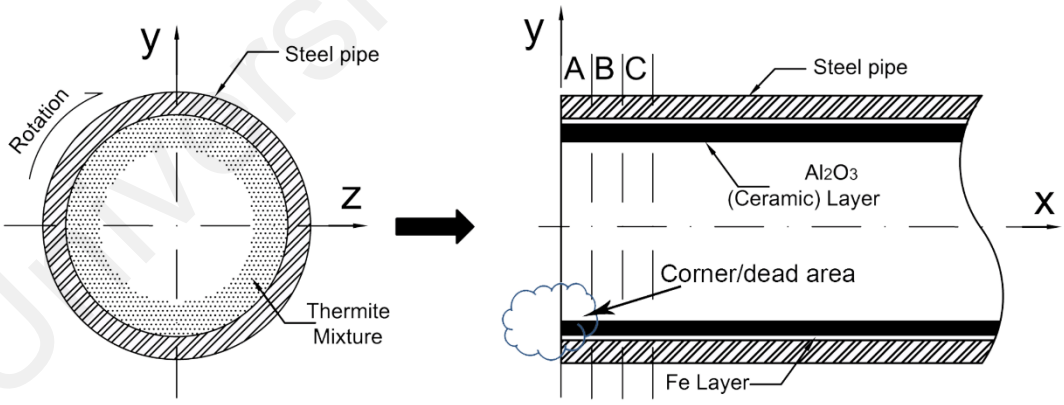

Figure 7.1: General scheme of the ceramic-lined steel pipe before and after reaction

The ceramic-coated pipe was sectioned using a wire cut electrical discharge (WC-EDM) machine according to Figure 7.1. Then it was cut into smaller pieces to be processed for grinding and characterization. A typical multilayer cross-section of the product is seen in Figure 7.2, Region (A). Figure 7.2 comprises microstructure images

taken by field emission scanning electron microscopy (FESEM). Three main layers of various compositions formed on the inner surface of the steel pipe according to the YZ plane in Figure 7.1. The thickness of each layer is demonstrated in Table 7.1. The SEM-EDX results signify separated layers of various compositions in the cross section.

The results of EDX elemental analysis for the main layers (layers 1, 2 and 4) and sub-layers of layer 3 are provided in Table 7.1 for region (A) in accordance with Figure 7.1 and plane YZ. According to EDX analysis results, non-identical elemental compositions were present at different points on the inner surface. At one point in layer 1, Fe was detected with Al_2O_3, meaning that phase separation did not occur completely in some areas of the ceramic layer. Al and O were also detected in layer 2 - the layer next to the main element (Fe).

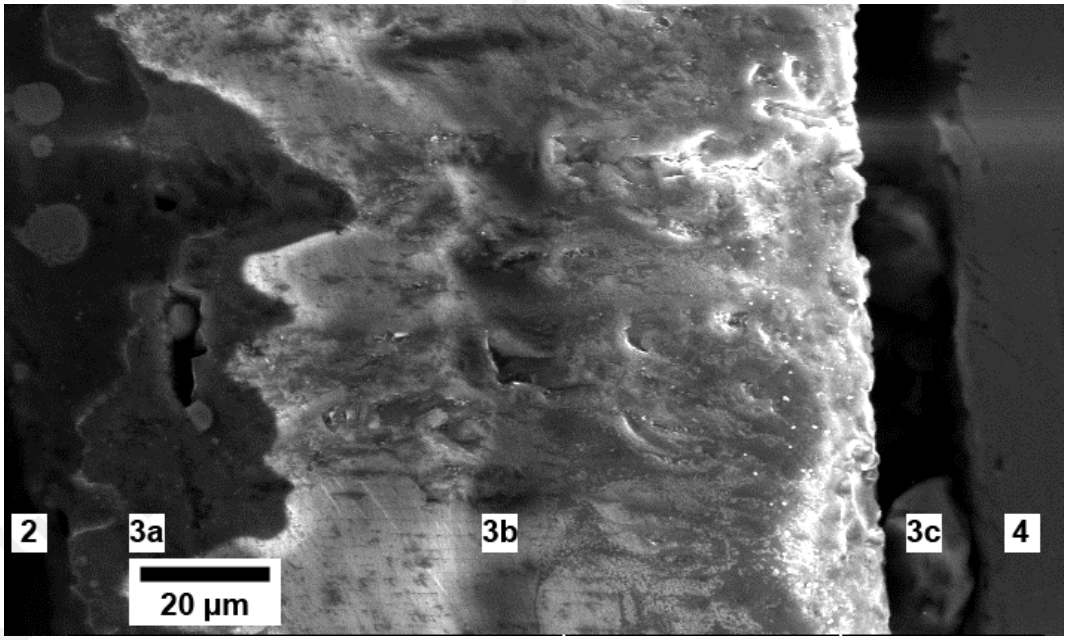

Figure 7.2: The micrograph (SEM) of the layers' cross section view

This behavior repeated in layer 3, while Fe element in various concentrations was detected in all sub-layers: 3a, 3b and 3c. Iron and carbon elements were found in the carbon steel pipe. The elemental composition of the inner surface in the cross-section view and inside view shows that the values are relatively close to each other. The microstructure of the cross-section view of region (A) is shown in Figure 7.2. This SEM

micrograph displays a typical feature of layers 2, 3, and 4. The microstructure graph indicates incomplete phase separation of the products compared with the theory of separation based on centrifugation (Odawara, 1990). This is possibly due to non-uniform results at various points. Powder size and proportion are as important as controlling the centrifugal force in the making of uniform products.

Table 7.1: The EDX results for each area and relative thickness measurement of a cross-section of Region A

Layers	Element Atomic Percentage %				Thickness measurement (μm)
	Al	O	Fe	C	
Cross section					
1	19.10	43.71	37.19	0.00	420.31
2	7.78	6.5	72.73	12.99	970.80
3a	37.32	53.26	8.04	1.37	20.70
3b	37.24	60.21	1.03	1.52	145.59
3c	12.48	59.55	27.94	0.03	40.38
4	0.00	0.00	97.21	2.79	-
Scan of inner surface	21.20	43.70	35.10	-	-

Figure 7.3(a) illustrates the formed metal-rich layer or equivalent position with respect to Figure 7.1, 2 and 3 at Region (A), layer 2 is at a 10 mm distance from the pipe's head in the X direction (0-10 mm from the pipe head). This layer appears to be extremely dense and has very low porosity. Based on the SEM-EDX results, the layer is Fe-rich.

The micrograph in Figure 7.3 (b) indicates rapid solidification of the combustion reaction products. This microstructure belongs to a point near the head-end of the ceramic surface, where the temperature gradient is at a maximum. A typical micrograph of the innermost layer at region (B) that is located 10-20 mm from the pipe head is depicted in Figure 7.4. Clearly, a well-grown structure with various gray and white areas is formed, and prominent boundaries and pores in the grain margins are seen.

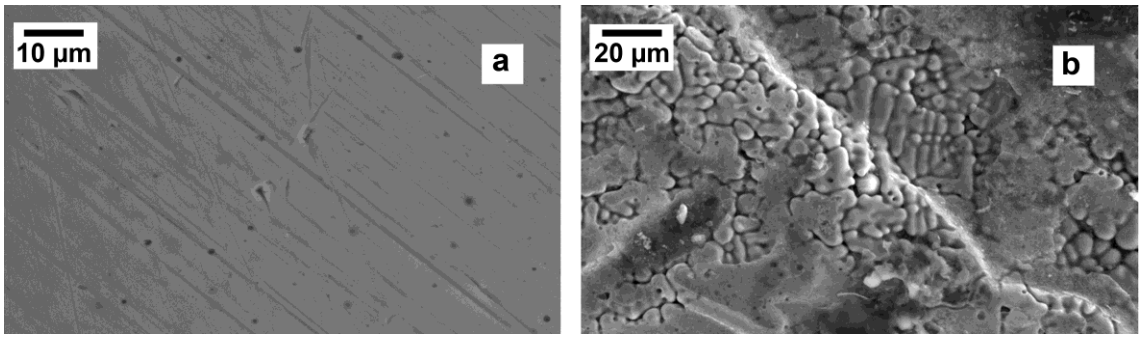

Figure 7.3: SEM micrograph innermost of region A on: (a) layer 2 metal-rich layer; (b) innermost layer of ceramic surface

The average size of the grains is roughly 81µm. The fast cooling rate results in non-well-formed grains with high porosity, followed by a re-melt phenomenon while the dead spaces in the head corner area block the ease of flow and distribution of molten material. The X-ray diffraction (XRD) pattern at this point is shown in Figure 7.5 (Region A).

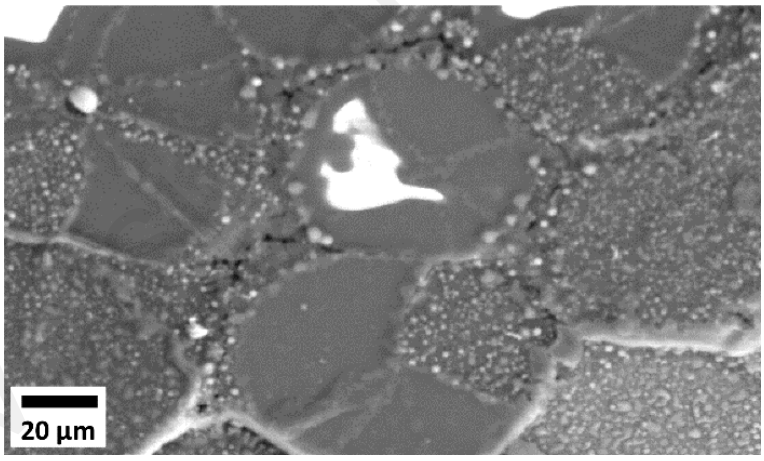

Figure 7.4: Innermost layer of ceramic surface, Region B (10-20 mm from the pipe head)

Figure 7.5 (a) represents the innermost layer of the ceramic surface at Region (C) located 20-30 mm from the pipe head. The grains are well oriented at the ceramic layer's surface. The formed grains are nearly unidirectional relative to the rotating directions. From a microscopic point of view, it can be interpreted that the formed ceramic layer is preferred in region (C), as it represents the whole product. The approximate size of the grains is roughly 19 µm according to FESEM measurements.

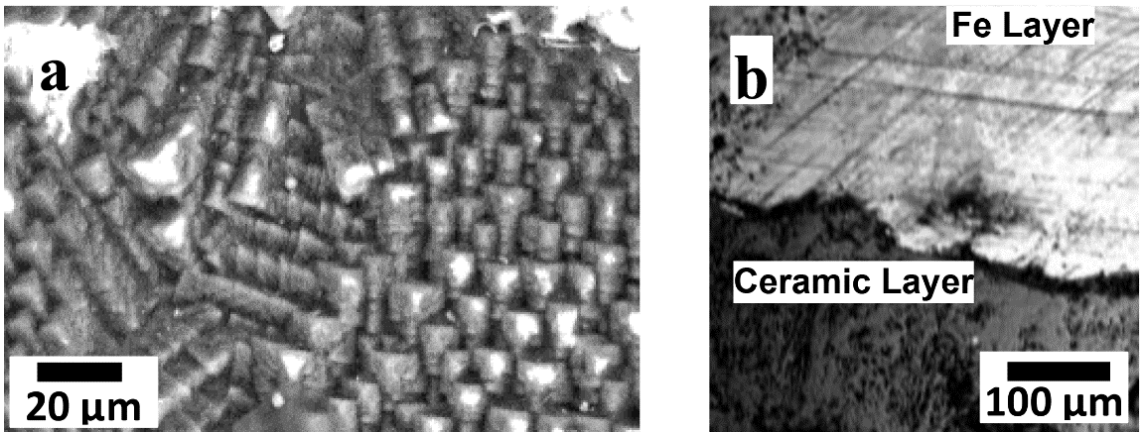

Figure 7.5: SEM micrograph of Region (C) on: a) Inner-most layer of ceramic surface; b) Cross-section of Region (C)

Figure 7.5 (b) reveals the presence of only two deposition layers inside the steel pipe. This was the expected, most preferred product and is an indication of good separation under centrifugal force. Usually, crystal growth initiation occurs from the innermost layer of the steel substrate (base pipe) in a fine columnar structure towards the center of the pipe and produces a strong metallurgical bond between the metal and intermetallic transition layer (Le et al., 2008). However, according to the current work, phase separation happened completely from region (C) in Figure 7.1, as other previous regions were disturbed.

A Mitutoyo SJ 201 profilometer measured the product's smoothness of the innermost surface on the alumina (the coated ceramic). The instrument was calibrated to avoid reading errors. After calibration, the samples were measured for smoothness at three different locations in each region, as per Figure 7.1. The average roughness (R_a) value for Region (A) was about 3.76 µm, for Region B it was 2.12 µm and about 1.72 µm for Region (C). In region (C), the difference between the highest and lowest peak (Ry_{max}) was around 0.27 µm, indicating a lower variation in that region, while the Ry_{max} for Regions (A) and (B) was 1.01 µm and 0.32 µm, respectively. The rapid heating and super-cooling of the material would have caused surface imperfections.

The ring cut prepared by EDM revealed more uniform structure and grain distribution in a strip about 10 mm wide located at 20-30 mm offset from the head-end of the pipe. The end and front zone structure look very different, while at the middle of the pipe a more uniform grain distribution was observed. There are several reasons for these results such as a blind end, very violent thermite reaction, out-gassing and outgoing powders from the pipe during the reaction. The cross section of the pipe's multilayered structure revealed an arrangement of 1.0-1.5 mm thickness that formed inside the pipe.

7.3 A preliminary study of the effect of a hot argon inert crucible on the phase formation in a Ti-C pellet (SM04)

A preliminary experiment was conducted in order to simulate the behavior of a Ti-C pellet while exposed to heat released from the thermite reaction. A Ti-C pellet mixture of the same starting chemical was supposed to be used in the centrifugal thermite-assisted Ti-C method compacted in a round-section stainless steel die. The compacting pressure was 3.5 tons and the steel die dimensions were 12 mm diameter and 5 mm thickness. The infrared pyrometer monitored the temperature and recorded the system's cooling behavior. The cooling rate of the specimen in the reaction chamber is plotted against time in Figure 7.6.

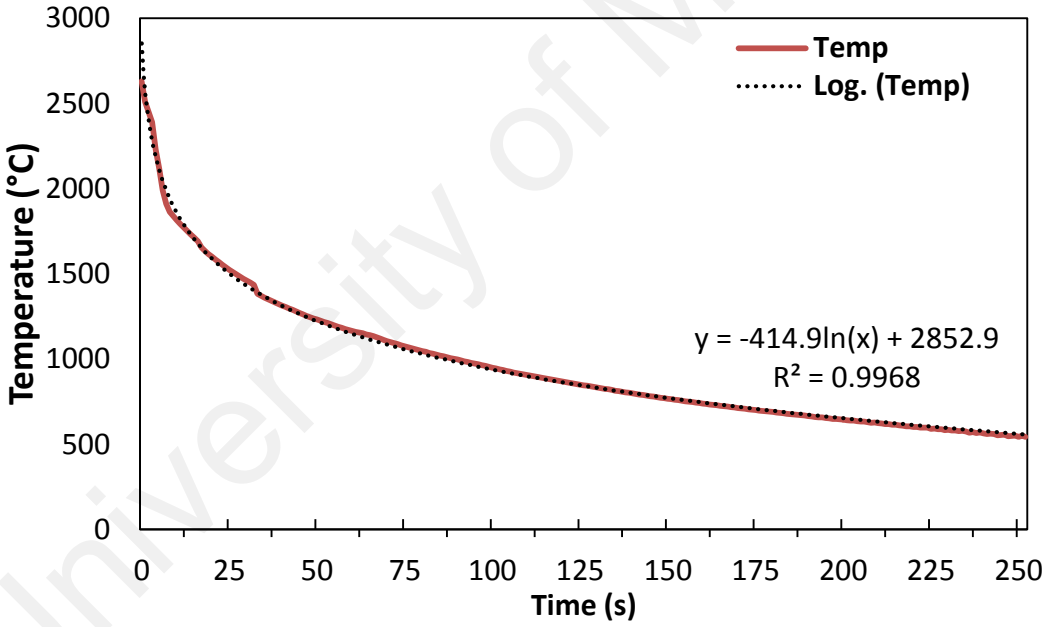

Figure 7.6: Time-temperature cooling profile of a Ti-C pellet in the chamber

The statistical trend line, or data regression, and its corresponding formula are represented by the dotted curve in Figure 7.6. The correlation relation value of R^2 = 0.9968 indicates a robust connection between the variables and the logarithmic formula. This cooling rate provides adequate insight into the surrounding region during exposure to sudden heat, such as a thermite reaction. Following cooling, the sample was removed from the chamber, cut through the cross-section, and ground for further analysis.

The FESEM micrograph of the sample is illustrated in Figure 7.7, and Figure 7.7 (a) presents a low magnification of the product. It is evident that a porous media formed in the compacted pellet. Figure 7.7 (b) and (c) show higher magnifications of the Ti-C pellet's typical point, denoting the presence of different materials and phases. The phases were identified using an X-ray diffraction pattern (XRD).

Some titanium carbide (TiC) formed and there some unreacted graphite powder and titanium were observed. The unreacted powder may be significant in experiments with other active elements that tend to wet them and form a new phase. The phases can be identified using an X-ray diffraction pattern.

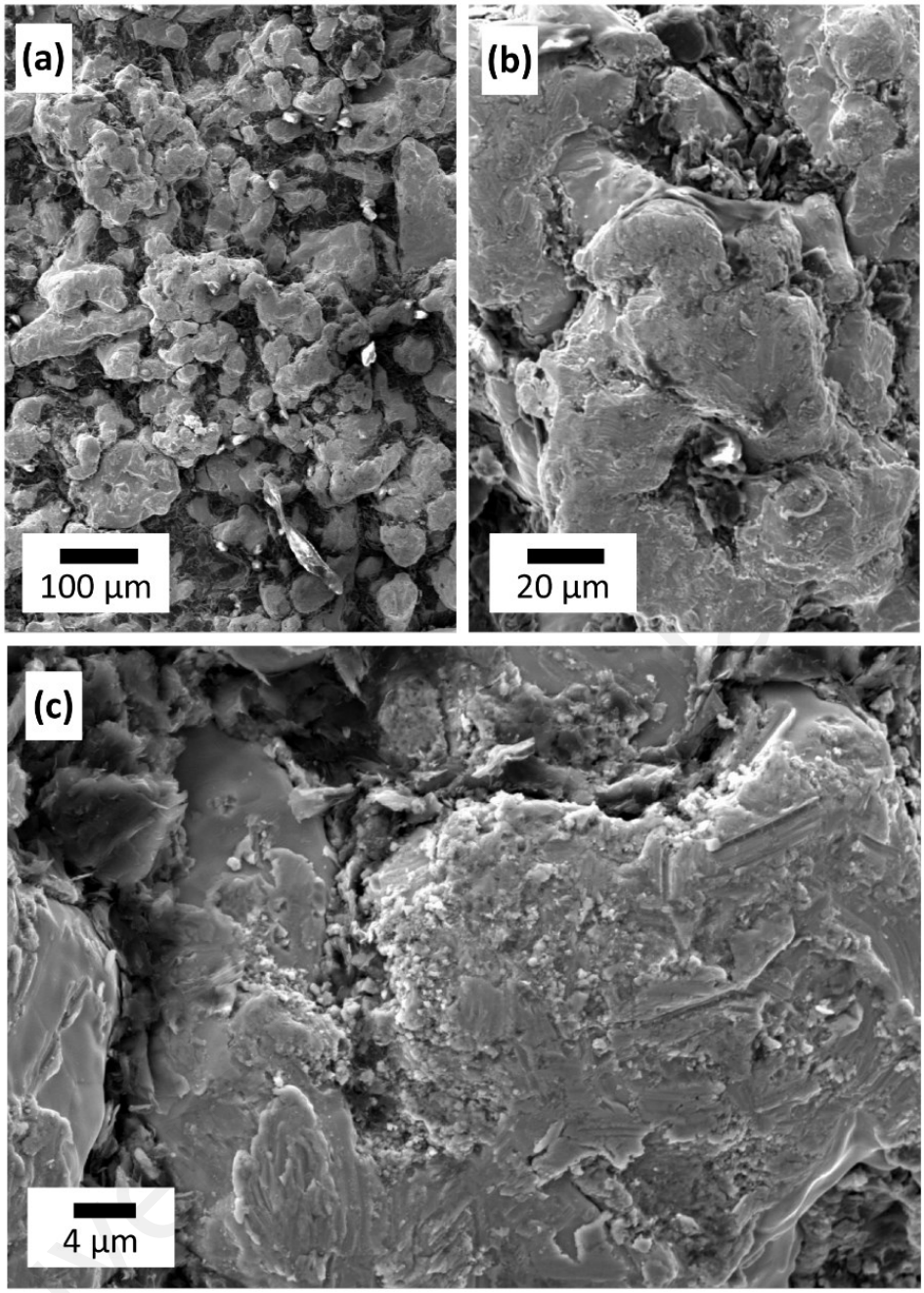

Figure 7.7: FESEM micrograph of a typical point on Ti-C synthesized in a hot inert crucible

The Ti-C pellet X-ray diffraction pattern is plotted in Figure 7.8. The diffraction data for the Rietveld analysis was collected in the angular range of $5.0131 < 2\theta < 79.9711°$ with 0.026 ° step size and 148.92 s scan step time. Phase identification was obtained by comparison with the Inorganic Crystal Structure Database (ICSD). The JCPDC card phase numbers (reference codes) are listed in Table 7.2.

A titanium carbide (TiC) phase formed and some unreacted graphite powder and titanium were observed as elemental material. Strong TiC peaks appeared in the XRD pattern at 2θ = 36.3, 42.27, 77.53˚. A sharp carbon peak exists as well. According to the Rietveld refinement method for phase quantification, the weight fraction of the phase was TiC = 18% and un-reacted Ti and C comprised 39 and 42%, respectively. The unreacted powder may play an important role in further processing with other potential reactive elements that tend to wet and form a new phase.

Table 7.2: JCPDC card numbers (pattern list) applied in XRD analysis

Ref. Code	Score	Compound Name	Scale Factor	Chemical Formula
96-120-0018	35	Graphite 2H	0.540	C4.00
96-901-1601	48	Titanium	0.039	Ti4.00
96-591-0092	44	Titanium carbide	0.031	Ti4.00 C4.00

Clearly, a self-sustaining chemical reaction occurred to the Ti-C pellet, beginning with the solid diffusion of Ti and C. According to Knyazik et al. (1985) the ignition temperature of the Ti+C mixture is close to the melting point of Ti. The ignition is associated to the fusion of Ti (Fan et al., 1999). In addition, the TiC synthesis reaction takes place prior to titanium fusion. Therefore, TiC is obtained under a comparatively slow heating rate and after a long reaction period, despite typical SHS processes (Contreras et al., 2004). Owing to the rapid heat dissipation, the Ti-C pellet did not have sufficient time to heat up well and propagate across the specimen. The pellet was characterized and further solid diffusion stopped. It was found that it was impossible for the unreacted phases to be divided into distinct zones because the pellet was thin and uniformly exposed to the heat. Although it was not a complete self-sustaining reaction, its application in centrifugal thermite-assisted composite processing is feasible. In the Fe-Ti-C system, solid diffusion is more likely to ensue until the initial material is finished.

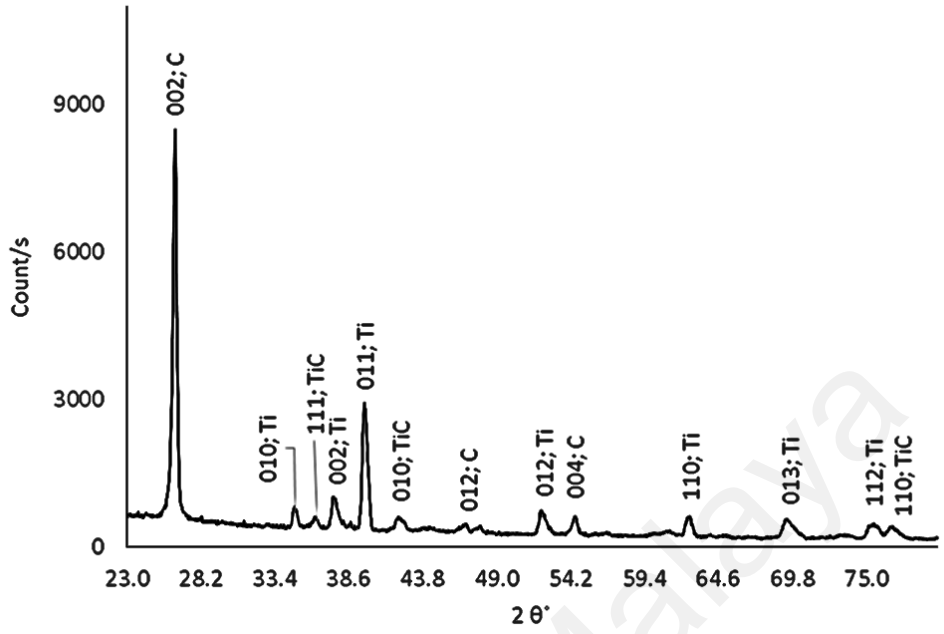

Figure 7.8: X-ray diffraction pattern of a typical point on Ti-C synthesized in a hot inert crucible

It can be concluded that the Ti-C pellet underwent a self-sustaining chemical reaction. Because the heat dissipated rapidly, the Ti-C pellet did not have sufficient time to heat up well and propagate across the specimen. However, it seemed to be an incomplete self-sustaining reaction, it is feasible to be applied in centrifugal thermite-assisted composite processing.

7.3.1 Microhardness and Young's Modulus

Mechanical properties were measured randomly over the sample surface in terms of microhardness and nanoindentation. The microhardness measurement revealed hardness values up to 562.9±104.9 MPa. Since the microhardness was measured arbitrarily on the cross-section, the relatively high standard deviation value is in agreement with the XRD result (Figure 7.8), indicating a large amount of unreacted phases and materials. The unreacted materials induced elevated hardness standard deviation due to the randomly selected indentation locations.

Nanomechanical characteristic evaluation of the composite was done in terms of nanoindentation. The method was described in Section 3.3.4. The indentation mark and loading-unloading plot are depicted in Figure 7.9 and Figure 7.10, respectively. The calculated E_{it} conforming to Young's modulus was 65 GPa, which is 16% of the nominal Young's modulus of a pure, single TiC crystal (Wiederhorn et al., 2006).

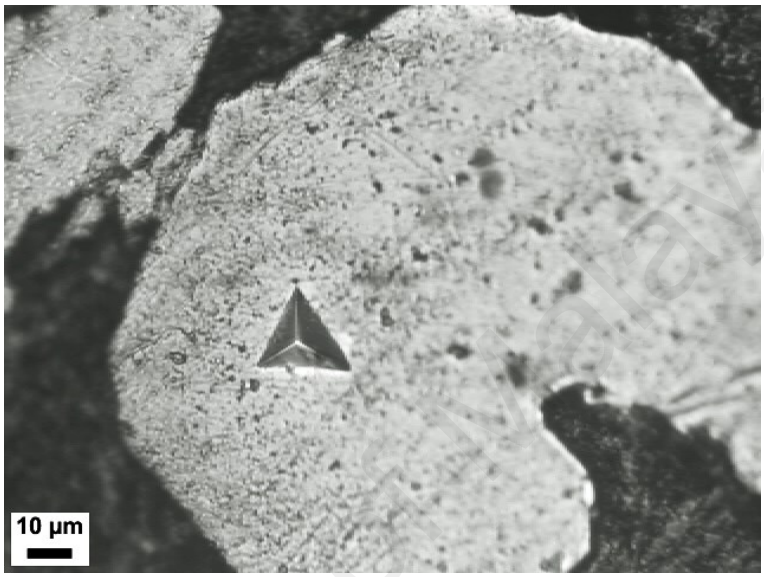

Figure 7.9: Berkovich indentation mark on Ti-C product

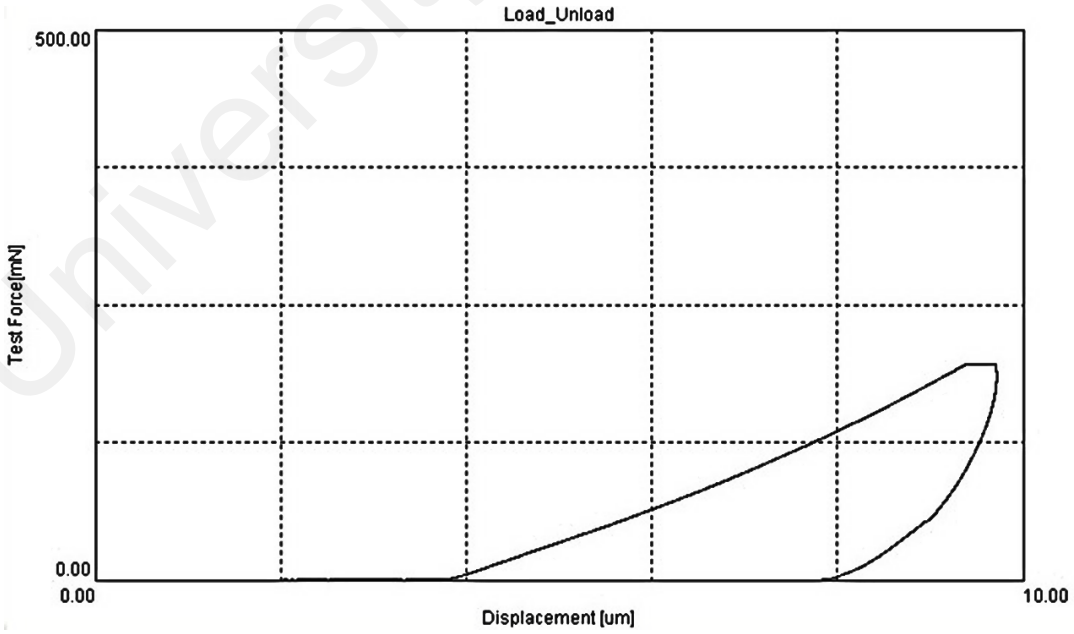

Figure 7.10: Loading and unloading plot of Nano-indentation (load 196.13 mN)

According to the XRD results (Figure 7.8), since the reaction did not completely propagate, the remaining unreacted initial reactants impelled a decline in the strength,

microstructure, and nanomechanical properties of the product. Cooling was rather faster than the required rate to allow the TiC combustion front to sustain throughout the specimen (Bertolino et al., 1999). The product can be employed in a combined reaction as a semi-synthesized pellet with the potential to partake in a secondary reaction or infiltration. The semi-product TiC/Ti/C demonstrated adequate performance in hybrid reactions of Ti+C/Fe_2O_3+Al. The infiltration mechanism of iron into TiC is discussed in the next section.

7.4 Evaluation of M+C embedded centrifugal thermite reaction (method 2)

Four experiments are discussed in this section, including Ti+C and Si+C embedded pellet processing using centrifugal thermite reaction using method (2). SM05, SM06, and SM07 represent Ti-based coating. On the other hand, SM08 regards the possibility of Si+C processing under centrifugal acceleration.

7.4.1 TiC-Fe-Al_2O_3 functional material production (SM05, SM06)

The experiment was designed as such that it formed the desired Al_2O_3-Fe and TiC. The heat generated by the centrifugal thermite reaction initiated the reaction between Ti and C, followed by phase formation and phase separation. The fast cooling rate after the thermite reaction is responsible for controlling the TiC exposure to sudden high temperature. This cooling temperature was plotted in Figure 7.11.

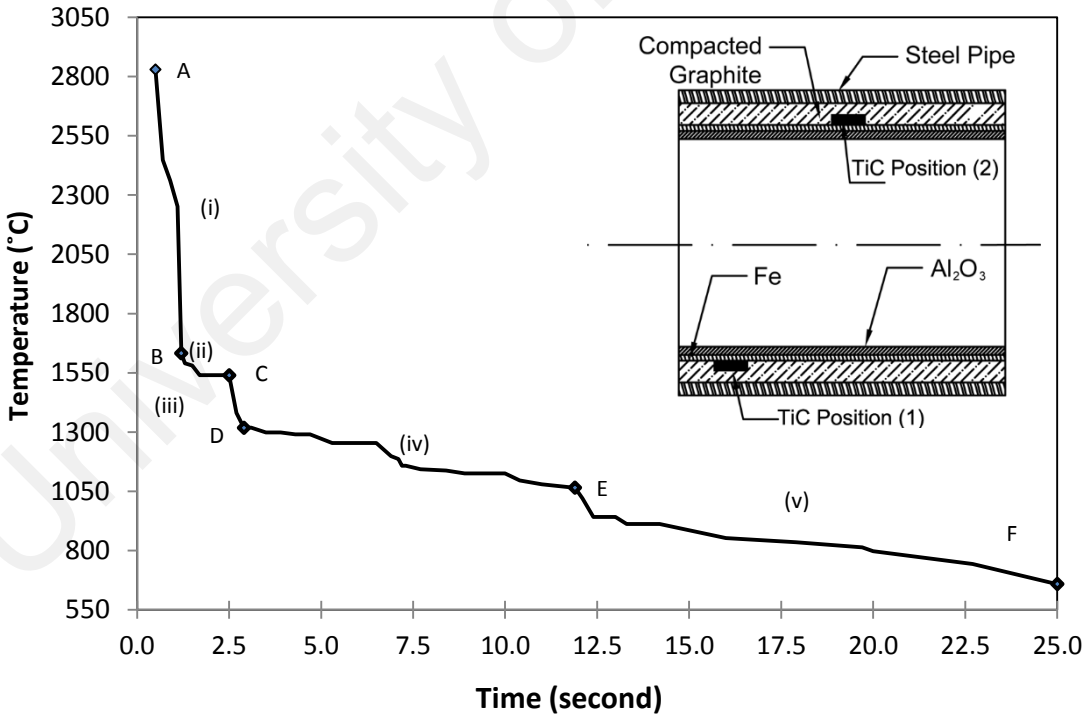

Figure 7.11: Temperature-time cooling profile of the reaction [Ti+C and Fe + Al_2O_3] under centrifugal acceleration measured with an infrared pyrometer

As shown in Figure 7.11, the Ti and C mixture pellets were exposed to a temperature above 2830 ˚C for a fraction of a second. It took less than half a second to increase from

room temperature up to 2830 ˚C (point A). In region (i), the temperature of the crucible dropped suddenly, followed by the end of the thermite reaction in the region at Point B.

The temperature was roughly stable for about 1.5s (region ii) near the melting point of Fe to reach point C. Then the crucible cooled down rapidly, which indicates that the phase transition of molten Fe probably ended (point C). This is because the melting temperature of pure Fe is above zone (iii) and the quick heat dissipation in region iii (C to D) as observed from the graph. At this time, the Fe phase solidified, and the temperature continued to drop at a slower rate [regions (iv) and (v)] to reach 600 ˚C in around 25 s (Point F). The cooling rate was nearly constant from D to F indicating that no ceramic phase transition took place in this interval and that the products completely formed. However, the steel phase transition might occur according to the steel phase diagram with respect to cooling rate.

The macro scale image of the as-cast Ti-based functionally graded coated product is illustrated in Figure 7.12. Figure 7.12 (a) shows the steel pipe with an alumina tube formed inside. The alumina tube is one of the thermite reaction products that got molded in the shape of a hollow cylinder when it was in the molten phase being exposed to high centrifugal acceleration.

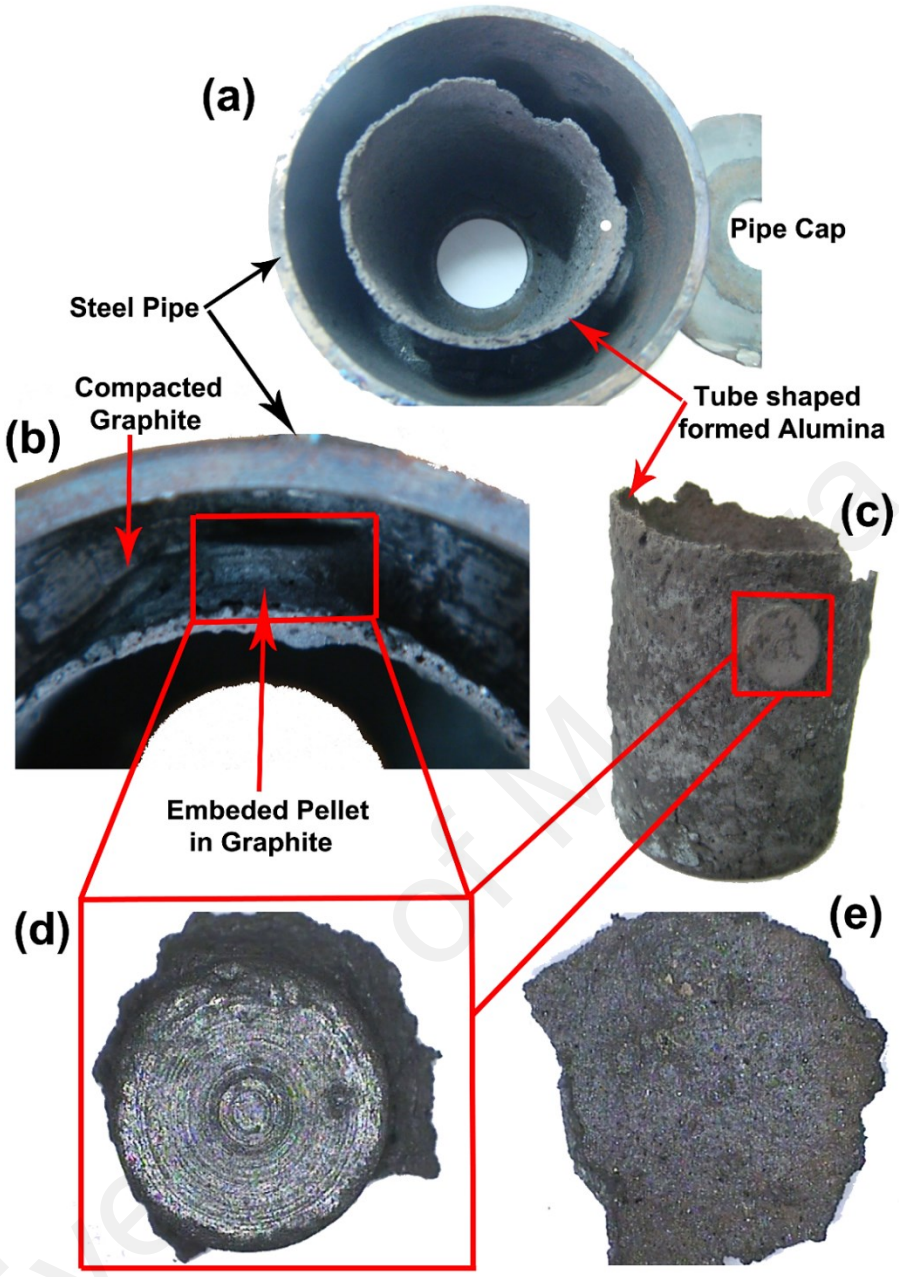

Figure 7.12: Macro scale image of the as-cast TiC-Fe-Al_2O_3 product (the pellet in position (1) is highlighted)

Figure 7.12, (b) shows an inset view of the steel pipe assembly, the compacted graphite, and alumina tube with the composite pellet inside. The surrounding graphite which acted as a refractory die was crushed from the pipe in order remove the sample from it. The Alumina tube is shown in Figure 7.12, (c), which is shaped out of molten iron and alumina after the thermite reaction due to the centrifugal acceleration. Figure 7.12, (d) is the rear view of the Ti-C pellet (12 mm diameter), and Figure 7.12 (e) is the front view of the pellet (inner-most layer) joined with a ferro-alumina layer. The

as-sintered Ti-C pellet coated with ferrro-alumina in Figure 7.12 (d, e) was removed from the tube. It was then cross-sectioned and ground for further processing and characterization.

X-ray diffraction (XRD) data for the Rietveld analysis was collected in the angular range of 10.0131 < 2θ <79.9711° with a 0.026° step size. Phase identification was obtained by making a comparison with the Inorganic Crystal Structure Database (ICSD). The XRD pattern and its corresponding Rietveld phase quantification of the sample's cross-sections are depicted in Figure 7.13 and Figure 7.14, respectively, for the two experiments. The XRD pattern in Figure 7.13 illustrates that the most relatively intense peaks are Ti (001), TiC (111, 002), and C (110) for both samples.

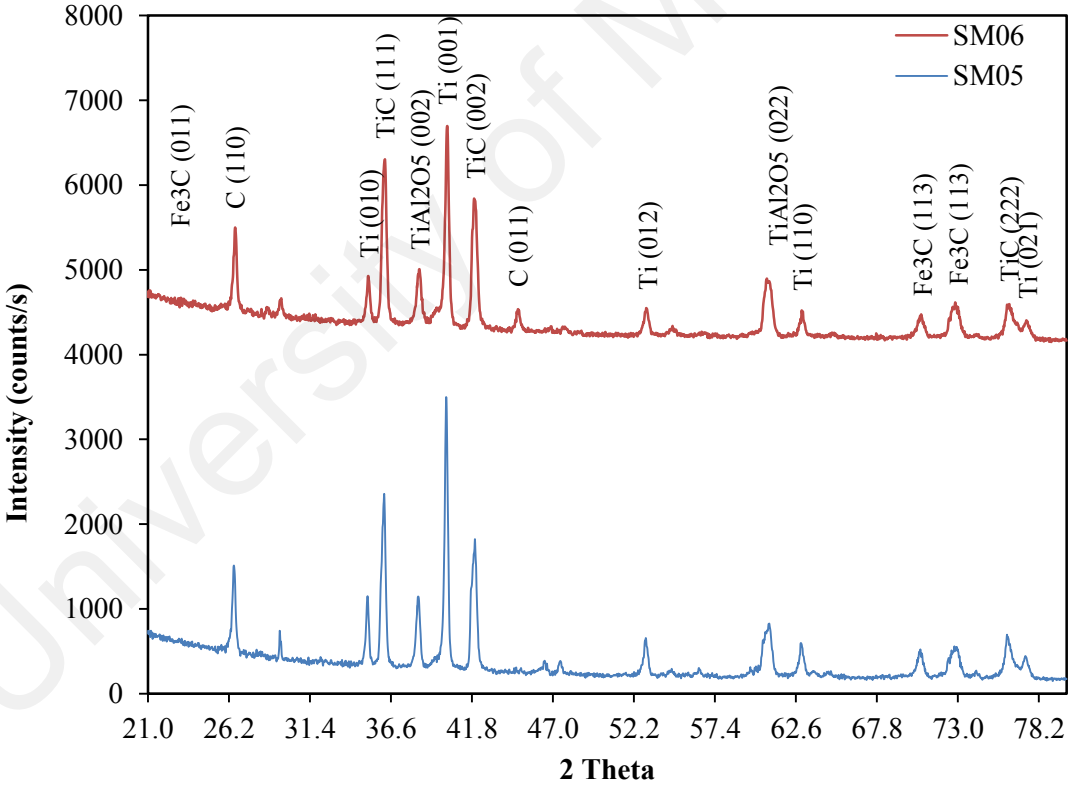

Figure 7.13: X-Ray diffraction pattern on cross-section

However, according to the Rietveld phase quantification results, Figure 7.14 indicates that more TiC product formed during the experiment in the case of position (1) compared with position (2). This behavior is due to the positioning of the Ti+C pellet in the pipe, whereby the pellet in position (1) was situated at the boundary near the pipe head. This

supports the experimental outcome presented in Section 7.2. The pipe head was exposed to excessive heat generated by the centrifugal thermite process that was located where the largest temperature gradient happened. The other phases detected by XRD included $TiAlO_5$, and Fe_3C.

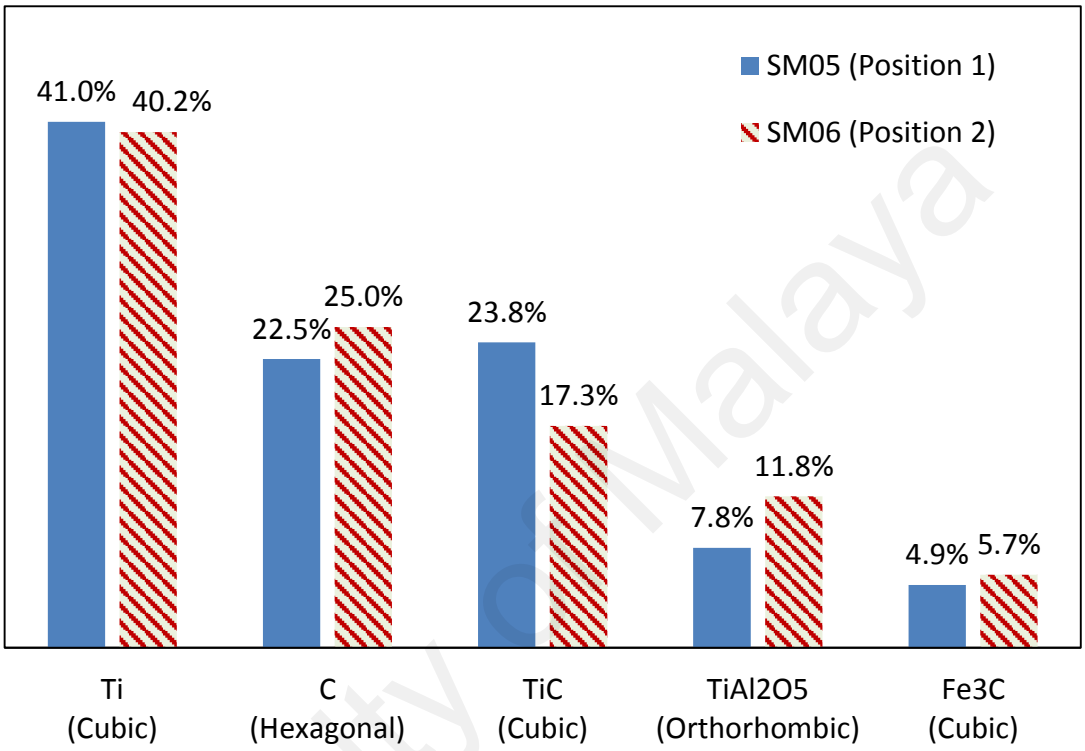

Figure 7.14: Phase Quantification based on Rietveld calculation

Field Emission Scanning Electron Microscopy (FESEM) equipped with EDAX was used to study the microstructure of various layers. Figure 7.15 shows a FESEM micrograph of a typical point at the surface and cross-section of the TiC-Al_2O_3-Fe composite. Table 7.3 displays the elemental analysis of a typical cross-sectional view of two TiC pellets following the experiment. A visual evaluation of the pellet revealed that there is a non-uniform crystal distribution in the layers.

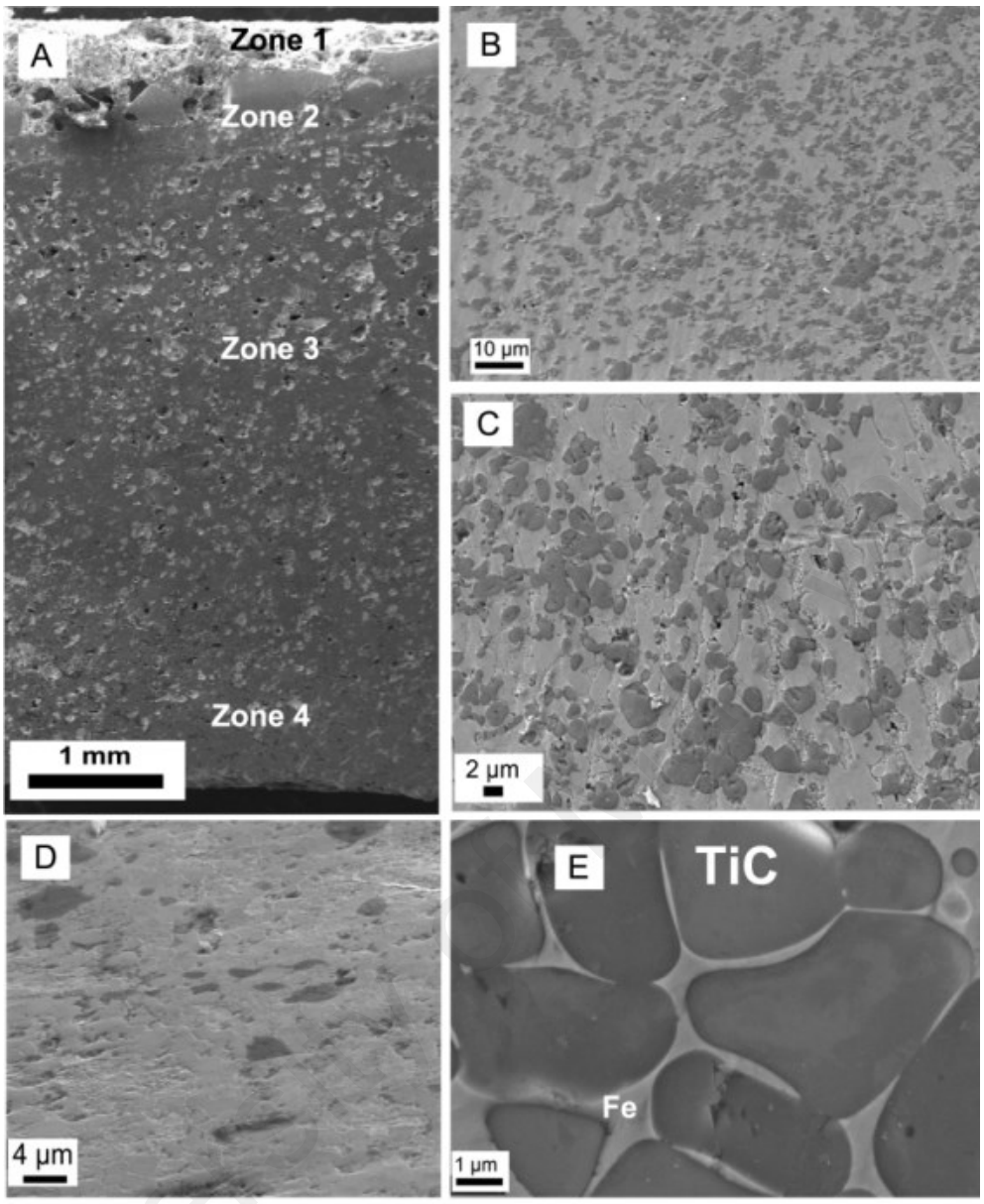

Figure 7.15: FESEM micrographs of a typical point on the Ti-based functionally graded coating: (A) the overall view of the cross-section with different zones; (B), (C) and (E) the cross-sections at higher magnifications of Zone 3 and Zone 4; (D) the view of the surface at the back of the sample in Zone 4

According to EDAX analysis (Table 7.3), it can be verified that Fe, Al, Al_2O_3 products diffused into the TiC pellet. It is known that the centrifugal force of a particle under centrifugal acceleration is $F=m.\omega^2.r$, when the rotation speed (ω) is constant but the centrifugal acceleration increases with a change in the particle's position from the axis of rotation (pipe axis) toward the pipe wall. In this case, the experimental EDX results from different positions (r) in the cross-sectional area can be experimental evidence that the

diffusion of Fe and Al has occurred under centrifugal acceleration force together with thermal diffusion.

The order of compound deposition in the layers completely changed during the reaction. Molten Fe was able to penetrate into the TiC layer due to higher density, while molten Al mostly remained in Zone 1. However, according to the available amount of Al in each zone, Al_2O_3 formed in the innermost layer relative to the outer layer (Figure 7.15, Zone 1). For this reason, a thick layer of Al_2O_3 joined the TiC pellet surface. The Al_2O_3 layer is rather metallurgical brazed and it joined the TiC substrate as the fraction of Al is decreased from Zone 1 to Zone 3. The sequence and density of the Al_2O_3 product in each zone were organized according to the centrifugal force and heat exchange in the crucible. A graded structure was created in a very short time, under three seconds.

Table 7.3: EDAX analysis of several areas at two TiC pellet cross-sections

Mass %	Element	Zone 1	Zone 2	Zone 3	Zone 4
SM05 (pellet in position 1)	CK	6.81	12.44	29.16	46.23
	OK	49.54	45.25	9.15	0.8
	AlK	39.18	19.5	0.69	-
	TiK	0.21	12.66	19.63	51.33
	FeK	4.26	10.15	41.37	1.64
SM06 (pellet in position 2)	CK	3.2	18.58	40.45	33.31
	OK	43.38	36.28	3.82	0.7
	AlK	50.54	19.02	0.94	-
	TiK	0.56	9.3	42.7	63.38
	FeK	2.32	16.82	12.09	2.61

The diffused Fe had a significant role to facilitate gradient phase transition and the centrifugal acceleration force has pushed the layers to bond together. After the thermite reaction had completed, it is expected no more unreacted starting thermite powder were left in the tube. As the melting point of Al_2O_3 is above 2200 ºC, and the chamber

temperature was above 2800 ºC, all the formed layers in the pipe with the multicomponent product, had enough time to arrange and deposit based on their relative densities. Thus, Al_2O_3 with the lower density compare with Fe deposited on the innermost layer and solidified quickly [Figure 6.3**,** region (ii)], while Fe product was still in the molten condition. That is why Fe was able to penetrate more into TiC layer deeply. The results of the EDX elemental analysis show that the maximum amount of Fe in SM05 had occurred in Zone 3, rather than in Zone 2 (Table 7.3). Fe penetration depends on setting parameters such as distance from the head of the tube, and amount of dissipated heat.

According to Figure 7.15 there are some areas left vacant between Al_2O_3 and TiC surface layer, which are filled with molten Fe. This observation agrees with EDAX analysis [Table 7.3]. The viscous Fe with higher density compared with TiC is trapped between Al_2O_3 and TiC. Therefore, when exposed to the high centrifugal force, the molten Fe will escape to the outermost layers. Figure 7.15 and EDAX results (Table 7.3) illustrate the formation of cermet, TiC-Al_2O_3-Fe. TiC and Fe grains are clearly distinguished as shown in Figure 7.15, E. According to EDAX result, there are some amounts of Al and Al_2O_3 diffused into the TiC pellet as well. It creates TiC-Al as well as TiC-Fe-Al_2O_3 composite. Figure 7.15, (D) is the surface view of the TiC pellet, which was not exposed to direct heat.

7.4.1.1 Micromechanical Properties

Table 7.4 represents hardness data of the TiC-Al_2O_3-Fe composite. The hardness values vary from a point to point. It is due to heterogeneity in phase-structure distribution in the inner surface and cross-section of the TiC-Al_2O_3-Fe product. The Fe content of TiC for the specimen of the SM05 was better distributed, and the average hardness of the product was higher compared with the specimen at SM06 test. This could be possibly due to better distribution Fe inside the composite in SM05.

The hardness of stoichiometry TiC has been reported to have a value of up to 3200 HV (Tjong & Ma, 2000). Bandyopadhyay and Das (2004) reported the hardness of the as-cast composite of TiC-Fe to be between 1800-2200 HV. In the present study, it is found that the hardness variation is directly related to the phase distribution and pores concentration. The overall maximum value of the hardness recorded was 2233 HV with the highest TiC peak on SM05 according to the XRD pattern, Figure 7.13.

Table 7.4 Vickers hardness (HV) gradients of TiC-Fe-Al_2O_3 product

	Element	Zone 1	Zone 2	Zone 3	Zone 4
SM05	HV Ave.	1150	1307	1479	1281
	HV Max.	1300	1993	1825	2233
	HV Min.	650	1037	898	806
SM06	HV Ave.	646	1046	1037	1051
	HV Max.	800	1521	1617	1521
	HV Min.	550	882	795	650

The minimum of 550 HV is based on XRD results and Figure 7.13, as there were more unreacted compounds. The diffused molten Fe had a significant role in facilitating gradient phase transition under the effect of centrifugal force, which made the layers bond. The relatively lower hardness value was recorded in Zone 1, which is most likely due to the porosity of the Al_2O_3 layer.

7.4.2 Evaluation of TiC-Fe-Al_2O_3 functional material production (SM07)

With respect to Section 3.2.2 and 5.4, a similar method was utilized to synthesize TiC-Fe-Al_2O_3 composite, but setting one (position one) was used where the pellet was situated at a boundary near the pipe's head. Once the reaction took place under the influence of centrifugal acceleration, molten Al_2O_3-Fe infiltrated the Ti+C pellet. An infrared pyrometer recorded the reaction temperature released that was up to 2925 ˚C.

Figure 7.16 displays the time-temperature behavior of the product. The pyrometer laser pointer was adjusted to capture temperature information of the TiC during reaction. Figure 7.16 (a) represents the maximum temperature detected by the pyrometer in the early stages of the thermite reaction. The temperature inclined sharply to nearly the melting point of iron at data point (b) and continued decreasing with a lower steepness until data point (c). After reaching the melting point of iron, the slope dropped sharply to data point (d). There was a sudden increase from 1336 to 1462 ˚C, where it is anticipated that the reaction between Ti and C started. Since the reaction between Ti and C is exothermic (Voudouris & Angelopoulos, 2011; Wen et al., 2012) and the pyrometer was adjusted to capture the temperature data of that particular area, the increment was very much expected to have originated from the Ti+C reaction. As the area of the pellet was much smaller than the pipe's, the heat dispersed rapidly. The temperature data of the coating surface layer consisting of alumina and iron was recorded.

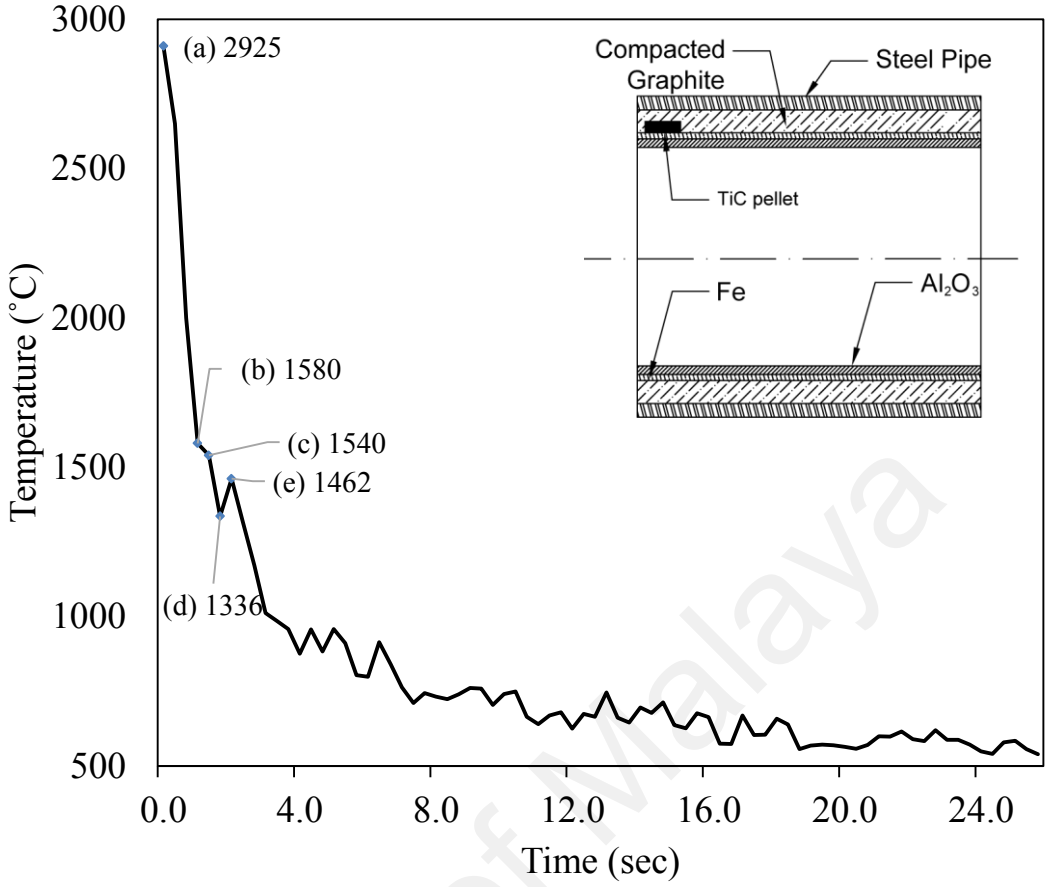

Figure 7.16: Time-temperature plot of the TiC-Fe-Al_2O_3 cooling profile of experiment SM07

Centrifugal force pushed the molten material to the inner surface of the Ti+C pellet. The molten semi-products forcibly penetrated the porous Ti+C media and formed an in-situ TiC-Fe-Al_2O_3 composite. This reaction lasted only 2.5 seconds from ignition until Fe solidification, at which point the reaction and infiltration presumably stopped. However, the cooling rate plot shows the behavior of the synthesized pellet up to 24 seconds after the reaction. The thermite reaction products (Fe and Al_2O_3) deposited according to their densities (Meng et al., 2007) at the graphite mold's innermost layer, and then diffused inside the TiC zone. The reactions created a porous TiC product.

The product that formed, i.e. TiC-Fe-Al_2O_3 composite, had a round, rough innermost layer surface, and was microscopically porous at the cross-section. The average roughness (R_a) value in Figure 7.17, region 4 (specimen's face), was about 3.12 µm. The

rapid heating and super-cooling process of the material would have caused surface imperfections. As for FESEM-EDAX analysis, an electron beam scanned along a preselected line across the sample, while X-rays detected discrete positions along the line. Line analysis of the X-ray energy spectrum in Figure 7.17 provided a plot of the relative elemental concentration for each element versus position along the white line in the center of the figure.

In Figure 7.17 layer (1) which was a TiC-rich area, there was only a small amount of Al representing Al_2O_3 or Al intermetallic detected, whereas a high amount of Fe diffusing into the TiC zone was identified. The intermetallic compounds comprising Ti, Al and Fe were mostly located in zone (2). All the starting elements participated in the reactions, increasing the quality of joining properties. However, Fe was distributed more uniformly through area (2). The product's middle layer (3) in Figure 7.17 contained the highest amount of Al. The carbon content was diffused in all layers, although titanium was diffused inside the Al-rich layer (3). The elemental composition of layer (4) was rich in Fe and had little C and Ti.

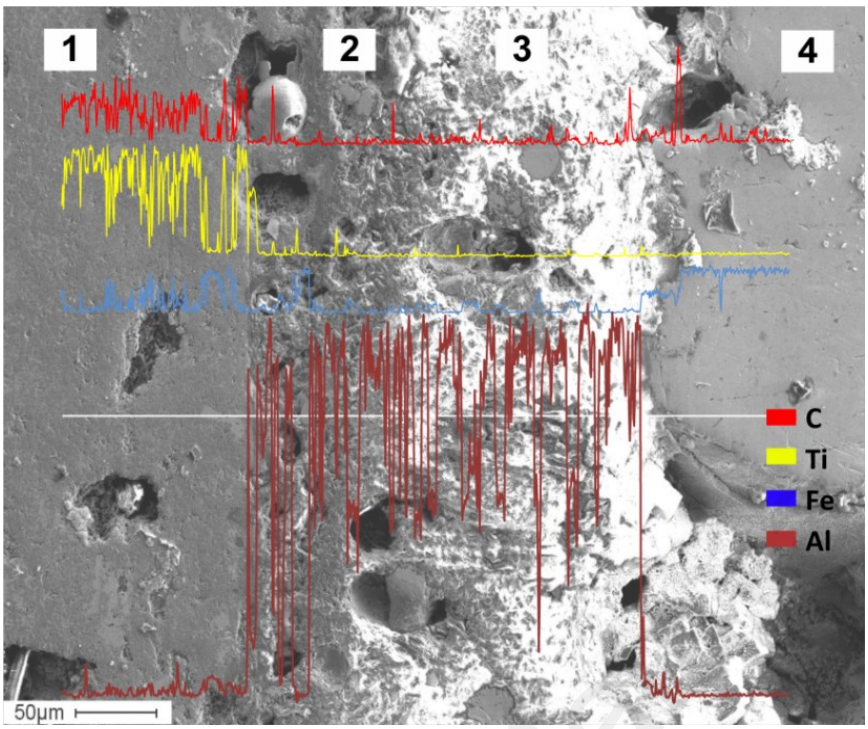

Figure 7.17: Line profile analysis of a typical area on the TiC-Fe-Al_2O_3 specimen

A typical area of the product's TiC zone is shown in Figure 7.18 (a) before and (b) after exposure to the environment, where different locations are highlighted based on EDAX elemental analysis. The pores of the Ti-C zone seemed to be filled with the molten composite due to high centrifugal acceleration acting as an external force. At high gravity pressure the molten composite wetted the ceramic surface and filled the pores (Muscat et al., 1994). There are extensive reports of molten metal capillary infiltrating a porous medium to form a ceramic-metal composite (Travitzky, 2012).

Figure 7.18 (b) illustrates a micrograph image of the sample that was exposed to environmental conditions, while the corresponding EDAX elemental analysis of different locations at points 1 and 2, and zone 3 are provided in Table 7.5. Several compounds were identified in the sample, including iron oxide, titanium dioxide, and carbon-based compounds such as TiC and Fe_3C. According to literature, corrosion begins at high interfacial energy and relatively weak bonding locations like grain boundaries (Askeland et al., 2011).

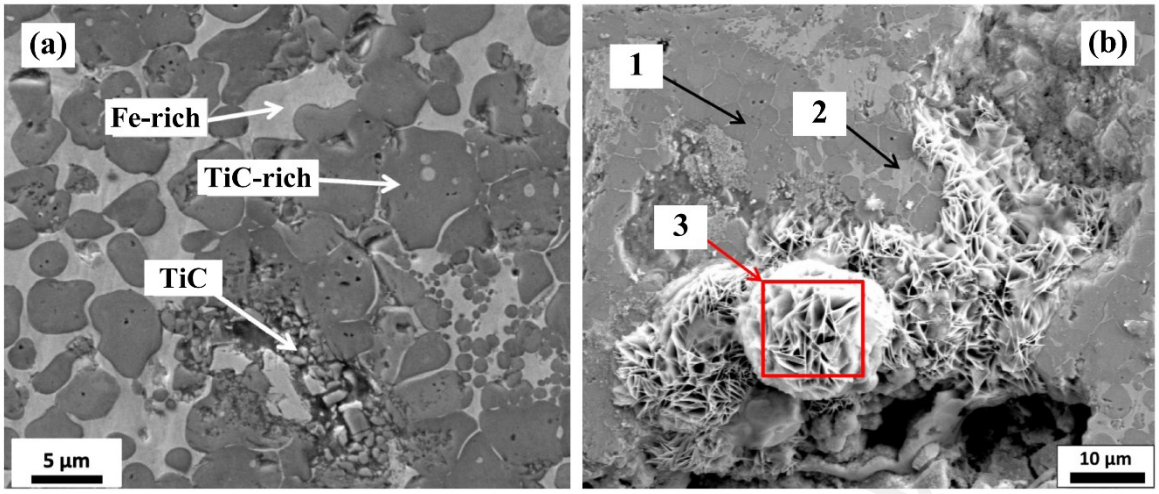

Figure 7.18: FESEM micrograph of product cross-section (a) before; and (b) after exposure to the corrosive environment

A scaling issue was also encountered that increased the surface area. This phenomenon is similar to corrosion problems mostly as a result of tuberculation (Ebacher et al., 2011). The findings are comparable to those of Tao et al. (2012) regarding the flower-like anatase TiO_2 hierarchical spheres assembled by nano-sheets synthesized by glycine via a hydrothermal approach. Tao et al. (2012) claimed that the obtained TiO_2 sample obtained demonstrated good photocatalytic activity of decomposing methyl orange under sunlight. The oxide layer in Figure 7.18 (b) is needle-like (flower-like) with sharp edges. This sort of surface changes are significant with respect to tribological behavior, as they cause fretting corrosion damage in biomedical applications (Diomidis et al., 2011). According to EDAX results, the corroded area consisted of FeO, Al_2O_3, TiO_2, and TiC components after three-day exposure to the environment.

Table 7.5: EDAX elemental analysis of different areas/points

Elements	C	O	Al	Ti	Fe
Point A	46.23	0.81	-	51.32	1.64
Point B	0.94	1.07	0.21	1.76	96.02
Area C	11.79	51.03	0.32	1.82	35.04

Diffraction data for the Rietveld analysis was collected in the angular range of 10.0131 < 2θ <59.5431° with a 0.026° step size. Phase identification was obtained by comparison with the Inorganic Crystal Structure Database (ICSD). X-ray diffraction pattern (XRD) of the whole specimen's cross-section elaborates the existing phases in Figure 7.19, and confirms the formation of a polycrystalline product with different TiC-Fe-Al_2O_3 composite phases. The compound's intermetallic peaks of tetragonal titanium aluminide (TiAl, Ti_3Al) were detected in the XRD pattern. The presence of intermetallic compounds enhances crystal properties into the form of ordered crystal structures (Wang et al., 2009)..

Table 7.6: JCPDC card number and their score used in the XRD pattern

Ref. Code	Score	Compound Name	Scale Factor	Chemical Formula
98-005-3784	69	Titanium - Alpha	0.985	Ti
98-061-8945	66	Titanium Carbide	0.554	TiC
98-003-1170	39	Graphite 2H	0.340	C1
98-002-4695	31	Wuestite	0.097	$Fe_{0.974}$ O
98-002-9341	6	Cohenite	0.060	Fe_3C
98-009-9782	10	Titanium Aluminide (1/1)	0.051	AlTi
98-016-7813	30	Titanium Aluminide (1/3) - Do22	0.933	Al_3Ti
98-010-7811	19	Aluminium Iron Titanium (2.54/0.35/1)	0.285	$Al_{2.535}Fe_{0.34}Ti$
98-015-1590	4	Aluminium Oxide - Hp	0.111	Al_2O_3

The Ti and Al atoms occupy specific locations in the crystal structure rather than random, as in the majority of solid solutions. Intermetallics have been noted to possess lower ductility properties, with environmental factors also playing a role in limiting ductility in intermetallics (Askeland et al., 2011). Impregnation becomes difficult owing to the exothermic reaction and different contractions of Fe and TiC during freezing.

According to XRD and Rietveld refinement results, 33.1% of the product was composed of TiC <111>, <011>, and <002> crystal direction with cubic structure. Hexagonal titanium <011>, <010> crystal direction 28.8% and hexagonal carbon <002>,

<004> crystal direction 23.0% elements did not react with each other but took part in metallurgical alloying and joining.

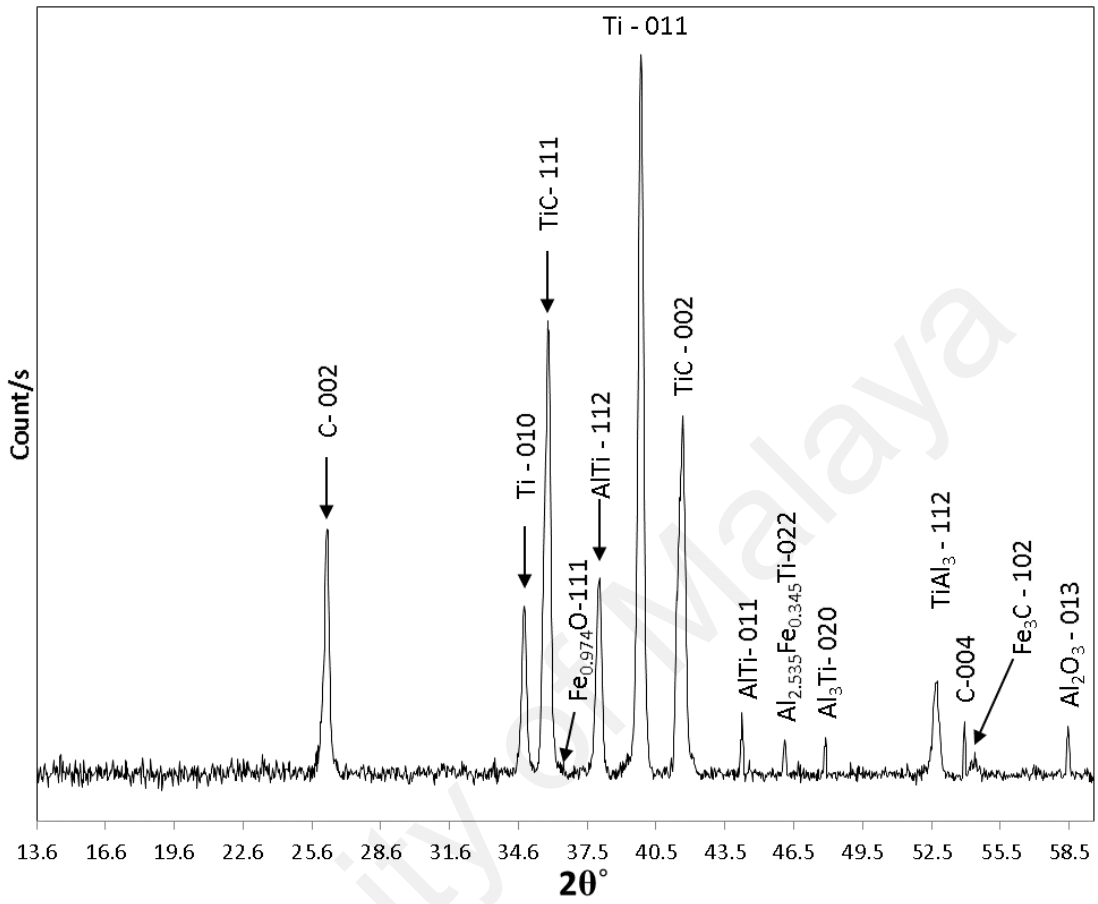

Figure 7.19: XRD diffraction pattern of specimen cross-section

1.5% of $Al_{2.54}Fe_{0.55}Ti$ system <111> crystal direction was formed. The ternary iron (Palm & Lacaze, 2006) had a cubic structure with a substantial capability of developing intermetallic-based materials for high temperature applications (Bendjeddou & Debili, 2010). The Al-Fe-Ti alloy also has ferromagnetism properties (Krein et al., 2010). The XRD pattern does not display a strong anatase peak. This compound grew as a thin layer on the top surface layer of the composite. Therefore, it was not readily detectable by normal XRD, but was perceived by FESEM. Alumina (Al_2O_3), Wuestite (FeO), and Cohenite (Fe_3C) were detected by XRD with 1.2%, 1.7%, and 2.6% quantities in the composite, respectively.

The quantitative phase analysis conducted using the Rietveld method is given in Table 7.7. The Ti and Al atoms occupy specific locations in the crystal structure rather than random, as is the case in the majority of solid solutions. Intermetallics have been shown to possess lower ductility properties, with environmental factors also playing a role in limiting ductility (Askeland et al., 2011). The XRD pattern does not display a strong anatase peak (titanium oxide [011]), as this compound grew as a thin film on the top surface layer of the composite, which was not readily detectable by normal XRD but was perceived by FESEM.

Table 7.7: Rietveld quantitative phase analysis of XRD

Compound	Chemical Formula	Rietveld Quantification	Crystal system
Titanium -Alpha	Ti	28.80%	Hexagonal
Titanium Carbide	TiC	33.10%	Cubic
Graphite -2H	C	23.00%	Hexagonal
Titanium Aluminide	TiAl	4.20%	Tetragonal
Titanium Aluminide	$TiAl_3$	3.90%	Tetragonal
Cohenite	Fe_3C	2.60%	Orthorhombic
Wuestite	FeO	1.70%	Cubic
Aluminum Iron Titanium	$Al_{2.54}Fe_{0.35}Ti$	1.50%	Cubic
Alumina	Al_2O_3	1.20%	Hexagonal

The relatively sharp peak (Ti, C) representing the amount of unreacted titanium and crystallized carbon may seem to be high due to the XRD mechanism that scanned the entire area of the sample's cross-section from the innermost layer up to the outer-most layer. Starting from the outer-most layer of the sample, the outer TiC pellet surface was not directly exposed to the heat. On the other hand, the reaction time was too short to propagate and transfer the generated heat inside the pellet; besides, the intermetallic layers may have prevented the rest of the specimen from reacting. The importance of the intermetallic layers is their support in providing a smooth transition of phases and compounds over the product volume.

7.4.2.1 Micromechanical Properties:

The mechanical properties in terms of micro-hardness conforming to Figure 7.18 (b) were measured in zones 1 and 2. The hardness reading results are plotted in Figure 7.20 versus the hardness results from literature (Bandyopadhyay & Das, 2004).

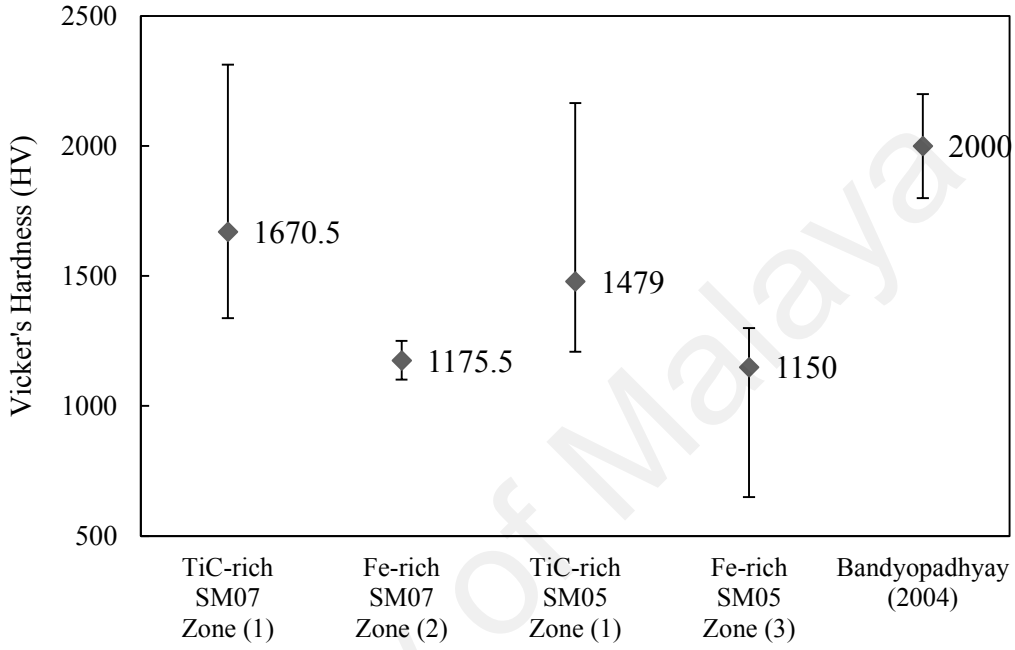

Figure 7.20: Average Vickers Hardness (HV) measurements of different typical points on the SM07 TiC-rich zone (1) and Fe-rich zone (2); SM05 TiC-rich and Fe-rich; TiC-Fe phase (Bandyopadhyay 2004)

The maximum Vickers hardness value (2313 HV) was observed in a TiC-rich region, whereas the maximum hardness value of the less TiC-rich area was 1251 HV. Nonetheless, the hardness variation is an indication of phase transition over the product's volume.

7.4.2.2 Nanomechanical properties

The indentation location was selected to cover a multi-compound area of the cross-section in order to better understand the sample's properties. The indentation location was measured for zones 2 and 3 corresponding to Figure 7.18 (a).

The loading-unloading conditions are as follows. The test force was set at 300 mN, loading speed 7.0067 mN/sec, and holding time at load 10 sec. The test was performed at room temperature. Sample Poisson's ratio was set 0.22. Two typical indentation marks are shown in Figure 7.21. Figure 7.21 (a) is indented on a Fe rich area where mostly iron phase with less TiC presence is. Figure 7.21 (b) is indented on Fe-TiC area with TiC rich component. A typical load-unload indentation curve is shown in Figure 7.22.

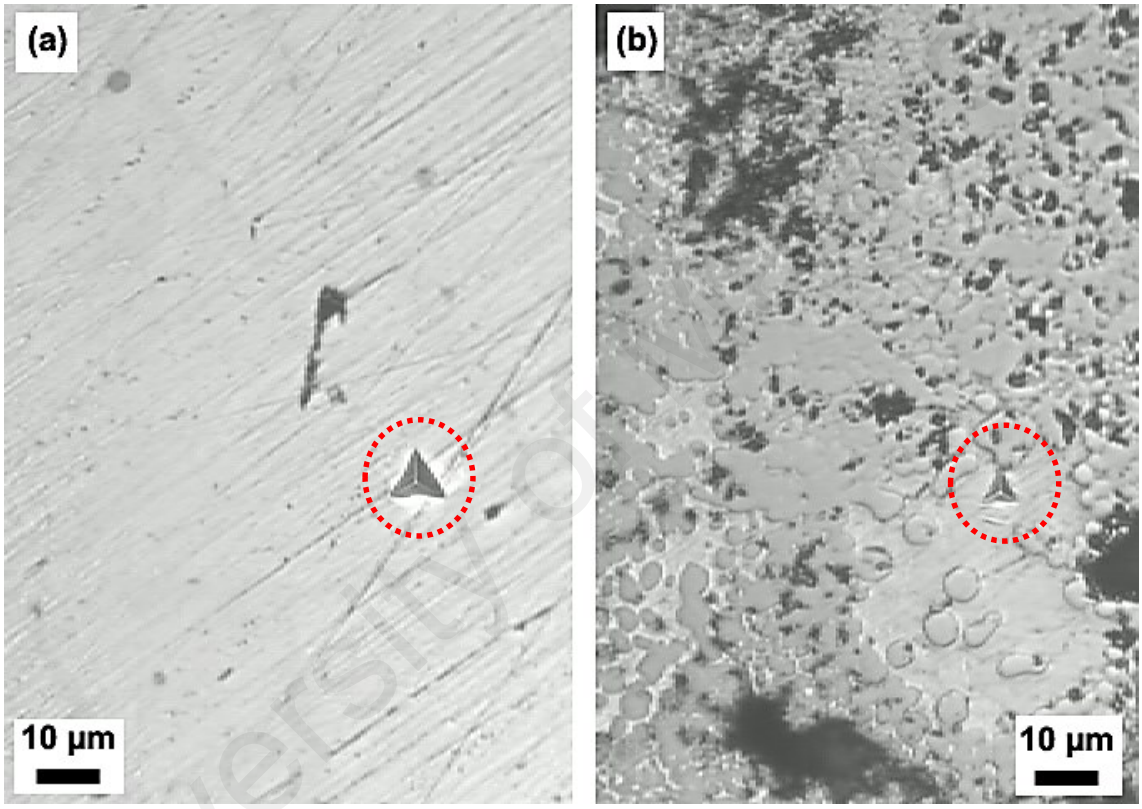

Figure 7.21: A typical image of indented surfaces, applied load were (a) 300 µm, (b) 100 µm

The calculated Young's modulus, E_{it}, of SM05, SM06, and SM07 is depicted in Table 7.8. As it can be seen, the three specimen got different E_{it} values, where the biggest standard deviation shows that different points on the specimens had varying values. Since each calculation is the average of five different readings of an identical specimen, every point had independent tensile behavior. The values were measured and calculated using a machine software interface.

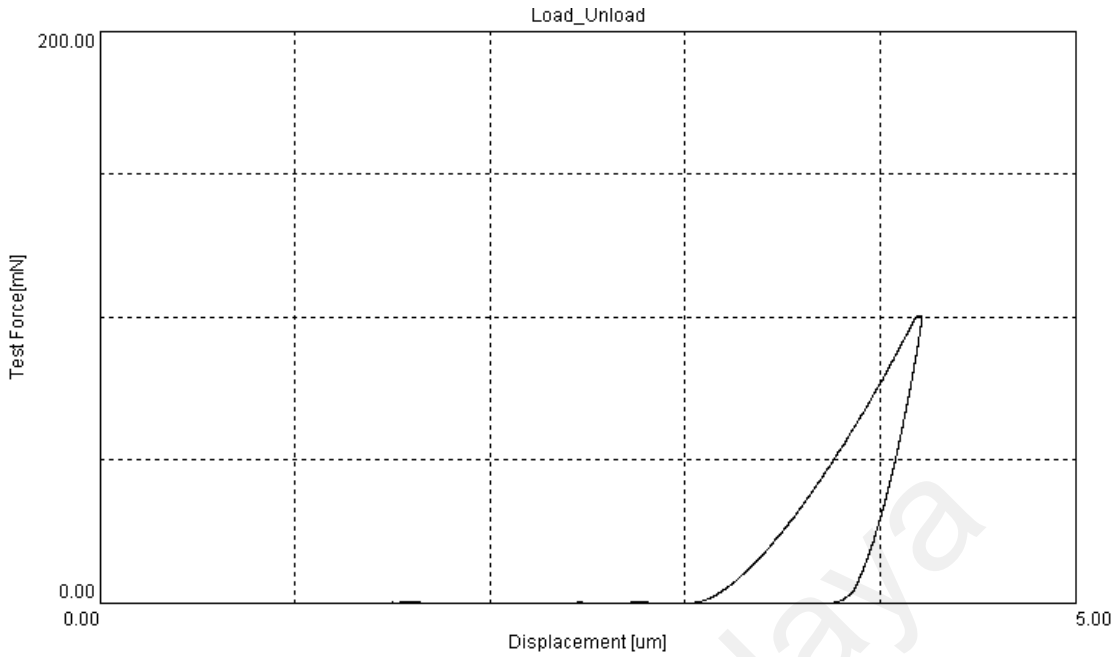

Figure 7.22: Typical force-displacement graph of load-unload of the TiC-Fe composite specimen

Table 7.8: Calculated Young's modulus for three different specimens on two zones

	Zone 2		Zone 3	
	Eit	STD	Eit	STD
SM05	105	12	151	22
SM06	85	14	135	31
SM07	98	11	138	26

7.4.2.3 Fracture toughness

The fracture toughness was determined using the extracted data from Vickers hardness and Nano-indentation technique according to Anstis et al. (1981) and Niihara (1983). The six points of Vickers readings are illustrated in Figure 7.24, corresponding to the diagram in Figure 7.23. Figure 7.24 (a) SM05, (b) SM06, and (c) SM07 are from a TiC-rich area corresponding to zone (3) from Figure 7.23, whereas Figure 7.24 (d), (e), and (f) show indentations in the Fe-rich areas corresponding to zone (2) of SM05, SM06, and SM07, respectively. The length 2c of the pair of cracks caused by the Vickers indentation was measured immediately after removing the indenter.

The Vickers indentation reading and fracture toughness were calculated and listed in Table 7.9. Obviously, non-significant cracks developed due to the inherent composite characteristics of TiC-Fe with several intermetallic constituents.

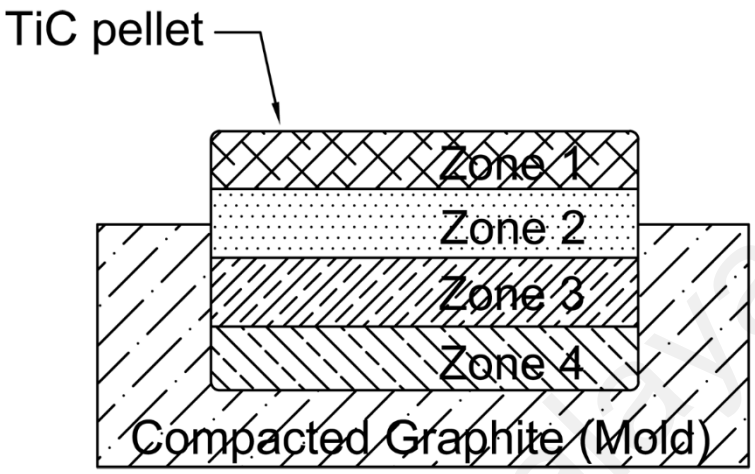

Figure 7.23: Schematic drawing of a TiC pellet exposed to centrifugal thermite process

The area corresponding to zone (3) of Figure 7.23 where the composition of Fe is relatively higher than in other regions, experienced greater crack propagation owing to Vickers indentation. However, this area does not exhibit significant cracks, but possesses side cracks. It is understood that a composite with TiC-Fe as a major component can play an important role in increasing the service life of a part while maintaining high hardness.

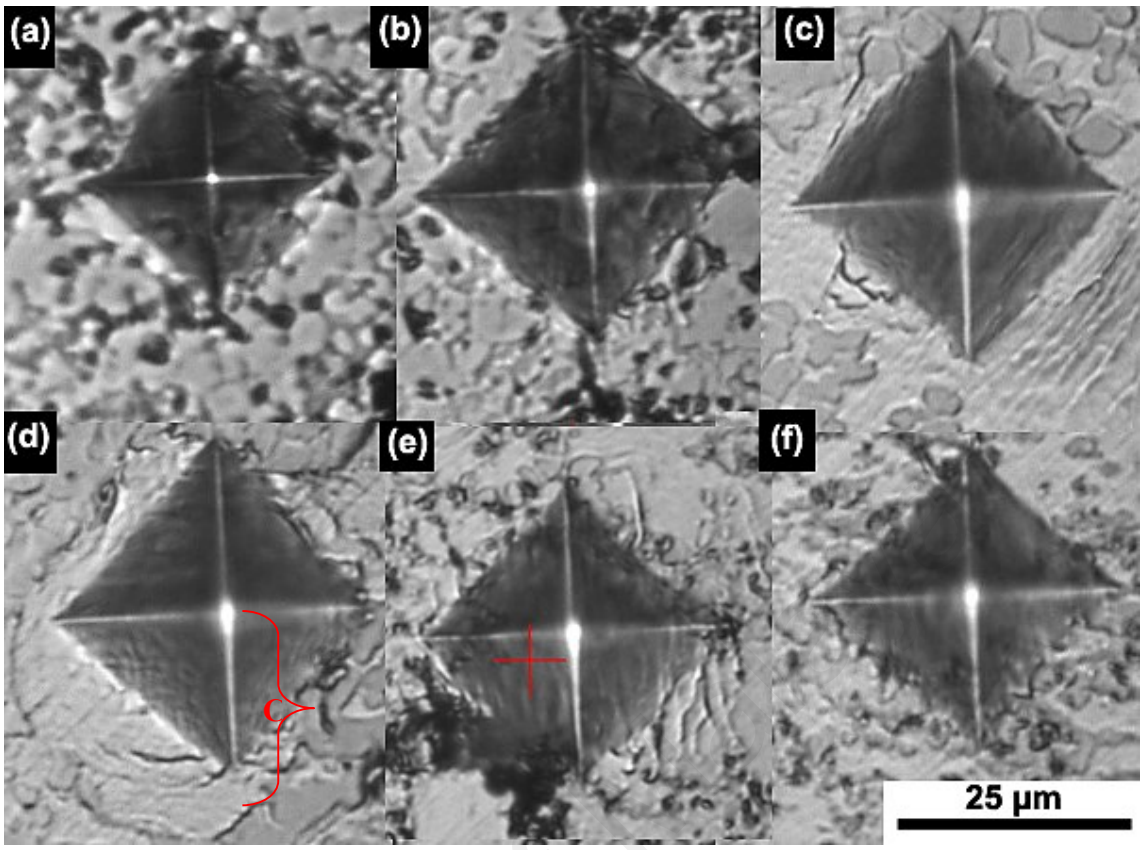

Figure 7.24: Vickers indentation marks at six different positions on the composite

Table 7.9: Vickers readings and the calculated fracture toughness of TiC-Fe-Al_2O_3

Image	Average Length (µm)	Hardness (GPa)	C (µm)	a (µm)	c/a	Eit (Gpa)	K_{IC} (MPa.$m^{1/2}$)
(a)	25.4	14.1	14	12.7	1.1	138	1.96
(b)	25.1	14.4	13.5	12.6	1.1	142	2.05
(c)	32.3	8.7	20	16.2	1.2	96	1.21
(d)	33.0	8.3	19	16.5	1.2	110	1.33
(e)	30.2	10.0	21	15.1	1.4	98	1.07
(f)	27.7	11.8	16	13.9	1.2	106	1.50

Therefore, the mechanical behavior of the specimen was changed over the volume (of the defined zones). Moreover, the calculated Young's modulus from the nanoindentation in Table 7.8 and the material's chemical composition (EDAX) from Table 7.5 seemed to vary over the different zones (volume), which makes the product a potential functionally graded coating with high hardness and good fracture toughness.

7.4.3 Evolution of the effect of centrifugal thermite reaction on an embedded Si+C pellet (method 2)

In experiment SM08, an attempt was made to produce an in-situ silicon carbide iron composite using thermite reaction energy under centrifugal acceleration. The as-sintered specimen was removed from the crucible for characterization. The visual observation of the specimen revealed that it was too loose and could be crushed easily with minimum force. The microstructure (FESEM) and corresponding elemental analysis (EDAX) of the specimen as it was facing the thermite reaction are featured in Figure 7.25 and Table 7.10, respectively.

The overall morphology of the specimen is depicted in Figure 7.25 (a) at low magnification. From a macroscopic point of view, the structure is not smooth with several defects and cracks. These cracks and defects are due to repositioning the specimen from the crucible since the specimen had a very loose structure. The corresponding elemental analysis reveals oxide formation that could be in form of alumina or silicon dioxide. Figure 7.25 (b) and (c) present closer views of the structure where the morphology of micro crystals is visible. The elemental analysis (Table 7.10) of various regions indicates that the compound had a non-uniform distribution in region (3) with no Al although the other two regions, (4) and (5) had less than 1% Al content.

The significance of tracing Al throughout the specimen is to recognize the phase formations and particle segregations in different zones. The presence of minute amounts of Al suggests that it is not possible to obtain pure phase formation. As demonstrated in previous research work, the segregation of metal impurities is the principle mechanism for Al due to the higher solubility in the Al-Si layer (Ferro & Derby, 1995).

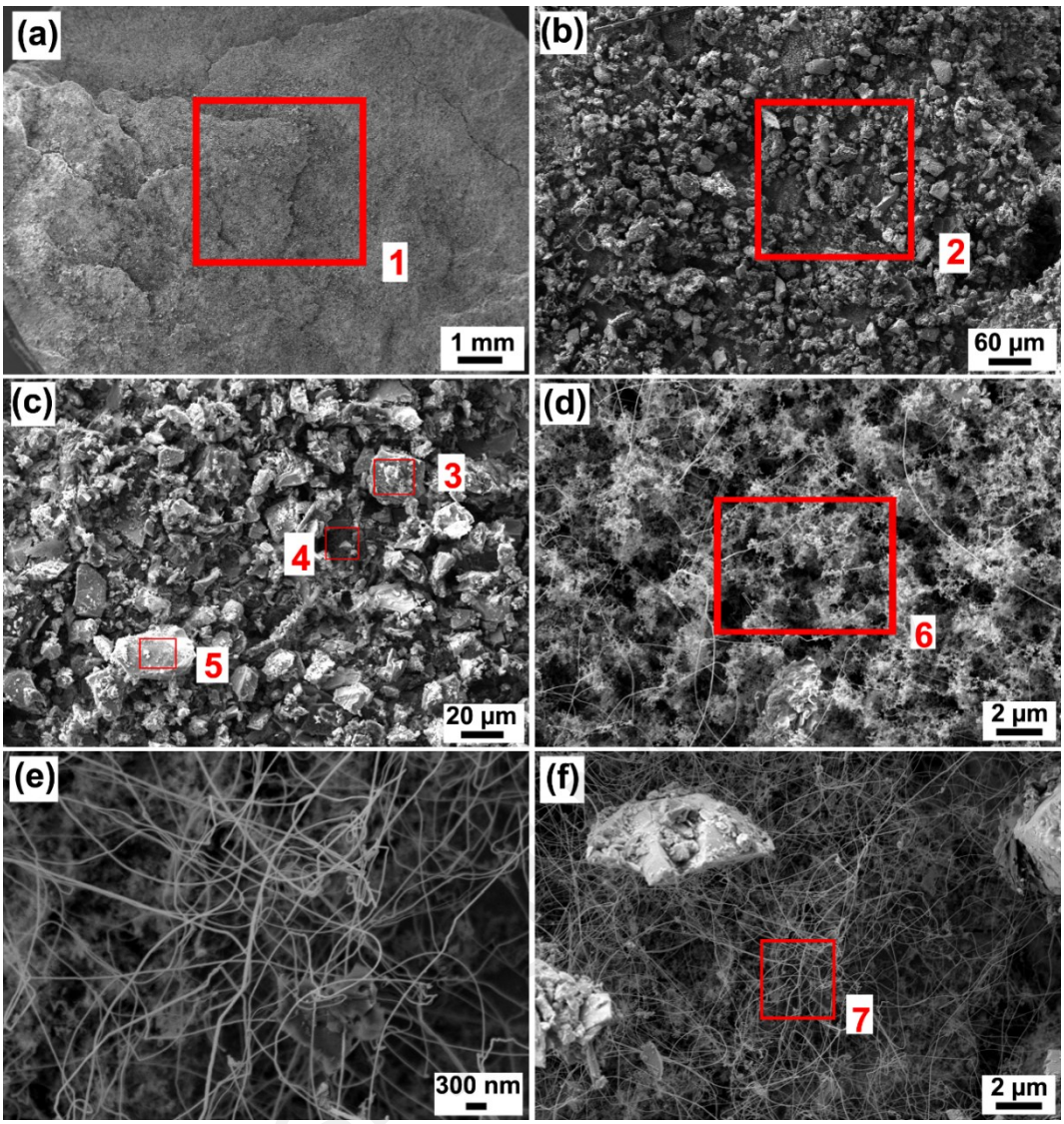

Figure 7.25: FESEM micrographs and EDAX elemental analyses of a Si-C pellet removed from the tube of a centrifugal thermite-assisted reaction: (a) overall topography; (b), (c), and (d) microstructure of typical points; (e) and (f) high magnification of region (d)

Figure 7.25 (d), (e), and (f) displays what the main structure of the specimen looks like, with mostly non-structured content and networks of Nanowires and whiskers. The elemental analysis describes the material as mainly an oxide phase. More silicon dioxide Nanowires formation was expected. The Nanowires net shape and orientations indicates that centrifugal force helped the wires to form in a directional path from the bottom to the top of the specimen.

Table 7.10: EDAX elemental analysis of different points on the Si+C pellet

Figure	Spotted area	Si	C	O	Al
(a)	1	46.15%	47.17%	6.20%	0.48%
(b)	2	51.49%	45.01%	3.04%	0.47%
(c)	3	88.15%	11.05%	0.80%	-
(c)	4	56.59%	33.13%	9.48%	0.80%
(c)	5	84.12%	8.96%	6.26%	0.67%
(d)	6	52.71%	24.38%	22.16%	0.75%
(f)	7	80.88%	10.02%	8.20%	0.90%

The X-ray diffraction pattern of a Si-C pellet that was exposed to thermite heat (front side) and not exposed to thermite heat but was affected by molten Fe flowing from the side of pellet between the pellet and crucible engraved area (rear side) is plotted in Figure 7.26. The corresponding phase quantification of both sides is additionally presented in Figure 7.27.

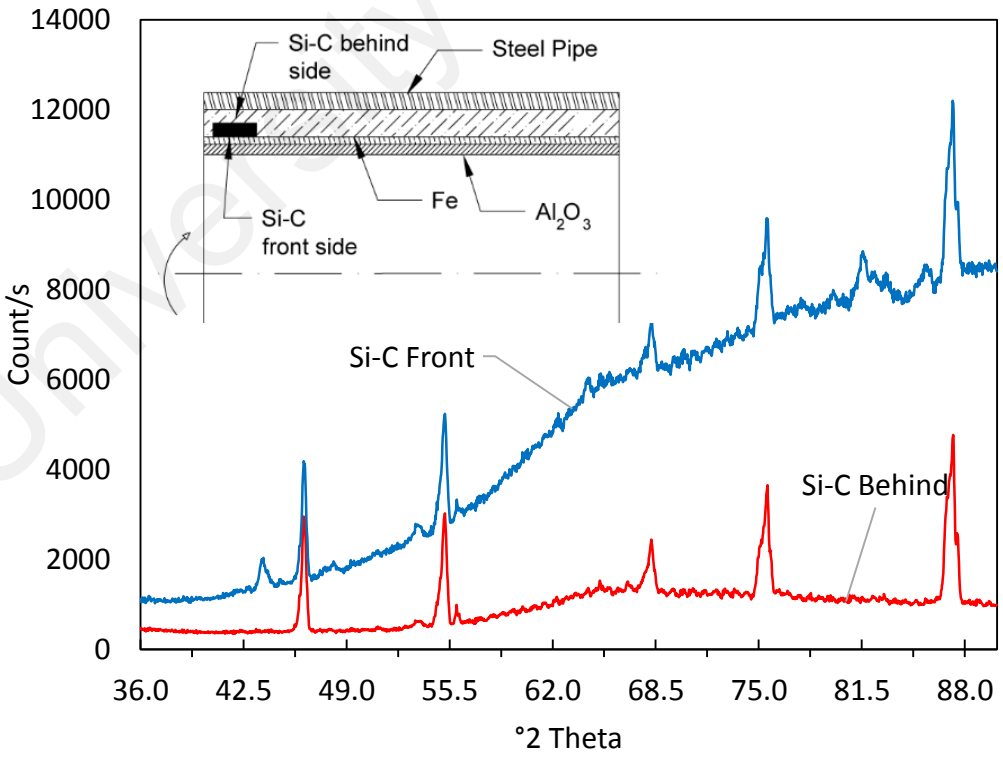

Figure 7.26: XRD pattern of Silicon-Carbon pellet after exposure to centrifugal SHS

It is clear in Figure 7.26, that unlike the Ti-C pellet, the Si-C pellet did not partake in the chain reaction following the thermite reaction since there were no significant bi-products (e.g. SiC, FeSi, etc.) detected in the XRD pattern. The XRD pattern revealed a highly amorphous sample content. Amorphous, or poorly crystalline materials, do not contribute to diffraction peaks, and so they cannot be determined by the Rietveld quantification method (Hill & Howard, 1987). Figure 7.27 illustrates only the crystalline material portion as established by Rietveld quantification. The only significant phase change that occurred in the specimen is alumina and FeSi. Again, this phenomenon is a result of the rapid heat dissipation, which disallows crystallization.

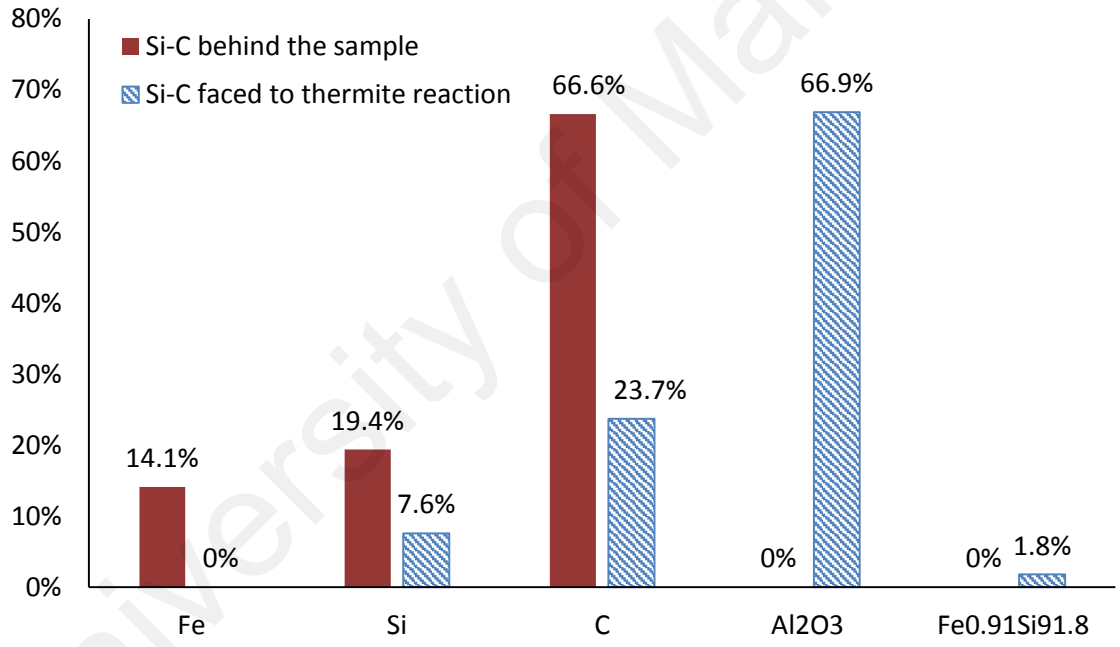

Figure 7.27: Phase quantification of the as-sintered Si-C specimen for the front and back sides

Though iron is reportedly highly soluble in liquid aluminum and its alloys, it has very slight solubility in the solid state (max. 0.05 wt%, 0.025 atom%) and so it tends to combine with other elements to form intermetallic phase particles of various types. In the absence of Si, the dominant phases formed are Al_3Fe and Al_6Fe, but in the presence of Si, as in the most widespread foundry alloys, the hexagonal Al_8Fe_2Si phase and the monoclinic/orthorhombic Al_5FeSi phase (also reported as $Al_{4.5}FeSi$ stoichiometry) are

dominant (Taylor, 2012). However, in this experiment aluminum was consumed in the iron reduction from Fe_2O_3. Consequently, the majority of the starting Al was converted into alumina. There were small amounts of Al traced throughout the specimen. Some of the Al diffused into the Si+C pellet and formed an intermetallic compound. However, the quantity of Al containing an intermetallic compound is quite poor according to the XRD results (Figure 7.26). The XRD outcome also suggests that the heavier material composed of Fe and its intermetallic compound was trapped at the bottom of the pellet.

It is evident that the requirements of Si-C combustion synthesis reaction were not satisfied to start the reaction and propagate along the specimen. This behavior conforms to a report by Schubert and Hüsing (2005). As explained earlier, SHS reactions are characterized by adiabatic combustion temperature T_{ad} that can be calculated by assuming that the enthalpy of the reaction heats the products and no energy is lost by heating the surrounding environment.

Hence, T_{ad} is a measure of the exothermicity of the reaction and defines the upper limit for any combustion system. Empirically, if $T_{ad} < 1200^{\circ}C$, combustion does not occur, and if $T_{ad} > 2200^{\circ}C$, self-propagating combustion occurs. In the range of $1200 < T_{ad} < 2200^{\circ}C$, a combustion wave cannot propagate but can be made to do so by special means such as pre-heating the reactants. For example, the reaction $\mathrm{Si + C \rightarrow SiC}$ $\left(T_{ad} = 1527\ ^{\circ}C, T_{ad} = 1300\ ^{\circ}C\right)$ is not a self-sustaining reaction (Schubert & Hüsing, 2005). Nevertheless, in the current method, it was not feasible to pre-heat the reactants. Because this technique is a combination of a centrifugal thermite process and a SiC SHS process, it leads to pre-mature reaction and may cause catastrophic incidents during high velocity rotation from a safety point of view. Therefore, synthesizing SiC from the thermite reaction heat under centrifugal acceleration using method (2) was not successful.

7.5 Ti-C-Al-Fe/TiN composite product under thermite centrifugal method (3)

The microstructure micrograph of two typical surface points of specimen SM09 is given in Figure 7.28. The corresponding elemental spectrum 1, 2 and 3 of the identified points is depicted in the figure as well. In accord with SEM observation and XRD results, the product did not form completely as it was designed. The physical shape of the pellet was not altered during the reaction.

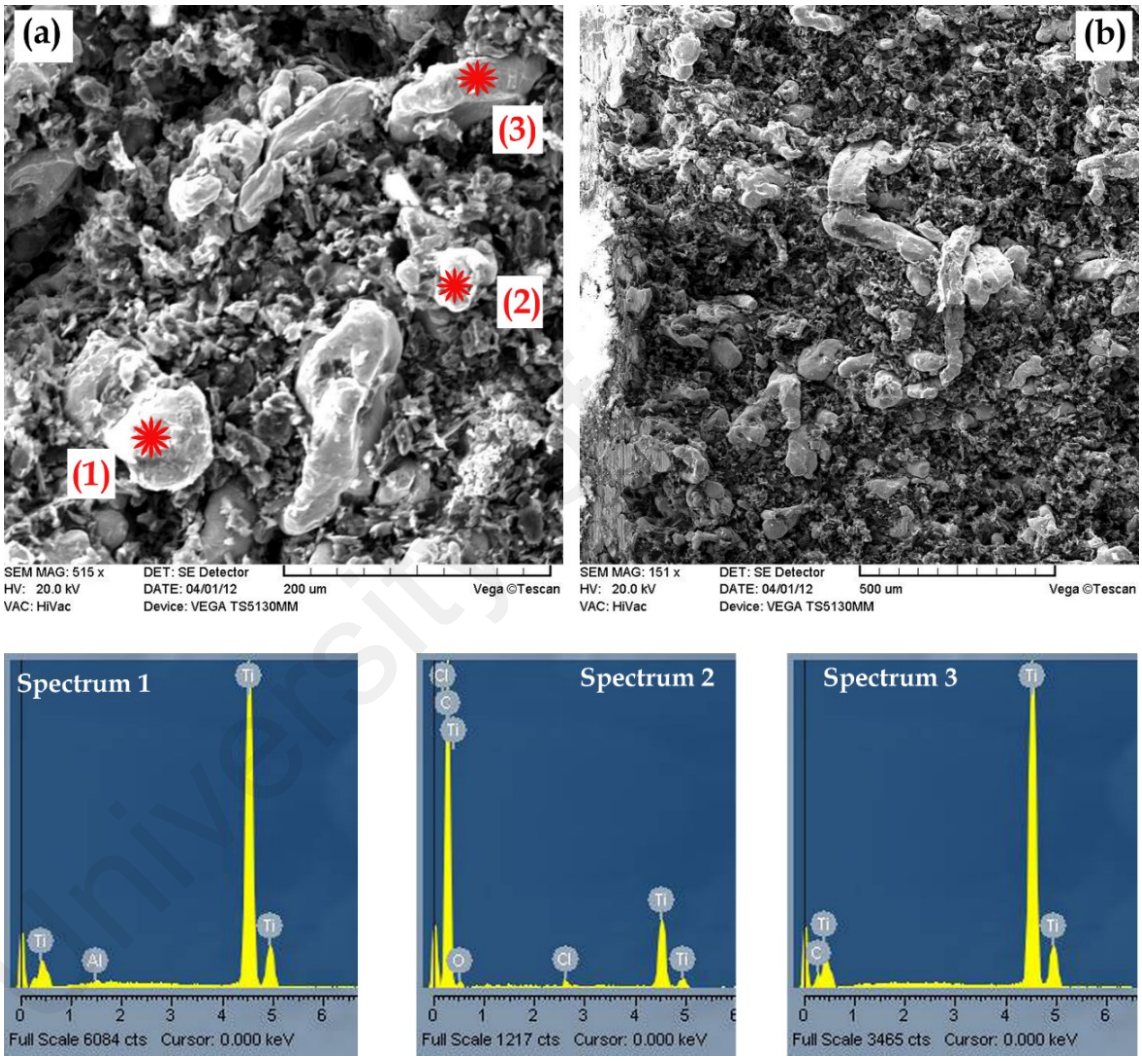

Figure 7.28: SEM micrograph and elemental analysis of the Ti+C surface

The process mainly affected the specimen's surface, as the product was exposed to thermite bi-products and hot fumes. The Ti+C pellet that exposed to extreme thermite reaction conditions is displayed in Figure 5.8 (a). The microstructure indicates that the specimen did not completely convert to a secondary product. Some surface areas

remained unaffected by the thermite reaction heat. The EDS of the corresponding region shows that aluminum and oxygen elements are not present in all EDS readings. In addition, a single TiC phase was detected by EDS (spectrum 3). The presence of the Cl element may be indicative of environmental contamination. Iron was not detected in EDS, since it only focused on a small area. The sample's surface was crushed easily using sandpaper. The crushed material was taken for XRD analysis.

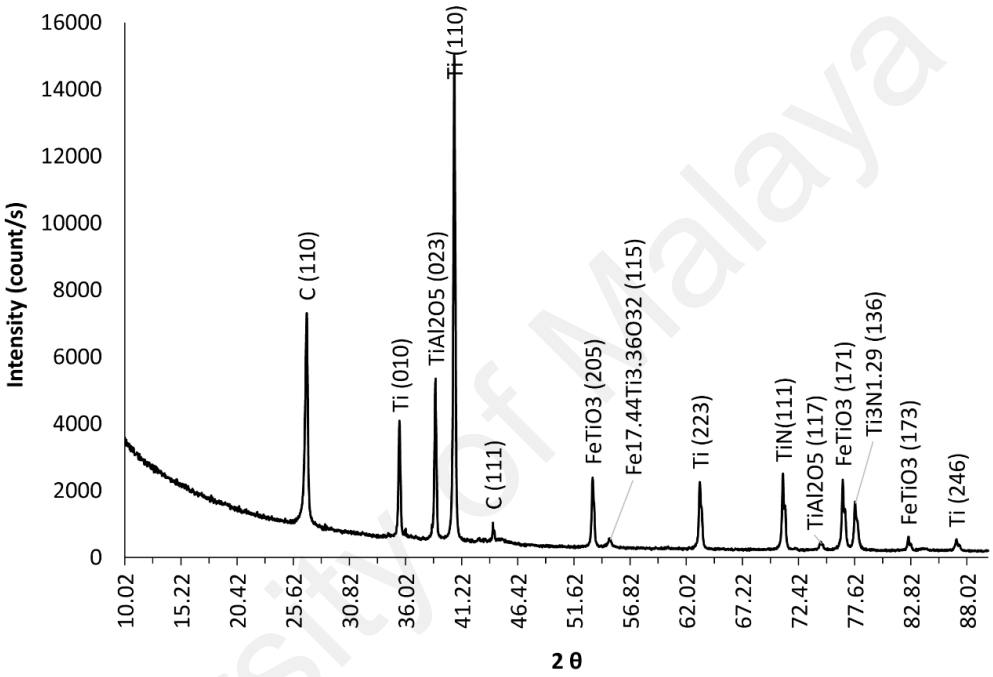

Figure 7.29: X-ray diffraction pattern of the sample surface

The XRD diffraction pattern and its JCPDS card list are illustrated in Figure 7.29 and Table 7.11, respectively. In accordance with XRD analysis, two other interesting phases formed during reaction, namely titanium nitride phases with (3/1.29) and (1/1) stoichiometry ratios. Since the experiment was conducted in an open-air environment, the source of nitrogen was expected to be from the surrounding. As the ignition temperature of titanium nitride (1100 ˚C) is lower than for titanium carbide, a reaction would be self-sustaining in the absence of preheat when T_{ad} should not be less than 1,527 ˚C (Liang et al., 2012; Maslov et al., 1978). Then, the titanium nitride grabbed the completion and reacted with the highly reactive titanium instead of the carbon (Moore & Feng, 1995). Ilmenite and titanomaghemite formed as a result of exposure to fumes from the thermite

reaction. Ilmenite is a magnetic titanium-iron oxide mineral, which is weak in structure and has been found as an oxygen carrier in chemical-looping combustion applied in fuel processing technology.

Table 7.11: JCPDC card reference list and their weight fractions

Ref. Code	Score	Compound Name	Chemical Formula	Weight Fraction
96-900-8518	23	Titanium	Ti	50.0%
96-900-8570	10	Graphite	C	22.3%
96-900-1115	12	Titanomaghemite	$Fe_{17.44}\ Ti_{3.36}\ O_{32}$	2.5%
96-101-1317	15	Osbornite	Ti N	1.8%
96-110-1045	13	Titanium nitride (3/1.29)	$Ti_9\ N_{3.87}$	5.5%
96-100-0061	7	Aluminium pentaoxotitanate	$TiAl_2O_5$	14.1%
96-101-1034	8	Ilmenite	$FeTiO_3$	3.8%

It has been reported that in instances of direct contact between molten Fe and Ti+C, the ceramic particle size and adiabatic reaction temperature markedly decrease (Zhang et al., 2011). This means that less thermal energy would be required for synthesis. Some XRD peaks display the presence of Fe element in the compound, comprising approximately 6 % of the product. Because an arbitrary spot was used for observation under SEM and EDS, no Fe was detected in the EDS spectrum. The SEM/EDS results (Figure 7.28), XRD pattern (Figure 7.29) and phase quantifications express the starting material and the percentage of final product formations. The TiC phase was not created mainly for the lack of steady-state heat generation and conduction through the specimen.

According to phase identification and quantification of the XRD results (Figure 7.29), 72% of the starting powders remained unreacted. The desired product of TiC and intermetallics did not form at all. Instead, 14% of the pellet surface phase changed to a

$TiAl_2O_5$ composite phase. The alumina originated from the thermite product as a fume that diffused into the Ti+C pellet.

The reason why TiC did not form as much as in earlier experiments (engraved in crucible, method (2)) was the lack molten Fe flowing toward the specimen and the steady state heat generation and conduction through the specimen. In the case of TiC combustion synthesis with Fe, adding Fe content to the system markedly reduced the adiabatic reaction temperatures (Zhang et al., 2011). Essentially, less thermal energy would be required to synthesize TiC.

In order to investigate the mechanical properties of as-cast matrix materials and composites, the specimen was examined with a Shimadzu micro-hardness tester, whose parameters were 98.07 mN load and 5 s holding time. The average microhardness result was 796.6 MPa, demonstrating that the product was not well densified or conformed to the characterization data.

7.6 SiC processing using plasma-assisted centrifugal method (4)

The as-sintered Si-C pellet, SM10, was removed from the specimen holder for characterization. SEM and XRD was performed at the top side of the specimen where it was closer to the axis of rotation. It is assumed that is where the most phase changes and transitions occurred. The morphology and microstructure analysis of the specimen are depicted in Figure 7.30. The X-ray diffraction pattern and corresponding phase quantification of the as-sintered specimen is analyzed in Figure 7.31.

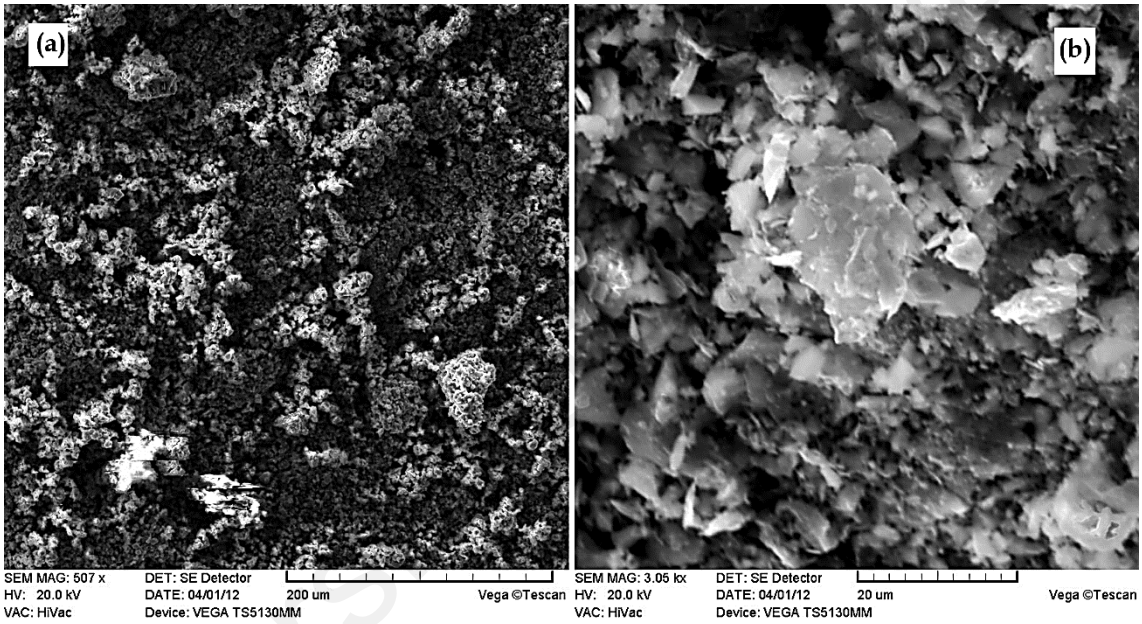

Figure 7.30: SEM micrograph of a Si+C sample exposed to centrifugal plasma method

Figure 7.30 (a) is a lower magnification of the specimen, showing a relatively porous structure. This sort of porous structure is an inherent property of pressure-less or low pressure powder processing. Figure 7.30 (b) shows that very fine microstructures formed but in relatively the same direction as the crystals. The crystals were unidirectional toward the axis of rotation.

The XRD analysis of the specimen signifies that only 3 % of the starting material took part in phase formation and the rest was not affected by the plasma field. The experiment was designed to produce the most possible silicon carbide (SiC). From the XRD phase

quantification, Rietveld analysis was able to estimate around 1% the SiC phase formation. About 2% of SiO_2 formed as well. When the graphite electrode came into contact with the specimen holder, the arc and plasma state formed due to the presence of argon around the electrode. The frequency of this formation is nearly 15 per second as the rotation speed was roughly 15 revolutions per second (RPS). Concerns with objects flying out from the reaction chamber limited the rotation speed. Therefore, specimen cooling was faster than the heating source. According to literature, Si requires sufficient time to dissolve the C component inside and form SiC (Narayan et al., 1994). The Moissanite 3C (SiC-3C) is stable between 1400 and about 1600 ˚C. This range indicates the temperature for silicon carbide formation (Schmalzried & Schwetz, 2010).

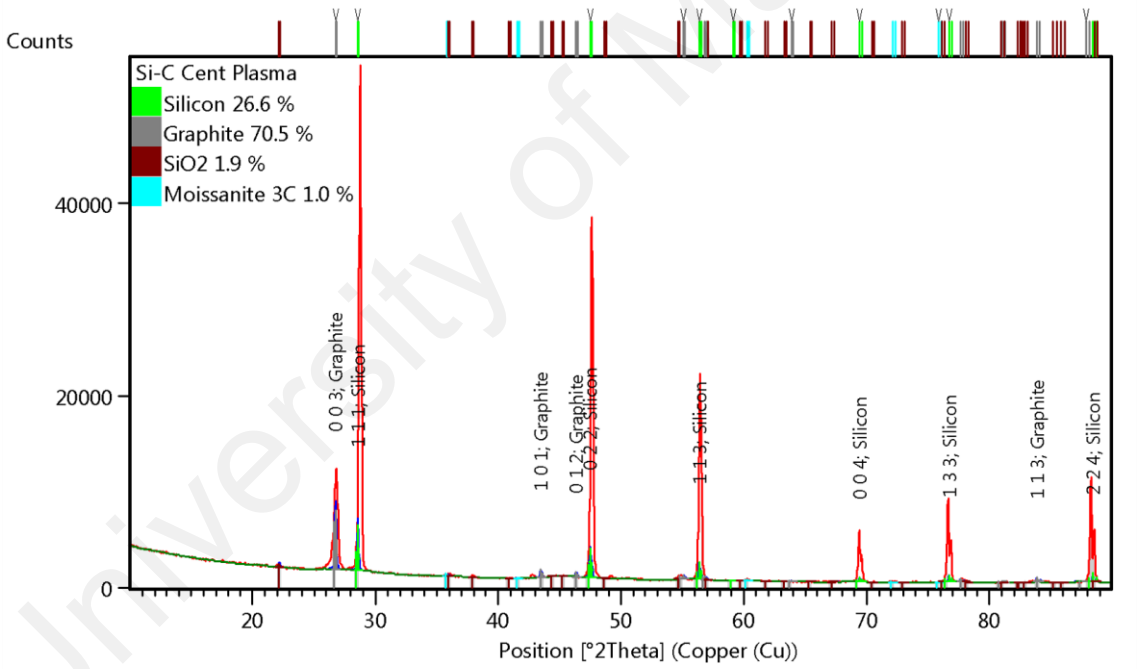

Figure 7.31: X-ray diffraction pattern of a sample exposed to centrifugal plasma method

Nevertheless, the reaction occurred in atmosphere with argon purging the chamber; the oxygen gas remained in the chamber. Additional oxygen could enter, as the pipe head (chamber cap) was kept open for the process devices to come into contact. Therefore, phases of silicon dioxide were detected in the XRD pattern.

7.7 Evaluation of M+C in DC-focused plasma arc processing method (5)

Two experiments are discussed in this section, including Ti+C and Si+C pellet processing exposed to massive heat generated by plasma. SM02 concerns the possibility of SiC processing under plasma condition and SM03 is for TiC processing.

7.7.1 The Effect of field plasma SHS reaction on SiC crystallization

Tungsten contamination was observed in a preliminary study that used a tungsten electrode as the plasma-generating component. Using a graphite electrode of the same carbon element content of green mixture would be helpful in reducing contamination during the high temperature course taken by the electrode. The thermal profile of the SiC plasma reaction is illustrated in Figure 7.32.

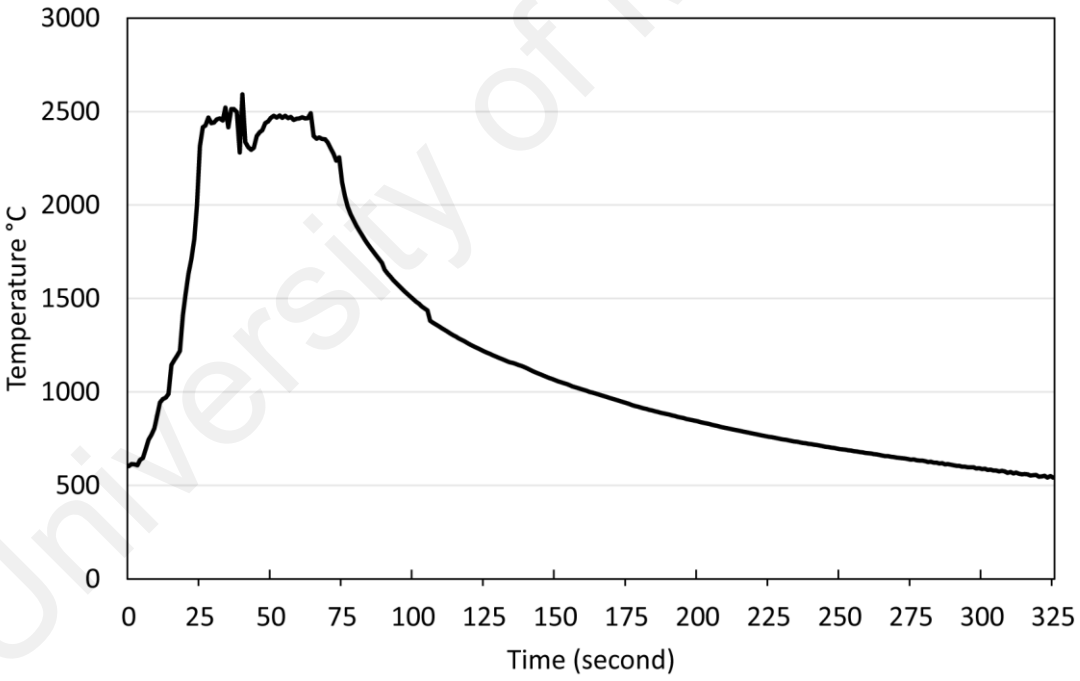

Figure 7.32: Time-Temperature heating and cooling profile of SiC plasma reaction

The laser spot was fixed to monitor specimen temperature. It shows how fast the temperature increased to around 2500 ˚C, after which it was kept relatively constant for about 50s. Finally, the plasma was turned off and the specimen allowed cooling down to

ambient temperature. In order to face the least oxide formation, the argon shielded the specimen before the plasma initiated and until it completely cooled.

The as-sintered SiC product was removed from the crucible for characterization and observations. The product was light green in color. The microstructure and morphology of the specimen is shown in Figure 7.33. Figure 7.33 (A), (B), and (C) was taken from an area directly exposed to the plasma zone. It is evident that the high thermal gradient affected the crystal and let it grow thin with multidirectional structures but size as broad as 240 μm. The reaction time had significant effect on crystal size as well as electrode type. Large, faceted, cubit SiC crystals formed in experiment SM02.

Figure 7.33 (D), (E), and (F) portray the microstructure of an area that was 6 mm from the head of the specimen. Although the chamber was purged with argon gas and the plasma did not directly attack the green mixture, some nano size oxide spots were detected in FESEM micrograph. The nano-oxide spots may have ensued due to entrapped air in the pellet during the compaction process. The elemental analysis of parts (B) and (F) from Figure 7.33 is depicted in Table 7.12. This table denotes that the white dots in parts E and F are mainly oxide and part (B) is a pure combination of Si and C as SiC.

Table 7.12: EDAX elemental analysis corresponding to Figure 7.33

Element	Part F	Part B
CK	9.96	52.34
OK	6.42	0
SiK	83.63	47.66

The X-ray diffraction pattern of the specimen's surface is depicted in Figure 7.34. From the XRD pattern, it is evident that 98.7% of surfaces are Moissanite 3C with a cubic structure. As the green mixture was prepared in accordance with the stoichiometric chemical formula, the presence of extra graphite with a hexagonal structure amounting to

about 1.3% is due to the carbon electrode decomposition and deposition on the specimen surface during plasma.

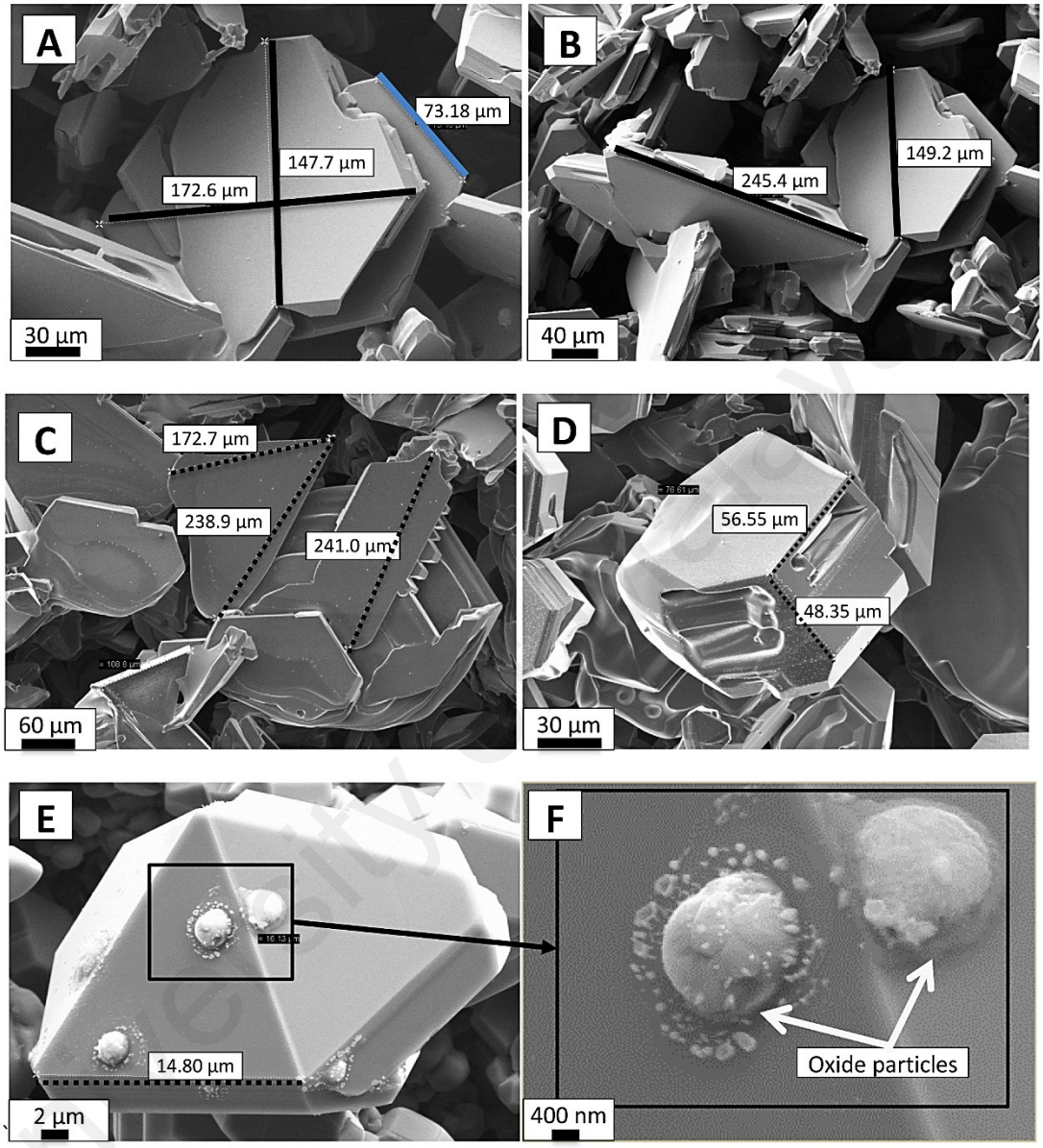

Figure 7.33: SiC crystals prepared using Reaction Chamber of Plasma Arc System (method 5)

According to Schmalzried and Schwetz (2010) SiC-3C silicon carbide forms between 1400 and about 1600 ˚C and SiC-15R above 2200 ˚C. Since the acquired temperature was above 2200 ˚C, achieving some SiC-15C was expected. It was also possible for product phase to change during the process of cooling and least possible the formation of silicon

carbide at 1400 ˚C for SiC-3C, then stabled at that phase which was later detected by XRD.

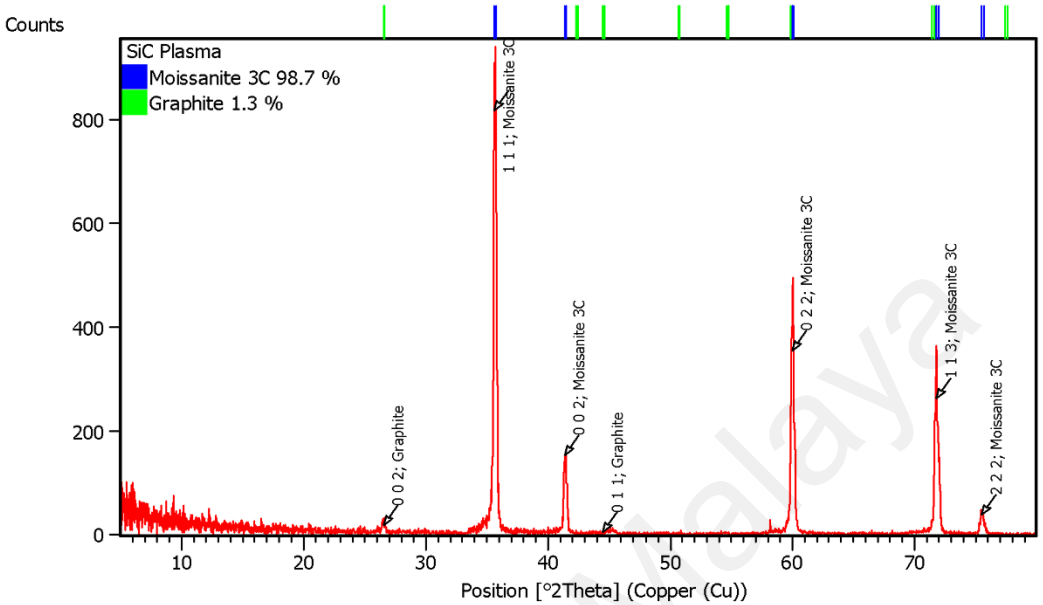

Figure 7.34: X-ray diffraction pattern of SiC specimen prepared using method (5)

Technically, it was not possible to measure the mechanical properties of the processed SiC because of the highly porous condition. The high residual porosity of SiC imposed a limitation in terms of mechanical strength (Washburn & Coblenz, 1988). This method successfully produced high-purity silicon carbide from silicon and carbon as starting reactants.

7.7.2 Titanium Carbide synthesis under normal gravity using plasma arc

From the macroscopic observation, it was found that the round compacted pellet shape was distorted under high temperature. There was no remaining sharp edge. The sample was exposed to the ultra-high temperature condition above the melting point of TiC. The boiling point of TiC is reportedly 3100 °C (Tong & Reddy, 2005). The pellet was sectioned using a low speed diamond wheel cutter. Then the sample was ground and polished using a Böhler grinder device. The microstructure of various points was studied by field emission scanning electron microscopy (FESEM) equipped with energy dispersive X-ray spectroscopy (EDAX). Figure 7.35 shows the morphology of a typical surface area, and the cross-section of the product.

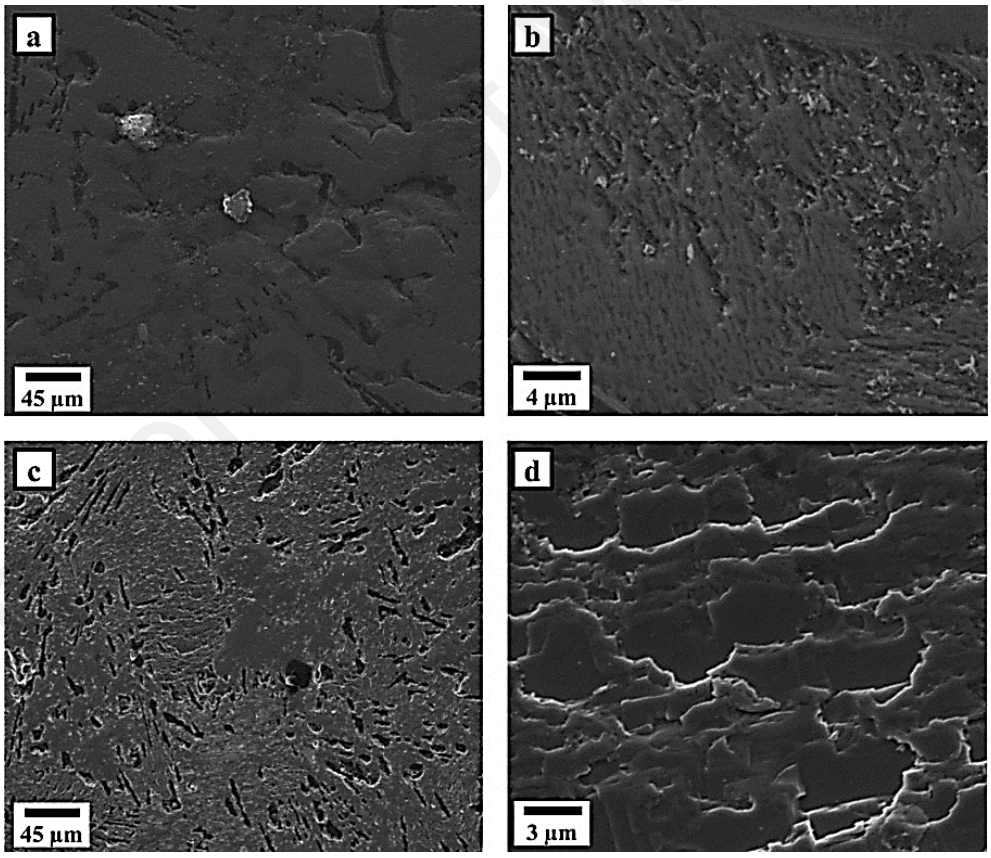

Figure 7.35: FESEM micrograph on a typical point of (a), (b) surface, and (c), (d) cross-section view of the TiC product

The EDAX analysis relatively shows the formation of an almost uniform elemental composition of Ti and C in the area (Table 7.13). Figure 7.35 (a) represents a typical point

at the top surface of the polished product at 500X magnitude. Figure 7.35 (b) depicts a higher magnification 6000X of the TiC product with the lined crystals with respect to plasma zone. Figure 7.35 (c) and (d) illustrate how the layers of molten TiC formed and solidified under 500X and 8000X, respectively. It is understood that after the TiC product formed in the early seconds. Then as the sample was kept exposed to the ultra-high temperature of the plasma, it had enough time to re-crystallize and assemble the crystals layer-by-layer (Figure 7.35 (d)).

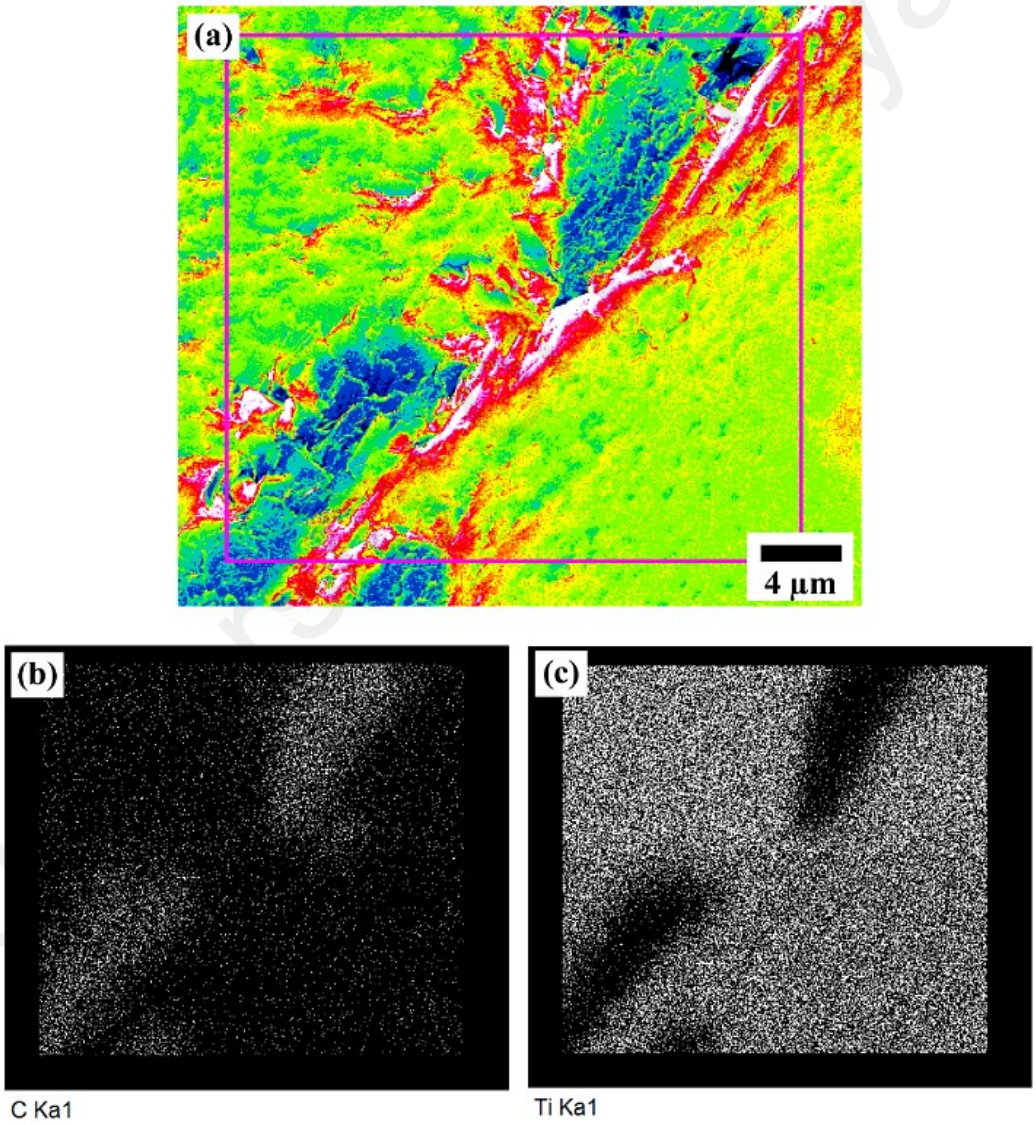

Figure 7.36: Elemental mapping spectrum of the TiC/C composite cross-section

Figure 7.36 shows the elemental distribution maps of the titanium and carbon content, as all elements are analyzed and normalized. The elemental maps for Ti and C show high homogeneity and correlations between elements, indicating the presence of very small-sized minerals. Figure 7.36 (a) depicts an electron image of the typical area for elemental distribution mapping. Figure 7.36 (b) and (c) represent the C and Ti elements, respectively.

The quantitative elemental analysis (EDAX) of the sample cross-section corresponding to Figure 7.36 is given in Table 7.13. Here, it can be seen that the stoichiometry ratio (weight %) of the participating elements changed and deviated from 50%.

Table 7.13: Quantitative elemental analysis (EDAX) of the sample cross-section

Element	Weight%	Atomic%
C K	42.40	74.50
Ti K	57.60	25.50
Totals	100.00	

Figure 7.37 represents the X-ray diffraction pattern (XRD) of the as-sintered product. The XRD pattern displays a very well crystallized product. The most intense peak is detected at $2\theta = 41.68^{\circ}$ with a (0 2 2) plane representing TiC. In addition, very faint C peaks were observed in the patterns. According to the Rietveld method, TiC and C content of this sample were determined to 87.3 vol%, and 12.7 vol%, respectively.

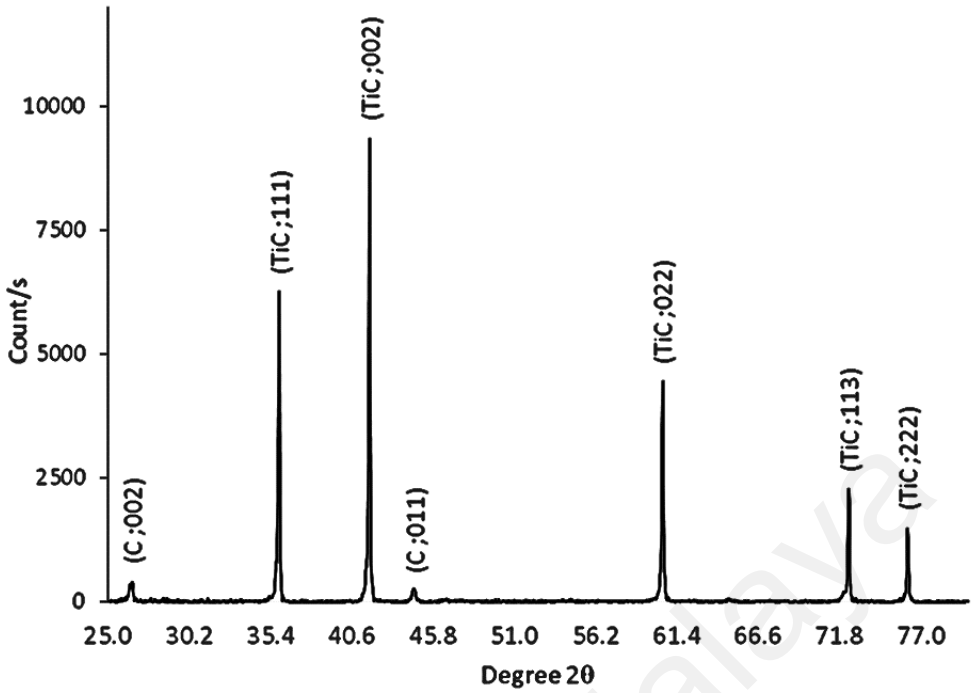

Figure 7.37: The XRD diffraction patterns obtained for the TiC product

The average crystallite size was estimated from the Scherrer equation (Pecharsky & Zavalij, 2009) after synthesis to 1862Å and 1731Å for TiC, and for C was 222, 169Å.

Table 7.14: TiC/C composite peak list calculated using X'Pert software

No.	Pos. [°2Th.]	d-spacing [Å]	Height [cts]	Crystallite Size only [Å]	Micro Strain only [%]	Phase
1	26.4314	3.36937	405.84	222.494	0.757	C
2	35.8876	2.50029	6620.09	1205.198	0.104	TiC
3	41.6846	2.16499	7418.29	1299.488	0.083	TiC
4	44.5237	2.03331	68.56	169.030	0.601	C
5	60.4398	1.53044	4123.98	1730.970	0.044	TiC
6	72.3511	1.30501	2230.16	1861.950	0.035	TiC
7	76.1258	1.24942	1249.53	1186.392	0.053	TiC

7.7.2.1 Mechanical Properties

Micro-hardness measurements were carried out at various points several times. The hardness reading information is plotted in Figure 7.38. In the current experiment an average Vickers's hardness of 3446 HV/4.903 N (33.79 GPa), with a maximum of 3660

HV/4.903 N (35.89 GPa) and a minimum of 3250 HV/4.903 N (31.86 GPa) was recorded. The product's hardness is on the verge of super-hard material classification.

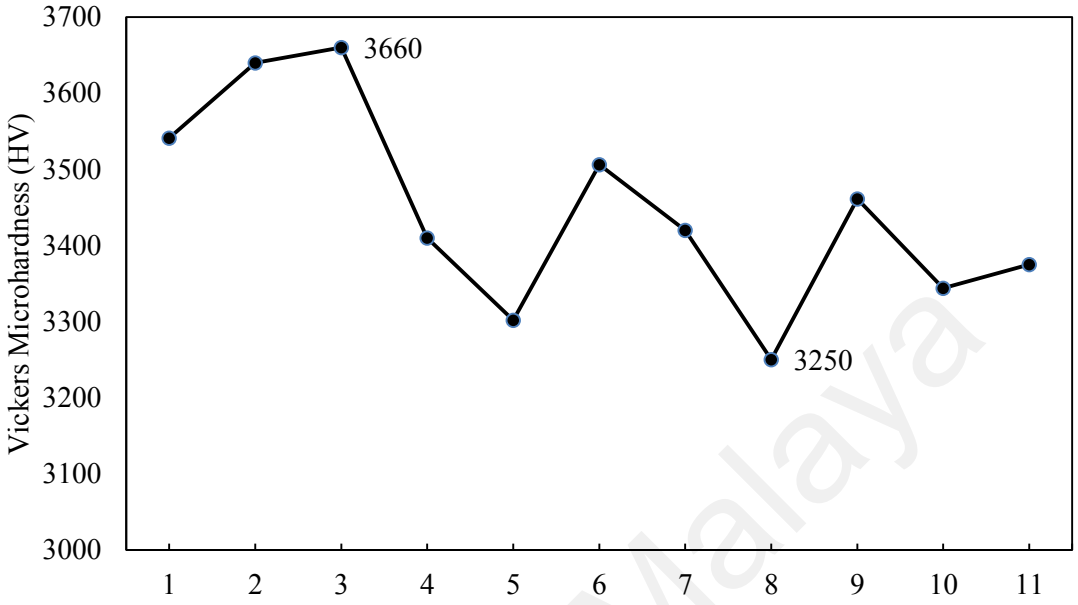

Figure 7.38: Micro-hardness measurement of TiC/C composite

Evidently, hardness variation is directly related to phase distribution and pore concentration. It has also been reported that this variation can be due to a partial elastic recovery of the imprint when removing the load (Brazhkin & Lyapin, 2005). Therefore, the 10 s dwell time was maintained to have enough relaxation time for less elastic recovery.

7.7.2.2 Nano-indentation

The indentation was measured for five different random locations on a specimen's cross-section. The average Young's modulus, E_{it}, was 212±32 GPa. A typical load-unload curve of an indentation is shown in Figure 7.39. The calculated Young's modulus is almost half of that reported for a TiC single crystal (Chermant et al., 1978; Riedel, 2000). The significant difference may be attributed to the micro and macro porous structure and defects of the product. Reducing the Young's modulus would significantly affect the toughness of the material.

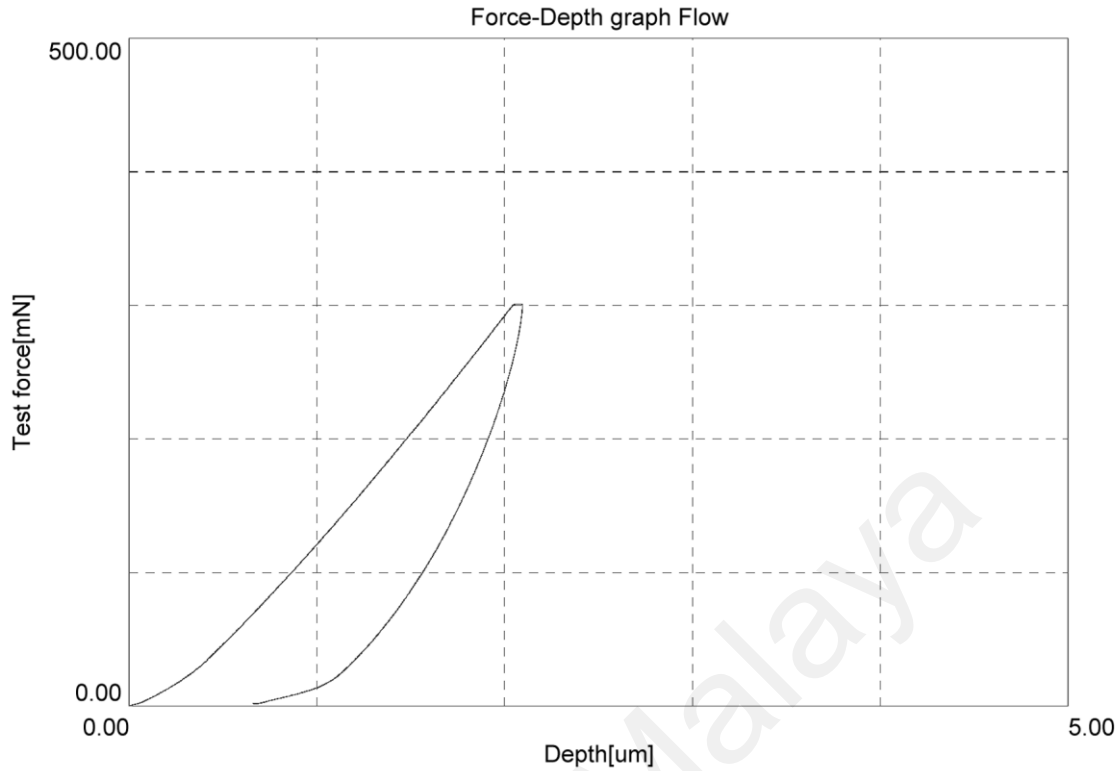

Figure 7.39: A typical force-displacement graph of load-unload for a TiC-Fe composite specimen

7.7.2.3 Fracture toughness

The length 2c of the pair of cracks caused by Vickers indentation was measured immediately after removing the indenter. In the case of c/a > 2.5, half-penny shaped crack patterns were generated, as proposed by Anstis et al. (1981) and the K_{IC} is calculated according to Eq. 3.5:

where E_{it} represents the elastic modulus (GPa) determined using Nano-indentation (Ave. E_{it} = 212 GPa), H is the hardness (Ave. H = 27 GPa), P is the applied load (P = 4.903 N), and *c*is the parameter of the Vickers indentation mark (μm) (Ave. c= 35 μm).

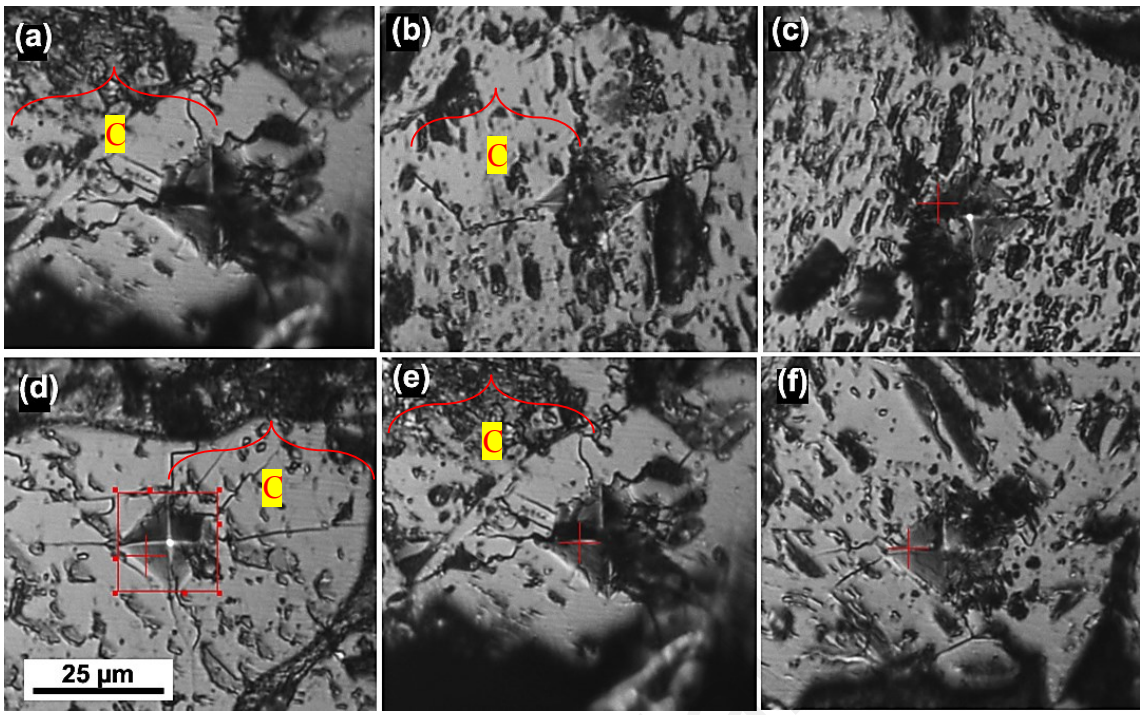

Figure 7.40: Vickers marks of six different locations on the cross-section of TiC/C composite

In the literature, the fracture toughness of a single crystal titanium carbide is reported from 1.7 to 3.8 MPa·m$^{1/2}$ (Chermant et al., 1978) and for a composite of Ti_3SiC_2 it is reportedly 14 MPa·m$^{1/2}$ (Wang et al., 2013). However, in the current study the fracture toughness obtained is K_{IC} = 0.87 MPa·m$^{1/2}$, which is very small compared with reported works. This can be due to the micro and macro porous structure of the TiC/C composite material. The presence of a carbon-carbon phase clearly affected the composite.

By combining Figure 7.37 (XRD analysis), Figure 7.36 (elemental distribution maps), and Figure 7.38 (micro-hardness), it can be interpreted that the unreacted carbon content is very well distributed in the product and in some parts it is found in higher concentrations, potentially owing to the highly localized energy transport. The micro-hardness value variations in the specimen could be due to unreacted carbon concentrations. The stoichiometric TiC hardness has been reported to have a value of up to 3200 HV (31.38 GPa) (Ding et al., 2013; Tjong & Ma, 2000). In the present study, the highest micro-hardness was 14% higher than reported. Therefore, the existence of a

crystallized C (0 0 1) and (0 1 1) plane enhanced the product's hardness properties. However, the fracture toughness (K_{IC} = 0.87 MPa·$m^{1/2}$) and Young's modulus (E_{it} = 212 GPa) have smaller values compare with literature.

7.8 Summary of experimental results

The summary of the five implemented methods is provided in Table 7.15. The current study results show that the centrifugal in-situ processing is comparable with non-centrifugal in terms of mechanical properties. The fracture toughness considerably increased in contrast to the TiC/C composite (SM03).

Table 7.15: Result summary for the five implemented methods

Test code	Applied Method	Starting material	Success	HV (GPa)	K_{IC} (MPa·$m^{1/2}$)	Young's Modulus (GPa)
SM01	(1)	Fe_2O_3, Al	Yes	26.4	-	-
SM05	(2)	Ti, C, Fe_2O_3, Al	Yes	4.9-21.86	1.33-1.96	105-177
SM06	(2)	Ti, C, Fe_2O_3, Al	Yes	5.39-15.86	1.07-2.05	85-166
SM07	(2)	Ti, C, Fe_2O_3, Al	Yes	9.8-22.68	1.21-1.50	98-164
SM08	(2)	Si, C, Fe_2O_3, Al	No	N/A	N/A	N/A
SM09	(3)	Ti, C, Fe_2O_3, Al	No	0.80	N/A	N/A
SM10	(4)	Si, C	No	N/A	N/A	N/A
SM02	(5)	Si, C	Yes	N/A	N/A	N/A
SM03	(5)	Ti, C	Yes	33.8-36.6	0.87	212
SM04	-	Ti, C	Semi	0.56	-	65

N/A: not applicable to the method, perhaps due to the structure's weakness or large portion of unreacted material.

The TiC-Fe aluminide composite fracture toughness is lower than reported by Subramanian and Schneibel (1998) measured using the two- and three-notch method. However, their processing method was different from the present work. According to Table 7.9, the fracture toughness demonstrates a harmonic change with volume. It is clear

that the hardness of the TiC-rich area increased, while at the same time, the fracture toughness also improved compared with the Fe-rich area. The gradual changes from the layer joined with alumina (Fe-rich) to the TiC-rich area confirm an improvement of mechanical properties. Moreover, the fracture toughness is much higher than for the TiC/C composite (0.87 $MPa.m^{1/2}$).

Method (2) was successful in processing Ti+C as a starting material, while Si+C was not successful according to FESEM, XRD and mechanical properties. Method (5) was successful for both Ti+C and Si+C.

Moreover, the MSPH simulation results are in agreement with the experimental results obtained using method (2). As the viscosity of alumina increases faster than that of iron, and the iron was protected by alumina from outside heat exchange, the iron remains in a molten medium for a longer period than alumina. This phenomenon allows the iron particles to wet and infiltrate the TiC porous media and form a strong composite.

7.9 Safety issue evaluation in the centrifugal combustion synthesis method

Some flying particles were collected after an unprotected thermite reaction. As Figure 7.41 shows, the molten material froze on the external layer of the pipe. Figure 7.41 (a) illustrates a pipe head after a centrifugal thermite process, while Figure 7.41 (b) and (c) show the magnified area of the pipe head with frozen molten materials. These materials rapidly solidified on their way out from the rotating reaction chamber.

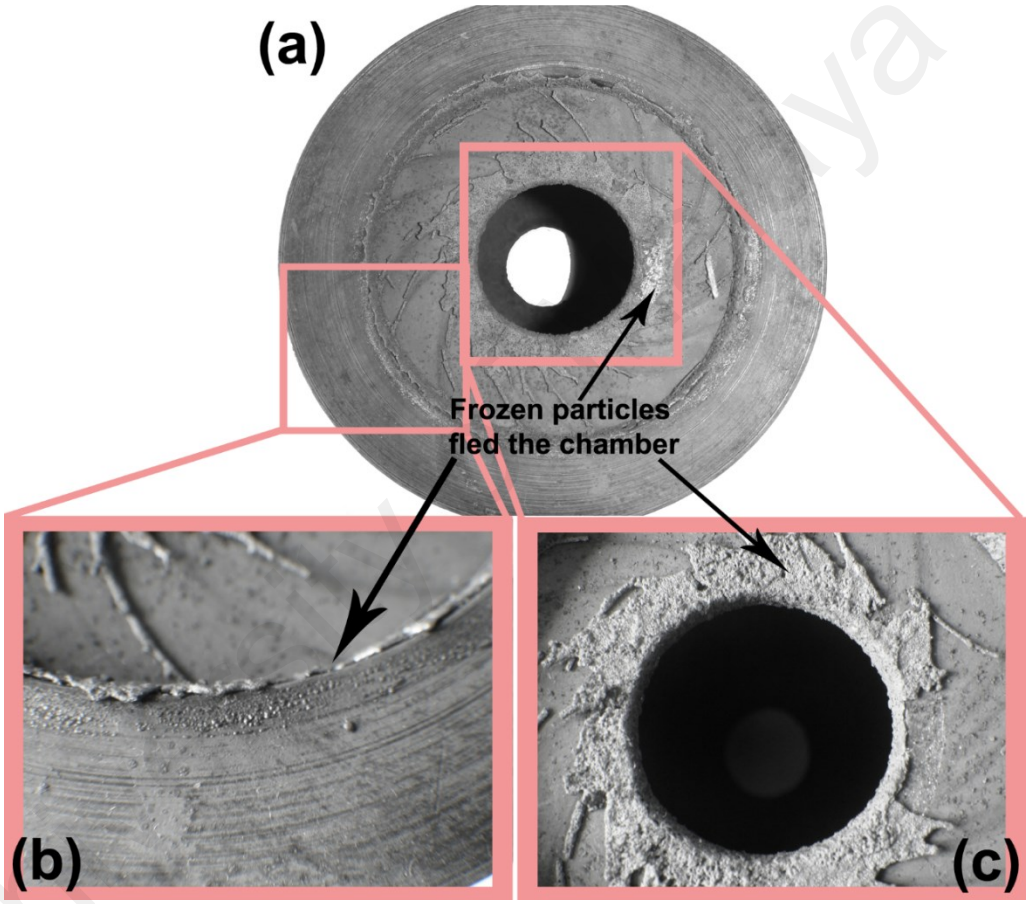

Figure 7.41: Condition of a pipe head with a cap installed after centrifugal thermite reaction

The material is sharp and the byproducts look dense. Because the reaction time is very short, a massive amount of molten material can leave the chamber if safety precautions are not considered. The process involves such an explosion, that some literature refers to it as a thermal explosion reaction (Filimonov et al., 2009; Horvitz et al., 2002).

It is anticipated that the same shape and material would fly out of the chamber at the time of reaction. The collected particles were analyzed using an X-ray diffractometer. The X-ray diffraction pattern of the thermite side-products is depicted in Figure 7.42. According to XRD analysis, the composition and phases of the material flying out of the chamber are alumina and iron. The speed of the particles has previously been determined. If we assume that the propagation rate is equal to particle speed, then the speed of particles leaving the reaction chamber is around 1.5 m/s (Odawara, 1990; Odawara, 2010).

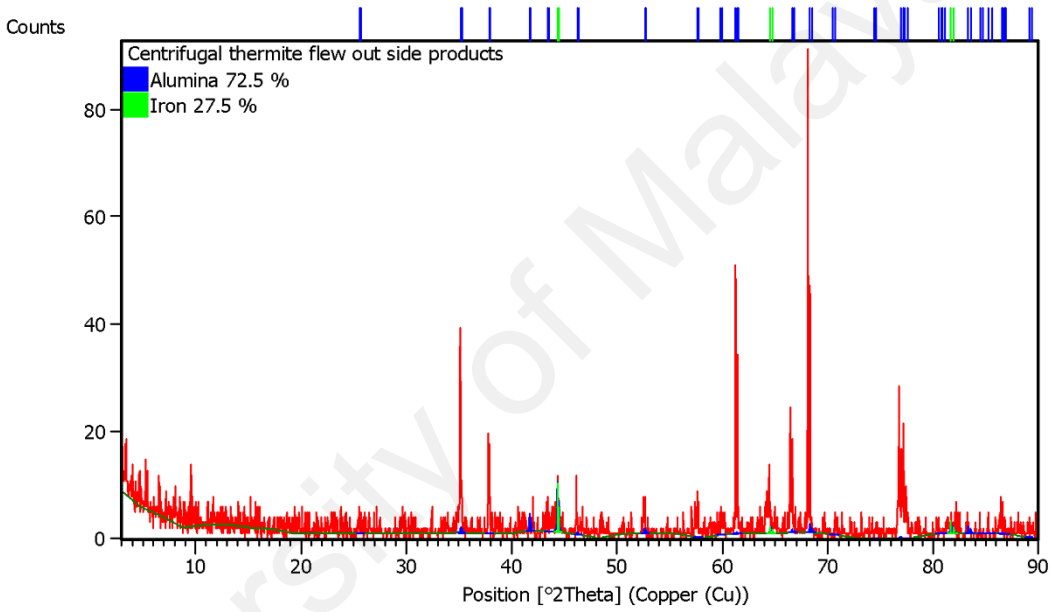

Figure 7.42: X-ray diffraction pattern of the thermite byproducts

CHAPTER 8: CONCLUSION AND SUGGESTION FOR FURTHER WORK

Five processing methods were developed and employed for the production of Ti and Si-based composites. All methods were evaluated and simulated to understand the mechanism of particle deposition. The most significant conclusions and suggestions for future work are mentioned in this chapter.

8.1 Conclusion

According to the experimental results, the following conclusions can be drawn for method (1), in which the conventional centrifugal thermite process was investigated:

1. The microstructure, composition, and elemental analysis revealed the phase formation of α-Al_2O_3 and Fe inside the carbon steel pipe, while the product's element concentrations and microstructures varied from point to point.
2. The structural setting at the metal-ceramic interface resulted in the formation of unexpected new phases not situated in density-gravity order after the separation process. A two-layered product, the most preferred result, was observed in region C - about 20 mm from the head of the pipe to the other pipe head with a maximum hardness value of 2765 HV.
3. In region A, the rapid solidification of the combusted product caused the high temperature gradient to re-melt and grains with high porosity in the dead spaces' corner areas of the pipe head formed.

The preliminary experiment on the Ti-C pellet revealed that in a rapidly cooling medium, not all the starting powder mixture can react and some remaining reactant powders have the potential to partake in another reaction. According to the experimental

results and simulations, the following conclusions can be drawn for method (2), where Ti+C and Si+C were embedded and exposed to a thermite reaction:

1. Joining the TiC product to Al_2O_3-Fe composite is possible using centrifugal-assisted SHS of aluminothermic reduction, and when combined with titanium and carbon reaction it formed a functional material in a single step.
2. The level of Fe infiltration into the TiC product of the specimen near the head of the pipe was greater and distributed better due to a higher heat gradient in that position.
3. The hardness value at the different product zones varied from point to point.
4. Mathematical modeling of particle deposition velocity and viscosity could describe the process of Fe infiltration versus time. Increasing melt viscosity due to decreasing temperature leads to significantly reduced speed of particle deposition onto TiC. The MSPH method provides very good estimation of velocity as well as velocity gradient of iron and alumina molten particles.
5. The MSPH estimated the magnitude of molten iron and alumina infiltration, depth, velocity and velocity gradient. The velocity gradient of particles revealed that product velocity decelerates as the viscosity increases versus time.
6. The mechanism of deposition and penetration of molten Fe into TiC during the two exothermic reactions of Fe_2O_3+Al and Ti+C under centrifugal force appeared to be dependent on density, temperature, and time profile, and can provide a model for the phase formation of a multi-layer product.
7. The observed reaction temperature of the centrifugal thermite-assisted combustion synthesis between Al and Fe_2O_3 was above 2925 ˚C. TiO_2 phases primarily formed after three days of exposure to a humid environment due to product surface corrosion. In-situ FGMs of TiC-Fe-Al_2O_3 with predefined

geometry and several intermetallic layers, mainly TiAl and Ti_3Al with improved mechanical properties, were successfully produced.

8. Processing SiC using method (2) was not successful, as not more than 1.8% of the starting material reacted. Therefore, this method is not recommended for SiC processing under the mentioned parameters.

The following conclusions can be drawn for the other processing techniques (methods 3, 4, and 5).

1. TiC processing using method (3), or applying thermite energy when the specimen was offset, was not successful, as the amount of product compared with the starting material was poor.
2. Processing SiC using method (4) was not successful and not more than 3% of the starting material reacted. Therefore, this method is not recommended for SiC processing using the mentioned parameters.
3. Titanium carbide-carbon (TiC/C) composite was successfully synthesized from starting elemental powders using self-propagating high-temperature synthesis technique in an ultra-high plasma inert medium (method 5). The micro-hardness of the product enhanced by 14%, whereas the Young's modulus and fracture toughness declined compared with literature.
4. Using Si+C particles as starting material could produce silicon carbide using method (5). The crystals seem to be broad in size and are faceted cubic shaped. Large crystals up to 270 μm were produced with the normal gravity plasma technique.

8.2 Suggestions for further work

- Local reinforcement can be directly inserted into a pipe side hole. Loading with thermite and running the experiments should follow. The reinforcing material can be TiNi, TiC, TiAl, or AlNi. As such, the mechanical properties of ceramic-coated pipes may enhance whereby local reinforcement could increase the service life significantly.

- A multi-scale analysis simulation model in three dimensions that combines MSPH with the finite element method is needed to study the process parameters and avoid exhaustive experimentation.

REFERENCES

Advani, A. H., Thadhani, H. N., Grebe, H. A., Heaps, R., Coffin, C., & Kottke, T. (1992). Dynamic modelling of material and process parameter effects on self-propagating high-temperature synthesis of titanium carbide ceramics. *Journal of Materials Science, 27*(12), 3309-3317

Andreev, D. E., Sanin, V. N., Sachkova, N. V., & Yukhvid, V. I. (2011). Cermet-lined tubes from industrial wastes by centrifugal SHS. *International Journal of Self-Propagating High-Temperature Synthesis, 20*(1), 27-32

Anstis, G. R., Chantikul, P., Lawn, B. R., & Marshall, D. B. (1981). A Critical Evaluation of Indentation Techniques for Measuring Fracture Toughness: I, Direct Crack Measurements. *Journal of the American Ceramic Society, 64*(9), 533-538

Askeland, D. R., Fulay, P. P., & Wright, W. J. (2011). *The science and engineering of materials*: Thomson Engineering.

Avallon, E., Baumeister, T., & M.Sadegh, A. (1996). *Mark`s Standard Handbook for Mechanical Engineering.* (10 ed.): McGraw-Hill.

Balout, B., & Litwin, J. (2012). Mathematical Modeling of Particle Segregation During Centrifugal Casting of Metal Matrix Composites. *Journal of Materials Engineering and Performance, 21*(4), 450-462

Bandyopadhyay, T. K., Chatterjee, S., & Das, K. (2004). Synthesis and characterization of TiC-reinforced iron-based composites Part I On synthesis and microstructural characterization. *Journal of Materials Science, 39*(18), 5735-5742

Bandyopadhyay, T. K., & Das, K. (2004). Synthesis and characterization of TiC-reinforced iron-based composites Part II on mechanical characterization. *Journal of Materials Science, 39*(21), 6503-6508

Batra, R. C., & Zhang, G. M. (2008). Modified Smoothed Particle Hydrodynamics (MSPH) basis functions for meshless methods, and their application to axisymmetric Taylor impact test. *Journal of Computational Physics, 227*(3), 1962-1981

Belytschko, T., Rabczuk, T., Huerta, A., & Fernández-Méndez, S. (2004). Meshfree Methods *Encyclopedia of Computational Mechanics*: John Wiley & Sons, Ltd.

Bendjeddou, L., & Debili, M. (2010). Structure and Hardness of Al-Fe-Ti Alloys. *Defect and Diffusion Forum, 305*, 23-32

Bertolino, N., Anselmi-Tamburini, U., Maglia, F., Spinolo, G., & Munir, Z. A. (1999). Combustion synthesis of Zr–Si intermetallic compounds. *Journal of Alloys and Compounds, 288*(1–2), 238-248

Birman, V., & Byrd, L. W. (2007). Modeling and Analysis of Functionally Graded Materials and Structures. *Applied Mechanics Reviews, 60*(5), 195-216

Boyer, R. R. (1996). An overview on the use of titanium in the aerospace industry. *Materials Science and Engineering: A, 213*(1–2), 103-114

Brazhkin, V. V., & Lyapin, A. G. (2005). The Bridge Between the Ideal and Real Mechanical Properties for Superhard Materials. In J. Lee, N. Novikov & V. Turkevich (Eds.), *Innovative Superhard Materials and Sustainable Coatings for Advanced Manufacturing* (Vol. 200, pp. 1-16): Springer Netherlands.

Burkes, D. E., & Moore, J. J. (2006). Combustion Synthesis of a Functionally Graded NiTi-TiC[sub x] Composite. *Journal of Engineering Materials and Technology, 128*(3), 445-450

Carter, C. B., & Norton, M. G. (2007). *Ceramic materials: science and engineering*: Springer.

Chatterjee, S., Shariff, S. M., Majumdar, J. D., & Choudhury, A. R. (2008). Development of nano-structured Al_2O_3-TiB_2-TiN coatings by combined SHS and laser surface alloying. *International Journal of Advanced Manufacturing Technology, 38*(9-10), 938-943

Chermant, J., Deschanvres, A., & Osterstock, F. (1978). Toughness and Fractography of TiC and WC. *Crack Growth and Microstructure*, 891-901

Cleary, P., Prakash, M., Ha, J., Sinnott, M., Nguyen, T., & Grandfield, J. (2004). Modeling of cast systems using smoothed-particle hydrodynamics. *JOM Journal of the Minerals, Metals and Materials Society, 56*(3), 67-70

Cleary, P. W., & Monaghan, J. J. (1999). Conduction Modelling Using Smoothed Particle Hydrodynamics. *Journal of Computational Physics, 148*(1), 227-264

Contreras, L., Turrillas, X., Vaughan, G. B. M., Kvick, Å., & Rodríguez, M. A. (2004). Time-resolved XRD study of TiC-TiB2 composites obtained by SHS. *Acta Materialia, 52*(16), 4783-4790

Crider, J. F. (1982). Self-propagating high-temperature synthesis: a Soviet method for producing ceramic materials. *Ceram. Eng. Sci. Proc., 3*

Das, K., Bandyopadhyay, T. K., & Das, S. (2002). A Review on the various synthesis routes of TiC reinforced ferrous based composites. *Journal of Materials Science, 37*(18), 3881-3892

Denry, I. L., & Holloway, J. A. (2004). Elastic constants, Vickers hardness, and fracture toughness of fluorrichterite-based glass–ceramics. *Dental materials : official publication of the Academy of Dental Materials, 20*(3), 213-219

Ding, J., Deng, C. J., Yuan, W. J., Zhu, H. X., & Li, J. (2013). Preparation of porous TiC/C ceramics using wooden template in molten salt media. *Advances in Applied Ceramics, 112*(3), 131-135

Diomidis, N., Mischler, S., More, N. S., Roy, M., & Paul, S. N. (2011). Fretting-corrosion behavior of β titanium alloys in simulated synovial fluid. *Wear, 271*(7–8), 1093-1102

Du, B., Paital, S. R., & Dahotre, N. B. (2013). Synthesis of TiB2–TiC/Fe nano-composite coating by laser surface engineering. *Optics & Laser Technology, 45*(0), 647-653

Du, Z., Fu, H., Fu, H., & Xiao, Q. (2005). A study of ceramic-lined compound copper pipe produced by SHS-centrifugal casting. *Materials Letters, 59*(14-15), 1853-1858

Ebacher, G., Besner, M., Lavoie, J., Jung, B., Karney, B., & Prévost, M. (2011). Transient Modeling of a Full-Scale Distribution System: Comparison with Field Data. *Journal of Water Resources Planning and Management, 137*(2), 173-182

Ebenstein, D. M., & Pruitt, L. A. (2006). Nanoindentation of biological materials. *Nano Today, 1*(3), 26-33

Fan, Q., Chai, H., & Jin, Z. (1999). Mechanism of combustion synthesis of TiC–Fe cermet. *Journal of Materials Science, 34*(1), 115-122

Fan, Q., Chai, H., & Jin, Z. (1999). Microstructural evolution of the titanium particles in the in-situ composition of TiC-Fe by the combustion synthesis. *Journal of Materials Processing Technology, 96*(1-3), 102-107

Fan, R. H., Lü, H. L., Sun, K. N., Wang, W. X., & Yi, X. B. (2006). Kinetics of thermite reaction in Al-Fe_2O_3 system. *Thermochimica Acta, 440*(2), 129-131

Feng, K., Xiong, J., Sun, L., Fan, H., & Zhou, X. (2010). The process of combustion synthesis of WC-Co composites under the action of an electric field. *Journal of Alloys and Compounds, 504*(1), 277-283

Feng, K. Q., Hong, M., Xiong, J., Fan, H. Y., & Guo, Z. X. (2012). Mechanism of combustion synthesis of TiC-Fe composites under the action of an electric field. *Powder Metallurgy, 55*(3), 235-241

Feng, P., Liu, W., Farid, A., Wu, J., Niu, J., Wang, X., & Qiang, Y. (2012). Combustion synthesis of (Mo1−xCrx)Si2 (x=0.00–0.30) alloys in SHS mode. *Advanced Powder Technology, 23*(2), 133-138

Fengjun, C., & Yisan, W. (2007). Microstructure of Fe–TiC surface composite produced by cast-sintering. *Materials Letters, 61*(7), 1517-1521

Ferro, A. C., & Derby, B. (1995). Wetting behaviour in the Al-Si/SiC system: interface reactions and solubility effects. *Acta Metallurgica et Materialia, 43*(8), 3061-3073

Filimonov, V. Y., Korchagin, M., Evstigneev, V., & Lyakhov, N. (2009). *Anomalous decrease in the activation energy and initiation temperature of a thermal explosion in the mechanically activated composition 3Ni+ Al*.

Friedrich, A., Winkler, B., Juarez-Arellano, E. A., & Bayarjargal, L. (2011). Synthesis of Binary Transition Metal Nitrides, Carbides and Borides from the Elements in the Laser-Heated Diamond Anvil Cell and Their Structure-Property Relations. *Materials, 4*(10), 1648-1692

Fujii, H., Sato, T., Lu, S., & Nogi, K. (2008). Development of an advanced A-TIG (AA-TIG) welding method by control of Marangoni convection. *Materials Science and Engineering: A, 495*(1–2), 296-303

Gao, F., Guo, Z., & Lin, T. (2008). Preparation of W-C-Fe cermet lined steel pipes by SHS-centrifugal process. *Journal of University of Science and Technology Beijing, 30*(6), 648-651

Gao, J. W., & Wang, C. Y. (2000). Modeling the solidification of functionally graded materials by centrifugal casting. *Materials Science and Engineering: A, 292*(2), 207-215

Gennari, S., Maglia, F., Anselmi-Tamburini, U., & Spinolo, G. (2003). SHS (Self-sustained high-temperature synthesis) of intermetallic compounds: effect of process parameters by computer simulation. *Intermetallics, 11*(11–12), 1355-1359

Gingold, R. A., & Monaghan, J. J. (1977). Smoothed particle hydrodynamics-theory and application to non-spherical stars. *Monthly notices of the royal astronomical society, 181*, 375-389

Glorieux, B., Millot, F., Rifflet, J. C., & Coutures, J. P. (1999). Density of Superheated and Undercooled Liquid Alumina by a Contactless Method. *International Journal of Thermophysics, 20*(4), 1085-1094

Gowtam, D., Rao, A., Mohape, M., Khatkar, V., Deshmukh, V., & Shah, A. (2008). Synthesis and characterization of in-situ reinforced Fe-TiC steel FGMs. *International Journal of Self-Propagating High-Temperature Synthesis, 17*(4), 227-232

Greco, A., Raphaelson, S., Ehmann, K., Wang, Q. J., & Lin, C. (2009). Surface Texturing of Tribological Interfaces Using the Vibromechanical Texturing Method. *Journal of Manufacturing Science and Engineering, 131*(6)

Greenwood, N. N., & Earnshaw, A. (1997). *Chemistry of the Elements*: Butterworth-Heinemann.

Hamedi, M. J., Torkamany, M. J., & Sabbaghzadeh, J. (2011). Effect of pulsed laser parameters on in-situ TiC synthesis in laser surface treatment. *Optics and Lasers in Engineering, 49*(4), 557-563

Hassani, S. (2009). Dirac delta function *Mathematical Methods* (pp. 139-170): Springer.

He, Z. M., Ma, J., & Tan, G. E. B. (2009). Fabrication and characteristics of alumina-iron functionally graded materials. *Journal of Alloys and Compounds, 486*(1-2), 815-818

Hill, R., & Howard, C. (1987). Quantitative phase analysis from neutron powder diffraction data using the Rietveld method. *Journal of Applied Crystallography, 20*(6), 467-474

Ho, Y.-H., & Hwang, W.-S. (1996). The Analysis of Molten Steel Flow in Billet Continuous Casting Mold. *ISIJ International, 36*(8), 1030-1035

Hobosyan, M. A., Khachatryan, H. L., Davidova, A., & Kharatyan, S. L. (2011). Chemically activated combustion synthesis of MoSi2/Al cermet foams. *Chemical Engineering Journal, 170*(1), 286-291

Holt, J. B., & Munir, Z. A. (1986). Combustion synthesis of titanium carbide: Theory and experiment. *Journal of Materials Science, 21*(1), 251-259

Horvitz, D., Gotman, I., Gutmanas, E. Y., & Claussen, N. (2002). In situ processing of dense Al2O3–Ti aluminide interpenetrating phase composites. *Journal of the European Ceramic Society, 22*(6), 947-954

Huang, H.-Y. (2009). Effects of shielding gas composition and activating flux on GTAW weldments. *Materials & Design, 30*(7), 2404-2409

Huang, X., Zhang, L., Zhao, Z., & Yin, C. (2012). Microstructure Transformation and Mechanical Properties of TiC−TiB2 Ceramics Prepared by Combustion Synthesis in High Gravity Field. *Materials Science and Engineering: A, 553*, 105-111

Jiang, Q. C., Zhao, F., Wang, H. Y., & Zhang, Z. Q. (2005). In situ TiC-reinforced steel composite fabricated via self-propagating high-temperature synthesis of Ni–Ti–C system. *Materials Letters, 59*(16), 2043-2047

Jin, H.-B., Li, J.-T., Cao, M.-S., & Agathopoulos, S. (2009). Influence of mechanical activation on combustion synthesis of fine silicon carbide (SiC) powder. *Powder Technology, 196*(2), 229-232

Kakani, S. (2006). *Material science*: New Age International.

Kiara, A. (2010). *Analysis of the smoothed particle hydrodynamics method for free-surface flows.* Ph. D., Massachusetts Institute of Technology, Massachusetts Institute of Technology. Retrieved from http://hdl.handle.net/1721.1/57890 (648975362)

Knyazik, V. A., Merzhanov, A. G., Solomonov, V. B., & Shteinberg, A. S. (1985). Macrokinetics of high-temperature titanium interaction with carbon under electrothermal explosion conditions. *Combustion, Explosion, and Shock Waves, 21*(3), 333-337

Koc, R., & Folmer, J. (1997). Carbothermal synthesis of titanium carbide using ultrafine titania powders. *Journal of materials science, 32*(12), 3101-3111

Korchagin, M. A., Grigor'eva, T. F., Bokhonov, B. B., Sharafutdinov, M. R., Barinova, A. P., & Lyakhov, N. Z. (2003). Solid-state combustion in mechanically activated SHS systems. II. Effect of mechanical activation conditions on process parameters and combustion product composition. *Combustion Explosion and Shock Waves, 39*(1), 51-58

Krein, R., Friak, M., Neugebauer, J., Palm, M., & Heilmaier, M. (2010). L21-ordered Fe–Al–Ti alloys. *Intermetallics, 18*(7), 1360-1364

Ksandopulo, G. (2011). SHS in conditions of rotation: Thermal and concentration combustion limits for oxide systems taken as an example. *International Journal of Self-Propagating High-Temperature Synthesis, 20*(4), 220-223

Kurosaki, K., Saito, Y., Muta, H., Uno, M., & Yamanaka, S. (2004). Nanoindentation studies of UO2 and (U,Ce)O2. *Journal of Alloys and Compounds, 381*(1–2), 240-244

Lai, W., Munir, Z. A., McCoy, B. J., & Risbud, S. H. (1997). Centrifugally-assisted combustion synthesis of functionally-graded materials. *Scripta Materialia, 36*(3), 331-334

Le, A. T., Kim, D. J., Lee, J. R., Km, C. G., & Chung, H. S. (2008). Properties of ceramic layer formed by centrifugal thermit reaction with silicon sludge replacement. *Materials Transactions, 49*(8), 1868-1873

Le, M. T., Kim, C. G., Ahn, Y. K., & Chung, H. S. (2008). Effect of a glass addition on the ceramic layer prepared by a thermite reaction under a centrifugal force. *Journal of Ceramic Processing Research, 9*(5), 544-548

Lee, W. C., & Chung, S. L. (1997). Ignition Phenomena and Reaction Mechanisms of the Self-Propagating High-Temperature Synthesis Reaction in the Titanium—Carbon—Aluminum System. *Journal of the American Ceramic Society, 80*(1), 53-61

Li, B., Liu, Y., Cao, H., He, L., & Li, J. (2009). Rapid fabrication of in situ TiC particulates reinforced Fe-based composites by spark plasma sintering. *Materials Letters, 63*(23), 2010-2012

Li, P., Kandalova, E. G., & Nikitin, V. I. (2005). In situ synthesis of Al–TiC in aluminum melt. *Materials Letters, 59*(19–20), 2545-2548

Li, W. G., Zhou, H. P., Zhao, Y. L., Yin, L., & Chen, K. X. (2003). The finite element analysis of the thermal stress of the ceramic lined composite steel pipe prepared by combustion synthesis. [Article]. *Rare Metal Materials and Engineering, 32*, 241-244

Liang, Y., Han, Z., Lin, Z., & Ren, L. (2012). Study on the reaction behavior of self-propagating high-temperature synthesis of TiC ceramic in the Cu–Ti–C system. *International Journal of Refractory Metals and Hard Materials, 35*(0), 221-227

Lin, J., Moore, J. J., Moerbe, W. C., Pinkas, M., Mishra, B., Doll, G. L., & Sproul, W. D. (2010). Structure and properties of selected (Cr–Al–N, TiC–C, Cr–B–N) nanostructured tribological coatings. *International Journal of Refractory Metals and Hard Materials, 28*(1), 2-14

Lin, T., Guo, S., Yin, S., & Guo, Z. (2002). Combustion Characteristics of Aluminum-Iron Oxide in SHS-Gravitational Process. *Journal of University of Science and Technology Beijing, 9*(3), 221

Liu, M., & Liu, G. (2010). Smoothed particle hydrodynamics (SPH): an overview and recent developments. *Archives of computational methods in engineering, 17*(1), 25-76

Lucy, L. B. (1977). A numerical approach to the testing of the fission hypothesis. *The astronomical journal, 82*, 1013-1024

Luo, P., Dong, S. J., Shi, Q. Y., & Mei, Z. Q. (2012). Preparation of TiB2-TiC Intermetallic Phase via Mechanical Alloying. *Advanced Materials Research, 403*, 634-639

Maitre, A., Cathalifaud, P., & Lefort, P. (1997). *Thermodynamics of titanium carbide and the oxycarbide Ti 2 OC.* Paper presented at the High Temp Mater Proc.

Maslov, V. M., Neganov, A. S., Borovinskaya, I. P., & Merzhanov, A. G. (1978). Self-propagating high-temperature synthesis as a method for determination of the heat of formation of refractory compounds. *Combustion, Explosion and Shock Waves, 14*(6), 759-767

Meng, Q. S., Chen, S. P., Zhao, J. F., Zhang, H., Zhang, H. X., & Munir, Z. A. (2007). Microstructure and mechanical properties of multilayer-lined composite pipes prepared by SHS centrifugal-thermite process. *Materials Science and Engineering: A, 456*(1-2), 332-336

Merzhanov, & Borovinskaya. (1971). SELF-PROPAGATED HIGH-TEMPERATURE SYNTHESIS OF REFRACTORY INORGANIC COMPOUNDS. *Doklady Akademii Nauk USSR, 204*

Merzhanov, A. G. (1990). *Self-propagating high-temperature synthesis: twenty years of search and findings*. N.Y.: VCH Publ.

Merzhanov, A. G. (1996). Combustion processes that synthesize materials. *Journal of Materials Processing Technology, 56*(1-4), 222-241

Merzhanov, A. G. (2011). Thermally coupled SHS reactions. *International Journal of Self-Propagating High-Temperature Synthesis, 20*(1), 61-63

Miyazaki, E., & Odawara, O. (2000, May 29-June,2 2000). *Centrifugal-Thermit process for production of composite pipes of various size.* Paper presented at the Proceeding of the Fourth International Workshop on Material Processing at high Gravity, Clarkson University, Postdam, New York, USA.

Monaghan, J. J. (2005). Smoothed particle hydrodynamics. *Reports on Progress in Physics, 68*(8), 1703

Monaghan, J. J. (2011). A turbulence model for Smoothed Particle Hydrodynamics. *European Journal of Mechanics - B/Fluids, 30*(4), 360-370

Moore, J. J., & Feng, H. J. (1995). Combustion synthesis of advanced materials: Part I. Reaction parameters. *Progress in Materials Science, 39*(4–5), 243-273

Moradkhani, A., Baharvandi, H., Tajdari, M., Latifi, H., & Martikainen, J. (2013). Determination of fracture toughness using the area of micro-crack tracks left in brittle materials by Vickers indentation test. *Journal of Advanced Ceramics, 2*(1), 87-102

Mossino, P. (2004). Some aspects in self-propagating high-temperature synthesis. *Ceramics International, 30*(3), 311-332

Mousavian, R. T., Sharafi, S., Roshan, M. R., & Shariat, M. H. (2011). Effect of mechanical activation of reagents' mixture on the high-temperature synthesis of Al2O3–TiB2 composite powder. *Journal of Thermal Analysis and Calorimetry, 104*(3), 1063-1070

Mousavian, R. T., Sharafi, S., & Shariat, M. H. (2011). Microwave-assisted combustion synthesis in a mechanically activated Al-TiO2-H3BO3 system. *International Journal of Refractory Metals and Hard Materials, 29*(2), 281-288

Mu, L., Yin, S., Yanping, W., & Heyi, L. (1997). The characteristics of combustion in a centrifugal-thermite process. *Materials Science and Engineering, 32*

Muhammad, N., Rogers, B. D., & Li, L. (2013). Understanding the behaviour of pulsed laser dry and wet micromachining processes by multi-phase smoothed particle hydrodynamics (SPH) modelling. *Journal of Physics D: Applied Physics, 46*(9), 095101

Munir, Z. A. (2001). Self-propagating High-temperature Synthesis. In K. H. J. Buschow, W. C. Robert, C. F. Merton, I. Bernard, J. K. Edward, M. Subhash & V. Patrick (Eds.), *Encyclopedia of Materials: Science and Technology* (pp. 8323-8327). Oxford: Elsevier.

Munir, Z. A., Lai, W. N., Risbud, S. H., & McCoy, B. J. (2000). USA Patent No. US6136452. USA Patent.

Munoz, J. D., Arizmendi, A., Mendoza-Allende, A., & Montemayor-Aldrete, J. A. (1997). High temperature activation energy for plastic deformation of titanium carbide single crystals as a function of the C : Ti atom ratio. *Journal of Materials Science, 32*(12), 3189-3193

Muscat, D., Harris, R. L., & Drew, R. A. L. (1994). The effect of pore size on the infiltration kinetics of aluminum in titanium carbide preforms. *Acta Metallurgica et Materialia, 42*(12), 4155-4163

Narayan, J., Raghunathan, R., Chowdhury, R., & Jagannadham, K. (1994). Mechanism of combustion synthesis of silicon carbide. [Article]. *Journal of Applied Physics, 75*(11), 7252

Niihara, K. (1983). A fracture mechanics analysis of indentation-induced Palmqvist crack in ceramics. *Journal of Materials Science Letters, 2*(5), 221-223

Niu, Y., Zheng, X., Ding, C., Li, H., Hu, C., Ren, M., & Sun, J. (2011). Microstructure characteristics of silicon carbide coatings fabricated on C/C composites by plasma spraying technology. *Ceramics International, 37*(5), 1675-1680

Nowacki, J. (2012). Problems of brazing cermets and steels over large surfaces. *Welding International, 26*(8), 585-592

Odawara, O. (1982). Japan Patent No. US4363832. US4363832,204583: J. Sendai.

Odawara, O. (1988). *Metal-Ceramic Composite Pipes Produced by a Centrifugal-Thermit Process.* Paper presented at the International Symposium on Combustion and Plasma Synthesis of High Temperature Materials, San Francisco Calif.

Odawara, O. (1990). Long Ceramic-Lined Pipes Produced by a Centrifugal Thermit Process. *Journal of the American Ceramic Society, 73*(3), 629-633

Odawara, O. (2010). Mass-Forced SHS Technology of Ceramic Materials. *Advances in Science and Technology, 63*, 302-311

Odawara, O., & Ikeuchi, J. (1986). Ceramic Composite Pipes Produced by a Centrifugal-Exothermic Process. *Journal of the American Ceramic Society, 69*(4), C-80-C-81

Oliver, W. C., & Pharr, G. M. (1992). Improved technique for determining hardness and elastic modulus using load and displacement sensing indentation experiments. *Journal of materials research, 7*(6), 1564-1583

Oliver, W. C., & Pharr, G. M. (2004). Measurement of hardness and elastic modulus by instrumented indentation: Advances in understanding and refinements to methodology. *Journal of Materials Research, 19*(01), 3-20

Orru, R., Simoncini, B., Virdis, P. F., & Cao, G. (1996). Computer-aided manufacturing of centrifugal SHS coatings. *Computers & Chemical Engineering, 20*(Supplement 2), S1185-S1190

Palm, M., & Lacaze, J. (2006). Assessment of the Al–Fe–Ti system. *Intermetallics, 14*(10-11), 1291-1303

Park, J., Lee, H. J., Lee, S. W., Ha, J. S., Nagata, S., Hong, S. K., . . . Yao, T. (2012). Surface Polarity Effects on the Hydride Vapor Phase Epitaxial Growth of GaN on 6H-SiC with a Chrome Nitride Buffer Layer. *Electrochemical and Solid State Letters, 15*(5), H148-H152

Patil, K. C., Aruna, S. T., & Ekambaram, S. (1997). Combustion synthesis. *Current Opinion in Solid State and Materials Science, 2*(2), 158-165

Patil, K. C., Aruna, S. T., & Mimani, T. (2002). Combustion synthesis: an update. *Current Opinion in Solid State and Materials Science, 6*(6), 507-512

Pearce, M., & Marek, R. (1968). Formation of Silicon and Titanium Carbides by Chemical Vapor Deposition. *Journal of the American Ceramic Society, 51*(2), 84-87

Pecharsky, V. K., & Zavalij, P. Y. (2009). Determination and Refinement of the Unit Cell *Fundamentals of Powder Diffraction and Structural Characterization of Materials* (pp. 407-495): Springer US.

Pei, J., Li, J.-T., Liu, G. H., & Chen, K.-X. (2009). Fabrication of bulk Al_2O_3 by combustion synthesis melt-casting under ultra-high gravity. *Journal of Alloys and Compounds, 476*(1-2), 854-858

Persson, P., Jarfors, A. E., & Savage, S. (2002). Self-propagating high-temperature synthesis and liquid-phase sintering of TiC/Fe composites. *Journal of materials processing technology, 127*(2), 131-139

Pop, A. P., Mihoc, G. B., & Mitu, L. (2011). The systemic analysis of metals manufacturing used in MEMS fabrication. *Annals of the oradea university. Fascicle of management and technological. Engineering, 4*, 117-124

Price, D. J. (2012). Smoothed particle hydrodynamics and magnetohydrodynamics. *Journal of Computational Physics, 231*(3), 759-794

Quang, V. V. (2008). *Dynamical, Rheological and Thermal Studies of High Temperature Oxide Liquids.* PhD, Aberystwyth University, UK. (2009-01-22T09:07:57Z)

Rahimian, M., Parvin, N., & Ehsani, N. (2010). Investigation of particle size and amount of alumina on microstructure and mechanical properties of Al matrix composite made by powder metallurgy. *Materials Science and Engineering: A, 527*(4–5), 1031-1038

Rahimipour, M., & Ahmadi, A. (2010). The Effect of Graphite Formation on Wear Properties of Fe-TiC Composite Containing 6% by Volume of Titanium Carbide. *Majlesi Journal of Materials Engineering, 3*(1), 29-36

Rambo, C., Cao, J., Rusina, O., & Sieber, H. (2005). Manufacturing of biomorphic (Si, Ti, Zr)-carbide ceramics by sol–gel processing. *Carbon, 43*(6), 1174-1183

Rauscher, S., Scheydecker, M., Weisskopf, K., & Haug, T. (2000). Process for manufacturing ceramic metal composite bodies, the ceramic metal composite body and its use. *UNITED STATES PATENT AND TRADEMARK OFFICE GRANTED PATENT*

Razavi, M., & Rahimipour, M. R. (2009). Effect of mechanical activation on syntheses temperature of TiC reinforced iron-based nano-composite from ilmenite concentrate. *Ceramics International, 35*(8), 3529-3532

Razavi, M., Yaghmaee, M. S., Rahimipour, M. R., Salman, S., & Tousi, R. (2010). The effect of production method on properties of Fe–TiC composite. *International Journal of Mineral Processing, 94*(3–4), 97-100

Rendtel, A., Moessner, B., & Schwetz, K. A. (2008). Hardness and Hardness Determination in Silicon Carbide Materials *Advances in Ceramic Armor: A Collection of Papers Presented at the 29th International Conference on Advanced Ceramics and Composites, January 23-28, 2005, Cocoa Beach, Florida, Ceramic Engineering and Science Proceedings* (pp. 161-168): John Wiley & Sons, Inc.

Riedel, R. (2000). *Handbook of Ceramic Hard Materials* (Vol. 1). Darmstadt, Germany: Wiley-VCH, Weinheim.

Rietveld, H. (1967). Line profiles of neutron powder-diffraction peaks for structure refinement. *Acta Crystallographica, 22*(1), 151-152

Rogachev, A. S., & Baras, F. (2007). Models of SHS: An overview. *International Journal of Self-Propagating High-Temperature Synthesis, 16*(3), 141-153

Rubtsov, N. M., Seplyarskii, B. S., Chernysh, V. I., Tsvetkov, G. I., & Bichurov, G. B. (2010). Gas-phase nature of Si-N bond formation in the self-propagating high-temperature synthesis of silicon nitride by the azide method. *Theoretical Foundations of Chemical Engineering, 44*(4), 458-460

Ryu, Z., Zheng, J., Wang, M., & Zhang, B. (2001). Synthesis and characterization of silicon carbide whiskers. *Carbon, 39*(12), 1929-1930

Schlick, C. M. (2009). *Industrial Engineering and Ergonomics: Visions, Concepts, Methods and Tools Festschrift in Honor of Professor Holger Luczak*. Aachen, Germany: Springer Publishing Company, Incorporated.

Schmalzried, C., & Schwetz, K. A. (2010). Silicon Carbide- and Boron Carbide-Based Hard Materials *Ceramics Science and Technology* (pp. 131-227): Wiley-VCH Verlag GmbH & Co. KGaA.

Schubert, U., & Hüsing, N. (2005). *Synthesis of Inorganic Materials* (second ed.): Wiley-VCH.

Sen, Sivakumar, & Gay. (1997). *Computer Integrated Manufacturing.* Paper presented at the Proceedings of the 4th International Conference, Singapore.

Seo, S. H., Song, J. S., & Oh, M. H. (2010). USA Patent No. USPAT7767021.

Shen, Y. F., Zou, Z. G., Xiao, Z. G., Liu, K., Long, F., & Wu, Y. (2011). Properties and electronic structures of titanium aluminides–alumina composites from in-situ SHS process. *Materials Science and Engineering: A, 528*(4–5), 2100-2105

Shi, Y. L., Guo, Z. M., Hao, J. J., Lin, T., & Zeng, X. (2012). Processing and Abrasive Wear Study of Fe-Al_2O_3-TiC Composite by Pressureless Ti-Activated Reactive Melt Infiltration. *Advanced Materials Research, 482*, 933-937

Shinde, M. D., Pawar, A. U., Karmakar, S., Seth, T., Raut, V., Rane, S., . . . Amalnerkar, D. (2010). Synthesis of uncapped silver nanoparticles using DC arc plasma technique: effect of change in plasma gas on morphological properties. *International Journal of Nanotechnology, 7*(9), 1110-1119

Song, I., Wang, L., Wixom, M., & Thompson, L. T. (2000). Self-propagating high temperature synthesis and dynamic compaction of titanium diboride/titanium carbide composites. *Journal of Materials Science, 35*(10), 2611-2617

Sonnenburg, K., Smarsly, B. M., & Brezesinski, T. (2009). Non-oxidic nanoscale composites: single-crystalline titanium carbide nanocubes in hierarchical porous carbon monoliths. *Physical Chemistry Chemical Physics, 11*(17), 3300-3304

Subrahmanya, J., & Vijayakumar, M. (1992). Review Self-propagating high-temperature synthesis. *Journal of Materials Science, 27*(23)

Subramanian, R., & Schneibel, J. H. (1998). FeAl–TiC and FeAl–WC composites—melt infiltration processing, microstructure and mechanical properties. *Materials Science and Engineering: A, 244*(1), 103-112

Sun, L., Sneller, A., & Kwon, P. (2008). Fabrication of alumina/zirconia functionally graded material: From optimization of processing parameters to phenomenological constitutive models. *Materials Science and Engineering: A, 488*(1-2), 31-38

Takaffoli, M., & Papini, M. (2012). Material deformation and removal due to single particle impacts on ductile materials using smoothed particle hydrodynamics. *Wear, 274–275*(0), 50-59

Takamiya, H., Okada, H., Sakai, Y., & Fukui, Y. (2011). Smoothed particle hydrodynamics analysis on semi-solid metal forming process. *Japan Journal of Industrial and Applied Mathematics, 28*(1), 183-203

Tao, Y.-g., Xu, Y.-q., Pan, J., Gu, H., Qin, C.-y., & Zhou, P. (2012). Glycine assisted synthesis of flower-like TiO2 hierarchical spheres and its application in photocatalysis. *Materials Science and Engineering: B, 177*(18), 1664-1671

Taylor, J. A. (2012). Iron-containing intermetallic phases in Al-Si based casting alloys. *Procedia Materials Science, 1*, 19-33

Tian, Y. S., Chen, C. Z., Chen, L. X., & Huo, Q. H. (2006). Effect of RE oxides on the microstructure of the coatings fabricated on titanium alloys by laser alloying technique. *Scripta Materialia, 54*(5), 847-852

Tjong, S. C., & Ma, Z. Y. (2000). Microstructural and mechanical characteristics of in situ metal matrix composites. *Materials Science and Engineering: R: Reports, 29*(3–4), 49-113

Tong, L., & Reddy, R. G. (2005). Synthesis of titanium carbide nano-powders by thermal plasma. *Scripta Materialia, 52*(12), 1253-1258

Travitzky, N. (2012). Processing of ceramic-metal composites. *Advances in Applied Ceramics, 111*(5), 286-300

Vasilescu, C., Drob, S., Neacsu, E., & Mirza Rosca, J. (2012). Surface analysis and corrosion resistance of a new titanium base alloy in simulated body fluids. *Corrosion Science*

Vepřek, S. (2008). Nanostructured Superhard Materials *Handbook of Ceramic Hard Materials* (pp. 104-139): Wiley-VCH Verlag GmbH.

Voudouris, N., & Angelopoulos, G. N. (2011). Modeling of TiC Coating Growth on Plain Carbon Steels: Application to the Fluidized Bed CVD Process. [Article]. *High Temperature Material Processes, 15*(2), 143-150

Wang, H., He, D., Xu, C., Tang, M., Li, Y., Dong, H., . . . Zhu, W. (2013). Nanostructured diamond-TiC composites with high fracture toughness. *Journal of Applied Physics, 113*(4), 043505-043505-043504

Wang, J., Song, R. G., Lin, X., & Huang, W. D. (2009). Microstructure and properties of laser cladding TiC/TiAl composite coatings on γ-TiAl intermetallic alloy. *Surface Engineering, 25*(3), 196-200

Wang, J., & Wang, Y. (2007). In-situ production of Fe–TiC composite. *Materials Letters, 61*(22), 4393-4395

Wang, Y.-F., & Yang, Z.-G. (2007). Finite element analysis of residual thermal stress in ceramic-lined composite pipe prepared by centrifugal-SHS. *Materials Science and Engineering: A, 460-461*, 130-134

Washburn, M., & Coblenz, W. (1988). Reaction-formed ceramics. *American Ceramic Society Bulletin, 67*, 356-363

Watanabe, Y., Inaguma, Y., Sato, H., & Miura-Fujiwara, E. (2009). A Novel Fabrication Method for Functionally Graded Materials under Centrifugal Force: The Centrifugal Mixed-Powder Method. *Materials, 2*(4), 2510-2525

Wen, F., Lin, T., & Liu, X. (2012). Effects of Microstructure Characterization of SHS TiC Reinforced Fe Composite Coating. *Procedia Engineering, 27*(0), 1738-1743

Wiederhorn, S., Fields, R., Low, S., Bahng, G.-W., Wehrstedt, A., Hahn, J., . . . Tagawa, T. (2006). Mechanical Properties. In H. Czichos, T. Saito & L. Smith (Eds.), *Springer Handbook of Materials Measurement Methods* (pp. 283-397): Springer Berlin Heidelberg.

Xi, W., Wang, H., Li, J., & Shi, C. (2012). A NiAl- and TiC-reinforced Fe-based nanocomposite prepared by the rapid-solidification thermite process. *Materials Science and Engineering: A, 541*(0), 166-171

Xi, W., Yin, S., Guo, S., & Lai, H. (2000). Stainless steel lined composite steel pipe prepared by centrifugal-SHS process. *Journal of Materials Science, 35*(1), 45-48

Yamamura, K., Takiguchi, T., Ueda, M., Deng, H., Hattori, A. N., & Zettsu, N. (2011). Plasma assisted polishing of single crystal SiC for obtaining atomically flat strain-free surface. *CIRP Annals - Manufacturing Technology, 60*(1), 571-574

Yang, H., Zhao, H., Li, Z., Zhang, K., Liu, X., & Tang, C. (2012). Microstructure evolution process of porous silicon carbide ceramics prepared through coat-mix method. *Ceramics International, 38*(3), 2213-2218

Yeh, C. L., & Wang, H. J. (2011). Combustion synthesis of vanadium borides. *Journal of Alloys and Compounds, 509*(7), 3257-3261

Young, R. A. (1993). *Introduction to the Rietveld method*. Oxford, UK: Oxford University Press.

Yu, G., Yan, W., Wang, S., Su, B., & Tan, B. (2006). Toughening mechanism of lined Al_2O_3-ZrO_2 multiphase ceramics in SHS composite pipes. *Journal of University of Science and Technology Beijing, Mineral, Metallurgy, Material, 13*(2), 178-182

Yu, Z., Shugang, S., Hongjun, N., & Mingyu, H. (2010). Study on Microstructure and Properties of Ceramic-lined Steel Pipes Prepared by Self-propagating High-temperature Centrifugal Process. *Hot Working Technology*

Yukhvid, Sanin, & Merzhanov. (2000, May 29-June,2 2000). *The influence of High Artificial Gravity on SHS Processes.* Paper presented at the Proceeding of the Fourth International Workshop on Material Processing at high Gravity, Clarkson University, Postdam, New York, USA.

Yukhvid, V. I. (1992). Modifications of SHS processes. *Pure and Applied Chemistry, 64*(7), 977-988

Zhang, & Batra, R. C. (2004). Modified smoothed particle hydrodynamics method and its application to transient problems. *Computational Mechanics, 34*(2), 137-146

Zhang, F., Wolf, G., Wang, X., & Liu, X. (2001). Surface properties of silver doped titanium oxide films. *Surface and Coatings Technology, 148*(1), 65-70

Zhang, G., Xiao, G., & Fan, Q. (2011). Numerical modeling of field-activated combustion synthesis process of the B4C system. *Materials Research Bulletin, 46*(3), 345-349

Zhang, M. X., Hu, Q. D., Huang, B., Li, J. Z., & Li, J. G. (2011). Study of formation behavior of TiC in the Fe–Ti–C system during combustion synthesis. *International Journal of Refractory Metals and Hard Materials, 29*(3), 356-360

Zhang, S., Zhou, X., & Qian, D. (2002). Properties of Ceramic-Lined Composite Steel pipes and their application. *Key Engineering Materials, 217*, 219

Zhang, W. H., Yuan, C. L., & Li, Y. (2012). Al_2O_3-TiC/Fe Functionally Gradient Material Prepared by SHS Casting. *Materials Science Forum, 704-705*, 6-10

Zhou, Q., Xue, L., Yan, Q., Chen, S., Qin, J., Yi, X., & Yan, Y. (2010). Microstructure of ceramic-lined composite steel pipe prepared by SHS-centrifugal process. *Tezhong Zhuzao Ji Youse Hejin/Special Casting and Nonferrous Alloys, 30*(7), 671-673

Zhou, Y., Li, C.-J., Yang, G.-J., Wang, H.-D., & Li, G. (2010). Effect of self-propagating high-temperature combustion synthesis on the deposition of NiTi coating by cold spraying using mechanical alloying Ni/Ti powder. *Intermetallics, 18*(11), 2154-2158

Zhu, Y., Sun, S., Ni, H., & Huang, M. (2011). Study on microstructure and properties of ceramic-lined composite steel pipes produced by centrifugal-SHS process. *Key Engineering Materials, 464*, 434-437

LIST OF PUBLICATIONS

Published Papers

	Title	Year
1	A novel fabrication method for TiC-Al_2O_3-Fe functional material under centrifugal acceleration	2013
Authors	R. Mahmoodian, M.A Hassan,R. G. Rahbari, R. Yahya, M. Hamdi	
Journal	Composites Part B, 50,187-192	
2	The Effects of an unexpected ceramic coating phase at the head of a pipe on joining and postprocessing of a ceramic-lined composite pipe	2013
Authors	R. Mahmoodian, R.G Rahbari, M. Hamdi, M.A Hassan	
Journal	JOM Journal of the Minerals, metals, and Materials Society 65 (1), 80-85	
3	Another attempt to adopt a machine for SHS lining ceramics inside pipes	2012
Authors	R Mahmoodian, R Rahbari, M Hamdi, M Sparham	
Journal	High Temperature Material Processes, 16(1), 15-23	
4	In-situ formation of the intermetallic layer of TiC-Fe-Al_2O_3-TiAl/Ti3Al composites by centrifugal combustion synthesis	2013
Authors	R. Mahmoodian, M.A Hassan, R. Yahya, M. Hamdi, R. G. Rahbari	
Journal	Composites Part B, (Manuscript# JCOMB-D-13-00311), Accepted	
5	Safety issues improvement in ceramic lined composite pipe produced Using SHS method	2011
Authors	R Mahmoodian, R Rahbari, M Hamdi	
Conference	2nd International Conference on Industrial Engineering and Operations, Kuala Lumpur, Malaysia 660-662	

Papers in Review Process

	Title	Year
6	Study of Ti+C combustion synthesis reaction in a controlled declining temperature state	2013
Authors	R. Mahmoodian, M.A Hassan, Sajjad Gh., M. Hamdi	
Journal	Combustion science and technology, (Manuscript# GCST-2013-0084), under review	
7	Modified smoothed particle hydrodynamics (MSPH) for analysis of centrifugal assisted TiC-Fe-Al_2O_3 combustion synthesis	2013
Authors	M.A Hassan, R. Mahmoodian, M. Hamdi	
Journal	Scientific Reports, (Manuscript# SREP-13-04563-T), under review	
8	Ti-based ceramic fuel cell processing using a hybrid centrifugal thermite assisted technique	2013
Authors	R. Mahmoodian, M.A Hassan, M. Hamdi, F. Yusof, A. Dabbagh	
Journal	Functional Material letters, (Manuscript# FML-S-13-00358), under review	

Paper to be submitted soon

	Title	Year
9	Si-C synthesis using the hybrid reaction of a centrifugal-assisted thermite method	2013
Authors	R. Mahmoodian, R. Yahya, M.A Hassan, M. Hamdi, A. Dabbagh	
Journal	-	
10	Study of bulk TiC/C produced via a pressure-less DC focus plasma arc technique	2014
Authors	R. Mahmoodian, M.A Hassan, R. Yahya, M. Hamdi	
Conference	38th International Conference & Exposition on Advanced Ceramics and Composites (ICACC), January 26 – 31, 2014, Daytona Beach, Florida	